Journal of Nanomaterials

Advances in Smart Nanomaterials: Environmental Perspective

Lead Guest Editor: Soubantika Palchoudhury
Guest Editors: Nirupam Aich and Ziyou Zhou

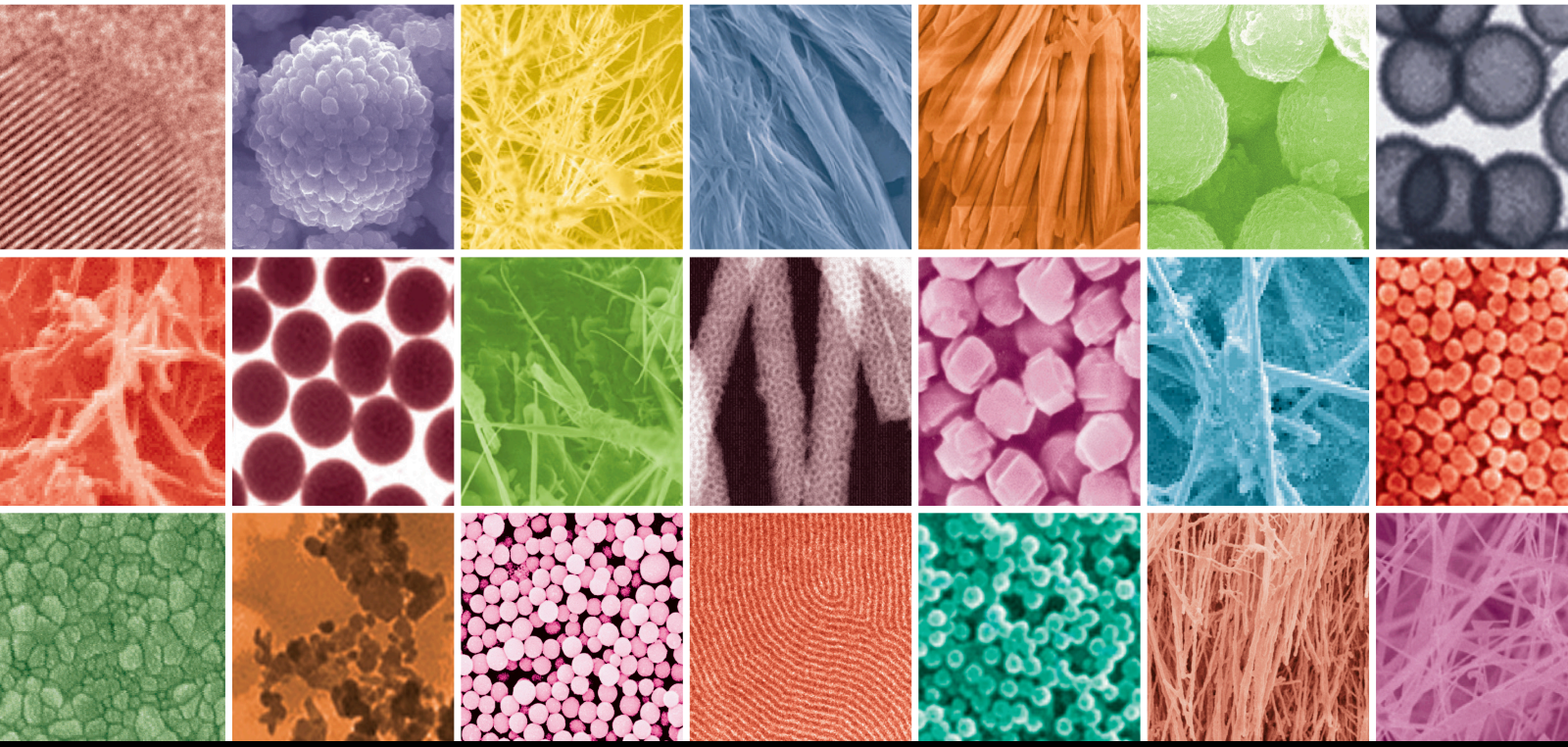

Advances in Smart Nanomaterials: Environmental Perspective

Journal of Nanomaterials

Advances in Smart Nanomaterials: Environmental Perspective

Lead Guest Editor: Soubantika Palchoudhury
Guest Editors: Nirupam Aich and Ziyou Zhou

Editorial Board

Contents

MnOx-CeOx Nanoparticles Supported on Graphene Aerogel for Selective Catalytic Reduction of Nitric Oxides

Zhuo Yao, Yuxiang Guo, Yujing Yang, Hong Huang, and Dianli Qu

Research Article (9 pages), Article ID 4239764, Volume 2019 (2019)

Hindawi
Journal of Nanomaterials
Volume 2020, Article ID 6715765, 2 pages
https://doi.org/10.1155/2020/6715765

Editorial

Advances in Smart Nanomaterials: Environmental Perspective

Soubantika Palchoudhury,[1] **Nirupam Aich**,[2] **and Ziyou Zhou**[3]

[1]*Civil and Chemical Engineering, University of Tennessee at Chattanooga, Tennessee, USA*
[2]*Civil, Structural, and Environmental Engineering, University of Buffalo, New York, USA*
[3]*Luna Innovations Inc., Virginia, USA*

Correspondence should be addressed to Soubantika Palchoudhury; soubantika-palchoudhury@utc.edu

Received 5 November 2019; Accepted 6 November 2019; Published 4 January 2020

There has been a remarkable progress in synthesis of "smart" nanomaterials over the past decade from realizing lightweight graphene structures, carbon-metal nanohybrids, biohybrid self-assembly nanoarchitectures, and stimuli-responsive polymeric materials to shape-controlled inorganic nanoparticles. These new nanomaterials have opened transformative possibilities in application, beyond our current technologies. They have catalyzed key innovations in flexible electronics, drug delivery, catalysis, environmental remediation, and sustainable agriculture. Amid these emerging new materials, risk assessment of nanomaterials has been a major research thrust for our field over the past decade. New nanometrology parameters have been established to suitably depict the properties and behavior of novel nanomaterials in the environment. Emerging material characterization techniques realized over the past decade have facilitated transformative advances in understanding complex properties of smart nanomaterials for new applications. There is a tremendous environmental significance to the progress of each of these in advanced nanomaterials. Though risk assessment has been widely reported in the field of environmental nanoscience, the huge potential of new nanomaterial-based technologies for environmental applications has not been closely captured. In this thematic special issue, we aim to highlight both the emerging applications of smart nanomaterials and the discoveries in nanomaterial toxicity from an environmental perspective. The following sections briefly describe the accepted papers in this special issue.

In the feature article by A. Boutchuen et al., plant growth in legumes was significantly enhanced by nearly 230-830% with one drop of hematite nanoparticles. Unlike conventional fertilizers that have to be directly added to the soil or hydroponic environment in large quantities, the nanoparticle dispersions were applied via a highly sustainable and novel seed presoaking approach. The hematite nanoparticles served as a more efficient and high-throughput Fe-enriching nutrient for the plants as compared to the currently available bulk fertilizers. The method is immensely attractive from an environmental aspect as a small quantity of the nanofertilizer could induce increased plant growth and vitality without the need for direct addition of chemicals to the environment. Another novelty of the study was a new, multimodal material characterization approach to assess the uptake and transport of hematite nanofertilizer within the plants using Fourier transform infrared spectroscopy (FTIR), hyperspectral imaging, and inductively coupled plasma optical emission spectroscopy (ICP-OES).

The feature review article by B. Gayen et al. captured one of the newest members of the nanoworld, carbon dots. Carbon dots were invented accidentally during the purification of single-walled carbon nanotubes in 2004. These nanoparticles, typically <10 nm in size, have the structural advantage of containing both sp^2 and sp^3-hybrid carbon networks compared to the sp^2 hybridization of graphene quantum dots. The detailed architecture, progress in synthesis strategies, and novel applications of the quantum dots are presented in the article. The combination of upconversion photoluminescence, chemiluminescence, phosphorescence, and band gap transition properties makes carbon dots a unique class of material. In addition, carbon dots show highly

promising results in a variety of key application areas including environmentally friendly light harvesting devices, drug delivery and bioimaging, chemical sensors, surface-enhanced Raman spectroscopy, and detectors. Therefore, this nanomaterial will be notable in terms of future technological progress.

K. Workeneh and team suggested a new and sustainable hydroxyapatite-adsorbent material synthesized from egg-shell waste for fluoride remediation from groundwater. The authors reported Langmuir and Freundlich adsorption isotherm models for this novel hydroxyapatite adsorbent, based on detailed fluoride adsorption experiments. The removal of fluoride was highly influenced by the pH, and a near complete removal of fluoride was achieved at pH 3 under controlled study environments. The egg-shell-derived hydroxyapatite showed 81% removal of fluoride with real groundwater samples, suggesting highly promising application of this material in groundwater remediation.

In the paper by M. V. Nsom et al., a pectin-starch magnetite nanocomposite was demonstrated as a new and more efficient adsorbent for methylene blue dye to purify the recycled waters from textile industries. The sponge-like nanocomposite was synthesized using a coprecipitation technique and characterized in detail. It was found that a higher starch : pectin ratio in the nanocomposite material facilitated increased adsorption of the dye from the textile effluent. This study further highlights the progress in new nanomaterials for environmental remediation applications.

P. D. Du et al. synthesized a new class of metal-organic framework, MIL-101, as a highly efficient heterogeneous photocatalyst for the degradation of Remazol Black B dye. The paper reported detailed material characterization, adsorption/desorption isotherms, and the catalytic activity of MIL-101. The mechanism of photocatalytic activity of this novel metal-organic framework was also suggested by the authors. Photocatalysis in MIL-101 was facilitated through electron transfer from the photoexcited organic ligands to the metal cluster of the metal-organic framework. This new photocatalyst exhibited excellent performance from the recyclability and stability perspective. The MIL-101 catalyst reported for the first time in this special issue could have transformative impacts in sustainable remediation of organic pollutants.

Another key review article of this special issue by T. A. Dontsova et al. highlighted the immense progresses made in the synthesis of metal oxide nanomaterials and nanocomposites and their significance in our current ecology and environmental applications. Metal oxides have been one of the most heavily researched families of nanomaterials over the past decade, both due to their unique structure and application potential. Special focus was given to TiO_2, ZnO, SnO_2, ZrO_2, and Fe_3O_4 nanomaterials. Different synthesis strategies, material properties, and application prospects of metal oxide nanomaterials were discussed in detail in this review.

Z. Yao et al. addressed another major area of environmental remediation, removal of nitric oxide pollutants released from industrial and vehicular sources. The paper reported new MnO_x-CeO_x hybrid nanoparticles supported on a lightweight and flexible graphene aerogel interface as monolithic catalysts for low temperature selective catalytic reduction of nitric oxide by ammonia. The hierarchically porous network of graphene aerogel and the nanoscale size provided key advantages to this material in terms of catalytic activity at lower operational temperatures. As a result, the novel nanocomposite catalyst induced a significantly high (90%) conversion rate of nitric oxides over a wide temperature range of 200–300°C, which is highly attractive for practical applications.

In the paper by X. Hu et al., novel MnO_2 nanospheres of hollow morphology were synthesized via a selective etching technique using $MnCO_3$ sacrificial templates. This new nanomaterial was applied as an adsorbent for pollutant dyes from water using methyl orange as a model dye. The influence of pH, contact time, and dye concentrations on the adsorption capacity of the hollow MnO_2 nanospheres was reported in this paper. The study also presented the adsorption kinetics of these novel nanoparticles and the fundamental thermodynamics behind their adsorption capacity. This new report is highly beneficial for applications in wastewater purification.

New findings on the risk assessment aspect of nanomaterials were captured by M. Patel et al. in this special issue. *Caenorhabditis elegans* (*C. elegans*) have been widely used as complete model organisms in risk assessment of different nanomaterials, but toxicity effects on subsequent generations of the organism are largely unknown. The article by M. Patel et al. reported key findings about the impact of engineered Au nanoparticles on generations of *C. elegans*. Au nanoparticles used in this study were synthesized via a facile biological route from chloroauric acid with pomegranate peel extract as the reducing agent. It was discovered that the Au NPs negatively affected the fertility of *C. elegans* and the reproductive toxicity was inherited by the next generations.

Conflicts of Interest

The authors declare no conflict of interest.

Acknowledgments

We thank our authors for their valuable contributions that made this special issue a success. We greatly appreciate our reviewers for their time and effort. SP acknowledges NSF REU award #1852042 for the support of this Special Issue.

Soubantika Palchoudhury
Nirupam Aich
Ziyou Zhou

Hindawi
Journal of Nanomaterials
Volume 2019, Article ID 3451307, 19 pages
https://doi.org/10.1155/2019/3451307

Review Article

Carbon Dots: A Mystic Star in the World of Nanoscience

Biswajit Gayen,[1] Soubantika Palchoudhury,[2] and Joydeep Chowdhury[3]

[1]*Department of Chemistry, Dr. Sudhir Chandra Sur Degree Engineering College, JIS Group of College, 540 Dum Dum Road, Kolkata 700074, India*
[2]*Department of Civil and Chemical Engineering, University of Tennessee at Chattanooga, Chattanooga, Tennessee 37403, USA*
[3]*Department of Physics, Jadavpur University, 88, Raja S. C. Mallick Road, Kolkata 700032, India*

Correspondence should be addressed to Joydeep Chowdhury; joydeep72_c@rediffmail.com

Received 15 March 2019; Accepted 17 June 2019; Published 11 December 2019

Academic Editor: Oscar Perales-Pérez

Carbon dots (CDs) have received significant attention worldwide from the beginning of this century, and recently, it has bloomed in every branch of applied sciences. Because of their outstanding physical and chemical properties together with biocompatibilities, CDs find a wide spectrum of applications in drug delivery, explosive detection, chemical sensing, food safety, bioimaging, energy conversion, photocatalysis, etc. This brief review is focused on the synthesis of CDs and their applications. The photophysical properties of CDs are also discussed herewith.

1. Introduction

Carbon dots (CDs) have emerged as most precious gifts in nanotechnology because of their magical properties and applications. CDs are typically carbon nanoparticles, most of them with average diameter less than 10 nm [1, 2]. These materials are derived from organic compounds and are stable in aqueous media which is extremely significant in terms of biological points of view [3]. Surface engineering plays a significant role for CDs in diversified applications like explosive detection, chemical sensing, food safety, bioimaging, drug delivery, energy conversion, and photocatalysis. Photophysical and chemical properties of CDs vary dramatically by tuning their shapes and sizes and also by doping heteroatoms such as oxygen, nitrogen, phosphorus, sulfur, and boron [4]. Moreover, photostability, high quantum yield, biocompatibility, low toxicity, water solubility, good conductivity, and environmental friendliness of CDs receive additional advantages over other well-recognized quantum dots (QDs) like grapheme quantum dots (GQDs), metal oxides (ZnO, TiO_2), and inorganic QDs (ZnO-PbS, CdSe, CuInS/ZnS, and CuInS/ZnS). In fact, noncarbon QDs are not much graceful in their field of applications compare to CDs, because of their serious health and environmental issues [5, 6]. CDs can be synthesized from both natural and synthetic organic precursors. Synthetic methodologies that are very frequently used in this concern are microwave irradiation, hydrothermal treatments, ultrasonic irradiation, laser ablation, electrochemical, arc discharge, and pyrolysis [7]. This short review has been specifically focused on the synthetic methodologies of CDs and their wide applications in pure and applied sciences.

2. Discovery of CDs

CDs were discovered accidentally in 2004 at the time of purification of single wall carbon nanotubes (SWCNTs) by Xu et al. [8]. Two years later, in 2006, Sun et al. first synthesized stable photoluminescent carbon nanoparticles of different sizes and named them "carbon quantum dots" (CQDs) [9]. Within a year, water soluble CDs passivated with poly-propionylethylenimine-*co*-ethylenimine had been reported by Sun et al. The as-prepared CDs showed two-photon-induced luminescence spectra and were utilized to detect human breast cancer MCF-7 cells [10].

3. Architecture of CDs

CD is the youngest member in the family of nanoworld. They are commonly spherical in shape having average diameter less than 10 nm [3]. GQDs have only sp^2-hybridized carbon framework whereas CDs are composed of both sp^2 and sp^3 hybrid carbon networks [11]. Moreover, they can be easily functionalized with hydroxyl, carboxyl, carbonyl, amino, and epoxy groups over their surfaces thereby offering extra advantages for binding with both inorganic and organic moieties (Figure 1) [12]. The functionalities specifically allow the surfaces of CDs to espouse either with hydrophilic or with hydrophobic character which finally provide the necessary thermodynamic stabilities in different solvents especially in water [13]. In addition to these, bare carbon nanoparticles do not exhibit any kind of photoluminescent activities while their surface modifications lead to exhibit strong photoluminescent signals [7]. Surface modification of CDs by different functionalities, passivating agent and solvent, reflects a smart variation in their properties [14].

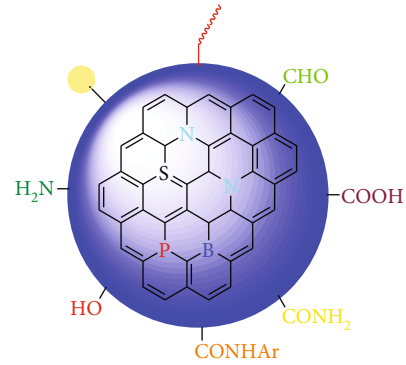

Figure 1: Generalized structure of CDs.

4. Synthesis

In the last few years, a number of facile synthetic methodologies have been developed for making CDs with varied functionalities and photophysical properties. Synthetic pathways for CDs are mainly classified into two categories: (a) "bottom-up" and (b) "top-down" approaches (Figure 2).

4.1. Bottom-Up Approach. In the "bottom-up" methodology, CDs are synthesized from small molecules by a microwave irradiation, hydrothermal, and pyrolysis method.

4.1.1. Microwave Irradiation Method. Microwave- (Mw-) assisted synthetic methodologies have recently received significant attention in the scientific community because of their time-saving, energy-efficient, and eco-friendly nature. In this methodology, carbonization of small organic molecule occurs by microwave heating within a very short period of time (Figure 3). In 2009, Zhu et al. first reported CDs with the aid of Mw methodology from carbohydrates with excellent photophysical properties within a very short period of reaction time [15]. Liu et al. synthesized photoluminescent CDs from glycerol and 4,7,10-trioxo-1,13-tridecylenediamine as a surface-passivating agent by a Mw irradiation method. They reported moderately high quantum yield (QY) of 12% due to the incorporation of amino groups (NH_2) over the surface of CDs (Figure 3) [16]. Feng et al. synthesized CDs with QY~46% by Mw irradiation from silkworm chrysalis [17]. The as-synthesized CDs were used in bioimaging due to their low toxicity and photoluminescent nature. Recently, Liu et al. synthesized photoluminescent CDs by a Mw heating method from citric acid, L-cysteine, and dextrin with high QY of 22%. As-synthesized CDs are reported to be photostable and were used in the detection of Cu^{2+} in drinking water [18]. Recently, Sun et al. synthesized *N*-ethylcarbazole functionalized CDs by a microwave method that exhibited very nice photoinduced redox properties [19].

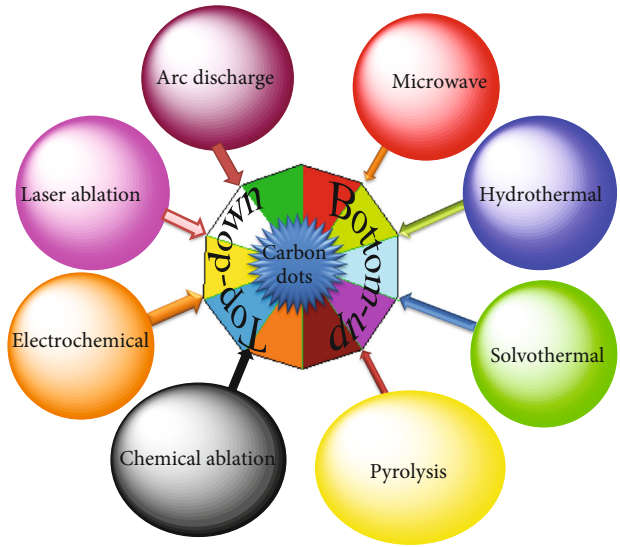

Figure 2: Different synthetic methodologies.

4.1.2. Hydrothermal Method. Hydrothermal methodology perhaps is the most promising method in recent years for the synthesis of CDs due to their nontoxic, environment friendly, low cost, and easy operational technique. In this methodology, a solution of organic precursors is sealed in a hydrothermal synthetic reactor where reaction occurs at high temperature and pressure (Figure 4(a)). In 2010, Zhang et al. first reported a one-pot hydrothermal method to make CD from ascorbic acid in the presence of ethanol as solvent. QY and average particle sizes of their synthesized CDs were 6.79% and ~2 nm, respectively [20]. Pang et al. reported synthesis of codoped nitrogen and sulfur in CDs (NS-CDs) derived from methionine by a hydrothermal method [21]. NS-CDs, as recovered in their synthesis, exhibit selective detections of heavy metal ions in water. Recently, Shen et al. reported synthesis of highly photoluminescent CDs from sweet potato as a natural source of carbon by a hydrothermal method with high QY. The as synthesized CDs utilized for detection of Fe^{3+} (Figure 4) [22]. In another report, Zhang et al. prepared surface-modified CDs by polyethylenimine from hyaluronic acid with very high QY 26%. The as-synthesized CDs used those photoluminescent CDs in tumor targeting and gene delivery [23].

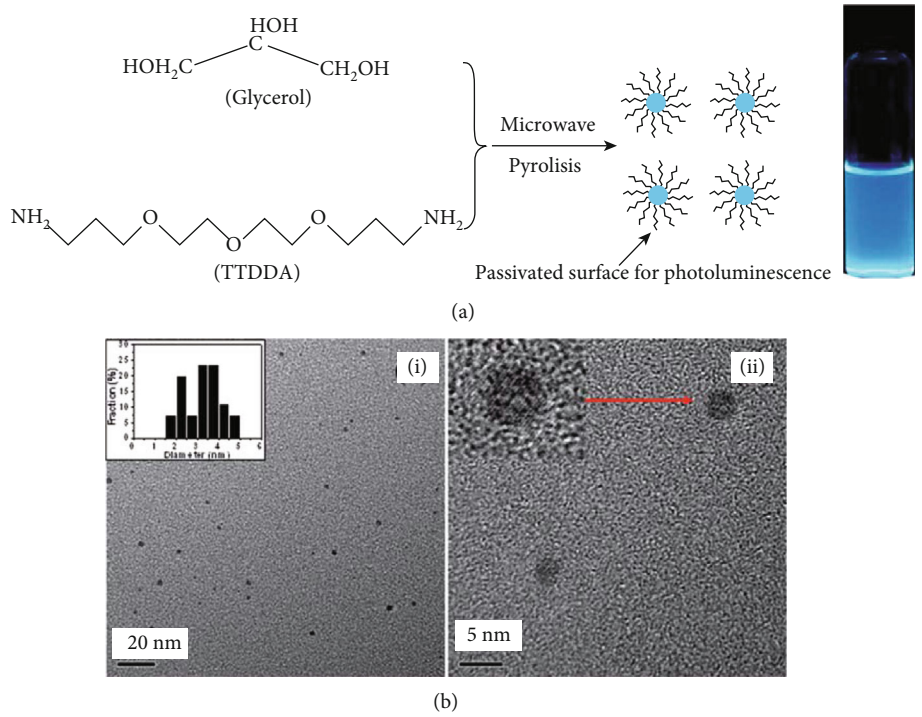

Figure 3: (a) Synthesis of CDs by a Mw irradiation method. (b) HR-TEM image of as-synthesized CDs as obtained from the Mw irradiation method: (i) 20 nm (size distribution histogram shown inset); (ii) 5 nm (magnification of a single nanoparticle shown inset) (reproduced with permission from [16]).

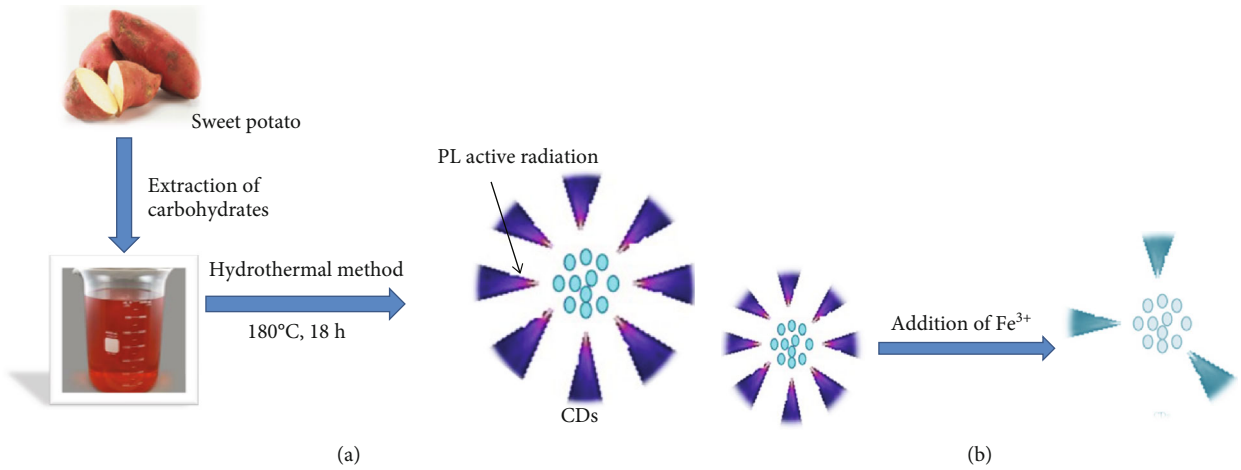

Figure 4: (a) Synthesis of CDs by a hydrothermal method from sweet potato; (b) sensing of Fe^{3+} ions by as-synthesized CDs.

4.1.3. Pyrolysis Method. Pyrolysis is a facile method to synthesize CDs from organic compounds by simple chemical reactions carried out at very high temperature in the presence of strong acid or alkali (Figure 5(a)). Martindale et al. synthesized CDs of average diameter ~6 nm by pyrolysis of citric acid at 180°C for generation of hydrogen fuel-utilizing solar energy [24]. Guo et al. synthesized stable CDs from hair (keratin) by a one-step pyrolysis method at 200°C for 24 hours of reaction time. They successfully recovered CDs and used their CDs in the detection of Hg^{2+} with higher sensitivity and selectivity [25]. Recently, Rong et al. synthesized highly photoluminescent nitrogen-doped CDs (N-CDs) derived from guanidinium chloride and citric acid by a pyrolysis method and fluorescence quenching observed in the presence of Fe^{3+} (Figure 5) [26]. N-CDs obtained by their synthesis were profoundly used in metal ion detections and in bioimaging.

4.2. Top-Down Approach. In the "top-down" methodology, CDs are synthesized by a laser ablation, electrochemical oxidation, and arc discharge method.

4.2.1. Electrochemical Method. The electrochemical method is used to synthesize ultrapure CDs from larger molecular

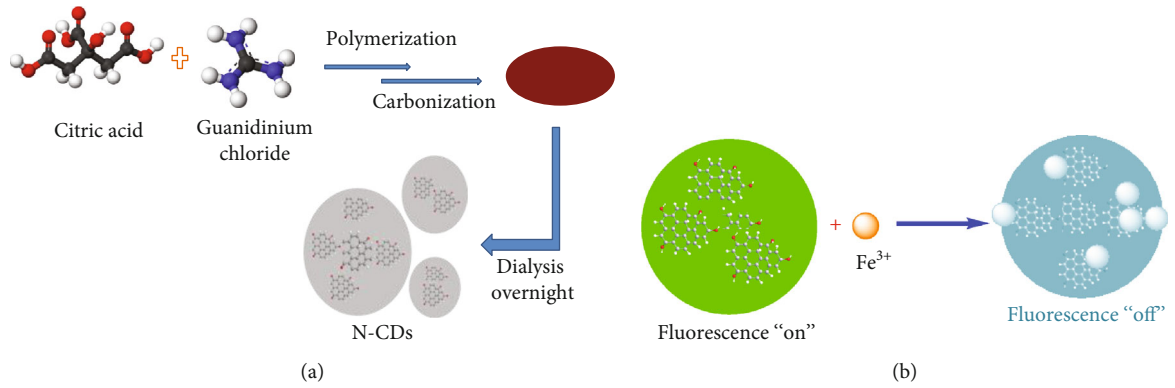

Figure 5: (a) Synthesis of CDs by a pyrolysis method; (b) fluorescence quenching in the presence of Fe^{3+}.

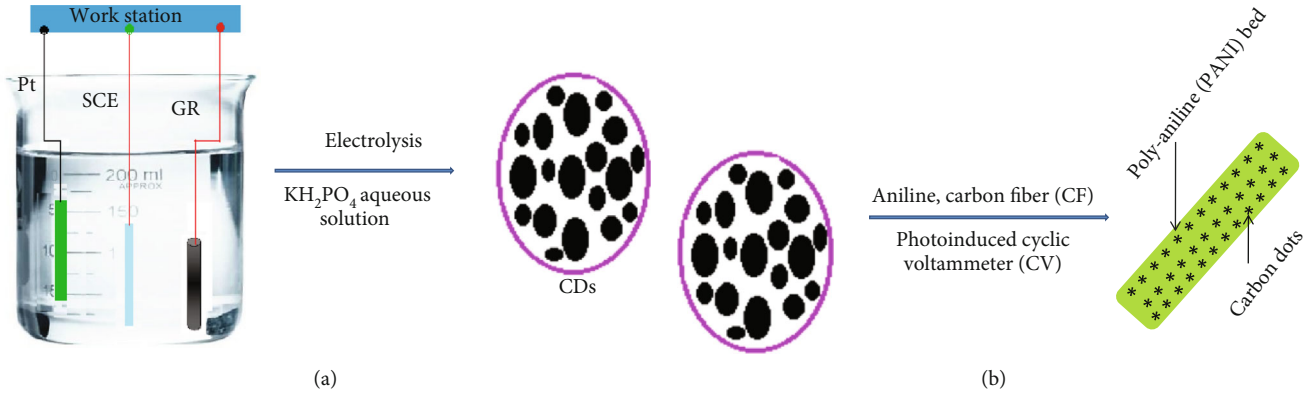

Figure 6: (a) Synthesis of CDs by an electrochemical method; (b) formation of CD-PANI hybrid composite from as-synthesized CDs.

matter like carbon nanotube, graphite, and carbon fiber by an electrolytic process where larger organic molecules are used as electrode in the presence of proper electrolytes (Figure 6). Zhou et al. first reported synthesis of CDs from multiwalled carbon nanotubes in the presence of tetrabutylammonium perchlorate as electrolyte [27]. Zheng et al. synthesized water soluble pure CDs by an electrochemical method using graphite as electrode in the presence of phosphate buffer at neutral pH. The as-prepared CDs were successfully applied as potential biosensor [28]. Li et al. prepared crystalline CDs by an electrochemical method from graphite. The as-prepared CDs exhibited size-dependent upconversion photoluminescence (PL) properties and are used in photocatalysis [29]. Recently, CD with polyaniline hybrid was synthesized by an electrochemical technique with high QY and purity. The as-synthesized CD-polyaniline composite reported to exhibit high capacitance and used in energy-related devices (Figure 6) [30].

4.2.2. Laser Ablation Method. The laser ablation technique has been widely used for making of CDs of varied sizes. In laser ablation route, complex organic macromolecules are exposed under laser radiation operated in CW or in pulsed mode and nanosized carbon particles are detached from the larger molecular structures (Figure 7(a)). Synthesis of CDs by a laser ablation technique was first reported by Sun et al. in 2006 from graphite powder [9]. They synthesized CDs upon laser excitation from a Nd:YAG (1064 nm, 10 Hz) source in an atmosphere of argon at 900°C and 75 kPa. Thongpool et al. synthesized CDs from bulk graphite in the presence of ethanol using a Nd:YAG laser of wavelength 1064 nm. The synthesized CDs showed a broad absorption spectrum peaked at 325 nm (Figure 7(b)) [31]. Recently, photoluminescent CDs of ~3 nm size have been synthesized by a laser irradiation technique from carbon glassy particles in the presence of polyethylene glycol 200. CDs so prepared are applied in bioimaging for cancer epithelial human cells [32].

4.2.3. Arc Discharge Method. CDs by an arc discharge method had been an accidental event. This method was first reported by Xu et al. during synthesis of SWCNTs [8]. Electrical discharge across two graphite electrodes results in the formation of small carbon fragment or CDs (Figure 8). Bottini et al. reported CDs derived from pristine and SWCNTs by means of an arc discharge method with bright PL in the violet-blue and blue-green region, respectively [33]. Recently, Boron- and nitrogen-doped QDs were synthesized by the arc discharge method from graphite. They used B_2H_6 for doping boron and NH_3 for nitrogen (Figure 8) [34].

5. Photophysical Properties of CDs

CDs, as obtained by different synthetic methodologies and precursors, show excellent optical properties and exhibit absorption, photoluminescence (PL), chemiluminescence

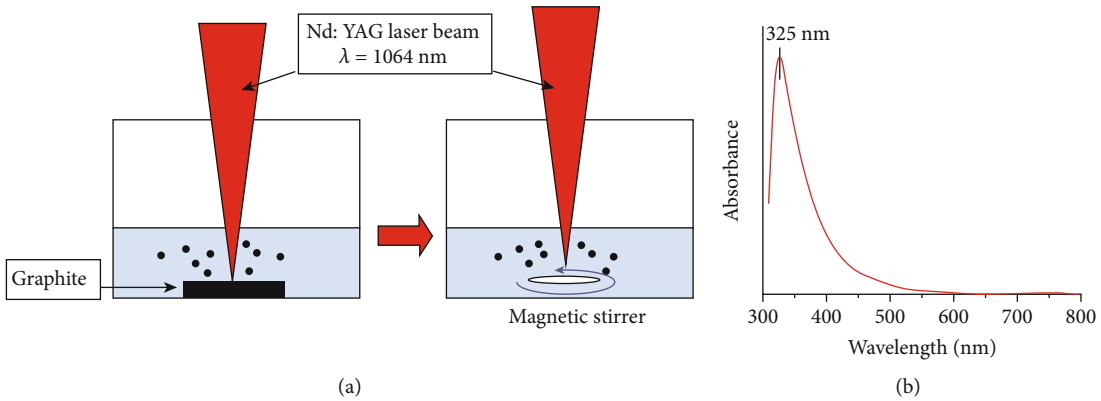

FIGURE 7: (a) Synthesis of CDs by a laser ablation method; (b) absorption spectrum of as-synthesized CDs (reproduced with permission from [31]).

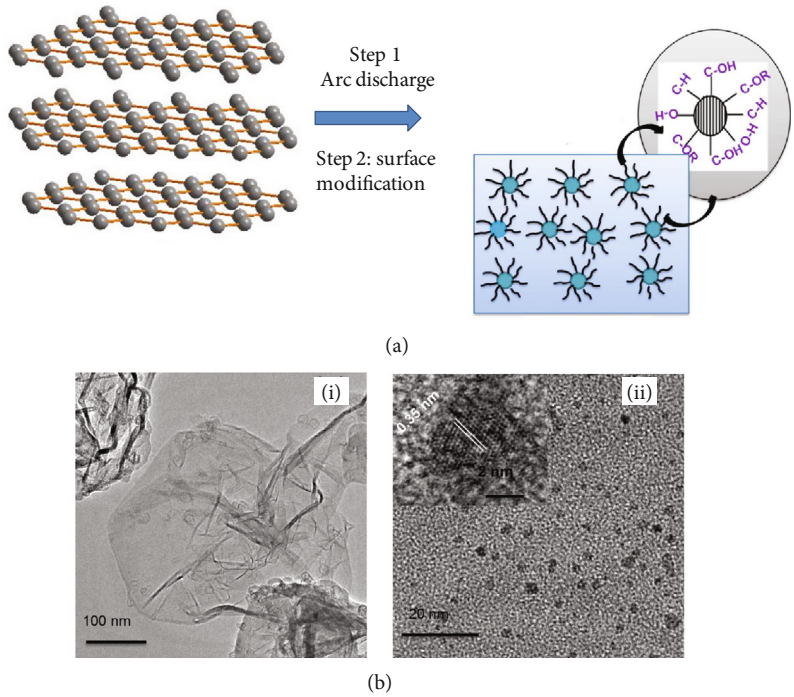

FIGURE 8: (a) Synthesis of quantum dots by an arc discharge method; (b) (i) TEM and (ii) HR-TEM image of as-synthesized quantum dots (reproduced with permission from [34]).

(CL), and phosphorescence spectra. In this section, the optical properties of CDs are described in brief.

5.1. Absorption Spectroscopy (UV-Vis). CDs generally exhibit broad optical absorption maxima in the ultraviolet (UV) region (250-350 nm) together with weak absorption tail in the visible region of UV-Vis spectra [35]. The absorption peaks appear at around ~240 nm are due to π-π^* electronic transition of C=C bonds, and peaks at around ~340 nm are owed to n-π^* transition from C=O bonds present as functionalities (Figure 9(a)) [36]. Surface engineering can modify the corresponding absorption spectra of CDs that can alter their emission spectra also [37]. Doping of heteroatom can also regulate absorption spectra for doped CDs by altering % heteroatom because of their alteration in the π-π^* energy level [38]. Surface defects ingrained in CDs are considered to be responsible for broad spectral features in their absorption spectra [39]. Moreover, carbonyl and amino functionalities promote red shifts of band maxima in UV-Vis spectra due to the variations in HOMO-LUMO energy levels of CDs because of fictionalizations (Figure 9(b)) [40].

5.2. Photoluminescence Spectroscopy. CDs show excellent PL behaviors. Appearance of photoluminescent peaks (λ_{em}) and their intensities depend on excitation wavelengths (λ_{ex}). Multiple PL spectra thus can easily be attained from single

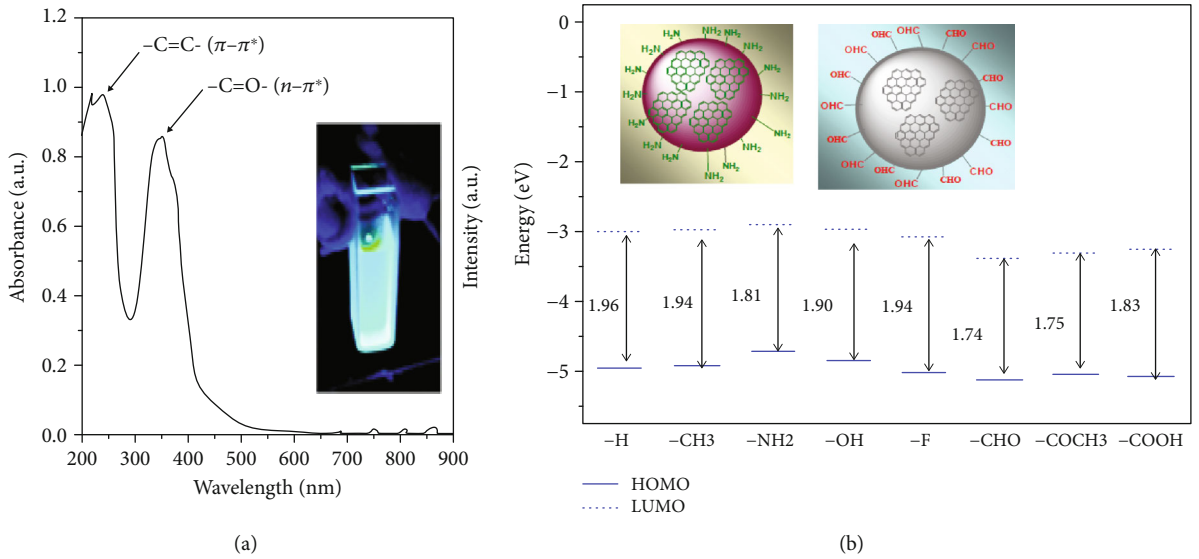

Figure 9: (a) UV-Vis absorption spectrum of CDs; (b) variation of HOMO-LUMO energy gap of CDs with functionalities (reproduced with permission from [36, 40]).

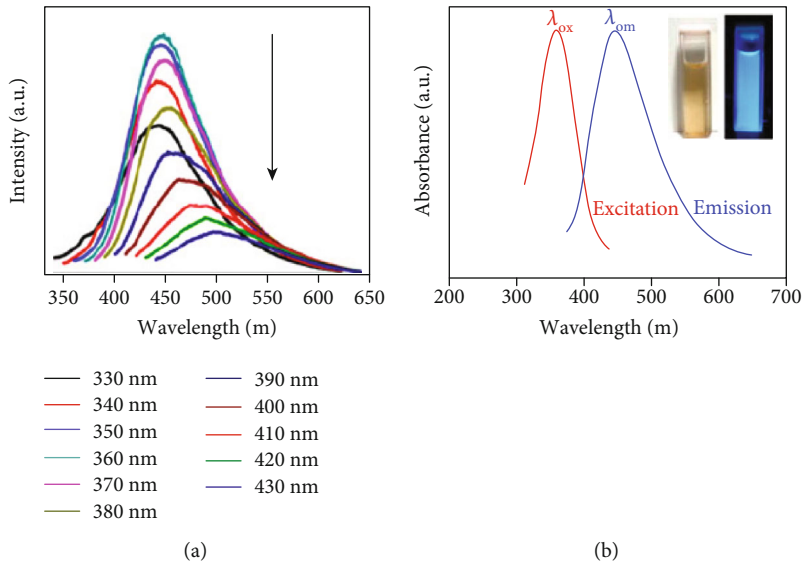

Figure 10: (a) PL spectra of CDs with variation of excitation wavelengths (λ_{ex}); (b) excitation and PL emission spectra of CDs in the blue-green region (reproduced with permission from [41]).

CD (Figure 10(a)). The PL maximum for CDs commonly appears in the blue and green region of the spectra (Figure 10(b)) [41]. PL behavior of CDs can be controlled by varying the initial precursors and synthetic methodologies and by surface engineering [42]. Interestingly, PL that generates from CDs almost remains unchanged under irradiation for long time [43] *vis-à-vis* to organic dyes that are susceptible to photobleaching [8]. Sun et al. reported CDs with an average particle size ~1.54 nm. The as-synthesized CDs exhibit PL spectra with peak maxima centred at ~460 nm, 540 nm, and 620 nm upon excitations with 380 nm, 460 nm, and 540 nm wavelengths, respectively [44]. Wang et al. reported N-CDs derived from *m*-aminobenzoic acid with highly intense PL maxima, peak appeared at 415 nm. They further reported amine-passivated CDs and used them as biosensors for the sensing of Fe^{3+} and pH [45]. Sun et al. reported CDs passivated with oligomeric ethylene glycol diamine (PEG_{1500N}). These passivated CDs exhibit photoinduced electron transfer (PET) reactions from quenching of its PL in the presence of 4-nitrotoluene, 2,4-dinitrotoluene, Ag^{+}, and N,N-diethylaniline (DEA) [46].

5.2.1. Upconversion PL. Few CDs exhibit upconversion PL. During upconversion, peak maxima in emission spectra appear at shorter wavelengths even upon excitation with longer wavelengths. Upconversion PL of CDs are effective in terms of higher efficiency and their inherent ability to penetrate within deep tissue without causing any damage

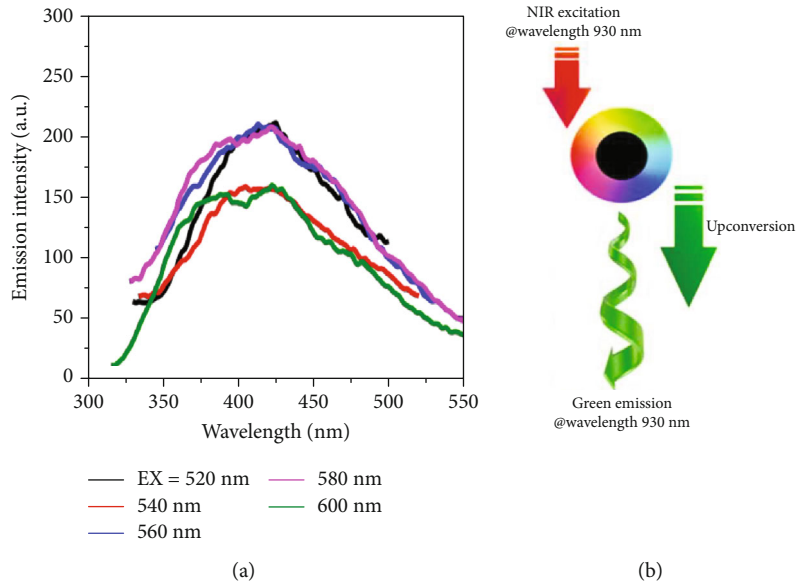

Figure 11: Upconversion PL spectra of CDs as obtained: (a) excitation wavelength (λ_{ex}) above 500 nm exhibited peak maxima at around ~420 nm; (b) above 900 nm (NIR region) exhibited green PL at 530 nm (reproduced with permission from [49, 51]).

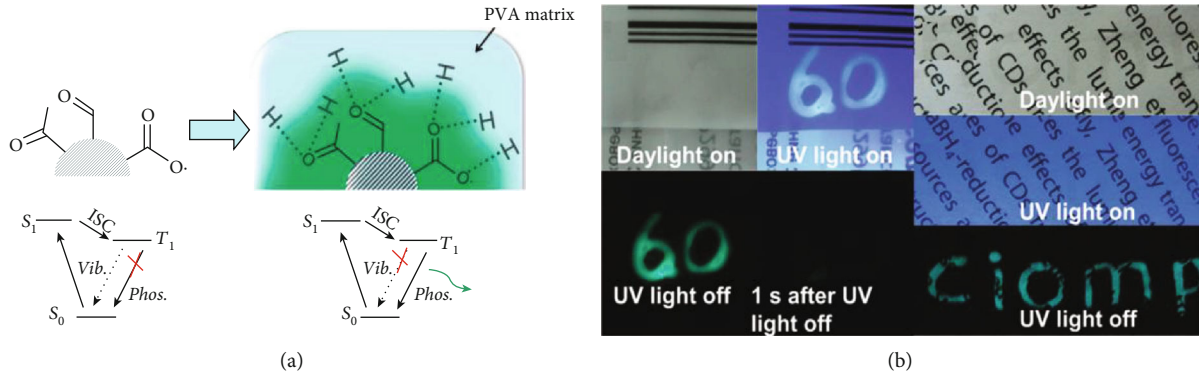

Figure 12: (a) Mechanism for room temperature phosphorescence showed by CD-PVA matrix; (b) visibility of invisible written words by CDs by UV light (reproduced with permission from [53]).

[47, 48]. Gude reported citric acid- and tyrosine-based N-CDs and showed upconversion PL by irradiation above 500 nm of λ_{ex} (Figure 11(a)) [49]. Cui et al. synthesized green photoluminescent CDs from ammonium citrate and ammonia. These CDs exhibited upconversion behavior and were used for HeLa cell imaging [50]. Recently, Gogoi et al. reported CDs derived from citric acid by the hydrothermal method which showed bright upconverted PL. The as-synthesized CDs, when exited with near infrared (NIR) radiation, PL spectra appeared in the UV-Vis region (Figure 11(b)) [51].

5.3. Phosphorescence Spectroscopy. CDs are reported to exhibit phosphorescence spectra. Carbonyl groups present on the spherical surface of CDs offer exited triplet state which are responsible for phosphorescence in CDs [52]. Deng et al. reported room temperature phosphorescence (RTP) of CDs derived from disodium salt of EDTA (ethylene diamine tetra-acetic acid) in polyvinyl alcohol (PVA) by forming CD-PVA composite. They obtained phosphorescence peak at 500 nm having extended lifetime of 380 ms by exiting the sample with 325 nm (Figure 12) [53]. Li et al. synthesized CDs from citric acid and urea by the hydrothermal method which showed excellent PL behaviors. Subsequently, they prepared CD-CA powder by centrifuging CD and cyanuric acid (CA) mixture. The aqueous solution of CD-CA powder so prepared is reported to emit green phosphorescent light that can be observed even with the naked eye at room temperature [54].

5.4. Chemiluminescence Spectroscopy. Chemiluminescence (CL) of CDs is another feature which is not explored too much as yet and endowed with wide prospects for future research. Lin et al. first reported CL of CDs where they obtained intense CL in the presence of $KMnO_4$ and cerium (IV) ion. Hole generated within the matrix of CD by various oxidants combine with electron and release energy as CL [55]. Zhao et al. reported CL from CD derived from glucose and PEG_{1500} as a surface-passivating agent (Figure 13(a)).

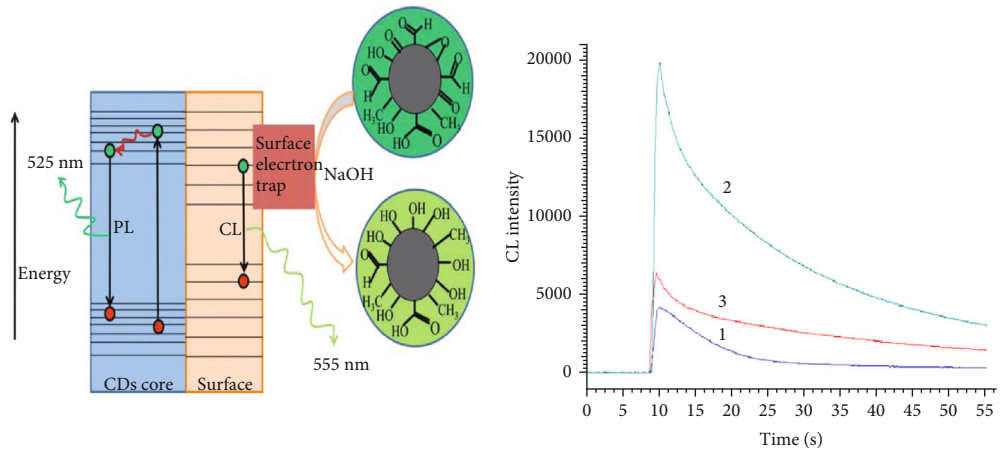

Figure 13: (a) Mechanism for CL generated from CDs (b) enhance CL intensities diagram for (1) luminol-$K_3Fe(CN)_6$, (2) CDs-luminol-$K_3Fe(CN)_6$, and (3) CDs-luminol-$K_3Fe(CN)_6$-2-methoxyestradiol (reproduced with permission from [56, 57]).

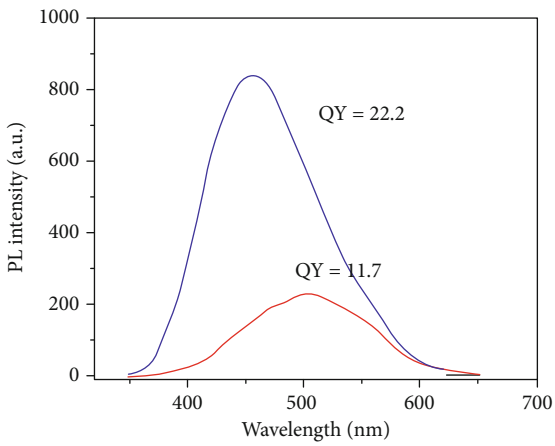

Figure 14: Tuning of QY for CDs (i) PL spectrum of quantum dots having carboxylic acid as functionality (red line) and (ii) having hydroxyl functionality (blue line) (reproduced with permission from [61]).

The as-synthesized CDs exhibited CL in the presence of dissolved oxygen present in an aqueous alkali medium [56]. Recently, Zhang et al. reported an enhancement of CL intensity for the luminol-$K_3Fe(CN)_6$ system when in the presence of CDs at alkaline pH. The as-fabricated CD composite material is used for the detection of anticancer drug 2-methoxyestradiol (Figure 13(b)) [57].

5.5. Quantum Yield. QY is the most important parameter for light-emitting systems and provides an index for their future possibilities to be used as photodevices. It has been reported that high QY can be achieved by surface fabrication on CDs [58, 59]. CDs synthesize from common precursors containing electron-withdrawing groups (EWGs) like carboxylic and epoxy decrease electron density in CDs and produce relatively low QY [60]. Surface engineering can convert EWGs to electron-donating groups (EDGs) by easy chemical conversion without much more alteration in the basic shape of the carbon nanoparticles (Figure 14) [61]. Doping CDs with heteroatom is another alternative approach that can generate new CDs with high QY by changing the bandgap and electron densities [62, 63]. Initially, CDs originated from candle soot, graphite, and citric acid exhibited very low QY maximum up to 10%. Recently, researchers have achieved very high QY. Zhuo et al. synthesized CDs with high QY of 80% in an aqueous medium by using citric acid and glutathione as starting materials [64].

5.6. Spectroscopic Origin of CDs. Significant progress in synthetic methodologies has been noticed in the last few years while explanation about the photophysical properties especially the PL of CDs has not been clearly understood until now. The PL behaviors of CDs are now being explained by (a) the bandgap transition and (b) the surface defect model.

5.6.1. Bandgap Transition Model. Quantum confinement effect (QCE) is thought to be responsible for PL in CDs. The size of CDs plays an important role for PL of CDs as because QCE are size-dependent phenomenon [65]. Li et al. reported alkali-assisted electrochemical fabrication of CDs varying size 1.2 nm to 3.8 nm. The as-prepared CD exhibited blue PL with emission maximum ~450 nm. The emission wavelengths can be easily tuned from blue to green, green to yellow, and red by altering sizes of CDs (Figure 15(a)) [29]. Theoretical modelling studies showed PL spectrum peak positions, intensities varied with variation of their particle sizes [66]. Sk et al. claimed higher electron delocalization of electron in the sp^2-hybridized cyclic network due to the presence of varied functionalities and doped heteroatom reduced bandgap energy by virtue of the QCE and resulted red-shifted PL spectra (Figure 15(b)) [67].

5.6.2. Surface Defect Model. PL exhibited by CDs are also envisaged due to surface defects formed in CDs which helps to capture excitations. Surface defects in CDs are normally generated due to surface oxidation, presence of functionalities, and doping of heteroatoms [68]. Surface oxidations lead

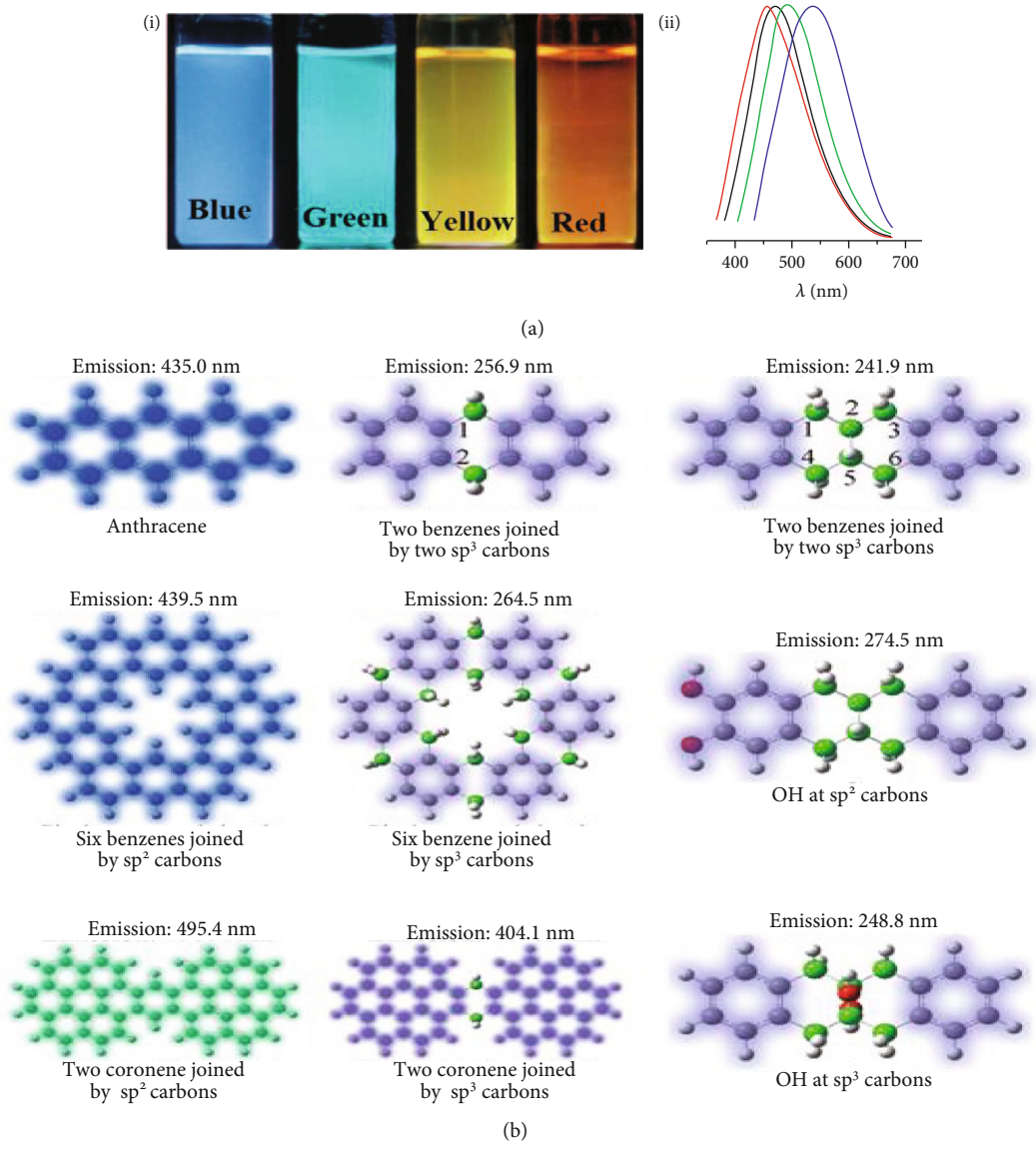

FIGURE 15: Tuning of PL for CDs: (a) (i) visible colours observed by the naked eye for different CDs; (ii) PL spectra for blue, green, yellow, and red CDs showed by red, black, green, and blue lines (b) with sp^2- and sp^3-hybrid functionalities (reproduced with permission from [29, 67]).

to higher surface defects, resulting in larger number of emissive sites within CDs (Figure 16(a)) [39, 69, 70]. Enhanced photoluminescent property has been explained by doping of heteroatom that altered electron density in the cyclic structure of CDs (Figure 16(b)) [71] and multiphoton PL mechanism followed by anti-Stoke transitions (Figure 16(c)) [49]. Chen et al., Hu et al., and other groups noticed significant variation of PL spectra of CDs which had been attributed to surface defects resulting in the alteration of bandgap energies [69]. Ding et al. observed red-shifted PL of CDs from 440 to 625 nm by rising oxygen percentage in CD matrix [70]. Tetsuka et al. reported similar phenomenon where they varied nitrogen content by functionality of primary amine [72].

6. Applications of CDs

6.1. Detection of Toxic Chemicals in Food. Serious health issues are destined due to the presence of toxic materials like heavy metal ions [73], pesticides [74], antibiotics [75], preservatives [76], and nonbiodegradable chemicals over a certain permissible limit in food staff [77]. CD-based PL quenching sensors are successfully employed for ultrasensitive detections of heavy and highly poisonous metal ions like Hg^{2+} (Figure 17(a)) [73, 78], Cr^{6+} [79], Pb^{2+} [80], Cu^{2+} [81], Al^{3+} [82], and Co^{2+} [83]. In most cases, linear relationships between quenching of PL intensity of CDs and concentration of metal ion present in samples have been observed [84]. Along with metal ions, anions like F^- [85], PO_4^{3-} [86], I^- [87], and $HClO_4^-$ [88] can also be detected by utilizing CD-based "off-on" logic gate sensor. These types of CD-based sensor are very much selective and independent over the presence of other ions (Figure 17(b)) [73, 89].

Excessive use of veterinary drugs in poultries can create severe health issues in animal bodies. Antibiotic used in poultries may leave antibiotic residues above danger level in animal-derived food products like in milks, eggs,

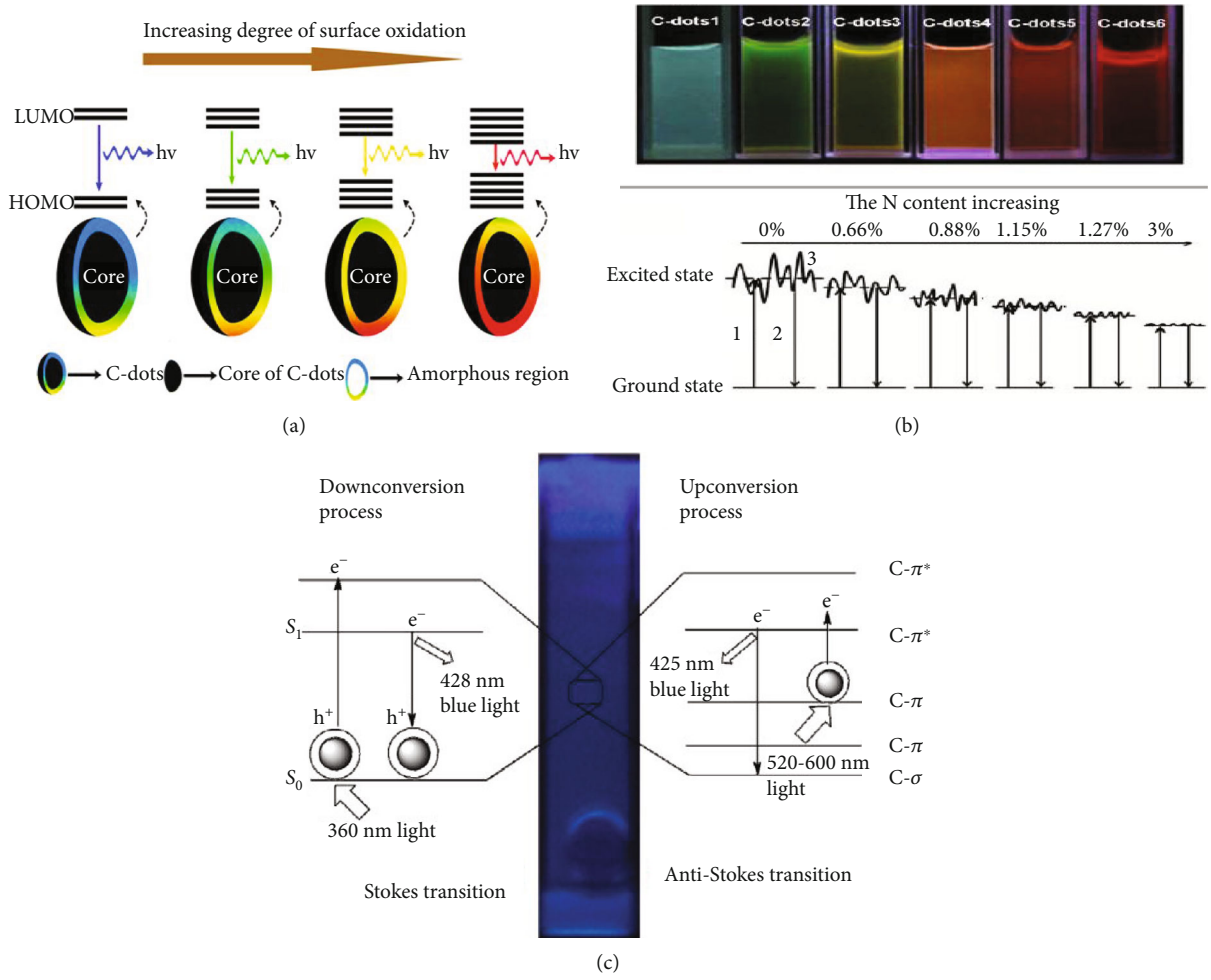

FIGURE 16: Tuning of PL for CDs: (a) alternation of PL intensities and peak positions by increasing surface oxidation; (b) peak positions by increasing the percentage of doping heteroatoms; (c) Stokes and anti-Stokes PL diagram for CDs (reproduced with permission from [49, 70, 71]).

and meats [90]. Residue corresponding to antibiotics was determined by CD-based composite sensor where either PL quenching (turn off) or enhancement (turn on) was observed. Antibiotics or their residues like tetracycline [91], cephalexin [92], ciprofloxacin [93], norfloxacin [94], oxytetracycline, and chlortetracycline [95] have been detected from raw milk, egg, meat, and human urine sample. Estrogen drugs those were used in animals, birds, for fast growth can also be traced out by CD-based sensor very effectively [96].

The presence of bacteria like *Escherichia coli* [97], *Bacillus subtilis*, *Listeria monocytogenes* [98], and *salmonella typhimurium* [99] in food is also detected by composite CDs. Other food additives like sugar, vitamin, amino acid, and different dyes used in food items are detected by means of CD-based sensor (Figure 17(c)) [100–102].

6.2. Detection of Explosives. Detection and monitoring of explosives have drawn worldwide attention [103] in concern with national and international security [104]. Picric acid, trinitrotoluene (TNT), and dinitrotoluene (DNT) are very commonly recognized explosives whose presence even in trace concentrations proves life threatening to mankind [105]. Thus, the detections of these chemicals are a challenging task for researchers. Technologies which are normally used for their detections are very expensive. Interestingly, CDs or CD-based composites are proved useful for their detections. There are several reports found where CDs utilized for sensitive detection of explosive with better efficiency and low-cost technology [106, 107]. Zhang et al. reported amino-containing surface-fabricated CDs that have the potential to detect TNT even at ultralow concentrations by the PL quenching technique [106]. Tb-CD-composites constructed with CDs and rare earth metal terbium (Tb) are employed for screening of picric acid ranging from 500 nM to 100 mM (Figure 18) [107].

6.3. Chemical Sensors. CD-based logic gate sensors are extensively used in the detection of different chemicals. YES, INH, NOT, NOR, AND, integrative NOR and INH, and integrative IMP plus NOR plus AND logic gates have been developed to sense different chemicals [108]. Jana et al. reported a composite logic gate sensor (CD-MnO_2) for sensing low concentration of NaAc and H^+, respectively (Figure 19(a))

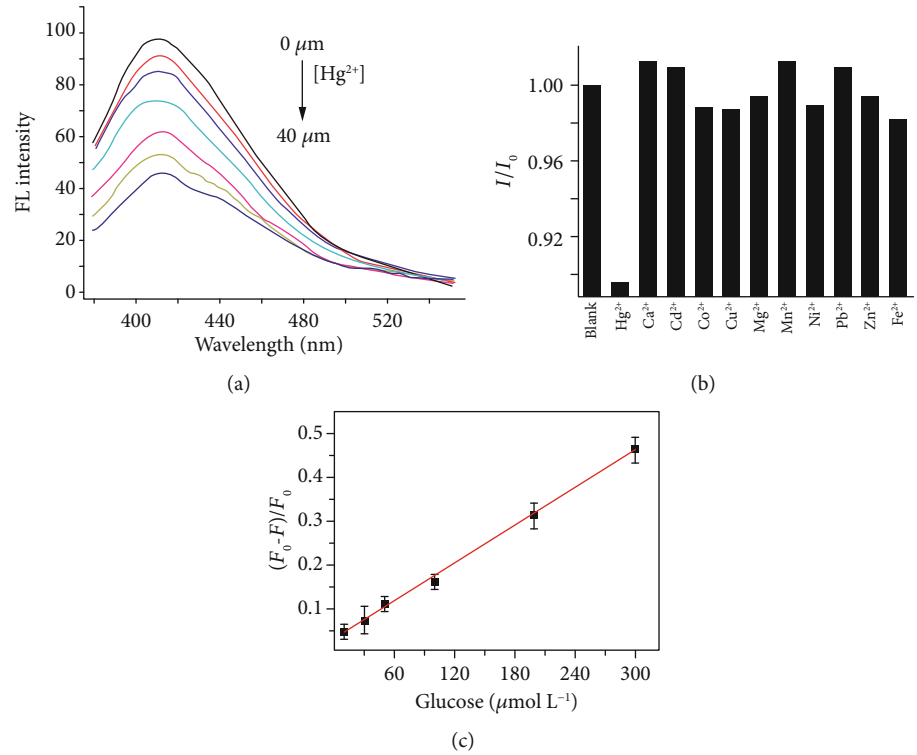

FIGURE 17: Detection of Hg^{2+} composite-CDs: (a) PL spectral intensities decrease with increasing of Hg^{2+} concentration; (b) selectivity CDs on Hg^{2+} over the presence of other metal ions; (c) a typical linear plot between PL intensities and glucose concentrations (reproduced with permission from [73, 100]).

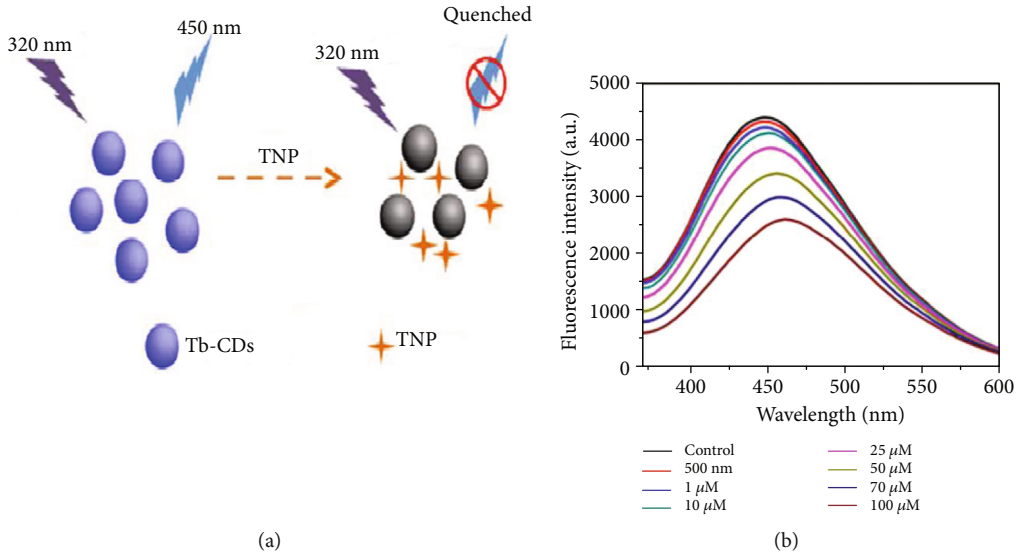

FIGURE 18: (a) Schematic presentation for determination of picric acid; (b) decrease of PL spectral intensities with increasing picric acid concentrations (reproduced with permission from [107]).

[109]. Interestingly, PL active N-CDs derived from D-(+)-glucose and spermine selectively interacted with right-handed B-DNA and modified it to left-handed Z-DNA under physiological salt conditions (Figure 19(b)) [110]. CDs derived from chitosan [111] and anchored with metal [112] find wide potential applications in biosensings, in cellular imagings, and in drug deliveries. Metal ion like Hg^{2+} ion and organic compound like glutathione have been simultaneously determined by CD-based logic gate sensor up to micromolar limit [113].

6.4. Surface Enhance Raman Spectroscopy (SERS). SERS has now been established as an elegant analytical technique to detect molecules at ultrasensitive concentrations down to a

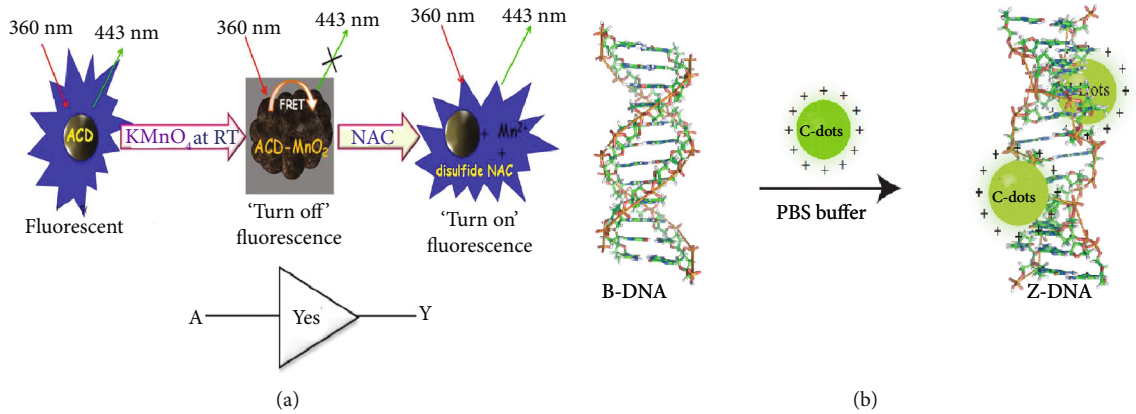

FIGURE 19: (a) Schematic presentation of a CD-based logic gate sensor; (b) conversion of B-DNA to Z-DNA by CDs (reproduced with permission from [109, 110]).

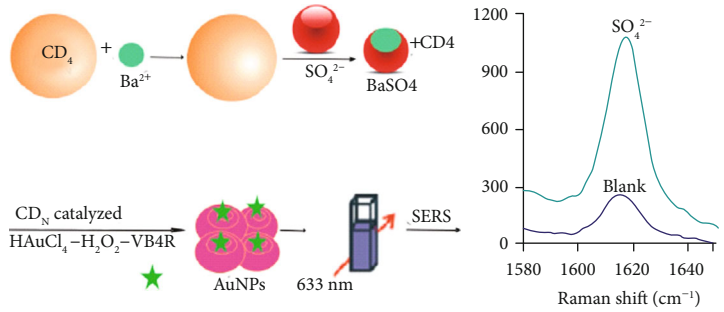

FIGURE 20: Determination of SO_4^{2-} by SERS intensity measurement (reproduced with permission from [117]).

single molecule detection limit [114–116]. However, SERS spectra as obtained from dielectric molecular assay and surface plasmon materials are not so much effective due to lack of proper interaction of the organic molecules with metal or metal complexes. Composite CDs remove such difficulties by behaving as mediator between active metal surfaces and the probe molecules. Wang et al. reported N-CDs which acted as catalyst for the formation of gold nanoparticles by the reaction between $HAuCl_4$ and H_2O_2. They quantitatively determined SO_4^{2-} concentration by means of SERS intensity measurement (Figure 20) [117]. Bhunia et al. reported a composite-SERS active film fabricated with polydimethylsiloxane (PDMS), CD, and silver nanoparticles. Such substrate exhibited SERS spectra, much well resolved than that reported for conventional SERS-active dyes as well as for bacterial samples [118]. Recently, Zhao et al. reported Ag-CD composites obtained by combination of N-CDs and Ag nanoparticle. The as-synthesized composites were used as a logic gate sensor and exhibited potential SERS activities [119].

6.5. Drug Delivery, Bioimaging, and Biosensing. CDs are extensively utilized in health and medicinal chemistry for drug deliveries and bioimagings and in the development of efficient biosensors [13] because of their excellent biocompatibility, water solubility, nontoxic, photoluminescent, and high photostability. Most of the nanomaterials reported as drug carriers have not shown any PL activities whereas CDs acted as super drug carrier because of their emissive nature which helped in tracing drugs in normal cell as well as abnormal (disease affected) cell. Zheng et al. reported CD modified with oxaliplatin and used it as an efficient cancer drugs [120]. Composite-CD released oxaliplatin within cell in an optimal condition of cell environment and exhibited their activities on malignant cells. Then, free CDs with their PL behavior assisted to carry out complete study about cancer cell. Recently, Shu et al. synthesized a composite assembly of curcumin with ionic liquid-based CDs which showed its efficacy as anticancer drug having excellent drug-carrying potential, high cell-penetration power, and high drug-loading capacity. The composite exhibited 69.2% drug loading and 87.5% cell viability on HeLa cells [121].

In vitro and *in vivo* bioimaging study is a very essential tool for clinical purposes for the detection and monitoring of disease-affected abnormal cell in animals. CDs derived from arginine have been successfully utilized *in vitro* cytotoxicity on different cells like MCF-7, HeLa, and NIH 3T3 with very high cell viability above 90% [122]. Recently, brighter fluorescent spectra of CDs doped with ZnS inorganic salt have been reported by Sun et al. These CDs are efficiently applied *in vivo* cell imaging study in mice [123]. Huang et al. reported modified CDs with dye ZW800 that exhibited excellent photoluminescent properties and were utilized in *in vivo* imaging to understand the circulation of blood and

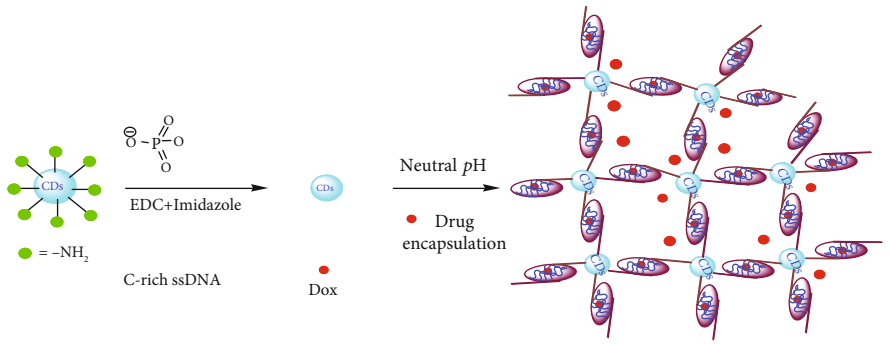

Figure 21: (a) Schematic pictorial presentation for encapsulation of drugs.

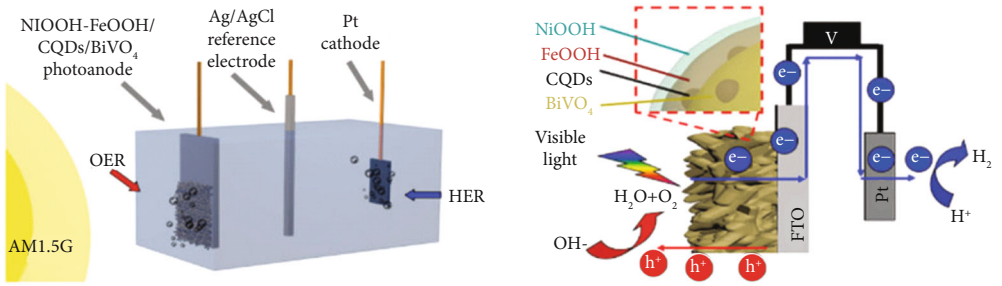

(a)

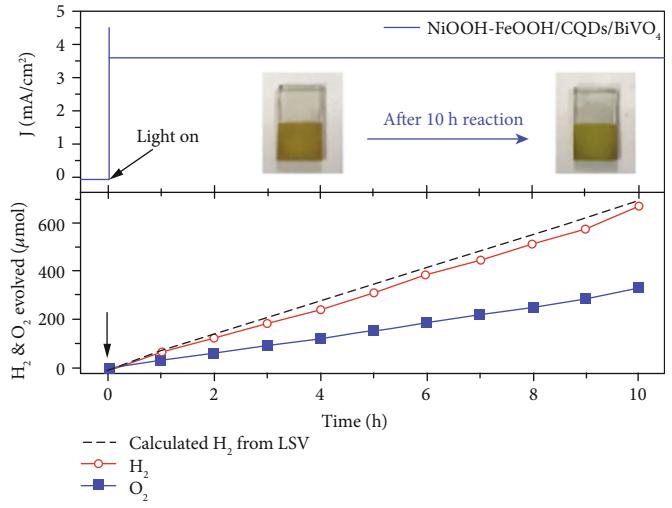

(b)

Figure 22: (a) A schematic pictorial diagram for H_2-fuel cell by splitting of water and probable mechanism; (b) amount of H_2 and O_2 generated with time in exposure of light (reproduced with permission from [128]).

in tumor detection [124]. Recently, Singh et al. reported CD-based drug carrier. They showed that their drug carrier interacted with cytosine-rich single-stranded DNA phosphoramidate linkage and released drug due to change in electrostatic interaction with DNA at optimum pH condition (Figure 21) [125].

6.6. Photocatalyst. Pure or composite CDs both can absorb light with a broad wavelength range and are used for different photocatalytic activities. Generation H_2 fuel from water by utilizing CD-based photocatalysts are the most promising research topic in recent years. Sun et al. recently reported photodecomposition of CO_2 by utilizing doped CDs with Au as photocatalyst [126]. Liu et al. reported a low cost and environmentally friendly CDs-C_3N_4 composite catalyst which successfully produced H_2 by splitting of water [127]. $BiVO_4$- and CD-containing composites have also been employed as photocatalyst for degradation of organic pollutants and water splitting (Figure 22) [128]. PEG_{1500N}-functionalized CDs coated with Au have the potential to convert most active components of greenhouse gas, CO_2, into formic or acetic acid [129]. A number of toxic

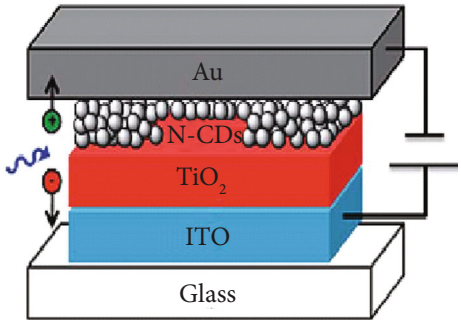

Figure 23: Schematic presentation of solar cell based on CDs (reproduced with permission from [134]).

chemicals can be damaged or better converted to less toxic chemical by CD-based photocatalyst [130]. Further, simple CDs can be used as photocatalyst in normal organic oxidation-reduction reaction. Li et al. reported that oxidation of benzyl alcohol to benzaldehyde can be achieved with a very high (92%) conversion rate and excellent selectivity (100%) by means of CD as photocatalyst [131].

6.7. Solar Energy Conversion. Doped CDs [14] introduce a new age in scientific world for the development of solar cells (SCs) by fabricating with CDs in the presence of other materials [132, 133]. In concern of pollution, development of eco-friendly solar cell free from any toxic chemical carries an extra importance. Carolan et al. first reported this achievement to form a completely eco-friendly composite SC device. Their device worked on a FRET-based mechanism (Figure 23) [134, 135] where doped CDs acted as photoactive as well as photoanode layer [136, 137]. Wang et al. reported N-CD-perovskite-based composite that acted as SCs with better efficiency in comparison to normal perovskite SCs [138]. Yang et al. reported unique SCs that worked in very low light even at night [139].

7. Future Perspectives and Conclusion

This review is focused on the recent progress of CDs in terms of their rational synthesis, surface engineering, and recent applications. Thousands of new synthetic methodologies of CDs are being reported every year, albeit simple and high yields still remain a challenge to their preparations in large scale. Despite of innumerable publications, there are no unequivocal theoretical explanations on the photophysical properties of CDs as yet that leave hence a bright scope of research for the physicists and physical chemists in the near future. Due to its biocompatibility, CDs are expected to replace inorganic quantum dots and will find wide applications in bioimaging and the preparation of logic gate biosensors. In addition, eco-friendly light-harvesting devices constructed with composite CDs are proving their unique presence in energy conversion sector. However, developmental works for low cost and better efficient light-harvesting devices are urgently needed in the future.

Conflicts of Interest

There is no conflict of interest.

Acknowledgments

The authors express their thanks to the Jadavpur University, Department of Higher Education, Science & Technology and Biotechnology (DHESTB, Govt. of West-Bengal) for the financial support through the research projects (Project Sanction No.: 202 (Sanc.)/ST/P/S&T/16G-22/2017), Council of Scientific and Industrial Research (CSIR) (Project Sanction No.: 03 (1437)/18/EMR-II)), and Science and Engineering Research Board (SERB) (File no. EMR/2017/000901, Diary No. SERB/F/10748/2018-2019).

References

[1] G. A. M. Hutton, B. C. M. Martindale, and E. Reisner, "Carbon dots as photosensitisers for solar-driven catalysis," *Chemical Society Reviews*, vol. 46, no. 20, pp. 6111–6123, 2017.

[2] J. Wang and J. Qiu, "A review of carbon dots in biological applications," *Journal of Materials Science*, vol. 51, no. 10, pp. 4728–4738, 2016.

[3] S. Y. Lim, W. Shen, and Z. Gao, "Carbon quantum dots and their applications," *Chemical Society Reviews*, vol. 44, no. 1, pp. 362–381, 2015.

[4] M. Tuerhong, Y. Xu, and X. B. Yin, "Review on carbon dots and their applications," *Chinese Journal of Analytical Chemistry*, vol. 45, no. 1, pp. 139–150, 2017.

[5] J. Geys, A. Nemmar, E. Verbeken et al., "Acute toxicity and prothrombotic effects of quantum dots: impact of surface charge," *Environmental Health Perspectives*, vol. 116, no. 12, pp. 1607–1613, 2008.

[6] R. Wang, K.-Q. Lu, Z.-R. Tang, and Y.-J. Xu, "Recent progress in carbon quantum dots: synthesis, properties and applications in photocatalysis," *Journal of Materials Chemistry A*, vol. 5, no. 8, pp. 3717–3734, 2017.

[7] M. Farshbaf, S. Davaran, F. Rahimi, N. Annabi, R. Salehi, and A. Akbarzadeh, "Carbon quantum dots: recent progresses on synthesis, surface modification and applications," *Artificial Cells, Nanomedicine, and Biotechnology*, vol. 46, no. 7, pp. 1331–1348, 2018.

[8] X. Xu, R. Ray, Y. Gu et al., "Electrophoretic analysis and purification of fluorescent single-walled carbon nanotube fragments," *Journal of American Chemical Society*, vol. 126, no. 40, pp. 12736-12737, 2004.

[9] Y.-P. Sun, B. Zhou, Y. Lin et al., "Quantum-sized carbon dots for bright and Colorful photoluminescence," *Journal of American Chemical Society*, vol. 128, no. 24, pp. 7756-7757, 2006.

[10] L. Cao, X. Wang, M. J. Meziani et al., "Carbon dots for multiphoton bioimaging," *Journal of the American Chemical Society*, vol. 129, no. 37, pp. 11318-11319, 2007.

[11] V. Georgakilas, J. A. Perman, J. Tucek, and R. Zboril, "Broad family of carbon nanoallotropes: classification, chemistry, and applications of fullerenes, carbon dots, nanotubes, graphene, nanodiamonds, and combined superstructures," *Chemical Reviews*, vol. 115, no. 11, pp. 4744–4822, 2015.

[12] C. Ding, A. Zhu, and Y. Tian, "Functional surface engineering of C-dots for fluorescent biosensing and in vivo bioimaging," *Accounts of Chemical Research*, vol. 47, no. 1, pp. 20–30, 2014.

[13] J. Zuo, T. Jiang, X. Zhao, X. Xiong, S. Xiao, and Z. Zhu, "Preparation and application of fluorescent carbon dots," *Journal of Nanomaterials*, vol. 2015, Article ID 787862, 13 pages, 2015.

[14] F. Yuan, S. Li, Z. Fan, X. Meng, L. Fan, and S. Yang, "Shining carbon dots: synthesis and biomedical and optoelectronic applications," *Nano Today*, vol. 11, no. 5, pp. 565–586, 2016.

[15] H. Zhu, X. Wang, Y. Li, Z. Wang, F. Yang, and X. Yang, "Microwave synthesis of fluorescent carbon nanoparticles with electrochemiluminescence properties," *Chemical Communications*, vol. 34, no. 34, pp. 5118–5120, 2009.

[16] C. Liu, P. Zhang, F. Tian, W. Li, F. Lib, and W. Liu, "One-step synthesis of surface passivated carbon nanodots by microwave assisted pyrolysis for enhanced multicolor photoluminescence and bioimaging," *Journal of Materials Chemistry*, vol. 21, no. 35, pp. 13163–13167, 2011.

[17] J. Feng, W.-J. Wang, X. Hai, Y.-L. Yu, and J.-H. Wang, "Green preparation of nitrogen-doped carbon dots derived from silkworm chrysalis for cell imaging," *Journal of Materials Chemistry B*, vol. 4, no. 3, pp. 387–393, 2016.

[18] Q. Liu, N. Zhang, H. Shi et al., "One-step microwave synthesis of carbon dots for highly sensitive and selective detection of copper ions in aqueous solution," *New Journal of Chemistry*, vol. 42, no. 4, pp. 3097–3101, 2018.

[19] X. Ren, W. Liang, P. Wang et al., "A new approach in functionalization of carbon nanoparticles for optoelectronically relevant carbon dots and beyond," *Carbon*, vol. 141, pp. 553–560, 2019.

[20] B. Zhang, C. -Y. Liu, and Y. Liu, "A Novel One-Step Approach to Synthesize Fluorescent Carbon Nanoparticles," *European Journal of Inorganic Chemistry*, vol. 2010, no. 28, pp. 4411–4414, 2010.

[21] Y. Pang, H. Gao, S. Wu, and X. Li, "Facile synthesis the nitrogen and sulfur co-doped carbon dots for selective fluorescence detection of heavy metal ions," *Materials Letters*, vol. 193, pp. 236–239, 2017.

[22] J. Shen, S. Shang, X. Chen, D. Wang, and Y. Cai, "Facile synthesis of fluorescence carbon dots from sweet potato for Fe^{3+} sensing and cell imaging," *Materials Science and Engineering C*, vol. 76, pp. 856–864, 2017.

[23] M. Zhang, X. Zhao, Z. Fang et al., "Fabrication of HA/PEI-functionalized carbon dots for tumor targeting, intracellular imaging and gene delivery," *RSC Advances*, vol. 7, no. 6, pp. 3369–3375, 2017.

[24] B. C. M. Martindale, G. A. M. Hutton, C. A. Caputo, and E. Reisner, "Solar hydrogen production using carbon quantum dots and a molecular nickel catalyst," *Journal of American Chemical Society*, vol. 137, no. 18, pp. 6018–6025, 2015.

[25] Y. Guo, L. Zhang, F. Cao, and Y. Leng, "Thermal treatment of hair for the synthesis of sustainable carbon quantum dots and the applications for sensing Hg^{2+}," *Scientific Reports*, vol. 6, no. 1, p. 35795, 2016.

[26] M. Rong, Y. Feng, Y. Wang, and X. Chen, "One-pot solid phase pyrolysis synthesis of nitrogen-doped carbon dots for Fe^{3+} sensing and bioimaging," *Sensors and Actuators B: Chemical*, vol. 245, pp. 868–874, 2017.

[27] J. Zhou, C. Booker, R. Li et al., "An electrochemical avenue to blue luminescent nanocrystals from multiwalled carbon nanotubes (MWCNTs)," *Journal of American Chemical Society*, vol. 129, no. 4, pp. 744-745, 2007.

[28] L. Zheng, Y. Chi, Y. Dong, J. Lin, and B. Wang, "Electrochemiluminescence of water-soluble carbon nanocrystals released electrochemically from graphite," *Journal of American Chemical Society*, vol. 131, no. 13, pp. 4564-4565, 2009.

[29] H. Li, X. He, Z. Kang et al., "Water-Soluble Fluorescent Carbon Quantum Dots and Photocatalyst Design," *Angewandte Chemie*, vol. 49, no. 26, pp. 4430–4434, 2010.

[30] Z. Zhao and Y. Xie, "Enhanced electrochemical performance of carbon quantum dots-polyaniline hybrid," *Journal of Power Sources*, vol. 337, pp. 54–64, 2017.

[31] V. Thongpool, P. Asanithi, and P. Limsuwan, "Synthesis of carbon particles using laser ablation in ethanol," *Procedia Engineering*, vol. 32, pp. 1054–1060, 2012.

[32] C. Doñate-Buendia, R. Torres-Mendieta, A. Pyatenko, E. Falomir, M. Fernández-Alonso, and G. Mínguez-Vega, "Fabrication by laser irradiation in a continuous flow jet of carbon quantum dots for fluorescence imaging," *ACS Omega*, vol. 3, no. 3, pp. 2735–2742, 2018.

[33] M. Bottini, C. Balasubramanian, M. I. Dawson, A. Bergamaschi, S. Bellucci, and T. Mustelin, "Isolation and characterization of fluorescent nanoparticles from pristine and oxidized electric arc-produced single-walled carbon nanotubes," *The Journal of Physical Chemistry B*, vol. 110, no. 2, pp. 831–836, 2006.

[34] S. Dey, A. Govindaraj, K. Biswas, and C. N. R. Rao, "Luminescence properties of boron and nitrogen doped graphene quantum dots prepared from arc-discharge-generated doped graphene samples," *Chemical Physics Letters*, vol. 595-596, pp. 203–208, 2014.

[35] S. N. Baker and G. A. Baker, "Luminescent carbon nanodots: emergent nanolights," *Angewandte Chemie International Edition*, vol. 49, no. 38, pp. 6726–6744, 2010.

[36] A. N. Emam, S. A. Loutfy, A. A. Mostafa, H. Awad, and M. B. Mohamed, "Cyto-toxicity, biocompatibility and cellular response of carbon dots–plasmonic based nanohybrids for bioimaging," *RSC Advances*, vol. 7, no. 38, pp. 23502–23514, 2017.

[37] S. Kim, S. W. Hwang, M.-K. Kim et al., "Anomalous behaviors of visible luminescence from graphene quantum dots: interplay between size and shape," *ACS Nano*, vol. 6, no. 9, pp. 8203–8208, 2012.

[38] X. Li, S. P. Lau, L. Tang, R. Ji, and P. Yang, "Sulphur doping: a facile approach to tune the electronic structure and optical properties of graphene quantum dots," *Nanoscale*, vol. 6, no. 10, pp. 5323–5328, 2014.

[39] L. Bao, Z. L. Zhang, Z. Q. Tian et al., "Electrochemical tuning of luminescent carbon nanodots: from preparation to luminescence mechanism," *Advanced Materials*, vol. 23, no. 48, pp. 5801–5806, 2011.

[40] Y. Li, H. Shu, X. Niu, and J. Wang, "Electronic and optical properties of edge-functionalized graphene quantum dots and the underlying mechanism," *The Journal of Physical Chemistry C*, vol. 119, no. 44, pp. 24950–24957, 2015.

[41] O. Adedokun, A. Roy, A. O. Awodugba, and P. S. Devi, "Fluorescent carbon nanoparticles from Citrus sinensis as efficient sorbents for pollutant dyes," *Luminescence*, vol. 32, no. 1, pp. 62–70, 2017.

[42] S. Zhu, Q. Meng, L. Wang et al., "Highly photoluminescent carbon dots for multicolor patterning, sensors, and bioimaging," *Angewandte Chemie*, vol. 52, no. 14, pp. 3953–3957, 2013.

[43] X. Li, H. Wang, Y. Shimizu, A. Pyatenko, K. Kawaguchi, and N. Koshizaki, "Preparation of carbon quantum dots with tunable photoluminescence by rapid laser passivation in ordinary organic solvents," *Chemical Communications*, vol. 47, no. 3, pp. 932–934, 2011.

[44] C. Sun, Y. Zhang, S. Kalytchuk et al., "Down-conversion monochromatic light-emitting diodes with the color determined by the active layer thickness and concentration of carbon dots," *Journal of Material Chemistry C*, vol. 3, no. 26, pp. 6613–6615, 2015.

[45] R. Wang, X. Wang, and Y. Sun, "One-step synthesis of self-doped carbon dots with highly photoluminescence as multifunctional biosensors for detection of iron ions and pH," *Sensors and Actuators B: Chemical*, vol. 241, pp. 73–79, 2017.

[46] X. Wang, L. Cao, F. Lu et al., "Photoinduced electron transfers with carbon dots," *Chemical Communications*, no. 25, pp. 3774–3776, 2009.

[47] Z. Wang, H. Liao, H. Wu, B. Wang, H. Zhao, and M. Tan, "Fluorescent carbon dots from beer for breast cancer cell imaging and drug delivery," *Analytical Methods*, vol. 7, no. 20, pp. 8911–8917, 2015.

[48] Q. Liu, B. Guo, Z. Rao, B. Zhang, and J. R. Gong, "Strong two-photon-induced fluorescence from photostable, biocompatible nitrogen-doped graphene quantum dots for cellular and deep-tissue imaging," *Nano Letters*, vol. 13, no. 6, pp. 2436–2441, 2013.

[49] V. Gude, "Synthesis of hydrophobic photoluminescent carbon nanodots by using L-tyrosine and citric acid through a thermal, oxidation route," *Belilstein Journal of Nanotechnology*, vol. 5, pp. 1513–1522, 2014.

[50] Y. Cui, C. Zhang, L. Sun, Z. Hu, and X. Liu, "Simple and efficient synthesis of strongly green fluorescent carbon dots with upconversion property for direct cell imaging," *Particle & Particle Systems Characterization*, vol. 32, no. 5, pp. 542–546, 2015.

[51] S. Gogoi and R. Khan, "NIR upconversion characteristics of carbon dots for selective detection of glutathione," *New Journal of Chemistry*, vol. 42, no. 8, pp. 6399–6407, 2018.

[52] Y. Wang and A. Hu, "Carbon quantum dots: synthesis, properties and applications," *Journal of Materials Chemistry C*, vol. 2, no. 34, pp. 6921–6939, 2014.

[53] Y. Deng, D. Zhao, X. Chen, F. Wang, H. Song, and D. S. Deng, "Long lifetime pure organic phosphorescence based on water soluble carbon dots," *Chemical Communications*, vol. 49, no. 51, pp. 5751–5753, 2013.

[54] Q. Li, M. Zhou, M. Yang, Q. Yang, Z. Zhang, and J. Shi, "Induction of long-lived room temperature phosphorescence of carbon dots by water in hydrogen-bonded matrices," *Nature Communications*, vol. 9, no. 1, p. 734, 2018.

[55] Z. Lin, W. Xue, H. Chen, and J. -M. Lin, "Classical oxidant induced chemiluminescence of fluorescent carbon dots," *Chemical Communications*, vol. 48, no. 7, pp. 1051–1053, 2012.

[56] L. Zhao, F. Di, D. Wang et al., "Chemiluminescence of carbon dots under strong alkaline solutions: a novel insight into carbon dot optical properties," *Nanoscale*, vol. 5, no. 7, pp. 2655–2658, 2013.

[57] M. Zhang, Y. Jia, J. Cao et al., "Carbon dots-enhanced luminol chemiluminescence and its application to 2-methoxyestradiol determination," *Green Chemistry Letters and Reviews*, vol. 11, no. 4, pp. 379–386, 2018.

[58] M. Krysmann, A. Kelarakis, P. Dallas, and E. Giannelis, "Formation mechanism of carbogenic nanoparticles with dual photoluminescence emission," *Journal of American Chemical Society*, vol. 134, no. 2, pp. 747–750, 2012.

[59] S. C. Ray, A. Saha, N. R. Jana, and R. Sarkar, "Fluorescent carbon nanoparticles: synthesis, characterization, and bioimaging application," *Journal Physical Chemistry C*, vol. 113, no. 43, pp. 18546–18551, 2009.

[60] K. P. Loh, Q. Bao, G. Eda, and M. Chhowalla, "Graphene oxide as a chemically tunable platform for optical applications," *Nature Chemistry*, vol. 2, no. 12, pp. 1015–1024, 2010.

[61] L.-L. Li, J. Ji, R. Fei et al., "A Facile Microwave Avenue to Electrochemiluminescent Two-Color Graphene Quantum Dots," *Advanced Functional Materials*, vol. 22, no. 14, pp. 2971–2979, 2012.

[62] Y. Zeng, D. Ma, W. Wang et al., "N, S co-doped carbon dots with orange luminescence synthesized through polymerization and carbonization reaction of amino acids," *Applied Surface Science*, vol. 342, pp. 136–143, 2015.

[63] Q. Xu, P. Pu, J. Zhao et al., "Preparation of highly photoluminescent sulfur-doped carbon dots for Fe(III) detection," *Journal of Materials Chemistry A*, vol. 3, no. 2, pp. 542–546, 2015.

[64] Y. Zhuo, H. Miao, D. Zhong, S. Zhu, and X. Yang, "One-step synthesis of high quantum-yield and excitation-independent emission carbon dots for cell imaging," *Materials Letters*, vol. 139, pp. 197–200, 2015.

[65] W. Kwon, Y. -H. Kim, C. -L. Lee et al., "Electroluminescence from graphene quantum dots prepared by amidative cutting of tattered graphite," *Nano Letters*, vol. 14, no. 3, pp. 1306–1311, 2014.

[66] G. Eda, Y. Y. Lin, C. Mattevi et al., "Blue photoluminescence from chemically derived graphene oxide," *Advanced Materials*, vol. 22, no. 4, pp. 505–509, 2010.

[67] M. A. Sk, A. Ananthanarayanan, L. Huang, K. H. Lim, and P. Chen, "Revealing the tunable photoluminescence properties of graphene quantum dots," *Journal of Materials Chemistry C*, vol. 2, no. 34, pp. 6954–6960, 2014.

[68] L. Bao, C. Liu, Z. -L. Zhang, and D. -W. Pang, "Photoluminescence-Tunable Carbon Nanodots: Surface-State Energy-Gap Tuning," *Advanced Materials*, vol. 27, no. 10, pp. 1663–1667, 2015.

[69] S. Hu, A. Trinchi, P. Atkin, and I. Cole, "Tunable photoluminescence across the entire visible spectrum from carbon dots excited by white light," *Angewandte Chemie*, vol. 54, no. 10, pp. 2970–2974, 2015.

[70] H. Ding, S. -B. Yu, J. -S. Wei, and H. -M. Xiong, "Full-color light-emitting carbon dots with a surface-state-controlled luminescence mechanism," *ACS Nano*, vol. 10, no. 1, pp. 484–491, 2016.

[71] L. Guo, J. Ge, W. Liu et al., "Tunable multicolor carbon dots prepared from well-defined polythiophene derivatives and their emission mechanism," *Nanoscale*, vol. 8, no. 2, pp. 729–734, 2016.

[72] H. Tetsuka, R. Asahi, A. Nagoya et al., "Optically Tunable Amino-Functionalized Graphene Quantum Dots," *Advanced Materials*, vol. 24, no. 39, pp. 5333–5338, 2012.

[73] L. Zhou, Y. Lin, Z. Huang, J. Ren, and X. Qu, "Carbon nanodots as fluorescence probes for rapid, sensitive, and label-free detection of Hg^{2+} and biothiols in complex matrices," *Chemical Communications*, vol. 48, no. 8, pp. 1147–1149, 2012.

[74] J. Hou, G. Dong, Z. Tian et al., "A sensitive fluorescent sensor for selective determination of dichlorvos based on the recovered fluorescence of carbon dots-Cu(II) system," *Food Chemistry*, vol. 202, pp. 81–87, 2016.

[75] Y. Feng, D. Zhong, H. Miao, and X. Yang, "Carbon dots derived from rose flowers for tetracycline sensing," *Talanta*, vol. 140, pp. 128–133, 2015.

[76] C. Lei, X. Zhao, S. Jiao et al., "A turn-on fluorescent sensor for the detection of melamine based on the anti-quenching ability of Hg2+to carbon nanodots," *Analitical Methods*, vol. 8, no. 22, pp. 4438–4444, 2016.

[77] L. Shi, Y. Li, X. Li et al., "Controllable synthesis of green and blue fluorescent carbon nanodots for pH and Cu^{2+} sensing in living cells," *Biosensors and Bioelectronics*, vol. 77, pp. 598–602, 2016.

[78] V. Roshni and D. Ottoor, "Synthesis of carbon nanoparticles using one step green approach and their application as mercuric ion sensor," *Journal of Luminescence*, vol. 161, pp. 117–122, 2015.

[79] J. Shen, S. Shang, X. Chen, D. Wang, and Y. Cai, "Highly fluorescent N, S-co-doped carbon dots and their potential applications as antioxidants and sensitive probes for Cr (VI) detection," *Sensors and Actuators B: Chemical*, vol. 248, pp. 92–100, 2017.

[80] Y. Liu, Q. Zhou, J. Li, M. Lei, and X. Yan, "Selective and sensitive chemosensor for lead ions using fluorescent carbon dots prepared from chocolate by one-step hydrothermal method," *Sensors and Actuators B: Chemical*, vol. 237, pp. 597–604, 2016.

[81] Y. Wang, W. Wu, M. Wu et al., "Yellow-visual fluorescent carbon quantum dots from petroleum coke for the efficient detection of Cu^{2+} ions," *New Carbon Materials*, vol. 30, no. 6, pp. 550–559, 2015.

[82] Y. Kim, G. Jang, and T. S. Lee, "Carbon nanodots functionalized with rhodamine and poly(ethylene glycol) for ratiometric sensing of Al ions in aqueous solution," *Sensors and Actuators B: Chemical*, vol. 249, pp. 59–65, 2017.

[83] X. Wen, L. Shi, G. Wen et al., "Green and facile synthesis of nitrogen-doped carbon nanodots for multicolor cellular imaging and Co^{2+} sensing in living cells," *Sensors and Actuators B: Chemical*, vol. 235, pp. 179–187, 2016.

[84] M. Zhou, Z. Zhou, A. Gong, Y. Zhang, and Q. Li, "Synthesis of highly photoluminescent carbon dots via citric acid and Tris for iron(III) ions sensors and bioimaging," *Talanta*, vol. 143, pp. 107–113, 2015.

[85] X.-Y. Sun, L.-L. Wu, J.-S. Shen et al., "Highly selective and sensitive sensing for Al3+ and F– based on green photoluminescent carbon dots," *RSC Advances*, vol. 6, no. 99, pp. 97346–97351, 2016.

[86] J. Xu, Y. Zhou, G. Cheng, M. Dong, S. Liu, and C. Huang, "Carbon dots as a luminescence sensor for ultrasensitive detection of phosphate and their bioimaging properties," *Luminescence*, vol. 30, no. 4, pp. 411–415, 2015.

[87] Z. Li, H. Yu, T. Bian et al., "Highly luminescent nitrogen-doped carbon quantum dots as effective fluorescent probes for mercuric and iodide ions," *Journal of Materials Chemistry C*, vol. 3, no. 9, pp. 1922–1928, 2015.

[88] B. Yin, J. Deng, X. Peng et al., "Green synthesis of carbon dots with down- and up-conversion fluorescent properties for sensitive detection of hypochlorite with a dual-readout assay," *Analyst*, vol. 138, no. 21, pp. 6551–6557, 2013.

[89] Y. Zhang, P. Cui, F. Zhang et al., "Fluorescent probes for "off-on" highly sensitive detection of Hg^{2+} and L-cysteine based on nitrogen-doped carbon dots," *Talanta*, vol. 152, pp. 288–300, 2016.

[90] J.-W. Zhou, X.-M. Zou, S.-H. Song, and G.-H. Chen, "Quantum dots applied to methodology on detection of pesticide and veterinary drug residues," *Journal of Agricultural and Food Chemistry*, vol. 66, no. 6, pp. 1307–1319, 2018.

[91] X. Yang, Y. Luo, S. Zhu, Y. Feng, Y. Zhuo, and Y. Dou, "One-pot synthesis of high fluorescent carbon nanoparticles and their applications as probes for detection of tetracyclines," *Biosensors Bioelectronics*, vol. 56, pp. 6–11, 2016.

[92] F. Akhgari, N. Samadi, K. Farhadi, and M. Akhgari, "A green one-pot, synthesis of nitrogen and sulfur co-doped carbon quantum dots for sensitive and selective detection of cephalexin," *Canadian Journal of Chemistry*, vol. 95, no. 6, pp. 641–648, 2017.

[93] S. Wang, Y. Wang, K. Yang, Y. Zhong, X. Yang, and Z. Chen, "Synthesis of carbon dots originated from hydroxypropylmethyl cellulose for sensing ciprofloxacin," *Analytical Science*, vol. 33, no. 10, pp. 1129–1134, 2017.

[94] J. Hua, Y. Jiao, M. Wang, and Y. Yang, "Determination of norfloxacin or ciprofloxacin by carbon dots fluorescence enhancement using magnetic nanoparticles as adsorbent," *Mikrochimica Acta*, vol. 185, no. 2, pp. 1–9, 2018.

[95] J. Song, J. Li, Z. Guo et al., "A novel fluorescent sensor based on sulfur and nitrogen co-doped carbon dots with excellent stability for selective detection of doxycycline in raw milk," *RSC Advances*, vol. 7, no. 21, pp. 12827–12834, 2017.

[96] C. Zhao, Y. Jiao, L. Zhang, and Y. Yang, "One-step synthesis of S, B co-doped carbon dots and their application for selective and sensitive fluorescence detection of diethylstilbestrol," *New Journal of Chemistry*, vol. 42, no. 4, pp. 2857–2864, 2018.

[97] I. P.-J. Lai, S. G. Harroun, S.-Y. Chen, B. Unnikrishnan, Y.-J. Li, and C.-C. Huang, "Solid-state synthesis of self-functional carbon quantum dots for detection of bacteria and tumor cells," *Sensors and Actuators B: Chemical*, vol. 228, pp. 465–470, 2016.

[98] D. Zhong, Y. Zhuo, Y. Feng, and X. Yang, "Employing carbon dots modified with vancomycin for assaying Gram-positive bacteria like _Staphylococcus aureus_," *Biosensors Bioelectronics*, vol. 74, pp. 546–553, 2015.

[99] R. Wang, Y. Xu, T. Zhang, and Y. Jiang, "Rapid and sensitive detection of *Salmonella typhimurium* using aptamer-conjugated carbon dots as fluorescence probe," *Analytical Methods*, vol. 7, no. 5, pp. 1701–1706, 2015.

[100] H. Wang, Y. Xie, S. Liu et al., "Presence of fluorescent carbon nanoparticles in baked lamb: their properties and potential application for sensors," *Journal of Agricultural and Food Chemistry*, vol. 65, no. 34, pp. 7553–7559, 2017.

[101] R. Purbia and S. Paria, "A simple turn on fluorescent sensor for the selective detection of thiamine using coconut water

derived luminescent carbon dots," *Biosensors and Bioelectronics*, vol. 79, pp. 467–475, 2016.

[102] H. Xu, X. Yang, G. Li, C. Zhao, and X. Liao, "Green synthesis of fluorescent carbon dots for selective detection of tartrazine in food samples," *Journal of Agricultural and Food Chemistry*, vol. 63, no. 30, pp. 6707–6714, 2015.

[103] S. S. R. Dasary, D. Senapati, A. K. Singh, Y. Anjaneyulu, H. Yu, and P. C. Ray, "Highly sensitive and selective dynamic light-scattering assay for TNT detection using *p*-ATP attached gold nanoparticle," *ACS Applied Materials & Interfaces*, vol. 2, no. 12, pp. 3455–3460, 2010.

[104] S. Kumar, N. Venkatramaiah, and S. Patil, "Fluoranthene based derivatives for detection of trace explosive nitroaromatics," *Journal of Physical Chemistry C*, vol. 117, no. 14, pp. 7236–7245, 2013.

[105] W. E. Tenhaeff, L. D. McIntosh, and K. K. Gleason, "Synthesis of Poly(4-vinylpyridine) Thin Films by Initiated Chemical Vapor Deposition (iCVD) for Selective Nanotrench-Based Sensing of Nitroaromatics," *Advanced Functional Materials*, vol. 20, no. 7, pp. 1144–1151, 2010.

[106] L. L. Zhang, Y. J. Han, J. B. Zhu, Y. L. Zhai, and S. J. Dong, "Simple and sensitive fluorescent and electrochemical trinitrotoluene sensors based on aqueous carbon dots," *Analytical Chemistry*, vol. 87, no. 4, pp. 2033–2036, 2015.

[107] B. B. Chen, Z. X. Liu, H. Y. Zou, and C. Z. Huang, "Highly selective detection of 2,4,6-trinitrophenol by using newly developed terbium-doped blue carbon dots," *Analyst*, vol. 141, no. 9, pp. 2676–2681, 2016.

[108] W.-S. Zou, Q.-C. Zhao, W.-L. Kong et al., "Multi-level fluorescent logic gate based on polyamine coated carbon dots capable of responding to four stimuli," *Chemical Engineering Journal*, vol. 337, pp. 471–479, 2018.

[109] J. Jana, T. Aditya, M. Ganguly, and T. Pal, "Carbon dot-MnO_2 FRET system for fabrication of molecular logic gates," *Sensors and Actuators B*, vol. 246, pp. 716–725, 2017.

[110] L. Y. Feng, A. D. Zhao, J. Ren, and X. Qu, "Lighting up left-handed Z-DNA: photoluminescent carbon dots induce DNA B to Z transition and perform DNA logic operations," *Nucleic Acids Research*, vol. 41, no. 16, pp. 7987–7996, 2013.

[111] X. Liu, J. Pang, F. Xu, and X. Zhang, "Simple approach to synthesize amino-functionalized carbon dots by carbonization of chitosan," *Scientific Reports*, vol. 6, no. 1, p. 31100, 2016.

[112] D. Chowdhury, N. Gogoi, and G. Majumdar, "Fluorescent carbon dots obtained from chitosan gel," *RSC Advances*, vol. 2, no. 32, pp. 12156–12159, 2012.

[113] Z. Bai, F. Yan, J. Xu et al., "Dual-channel fluorescence detection of mercuric (II) and glutathione by down- and up-conversion fluorescence carbon dots," *Spectrochimica Acta Part A: Molecular and Biomolecular Spectroscopy*, vol. 205, pp. 29–39, 2018.

[114] S. Saha, M. Ghosh, B. Dutta, and J. Chowdhury, "Silver coated gold nanocolloids entrapped in organized Langmuir-Blodgett Film of stearic acid: Potential evidence of a new SERS active substrate," *Applied Surface Science*, vol. 362, pp. 364–373, 2016.

[115] S. D. Roy, M. Ghosh, and J. Chowdhury, "Near-Field Response on the Far-Field Wavelength-Scanned Surface-Enhanced Raman Spectroscopic Study of Methylene Blue Adsorbed on Gold Nanocolloidal Particles," *Journal of Physical Chemistry C*, vol. 122, no. 20, pp. 10981–10991, 2018.

[116] V. Živanović, Z. Kochovski, C. Arenz, Y. Lu, and J. Kneipp, "SERS and cryo-EM directly reveal different liposome structures during interaction with gold nanoparticles," *Journal of Physical Chemistry Letters*, vol. 9, no. 23, pp. 6767–6772, 2018.

[117] L. Wang, C. Li, Y. Luo, and Z. Jiang, "Preparation of highly catalytic N-doped carbon dots and their application in SERS sulfate sensing," *Materials*, vol. 11, no. 9, p. 1655, 2018.

[118] S. K. Bhunia, L. Zeiri, J. Manna, S. Nandi, and R. Jelinek, "Carbon-dot/silver-nanoparticle flexible SERS-active films," *ACS Applied Materials and Interfaces*, vol. 8, no. 38, pp. 25637–25643, 2016.

[119] Y. Su, B. Shi, S. Liao, J. Zhao, L. Chen, and S. Zhao, "Silver nanoparticles/N-doped carbon-dots nanocomposites derived fromSiraitia Grosvenoriiand its logic gate and surface-enhanced raman scattering characteristics," *ACS Sustainable Chemistry & Enggineering*, vol. 4, no. 3, pp. 1728–1735, 2016.

[120] M. Zheng, S. Liu, J. Li et al., "Integrating oxaliplatin with highly luminescent carbon dots: an unprecedented theranostic agent for personalized medicine," *Advanced Materials*, vol. 26, no. 21, pp. 3554–3560, 2014.

[121] Y. Shu, J. Lu, Q.-X. Mao et al., "Ionic liquid mediated organophilic carbon dots for drug delivery and bioimaging," *Carbon*, vol. 114, pp. 324–333, 2017.

[122] H. Fu, Z. Ji, X. Chen et al., "A versatile ratiometric nanosensing approach for sensitive and accurate detection of Hg^{2+} and biological thiols based on new fluorescent carbon quantum dots," *Analytical Bioanalytical Chemistry*, vol. 409, no. 9, pp. 2373–2382, 2017.

[123] S. T. Yang, L. Cao, P. G. Luo et al., "Carbon dots for optical imaging in vivo," *Journal of American Chemical Society*, vol. 131, no. 32, pp. 11308-11309, 2009.

[124] X. Huang, F. Zhang, and L. Zhu, "Effect of injection routes on the biodistribution, clearance, and tumor uptake of carbon dots," *ACS Nano*, vol. 7, no. 7, pp. 5684–5693, 2013.

[125] S. Singh, A. Mishra, R. Kumari, K. K. Sinha, and M. K. Singh, "Carbon dots assisted formation of DNA hydrogel for sustained release of drug," *Carbon*, vol. 114, pp. 169–176, 2017.

[126] L. Cao, S. Sahu, and P. Anilkumar, "Carbon nanoparticles as visible-light photocatalysts for efficient CO_2 conversion and beyond," *Journal of American Chemical Society*, vol. 133, no. 13, pp. 4754–4757, 2011.

[127] J. Liu, Y. Liu, N. Liu et al., "Metal-free efficient photocatalyst for stable visible water splitting via a two-electron pathway," *Science*, vol. 347, no. 6225, pp. 970–974, 2015.

[128] K.-H. Ye, Z. Wang, J. Gu et al., "Carbon quantum dots as a visible light sensitizer to significantly increase the solar water splitting performance of bismuth vanadate photoanodes," *Energy & Environmental Science*, vol. 10, no. 3, pp. 772–779, 2017.

[129] J. Wang, S. Sahu, S. K. Sonkar et al., "Versatility with carbon dots from overcooked BBQ to brightly fluorescent agents and photocatalysts," *RSC Advances*, vol. 3, no. 36, pp. 15604–15607, 2013.

[130] H. Wang, Z. Wei, H. Matsui, and S. Zhou, "Fe_3O_4/carbon quantum dots hybrid nanoflowers for highly active and recyclable visible-light driven photocatalyst," *Journal of Materials Chemistry A*, vol. 2, no. 38, pp. 15740–15745, 2014.

[131] H. Li, R. Liu, S. Lian, Y. Liu, H. Huang, and Z. Kang, "Near-infrared light controlled photocatalytic activity of carbon

quantum dots for highly selective oxidation reaction," *Nanoscale*, vol. 5, no. 8, pp. 3289–3297, 2013.

[132] C. Piliego, L. Protesescu, S. Z. Bisri, M. V. Kovalenko, and M. A. Loi, "5.2% efficient PbS nanocrystal Schottky solar cells," *Energy & Environmental Science*, vol. 6, no. 10, pp. 3054–3059, 2013.

[133] V. Gupta, N. Chaudhary, R. Srivastava, G. D. Sharma, R. Bhardwaj, and S. Chand, "Luminscent graphene quantum dots for organic photovoltaic devices," *Journal of American Chemical Society*, vol. 133, no. 26, pp. 9960–9963, 2011.

[134] D. Carolan, C. Rocks, D. B. Padmanaban, P. Maguire, V. Svrcek, and D. Mariotti, "Environmentally friendly nitrogen-doped carbon quantum dots for next generation solar cells," *Sustainable Energy & Fuels*, vol. 1, no. 7, pp. 1611–1619, 2017.

[135] T. Forster, "Intermolecular energy migration and fluorescence," *Annals of Physics*, vol. 437, no. 2, pp. 55–75, 1948.

[136] X. Yan, X. Cui, B. Li, and L. -S. Li, "Large, solution-processable graphene quantum dots as light absorbers for photovoltaics," *Nano Letters*, vol. 10, no. 5, pp. 1869–1873, 2010.

[137] P. Mirtchev, E. J. Henderson, N. Soheilnia, C. M. Yip, and G. A. Ozin, "Solution phase synthesis of carbon quantum dots as sensitizers for nanocrystalline TiO2solar cells," *Journal of Materials Chemistry*, vol. 22, no. 4, pp. 1265–1269, 2012.

[138] Y. Wang, J. Zhang, S. Chen, H. Zhang, L. Li, and Z. Fu, "Surface passivation with nitrogen-doped carbon dots for improved perovskite solar cell performance," *Journal of Materials Science*, vol. 53, no. 12, pp. 9180–9190, 2018.

[139] J. Yang, Q. Tang, Q. Meng et al., "Photoelectric conversion beyond sunny days: all-weather carbon quantum dot solar cells," *Journal of Materials Chemistry A*, vol. 5, no. 5, pp. 2143–2150, 2017.

Hindawi
Journal of Nanomaterials
Volume 2019, Article ID 7430687, 12 pages
https://doi.org/10.1155/2019/7430687

Research Article

Synthesis of MnO_2 Hollow Nanospheres through Selective Etching Method as an Effective Absorbent to Remove Methyl Orange from Aqueous Solution

Xiaohui Hu,[1,2,3] Fangsong Zhang,[1,2,3] Hong Wang,[1,2,3] Xinyi Zhang,[1,2,3] and Linfeng Zhang[1,2,3,4]

[1]*Key Laboratory for Green Chemical Process of Ministry of Education, Wuhan Institute of Technology, Wuhan 430205, China*
[2]*Key Laboratory of Novel Reactor and Green Chemical Technology of Hubei Province, Wuhan Institute of Technology, Wuhan 430205, China*
[3]*School of Chemical Engineering and Pharmacy, Wuhan Institute of Technology, Wuhan 430205, China*
[4]*School of Chemical Engineering and Technology, Tianjin University, Tianjin 300072, China*

Correspondence should be addressed to Linfeng Zhang; lfzhang@wit.edu.cn

Xiaohui Hu and Fangsong Zhang contributed equally to this work.

Received 14 May 2019; Revised 9 September 2019; Accepted 16 September 2019; Published 6 November 2019

Guest Editor: Ziyou Zhou

The discharge of dye wastewater has become an unavoidable problem for human health and the environment. Developing an economical and rapid method to prepare effective adsorbents for selective removal of dyes is extremely urgent. In this work, MnO_2 hollow nanospheres (MHNSs) were prepared through the selective etching method with the $MnCO_3$ as the sacrificial template. The effect of the pH value, contact time, and initial concentration on the adsorption of methyl orange (MO) onto the MHNSs was systematically investigated. The unique mesoporous hollow structure and large BET surface area (43.74 m^2/g) of MHNSs lead to an excellent adsorption capacity (1677.14 mg/g) at the optimal condition. Furthermore, the prepared MHNSs also showed great stability (90% removal rate after four cycles). The adsorption kinetics data fitted well with the pseudo-second-order kinetic model ($R^2 > 0.9997$). The overall process was jointly controlled by external mass transfer and intraparticle diffusion, and intraparticle diffusion was the dominant factor. The adsorption isotherm results showed that the Freundlich model was more accurate to describe the experimental data than the Langmuir model. The thermodynamic analysis showed that the adsorption of MO on MHNSs was spontaneous and exothermic. Moreover, the calculated ΔG° and the XPS spectra showed that the process was mainly a physical process. It is expected that MHNS has a potential application for purifying dye wastewater due to its great adsorption performance and excellent stability.

1. Introduction

Water pollution has become a worrying challenge for human health and the ecosystem [1–7]. The release of dye wastewater leads to serious environmental problems. However, the treatment of this class of wastewater has proven to be quite difficult because of its stable and complex aromatic structure [8–12]. Therefore, there is an urgent need to design an efficient method for removing dye molecules from wastewater. Various technologies such as photoelectrocatalysis, membrane filtration, chemical oxidation, and adsorption have been proposed to solve this problem [13–18]. Nevertheless, these methods are often expensive, technically demanding, or only effective at a certain concentration. The adsorption technology has been considered to be an efficient, nontoxic, and economic water treatment technique, and the key of this technology is to develop highly effective adsorbents.

Currently, as one of typical metal oxides, manganese oxide with various structures and morphologies was widely used in the fields of catalysis, electrochemical supercapacitors,

and adsorption. The morphology and structure of prepared manganese oxide are seriously restricted by its synthetic route and conditions. Many researchers have prepared manganese oxide composite adsorbents with uniform microstructure and highly specific surface area through molten salt, sol-gel, coprecipitation, and hydrothermal processes [19–23]. Among reported materials, the hollow micro-/nanostructures are a special class of materials due to their unique morphologies, which have superior advantages such as high BET surface area, surface permeability, and potential scale-dependence [24–27]. Gheju et al. have reported an efficient MnO_2 adsorbent for adsorption of Cr^{6+} and investigated the influence of the pH value, temperature, and initial Cr^{6+} concentration [28]. The highest adsorption capacity was obtained at 20°C and pH 5.9. Li. et al. have successfully synthesized hierarchical hollow MnO_2 microspheres by a hydrothermal method, and the prepared materials show high performance for the adsorption of benzene [29]. However, conventional MnO_2-based adsorbents were usually irregular nanoparticles or required a high temperature/pressure condition. Therefore, it is necessary to design a simple operation and short-reaction-time method for preparing a MnO_2 adsorbent with high efficiency.

In this study, hollow manganese dioxide adsorbents with high efficiency were prepared by a low-temperature acid etching method [30]. The size and shell thickness of the hollow manganese oxide could be exactly controlled by adjusting the amount of etch acid and reaction time. Subsequently, the adsorption capacity of prepared hollow manganese oxide microspheres under different pHs, temperatures, and initial concentrations was evaluated by the adsorption of MO. The adsorption kinetics, rate-determining step, and thermodynamic analysis of the adsorption process were also investigated. Moreover, the possible mechanism of a MO molecule absorbed onto the MHNSs was studied and discussed.

2. Experimental

2.1. Materials. Methyl orange, sodium hydroxide, hydrochloric acid, potassium permanganate, manganese nitrate, ammonium carbonate, and polyethylene glycol were all purchased from Sinopharm Chemical Reagent Co. Ltd.

2.2. Synthesis of the MHNSs. Typically, 1.6 g $Mn(NO_3)_2$ (50% solution) and 0.5 g PEG powder were dissolved in 100 mL of ethanol-water solution ($v : v = 1 : 1$) under 40°C water bath. Afterward, 1.6 g $(NH_4)_2CO_3$ powder was dissolved into 20 mL deionized water and then transferred to a 20 mL syringe. The above $(NH_4)_2CO_3$ solution was slowly dripped into the manganese nitrate solution, and the entire drip process was completed within 2 h. After aging for 4 h, the product was collected, washed, and fully dried at 60°C. Then, 0.5 g of prepared $MnCO_3$ powder was dispersed in 20 mL of distilled water and 25 mL of 0.03 M $KMnO_4$ solution was added into the suspension. Then, 8 mL 2.5 M hydrochloric acid solution was added into the mixture with fierce stirring. The etching reaction was sustained for 2 min, then the product was filtered immediately and washed with distilled water. Finally, the obtained solid was dried in a vacuum oven at 60°C for 12 h.

2.3. Characterization of the Samples. The crystal structure of the prepared $MnCO_3$ template and MHNSs was studied with X-ray powder diffraction (XRD, Bruker D8 Advance, Cu Kα, $\lambda = 0.15418$ nm). The morphology of the samples was characterized by field emission scanning electron microscopy (FESEM, ZEISS Merlin compact) and transmission electron microscopy (TEM, TecnaiG2 F2o S-TWIN). The surface functional groups were analyzed by Fourier transform infrared (FT-IR) spectra (Nicolet 5700). The BET surface area, pore volume, and pore size distribution of the MHNSs characterized at 77 K were investigated using an Autosorb-iQ Quantachrome surface area and porosity analyzer. The surface compositions were analyzed by X-ray photoelectron spectroscopy (XPS, ESCALab 250Xi).

2.4. Evaluation of the Adsorption Capacity. The MO solution was used as a model pollutant to evaluate the adsorption performance of the as-prepared MHNSs. In order to study the effect of initial concentrations, the MO solution with selected concentrations (50, 100, 150, 200, 250, and 300 mg L^{-1}) was prepared. Similarly, the pH value of the solution was adjusted from 2.0 to 11.0 using 1 M HCl or NaOH to investigate the effect of pH value. The 20 mg MHNS adsorbent was added into 200 mL MO solution, and the solution was kept at 15°C under stirring at 300 rpm. At selected intervals, about 3 mL suspension was collected and filtered to remove the catalysts using a 0.45 μm membrane filtration. The MO concentration was recorded on a Lambda 35 UV-Vis spectrometer. The equilibrium absorption capacity of the MHNSs q_e (mg g^{-1}) was calculated using the following equation [31, 32]:

$$q_e = \frac{V(C_0 - C_e)}{m}, \quad (1)$$

where C_0 (mg/L) is the initial MO concentration, C_e (mg/L) is the equilibrium MO concentration, V (L) is the volume of the solution, and m (g) is the mass of the added MHNS adsorbents.

The reusability of the MHNSs was a very important factor for industrial application. In the stability evaluation, the used adsorbent was collected. Then, the stability test of the MHNSs was conducted by repeating the MO solution under the same conditions for five cycles without any regeneration treatment [33, 34].

3. Results and Discussion

3.1. XRD, Morphology, and the BET Measurements of the MHNSs. In this study, low-cost $(NH_4)_2CO_3$ and $KMnO_4$ were selected as the raw materials. The MHNSs were successfully fabricated by the selective etching method with the $MnCO_3$ as the template. The typical SEM and TEM images of the $MnCO_3$ template and MHNSs are shown in Figure 1. The $MnCO_3$ templates show a well-defined microsphere structure with a diameter of about 2 μm, and the microspheres show a slight agglomeration between each other. Furthermore, some broken microspheres demonstrated that the spherical hollow structure of prepared MHNSs is derived from the selective etching of the $MnCO_3$ template. The

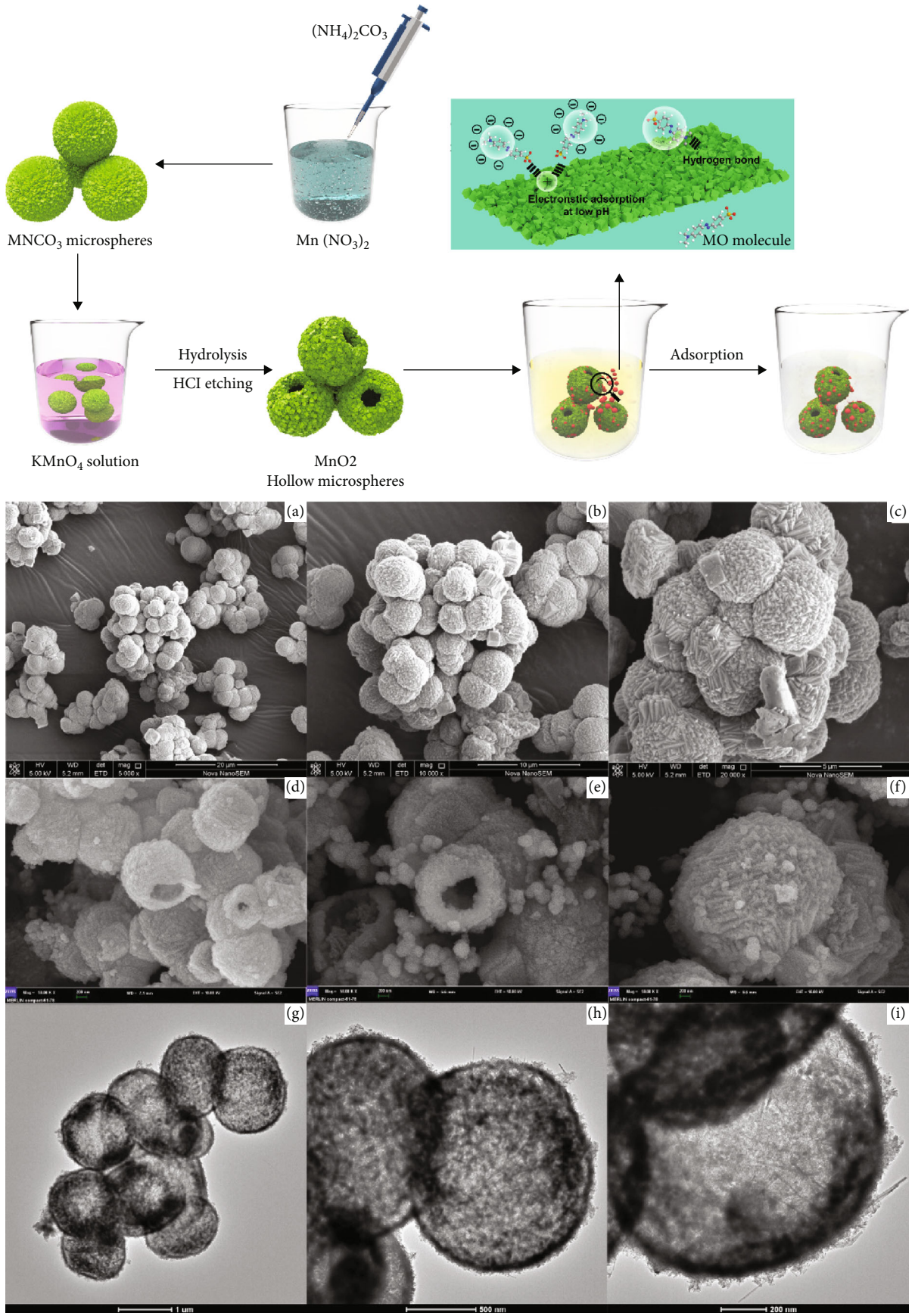

Figure 1: Scheme illustration and the typical SEM and TEM images of the samples.

thickness of the spherical shell was about 300 nm. As shown in the high-resolution images, the original smooth nanosheets were replaced by the rough MnO_2 nanoparticles. When the $KMnO_4$ solution was added, the MnO_2 nanoparticles formed by hydrolysis were adhered on the surface of the $MnCO_3$ template. At the same time, the $MnCO_3$ template was selectively etched by the HCl solution, then the MHNSs with a spherical hollow structure were obtained. Meanwhile, it can be observed that some dispersed MnO_2 microsphere with the diameter at 200~300 nm coated on the surface of the hollow spheres. Furthermore, the hollow structure of prepared MHNSs was confirmed by the TEM techniques (Figure 1(g)–1(i)). The diameter of the hollow shells range from 1 μm to 2 μm, and the shell thickness was about 300 nm, which was consistent with the SEM analysis. Thus, a plausible formation mechanism was proposed in the scheme illustration figure (as shown in Figure 1).

Figure 2 showed the XRD patterns of prepared $MnCO_3$ and MHNS samples. The diffraction peaks at $2\theta = 24.25^\circ$, 31.36°, and 51.68° can be assigned to the (012), (104), and (116) planes of $MnCO_3$ (JCPDS card no. 44-1472), respectively. For the MHNS sample, the diffraction peaks at $2\theta = 37.12^\circ$, 45.01°, and 65.70° correspond to the (311), (400) and (440) crystal planes, respectively, which was consistent with the α-MnO_2 (JCPDS card no. 44-0992). However, it can be observed that the MHNSs exhibit low and broad diffraction peaks. As mentioned in the FESEM discussions, the $KMnO_4$ will hydrolyze to form MnO_2 nanoparticles coated on the surface of the $MnCO_3$ template. Meanwhile, the MnO_2 maintains a low level of crystallinity due to the low-temperature and short-time reaction conditions. Thus, the characteristic peak intensity of the MHNSs was weak compared to that of prepared $MnCO_3$ templates.

In order to investigate the specific surface area, pore size distribution and pore volume of the MHNSs, the N_2 adsorption-desorption isotherm was conducted and the result was as shown in Figure 3. The N_2 adsorption-desorption isotherms exhibit type-IV isotherms. The BET surface area, total pore volume, and average pore size are determined to be 43.74 $m^2\ g^{-1}$, 0.1133 $cm^3\ g^{-1}$, and 1.04 nm, respectively. Thus, it can be concluded that the prepared MHNS sample is dominated by mesopores, promoting the adsorption ability for the MO molecule.

3.2. Effect of pH Value on MO Adsorption. Many studies have reported that the adsorption capacity of the adsorbent was pH-dependent. The reason can be that the pH value can influence the surface charge of the adsorbent and the degree of ionization/dissociation of the MO molecules. Thus, the adsorption on MO at different pH values are performed and shown in Figure 4. With the increase of pH value from 2.0 to 11.0, the adsorption capacity of MHNSs on MO decreases from 99% to 2%. Obviously, MHNSs can only effectively adsorb MO molecules under acidic conditions, but it could hardly act at alkaline or neutral solution conditions. Since most of the free hydroxyl groups on the surface of MHNSs are derived from the hydrogen ions in the solution, the surface is positively charged. However, the sulfonate ions ionized by methyl orange molecules are negatively charged under acidic condition. Therefore, the negatively charged sulfonate ions will be adhered to the positively charged MHNS surface, then forming the ligand complex.

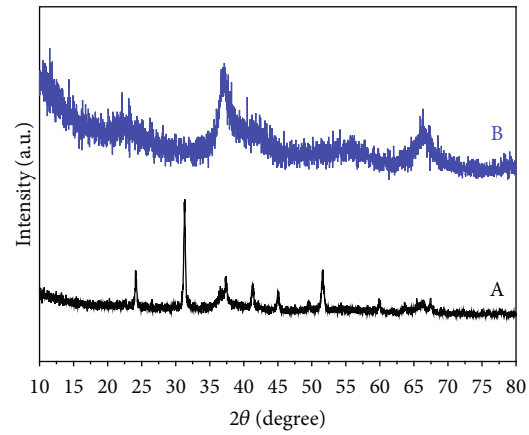

Figure 2: XRD patterns of the $MnCO_3$ template (A) and the MHNS samples (B).

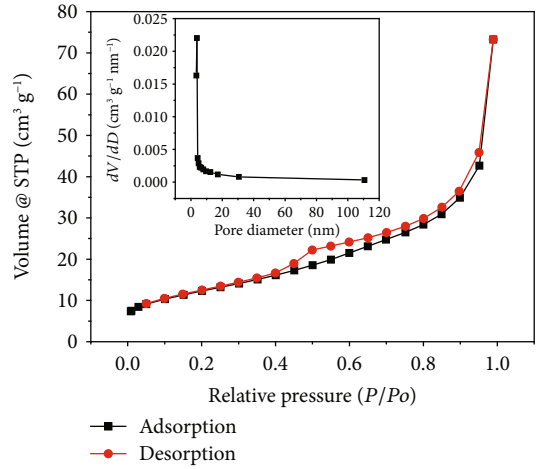

Figure 3: N_2 adsorption-desorption isotherm (inset: the pore size distribution).

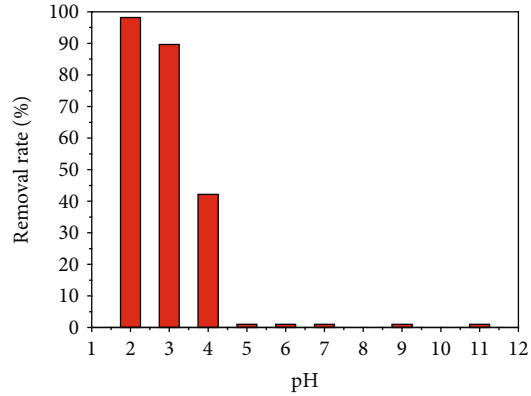

Figure 4: Effect of solution pH on the MO adsorption (experimental conditions: initial dye concentration: 50 $mg\ L^{-1}$, adsorbent dosage: 20 mg/200 mL, temperature: 288 K, and contact time: 120 min).

At an acidic pH value, the solution is rich of hydrated hydrogen ions (H^+ and H_3O^+), and the surface of MHNSs become more positively charged, which makes it more likely to adsorb MO in solution. On the contrary, the adsorption efficiency is relatively low under alkaline conditions. Moreover, there is a competitive adsorption relationship between the negatively charged MO ions and excessive hydroxide ions. With the increase of pH value, the concentration of hydroxide ions in the solution increases and the negative charge on the surface of MHNSs increases. So the Coulombic repulsion between the hydroxide ions and the anionic dye was enhanced, and the adsorption activity of MHNSs on the MO solution was decreased. Therefore, the significant influence of the adsorption amount of the MHNS surface was caused by the pH value of the solution, indicating that the electrostatic interaction may be the main mechanism for the adsorption process of anionic dyes. It can also be seen from Figure 5 that the adsorption process of MHNSs on MO is very fast, in which almost 90% of MO molecules were removed within 5 min.

3.3. Effect of Contact Time and Initial Concentration. Three initial concentrations (50, 100, and 150 mg L^{-1}) of MO solutions were chosen to investigate the equilibrium time and the adsorption capacity of prepared MHNSs and the results was shown as in the Figure 6. With the increase of the initial concentration, the equilibrium absorption capacity (q_e) of the MHNSs increased from 475.95 mg g^{-1} to 1420.08 mg g^{-1}, indicating that the initial concentration had a significant impact on the adsorption capacity. The reason can be ascribed to the increasing driving force of concentration gradient. Moreover, the adsorption rate of MO was rapid at the initial 30 min and then slows (at the contact time of 30~120 min). During the initial stage, the MO molecules were rapidly absorbed by the MHNS adsorbent due to the sufficient adsorption sites on the surface. Then, the adsorption rate slowed down with the dwindling number of active sites and the increasing mutual repulsive forces between the MO molecules on the surface of MHNSs and the bulk solution. The reusability of the MHNS adsorbent was tested with the initial concentration of MO solution at 50 mg L^{-1}, and the results are shown in Figure 7. It was found that the removal rate of MO was still maintained at 90% after four cycles. Therefore, it can be concluded that the MHNS adsorbent exhibited well adsorption stability on the MO solution.

3.4. Evaluation of Adsorption Kinetics. The Lagergren-first-order equation, pseudo-second-order equation, and intraparticle diffusion model were used to investigate the adsorption kinetics of the MO molecule on MHNSs, and the correlation coefficient value (R^2) was used to select the best-fit model [35, 36]. Figures 8–10 present the analysis results of MHNSs acted on the MO solution with different dynamic models. The pseudo-first-order kinetic model was specified as follows [37, 38]:

$$\ln(q_e - q_t) = \ln(q_e) - k_1 t, \quad (2)$$

where q_t (mg/g) is the adsorption capacity at time t (min), q_e (mg/g) is the equilibrated adsorption capacity, and k_1 (min^{-1}) is the rate constant of the pseudo-first-order kinetic model.

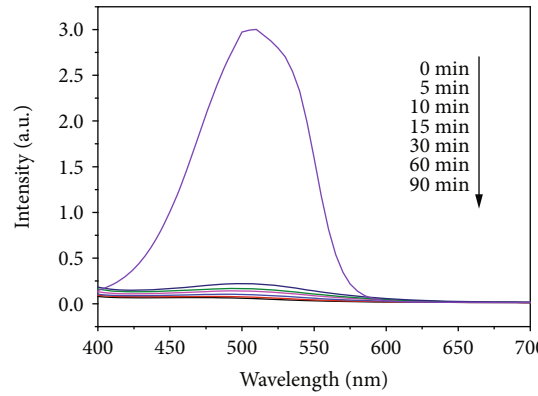

Figure 5: Time-dependent absorbance spectra of the adsorption process at selected intervals.

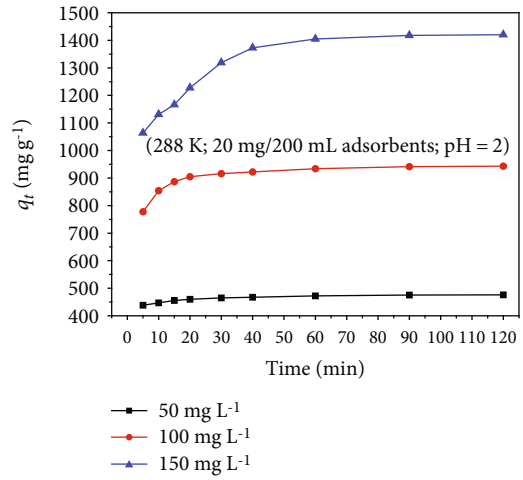

Figure 6: Effect of contact time on MO adsorption at different initial concentrations.

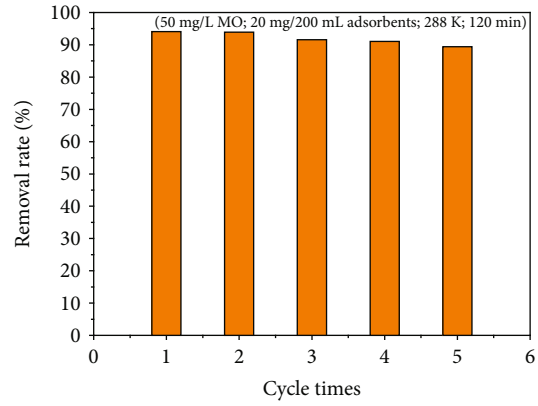

Figure 7: Efficiency of the MHNS composite after five cycles.

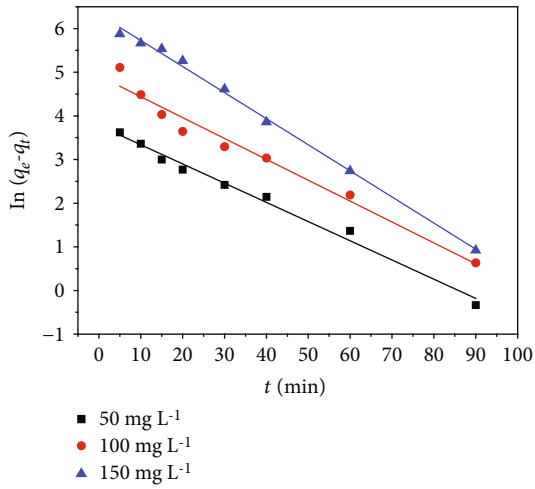

Figure 8: Regressions of kinetic plots at different initial concentrations: pseudo-first-order kinetic model.

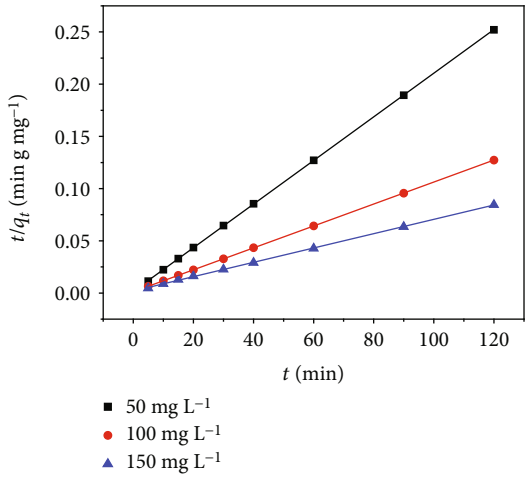

Figure 9: Regressions of kinetic plots at different initial concentrations: pseudo-second-order kinetic model.

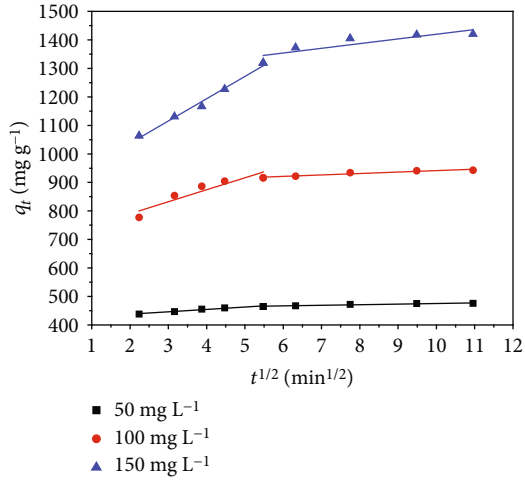

Figure 10: Regressions of kinetic plots at different initial concentrations: intraparticle mass transfer diffusion model.

The value of k_1 can be calculated from the plots of ln $(q_e\text{-}q_t)$ verse t according to the equation. The linear formula of the pseudo-second-order kinetic model can be expressed as follows [39, 40]:

$$\frac{t}{q_t} = \frac{1}{k_2 q_e{}^2} + \frac{t}{q_e}, \tag{3}$$

where k_2 (g mg^{-1} min^{-1}) is the rate constant of the pseudo-second-order kinetic model.

The slope and intercept of the linear plots of t/q_t against t was used to calculate the value of k_2 and q_e according to the equation.

Then, the initial adsorption rate h (mg g^{-1} min^{-1}) was determined as follows [41]:

$$h = k_2 q_e{}^2. \tag{4}$$

The actual rate-controlling step of the MO absorbed on the MHNSs was very crucial for researching the adsorption mechanism. However, the aforementioned two kinetic models could not predict it exactly, then the intraparticle mass transfer diffusion model proposed by Weber-Morris was employed. And the calculation equation was as follows [42, 43]:

$$q_t = k_i t^{1/2} + C, \tag{5}$$

where k_i (mg g^{-1} min$^{-1/2}$) is the intraparticle diffusion rate constant and C is the constant that reflects the thickness of the boundary layer.

The graph of q_t against the square root of time can be used calculated the value of k_i and the constant C.

The three kinetic model parameters of MO adsorption onto MHNSs with different initial concentrations are shown in Table 1. It could be observed that all the experimental data agreed well with the pseudo-second-order kinetic model ($R^2 > 0.9997$). Therefore, the pseudo-second-order kinetic model was selected to analyze the adsorption process of MO molecule onto MHNSs in this study.

Generally, the adsorption process of MO on the MHNSs was controlled by the following three steps: external mass diffusion, intraparticle diffusion, and the adsorption on the MHNS surface. Because the adsorption process was very fast, this rate-limiting step often was not considered in this study. In order to determine the exact rate-controlling step, the intraparticle diffusion model was involved in the analysis process for MO adsorption on the MHNSs, and the results are shown in Figure 10.

Multivariate linear regression was used to analyze the MHNS adsorption MO data. According to the intraparticle diffusion model, the linear plot of adsorption capacity versus square rout of time ($t^{1/2}$) indicated that there were two obvious regions in the graph. The first region was from 0 to 30 minutes, and the second one was 30-120 minutes. The linear portion in the first region has a larger slope, which represents the external mass transfer process. However, during the second stage, the adsorption capacity of MHNSs on MO still

Table 1: Parameters of pseudo-first- and pseudo-second-order adsorption kinetic models and the intraparticle diffusion model at various concentrations.

C_0 (mg L^{-1})	$q_{e,\exp}$	Pseudo-first-order model		
		k_1	q_e	r^2
50	475.95	0.04402	43.793	0.9869
100	942.99	0.04788	136.904	0.9683
150	1420.08	0.0598	560.220	0.9962

C_0 (mg L^{-1})	Pseudo-second-order model			Intraparticle diffusion model			
	$k_2 \times 10^{-3}$	q_e	r^2	h	k_i	C	r^2
50	2.7822	478.469	0.9999	636.943	8.339	421.176	0.9562
100	0.9187	952.381	0.9999	833.333	42.114	705.854	0.8299
150	0.2349	1458.99	0.9997	500.000	78.136	881.039	0.9830

increased with $t^{1/2}$, but compared with the first stage, the slope of the linear portion was much smaller. This can be ascribed to the second stage which was controlled by the intraparticle diffusion. Additionally, all the linear portions did not pass through the origin, indicating that the intraparticle diffusion was not the only rate-controlling step in the MHNS adsorption process. The ratio of the diffusion duration of the external mass to the intraparticle is about 1 : 3, which means that the whole adsorption process was controlled by the external mass transfer and the intraparticle diffusion, and the intraparticle diffusion was superior to the external mass transfer.

3.5. Adsorption Isotherm Study. In order to further study the adsorption interaction between the MO and the MHNSs, the equilibrium adsorption data were analyzed and fitted using the Langmuir and Freundlich isothermal models in this study [44, 45]. The Langmuir isotherm can be expressed as follows:

$$\frac{C_e}{Q_e} = \frac{1}{Q_m K_L} + \frac{1}{Q_m} C_e, \tag{6}$$

where Ce (mg/L) is the equilibrium concentration, Q_e (mg/g) is the adsorption capacity of adsorbate per unit mass, Q_m is the Langmuir constant, and K_L is the adsorption rate.

The essential characteristic of the Langmuir equation was expressed by the dimensionless separation factor R_L:

$$R_L = \frac{1}{1 + K_L C_0}, \tag{7}$$

where K_L (L/mg) is the Langmuir isotherm constant, C_0 (mg/L) is the initial MO concentration, and R_L is the type of isotherm.

The linear form of the Freundlich equation is

$$\ln Q_e = \ln K_F + \frac{1}{n} \ln C_e, \tag{8}$$

where K_F (L/mg) is the adsorption capacity, and n is the definition of how favorable the adsorption process is.

As shown in Table 2, the R_L value of the Langmuir model was between 0 and 1 and the n value of the Freundlich model was between 1 and 10. These results indicated that the adsorption process of MO molecules on the MHNSs was favorable. In addition, the correlation coefficient results of different models showed that the Freundlich model had a better fit of experimental data than that of the Langmuir model. When the temperature of the adsorption process increased from 273 K to 303 K, the maximum adsorption capacity of MO molecules on MHNSs decreased significantly from 1677.14 mg/g to 1589.40 mg/g. The maximum adsorption capacity of MHNSs and other adsorbents reported in literature on MO solution are listed in Table 3. It can be seen from the table that the saturated adsorption capacity of MHNSs was much higher than that of other adsorbents. Therefore, it can be considered that the prepared MHNSs have a potential application in the sewage treatment field.

3.6. Thermomechanical Analysis. In general, depth information such as the internal energy transformation can be analyzed by the thermodynamic parameters in the adsorption process. The standard Gibbs free energy change ΔG°, the standard molar enthalpy change ΔH° and the standard molar entropy change ΔS° were determined according to the adsorption thermodynamic equilibrium constants at different temperatures. For the adsorption process, the adsorption equilibrium constant K_0 can be defined by the following formula [55, 56]:

$$K = \frac{\alpha_s}{\alpha_e} = \left(\frac{\gamma_s}{\gamma_e}\right) \cdot \left(\frac{q_e}{C_e}\right), \tag{9}$$

where α_s is the activity (effective concentration) of adsorbed methyl orange and α_e is the activity of methyl orange in the equilibrium solution. γ_s is the activity coefficient of adsorption methyl orange. γ_e is the activity coefficient of methyl orange in equilibrium solution. With the progress of adsorption, the concentration of methyl orange in the solution keeps decreasing and tends to zero when the adsorption equilibrium is reached. Therefore, the equilibrium constant

Table 2: Parameters of the adsorption isotherm for the removal of MO by the MHNSs at different temperatures.

T (K)	Langmuir				Freundlich		
	q_m (mg g^{-1})	b	r^2	R_L	n	K_F	r^2
273	1718.712	0.2824	0.9992	0.01167~0.06614	1.6213	380.8478	0.9257
288	1688.416	0.2278	0.9989	0.01442~0.08071	1.1274	214.6052	0.9786
303	1633.290	0.2089	0.9981	0.01571~0.08737	1.1029	191.8282	0.9899

Table 3: Comparison of the adsorption capacities of MO onto various adsorbents.

Adsorbates	Adsorbents	q_{max} (mg g^{-1})	Reference
MO	Amine modified PIM-1 ultrafine fibers	312.50 mg g^{-1}	[46]
	3-dimensional (3D) flower-like Ni/Al@PAB LDH	412.80 mg g^{-1}	[47]
	Date palm ash (DPA) and MgAl-LDH composites	242.98 mg g^{-1}	[48]
	Magnetic lignin-based carbon nanoparticles (MLBCN)	113.00 mg g^{-1}	[49]
	Chitosan-lysozyme biocomposite (CLC)	435.00 mg g^{-1}	[50]
	MnO_2-graphene-carbon nanotube (MnO_2-G-CNT)	476.19 mg g^{-1}	[51]
	$CaFe_2O_4$ and ZrO_2 magnetic nanocomposite (CaF-ZO-MNC)	370.37 mg g^{-1}	[52]
	An amorphous solid contains large cationic aMOC-1	359.00 mg g^{-1}	[53]
	β-CD and PEI bifunctionalized magnetic (Fe_3O_4-PEI/β-CD)	192.20 mg g^{-1}	[54]
	The MnO_2 hollow nanospheres (MHNSs)	1677.13 mg g^{-1}	This work

K_0 value could be obtained by plotting $\ln(q_e/C_e)$ versus q_e and extrapolating q_e equal to zero.

For any interaction, the adsorption standard Gibbs free energy change ΔG° can be expressed by

$$\Delta G^\circ = -RT \ln(K_0),$$
$$\Delta G^\circ = \Delta H^\circ - T\Delta S^\circ. \quad (10)$$

From the above two formulas, K_0 can be concluded as follows:

$$\ln(K_0) = -\frac{\Delta H^\circ}{RT} + \frac{\Delta S^\circ}{R}, \quad (11)$$

where R is the standard gas constant (8.314 J mol^{-1} K^{-1}) and T is the Kelvin temperature (K); ΔH° and ΔS° can be calculated from the slope and intercept of plot $\ln(K_0)$ versus $1/T$. The thermodynamic data is listed in Table 4. It can be seen that the ΔG° values at the three temperatures were all negative, indicating that the adsorption of MO on the surface of MHNSs was a spontaneous process and thermodynamically feasible. In general, the ΔG° of the physical adsorption process was less than that of the chemical adsorption process. Normally, the ΔG° value of the physical adsorption process was between -20 and 0 kJ mol^{-1}, while that of the chemisorption process was between -400 and -80 kJ mol^{-1} [57]. And the adsorption standard value ΔH° of the physical process was 2~21 kJ mol^{-1} [58]. Therefore, the value of ΔH° (-16.825) also suggested that the adsorption of MO onto the surface of MHNSs was mainly a physical process, which was also consistent with the previous results. Therefore, the adsorption process of MO on MHNSs was mainly a physical process. Moreover, the negative value of ΔH° revealed that the adsorption process is an exothermic process, which was well consistent with the aforementioned results that the adsorption capacity of MO decreased with the increase of temperature. Meanwhile, the negative ΔS° of the adsorption demonstrated that the MO molecule in bulk solution was in a more chaotic distribution compared to the ordered state (adsorbed on the surface of MHNSs).

Table 4: Values of thermodynamic parameters for the adsorption of the MO dye on the MHNSs.

T (K)	$\ln K_0$	ΔG° (kJ mol^{-1})	ΔH° (kJ mol^{-1})	ΔS° (J mol^{-1} K^{-1})
273	7.3756	-16.740		
288	6.7616	-16.189	-16.825	-1.160
303	6.6528	-16.759		

3.7. Adsorption Mechanism Analysis. In order to further study the mechanism of the MO adsorption process on adsorbents, the FT-IR spectra of the fresh and used MHNS samples are shown in Figure 11. The weak peaks around at about 530 cm^{-1} in the low frequency region could be attributed to the Mn-O and Mn-O-Mn shrink vibration [59, 60]. Importantly, the FT-IR spectra of the MHNS-MO sample were significantly different from its original spectrum. In the case of the MHNS-MO sample, the new peaks located at 1039, 1193, and 1384 cm^{-1} correspond to the contraction vibrations of the -S=O, CH_3-, and CN bonds, respectively. And the peaks located at 818, 849 cm^{-1} can be indexed to the fingerprint region indicating that MO molecules were concentrated on the surface of MHNSs [61, 62].

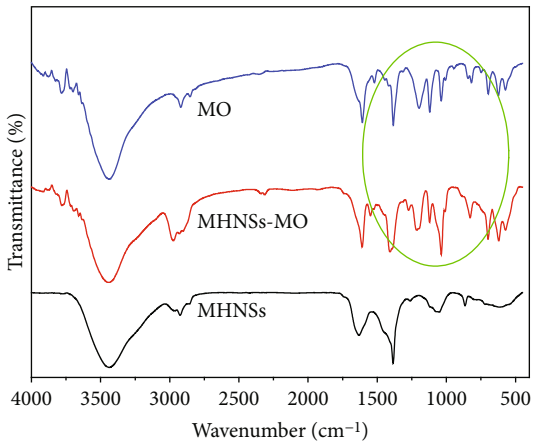

Figure 11: FT-IR spectra of pure MO and the MHNS composites before and after adsorption of MO.

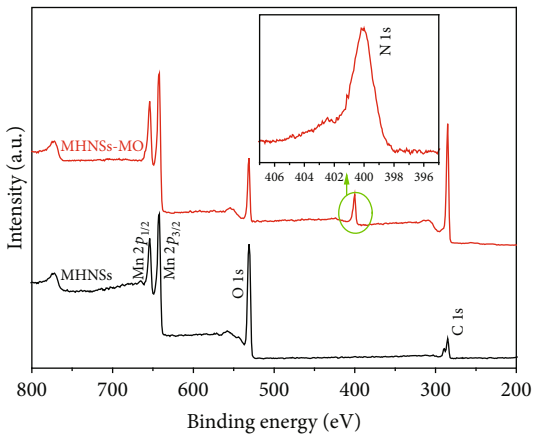

Figure 12: XPS spectra of the MHNS composites before and after adsorption of MO.

Generally, adsorption reaction may cause some changes of physical properties changes in the adsorbent, and the resulting change may help to investigate the adsorption reaction. As shown in Figure 12, the surface chemical composition and valence state of MHNSs before and after adsorption of MO molecules were characterized by XPS. It can be seen that the peaks of Mn $2p_{3/2}$ and Mn $2p_{1/2}$ were located at 642.1 eV and 653.5 eV, respectively, indicating that the Mn of the prepared MHNSs were in the form of Mn^{4+}. The energy separation between the two peaks was 11.4 eV, which was well in agreement with the previous literatures [63, 64]. Furthermore, the position and intensity of the Mn 2*p* peaks did not change after the adsorption, which confirmed that the adsorption process of MO did not cause a significant change in the oxidation state of manganese. Additionally, it was found that there was a weak N 1s peak located at 399.8 eV for the adsorbed MHNS-MO spectrum, which indicated that a large amount of MO was adsorbed onto the MHNSs. These results indicated that the adsorption of MO molecules did not change the chemical composition and valence states of MHNSs. This adsorption process was mainly a physical process, which was consistent with the conclusions in thermomechanical analysis.

4. Conclusions

The MnO_2 hollow nanospheres (MHNSs) were prepared through a selective etching method using $MnCO_3$ as sacrificial templates. The crystal structure, morphology, and BET surface area were investigated. The adsorption capacity of MO onto the MHNSs was systematically investigated by adjusting the pH value, the initial MO concentration, and the contact time. The prepared MHNSs showed an excellent adsorption capacity toward MO compared to other adsorbents. The adsorption kinetics followed the pseudo-second-order model. Moreover, the overall process was apparently controlled by the external mass transfer and intraparticle diffusion based on the adsorption kinetics data. The thermodynamic analysis showed that the adsorption of MO on MHNSs was a spontaneous, exothermic, and physical process. Similarly, the XPS results also confirmed that the adsorption was mainly a physical process. The superior adsorbing performance of the MHNSs could be attributed to their unique hollow structure and large BET surface area, which provided much active adsorption sites. It is expected that the prepared MHNSs may be a promising adsorbent for water treatment due to its superior adsorbing performance and good stability.

Data Availability

All data included in this study are available upon request by contact with the corresponding author.

Conflicts of Interest

The authors declare that there is no conflict of interest regarding the publication of this paper.

Acknowledgments

This project was financially supported by projects of the China Postdoctoral Science Foundation (No. 2017M610491), Key Program of Natural Science Foundation of Hubei Province (No. 2016CFA079), Scientific Research Plan Project of Education department of Hubei province (No. B2017057), and the Principal Fund of Wuhan Institute of Technology (NO. 2018003).

References

[1] R. Xu, J. Mao, N. Peng, X. Luo, and C. Chang, "Chitin/clay microspheres with hierarchical architecture for highly efficient removal of organic dyes," *Carbohydrate Polymers*, vol. 188, pp. 143–150, 2018.

[2] Z. Wen, J. Ke, J. Xu, S. Guo, Y. Zhang, and R. Chen, "One-step facile hydrothermal synthesis of flowerlike Ce/Fe bimetallic oxides for efficient As(V) and Cr(VI) remediation: performance and mechanism," *Chemical Engineering Journal*, vol. 343, pp. 416–426, 2018.

[3] Z. Wen, Y. Zhang, Y. Wang, L. Li, and R. Chen, "Redox transformation of arsenic by magnetic thin-film MnO_2 nanosheet-coated flowerlike Fe_3O_4 nanocomposites," *Chemical Engineering Journal*, vol. 312, pp. 39–49, 2017.

[4] Z. Gao, S. Xie, B. Zhang, X. Qiu, and F. Chen, "Ultrathin Mg-Al layered double hydroxide prepared by ionothermal synthesis in a deep eutectic solvent for highly effective boron removal," *Chemical Engineering Journal*, vol. 319, pp. 108–118, 2017.

[5] S. Luo, F. Qin, Y. Ming, H. Zhao, Y. Liu, and R. Chen, "Fabrication uniform hollow Bi_2S_3 nanospheres *via* Kirkendall effect for photocatalytic reduction of Cr(VI) in electroplating industry wastewater," *Journal of Hazardous Materials*, vol. 340, pp. 253–262, 2017.

[6] F. Chen, S. Xie, X. Huang, and X. Qiu, "Ionothermal synthesis of Fe_3O_4 magnetic nanoparticles as efficient heterogeneous Fenton-like catalysts for degradation of organic pollutants with H_2O_2," *Journal of Hazardous Materials*, vol. 322, Part A, pp. 152–162, 2017.

[7] S. Guo, A. Naeem, H. Fida, M. Hamayun, M. Muska, and J. Chen, "Removal of Cu(II) from aqueous solution by iron vanadate: equilibrium and kinetics studies," *Desalination and Water Treatment*, vol. 75, pp. 124–131, 2017.

[8] S. Guo, Z. Yang, Z. Wen, H. Fida, G. Zhang, and J. Chen, "Reutilization of iron sludge as heterogeneous Fenton catalyst for the degradation of rhodamine B: role of sulfur and mesoporous structure," *Journal of Colloid and Interface Science*, vol. 532, pp. 441–448, 2018.

[9] J. Ke, X. Li, Q. Zhao, B. Liu, S. Liu, and S. Wang, "Upconversion carbon quantum dots as visible light responsive component for efficient enhancement of photocatalytic performance," *Journal of Colloid and Interface Science*, vol. 496, pp. 425–433, 2017.

[10] H. Fida, G. Zhang, S. Guo, and A. Naeem, "Heterogeneous Fenton degradation of organic dyes in batch and fixed bed using La-Fe montmorillonite as catalyst," *Journal of Colloid and Interface Science*, vol. 490, pp. 859–868, 2017.

[11] J.-X. Yu, W. L. Xiong, J. Zhu, J. D. Chen, and R. A. Chi, "Removal of Congo red from aqueous solution by adsorption onto different amine compounds modified sugarcane bagasse," *Clean Technologies and Environmental Policy*, vol. 19, no. 2, article 1243, pp. 517–525, 2017.

[12] Z. He, J. Yu, Y. Qi, and R. A. Chi, "PMDA-modified biosorbents for enhancement adsorption of basic magenta," *Environmental Earth Sciences*, vol. 70, no. 2, article 2147, pp. 635–642, 2013.

[13] S. Song, K. Wu, H. Wu, J. Guo, and L. Zhang, "Multi-shelled ZnO decorated with nitrogen and phosphorus co-doped carbon quantum dots: synthesis and enhanced photodegradation activity of methylene blue in aqueous solutions," *RSC Advances*, vol. 9, no. 13, pp. 7362–7374, 2019.

[14] L. Chen, J. Wei, W. Wang, and C. Wang, "Combination of microalgae cultivation with membrane processes for the treatment of municipal wastewater," *Water Science & Technology*, vol. 68, no. 11, pp. 2374–2381, 2013.

[15] M. Zhang, L. Wang, T. Zeng et al., "Two pure MOF-photocatalysts readily prepared for the degradation of methylene blue dye under visible light," *Dalton Transactions*, vol. 47, no. 12, pp. 4251–4258, 2018.

[16] H. Wang, L. Liang, X. Cheng, Y. Luo, and S. Sun, "Facile fabrication of porous ZnS and ZnO films by coaxial electrospinning for highly efficient photodegradation of organic dyes," *Photochemistry and Photobiology*, vol. 94, no. 1, pp. 17–26, 2018.

[17] J. Huang, Y.'. Ming, Y. du, Y. Wang, and C. Wang, "Study on the effect of the three-dimensional electrode in degradation of methylene blue by lithium modified rectorite," *Journal of Analytical Methods in Chemistry*, vol. 2016, Article ID 8198235, 6 pages, 2016.

[18] G. Cheng and F. J. Stadler, "Achieving phase transformation and structure control of crystalline anatase TiO_2@C hybrids from titanium glycolate precursor and glucose molecules," *Journal of Colloid and Interface Science*, vol. 438, pp. 169–178, 2015.

[19] Z. Wen, Y. Zhang, S. Guo, and R. Chen, "Facile template-free fabrication of iron manganese bimetal oxides nanospheres with excellent capability for heavy metals removal," *Journal of Colloid and Interface Science*, vol. 486, pp. 211–218, 2017.

[20] J. Qian, H. Jin, B. Chen et al., "Aqueous manganese dioxide ink for paper-based capacitive energy storage devices," *Angewandte Chemie (International Ed. in English)*, vol. 54, no. 23, pp. 6800–6803, 2015.

[21] Y. Sun, Z. Fang, C. Wang, K. R. R. M. Ariyawansha, A. Zhou, and H. Duan, "Sandwich-structured nanohybrid paper based on controllable growth of nanostructured MnO_2 on ionic liquid functionalized graphene paper as a flexible supercapacitor electrode," *Nanoscale*, vol. 7, no. 17, pp. 7790–7801, 2015.

[22] T. Raj Kumar, G. Gnana Kumar, and A. Manthiram, "Biomass-derived 3D carbon aerogel with carbon shell-confined binary metallic nanoparticles in CNTs as an efficient electrocatalyst for microfluidic direct ethylene glycol fuel cells," *Advanced Energy Materials*, vol. 9, no. 16, article 1803238, 2019.

[23] G. Jenita Rani, M. A. Jothi Rajan, and G. Gnana kumar, "Reduced graphene oxide/$ZnFe_2O_4$ nanocomposite as an efficient catalyst for the photocatalytic degradation of methylene blue dye," *Research on Chemical Intermediates*, vol. 43, no. 4, pp. 2669–2690, 2017.

[24] H.-P. Jing, C.-C. Wang, Y.-W. Zhang, P. Wang, and R. Li, "Photocatalytic degradation of methylene blue in ZIF-8," *RSC Advances*, vol. 4, no. 97, pp. 54454–54462, 2014.

[25] J. Salamon, Y. Sathishkumar, K. Ramachandran et al., "One-pot synthesis of magnetite nanorods/graphene composites and its catalytic activity toward electrochemical detection of dopamine," *Biosensors and Bioelectronics*, vol. 64, pp. 269–276, 2015.

[26] G. Gnana Kumar, G. Amala, and S. M. Gowtham, "Recent advancements, key challenges and solutions in non-enzymatic electrochemical glucose sensors based on graphene platforms," *RSC Advances*, vol. 7, no. 59, pp. 36949–36976, 2017.

[27] M. Ranjani, Y. Sathishkumar, Y. S. Lee, D. Jin Yoo, A. R. Kim, and G. Gnana kumar, "Ni–Co alloy nanostructures anchored on mesoporous silica nanoparticles for non-enzymatic glucose sensor applications," *RSC Advances*, vol. 5, no. 71, pp. 57804–57814, 2015.

[28] M. Gheju, I. Balcu, and G. Mosoarca, "Removal of Cr(VI) from aqueous solutions by adsorption on MnO_2," *Journal of Hazardous Materials*, vol. 310, pp. 270–277, 2016.

[29] D. Li, X. Wu, and Y. Chen, "Synthesis of hierarchical hollow MnO2Microspheres and potential application in abatement of VOCs," *Journal of Physical Chemistry C*, vol. 117, no. 21, pp. 11040–11046, 2013.

[30] Y. Chen, Q. Wang, and T. Wang, "Facile large-scale synthesis of brain-like mesoporous silica nanocomposites via a selective etching process," *Nanoscale*, vol. 7, no. 39, pp. 16442–16450, 2015.

[31] J. Ke, X. Duan, S. Luo et al., "UV-assisted construction of 3D hierarchical rGO/Bi_2MoO_6 composites for enhanced photocatalytic water oxidation," *Chemical Engineering Journal*, vol. 313, pp. 1447–1453, 2017.

[32] J. Xiong, G. Cheng, F. Qin, R. Wang, H. Sun, and R. Chen, "Tunable BiOCl hierarchical nanostructures for high-efficient photocatalysis under visible light irradiation," *Chemical Engineering Journal*, vol. 220, pp. 228–236, 2013.

[33] S. Danwittayakul, M. Jaisai, T. Koottatep, and J. Dutta, "Enhancement of photocatalytic degradation of methyl orange by supported zinc oxide nanorods/zinc stannate (ZnO/ZTO) on porous substrates," *Industrial & Engineering Chemistry Research*, vol. 52, no. 38, pp. 13629–13636, 2013.

[34] L. Zhang, K. Wu, Y. Zhou et al., "Synthesis of MnO_2@graphene oxide flower-like nanocomposite as adsorbent for methyl orange decolouration," *Micro & Nano Letters*, vol. 12, no. 5, pp. 335–337, 2017.

[35] M. K. Sahu, S. Mandal, L. S. Yadav, S. S. Dash, and R. K. Patel, "Equilibrium and kinetic studies of Cd(II) ion adsorption from aqueous solution by activated red mud," *Desalination and Water Treatment*, vol. 57, no. 30, pp. 14251–14265, 2015.

[36] J. Shou and M. Qiu, "Adsorption of copper ions onto activated carbon from capsicum straw," *Desalination and Water Treatment*, vol. 57, no. 1, pp. 353–359, 2014.

[37] M. Loredo-Cancino, E. Soto-Regalado, R. B. García-Reyes et al., "Adsorption and desorption of phenol onto barley husk-activated carbon in an airlift reactor," *Desalination and Water Treatment*, vol. 57, no. 2, pp. 845–860, 2015.

[38] T. N. Ramesh, D. V. Kirana, A. Ashwini, and T. R. Manasa, "Calcium hydroxide as low cost adsorbent for the effective removal of indigo carmine dye in water," *Journal of Saudi Chemical Society*, vol. 21, no. 2, pp. 165–171, 2017.

[39] Y. Xie, C. He, L. Liu et al., "Carbon nanotube based polymer nanocomposites: biomimic preparation and organic dye adsorption applications," *RSC Advances*, vol. 5, no. 100, pp. 82503–82512, 2015.

[40] H. Faghihian, S. N. Mirsattari, and K. Asghari, "Kinetics & thermodynamics of Cu(II) adsorption by imprinted salen-functionalized silica gel," *Desalination and Water Treatment*, vol. 52, no. 37-39, pp. 7205–7217, 2013.

[41] P. Koilraj and S. Kannan, "Aqueous fluoride removal using ZnCr layered double hydroxides and their polymeric composites: batch and column studies," *Chemical Engineering Journal*, vol. 234, pp. 406–415, 2013.

[42] J. Ma, M. Yang, F. Yu, and J. Zheng, "Water-enhanced removal of ciprofloxacin from water by porous graphene hydrogel," *Scientific Reports*, vol. 5, no. 1, article 13578, 2015.

[43] B. Cheknane, F. Zermane, M. Baudu, O. Bouras, and J. P. Basly, "Sorption of basic dyes onto granulated pillared clays: thermodynamic and kinetic studies," *Journal of Colloid and Interface Science*, vol. 381, no. 1, pp. 158–163, 2012.

[44] F. Ayari, E. Srasra, and M. Trabelsi-Ayadi, "Low-cost adsorbents for a dye uptake from contaminated water modeling of adsorption isotherms: the Langmuir, Freundlich and Elovich models," *Surface Engineering and Applied Electrochemistry*, vol. 44, no. 6, pp. 489–498, 2008.

[45] B. Kwakye-Awuah, E. Von-Kiti, I. Nkrumah, R. Erdoo Ikyreve, I. Radecka, and C. Williams, "Parametric, equilibrium, and kinetic study of the removal of salt ions from Ghanaian seawater by adsorption onto zeolite X," *Desalination and Water Treatment*, vol. 57, no. 45, pp. 21654–21663, 2016.

[46] B. Satilmis and T. Uyar, "Amine modified electrospun PIM-1 ultrafine fibers for an efficient removal of methyl orange from an aqueous system," *Applied Surface Science*, vol. 453, pp. 220–229, 2018.

[47] S. Chen, Y. Huang, X. Han et al., "Simultaneous and efficient removal of Cr(VI) and methyl orange on LDHs decorated porous carbons," *Chemical Engineering Journal*, vol. 352, pp. 306–315, 2018.

[48] N. I. Blaisi, M. Zubair, Ihsanullah et al., "Date palm ash-MgAl-layered double hydroxide composite: sustainable adsorbent for effective removal of methyl orange and eriochrome black-T from aqueous phase," *Environmental Science and Pollution Research*, vol. 25, no. 34, pp. 34319–34331, 2018.

[49] Y.-z. Ma, D.-f. Zheng, Z.-y. Mo, R.-j. Dong, and X.-q. Qiu, "Magnetic lignin-based carbon nanoparticles and the adsorption for removal of methyl orange," *Colloids and Surfaces A: Physicochemical and Engineering Aspects*, vol. 559, pp. 226–234, 2018.

[50] K. Rathinam, S. P. Singh, C. J. Arnusch, and R. Kasher, "An environmentally-friendly chitosan-lysozyme biocomposite for the effective removal of dyes and heavy metals from aqueous solutions," *Carbohydrate Polymers*, vol. 199, pp. 506–515, 2018.

[51] Y. Liu, Y. Tian, C. Luo, G. Cui, and S. Yan, "One-pot preparation of a MnO_2-graphene-carbon nanotube hybrid material for the removal of methyl orange from aqueous solutions," *New Journal of Chemistry*, vol. 39, no. 7, pp. 5484–5492, 2015.

[52] M. Bhowmik, A. Debnath, and B. Saha, "Fabrication of mixed phase calcium ferrite and zirconia nanocomposite for abatement of methyl orange dye from aqua matrix: optimization of process parameters," *Applied Organometallic Chemistry*, vol. 32, no. 12, article e4607, 2018.

[53] Y. Gao, S. Q. Deng, X. Jin, S. L. Cai, S. R. Zheng, and W. G. Zhang, "The construction of amorphous metal-organic cage-based solid for rapid dye adsorption and time-dependent dye separation from water," *Chemical Engineering Journal*, vol. 357, pp. 129–139, 2019.

[54] B. Chen, S. Chen, H. Zhao, Y. Liu, F. Long, and X. Pan, "A versatile β-cyclodextrin and polyethyleneimine bi-functionalized magnetic nanoadsorbent for simultaneous capture of methyl orange and Pb(II) from complex wastewater," *Chemosphere*, vol. 216, pp. 605–616, 2019.

[55] I. I. Fasfous, E. S. Radwan, and J. N. Dawoud, "Kinetics, equilibrium and thermodynamics of the sorption of tetrabromobisphenol A on multiwalled carbon nanotubes," *Applied Surface Science*, vol. 256, no. 23, pp. 7246–7252, 2010.

[56] R. Niwas, U. Gupta, A. A. Khan, and K. G. Varshney, "The adsorption of phosphamidon on the surface of styrene supported zirconium (IV) tungstophosphate: a thermodynamic study," *Colloids and Surfaces A: Physicochemical and Engineering Aspects*, vol. 164, no. 2-3, pp. 115–119, 2000.

[57] Y. Yu, Y.-Y. Zhuang, Z.-H. Wang, and M.-Q. Qiu, "Adsorption of water-soluble dyes onto modified resin," *Chemosphere*, vol. 54, no. 3, pp. 425–430, 2004.

[58] Y. Liu and Y.-J. Liu, "Biosorption isotherms, kinetics and thermodynamics," *Separation and Purification Technology*, vol. 61, no. 3, pp. 229–242, 2008.

[59] G. Gnana kumar, Z. Awan, K. Suk Nahm, and J. Stanley Xavier, "Nanotubular MnO_2/graphene oxide composites for the application of open air-breathing cathode microbial fuel cells," *Biosensors and Bioelectronics*, vol. 53, pp. 528–534, 2014.

[60] M. Hu, K. S. Hui, and K. N. Hui, "Role of graphene in MnO_2/-graphene composite for catalytic ozonation of gaseous toluene," *Chemical Engineering Journal*, vol. 254, pp. 237–244, 2014.

[61] J. Ma, F. Yu, L. Zhou et al., "Enhanced adsorptive removal of methyl orange and methylene blue from aqueous solution by alkali-activated multiwalled carbon nanotubes," *ACS Applied Materials & Interfaces*, vol. 4, no. 11, pp. 5749–5760, 2012.

[62] Ş. S. Bayazit, "Magnetic multi-wall carbon nanotubes for methyl orange removal from aqueous solutions: equilibrium, kinetic and thermodynamic studies," *Separation Science and Technology*, vol. 49, no. 9, pp. 1389–1400, 2014.

[63] K. Luo, S.-X. Zhao, Y.-F. Wang, S.-J. Zhao, and X.-H. Zhang, "Synthesis of petal-like δ-MnO_2 and its catalytic ozonation performance," *New Journal of Chemistry*, vol. 42, no. 9, pp. 6770–6777, 2018.

[64] H. Liu, Z. Hu, Y. Su, H. Ruan, R. Hu, and L. Zhang, "MnO_2nanorods/3D-rGO composite as high performance anode materials for Li-ion batteries," *Applied Surface Science*, vol. 392, pp. 777–784, 2017.

Hindawi
Journal of Nanomaterials
Volume 2019, Article ID 8767943, 7 pages
https://doi.org/10.1155/2019/8767943

Research Article

Reproductive Toxicity of Pomegranate Peel Extract Synthesized Gold Nanoparticles: A Multigeneration Study in *C. elegans*

Mahnoor Patel[1], **Nikhat J. Siddiqi**[2], **Preeti Sharma**[1], **Abdullah S. Alhomida**[2], **and Haseeb A. Khan**[2]

[1]*Department of Biotechnology, Veer Narmad South Gujarat University, 395007, Surat, Gujarat, India*
[2]*Department of Biochemistry, College of Science, King Saud University, Riyadh 11451, Saudi Arabia*

Correspondence should be addressed to Haseeb A. Khan; khan_haseeb@yahoo.com

Received 28 April 2019; Revised 30 June 2019; Accepted 11 July 2019; Published 28 August 2019

Guest Editor: Ziyou Zhou

C. elegans is a preferential model for testing environmental toxicity of compounds including nanomaterials. The impact of multigeneration exposure of gold nanoparticles (AuNPs) on the lifespan and fertility of *C. elegans* is not known and therefore is investigated in this study. We used pomegranate (*Punica granatum*) peel extracts as a reducing agent to synthesize gold nanoparticles (PPE-AuNPs) from chloroauric acid. Nematodes were grown till adult stage and then exposed to 25, 50, and 100 μg/ml of PPE-AuNPs at 20°C for 72 hours and then assessed for lifespan and fertility. The same protocols were followed for subsequent F1, F2, and F3 generations. The results showed that PPE-AuNPs dose-dependently but insignificantly reduced the lifespan of *C. elegans*. Exposure of PPE-AuNPs significantly and dose-dependently reduced the fertility of *C. elegans* in terms of the number of eggs produced. The reproductive toxicity of PPE-AuNPs was found to be minimal in parental generation (F0) and maximal in F3 generation. In conclusion, biologically synthesized PPE-AuNPs adversely affect the fertility of *C. elegans* while the factors responsible for reproductive toxicity are inherited by subsequent generations.

1. Introduction

There is a growing trend for the synthesis and widespread use of nanoparticles (NPs) for applications in different areas such as medicine, engineering, bioremediation, cosmetics, and food industry [1–7]. Such a wider scope of engineered NPs needs to be channelized by their prudent use for availing their benefits without ignoring their adverse effects on humans and the environment [8]. The extensive use of nanoparticle has led to their release in the environment causing them to be considered environmental toxicants [9]. Among the metallic NPs, gold nanoparticles (AuNPs) have been recognized as promising tools for biomedical applications due to their biocompatibility and ease in functionalization [10, 11]. Although gold is a chemically inert material, its transformation into nanoscale imparts the antigenic quality as several studies have shown an acute phase immune activation following injection of AuNPs in rats [12–15] and mice [16, 17]. However, the primed animals (preexposed to AuNPs) showed protection against AuNP-induced acute immune activation in the form of reduced expression of proinflammatory cytokines [18].

Caenorhabditis elegans (*C. elegans*) is a free-living, transparent nematode with a short life cycle of a few days and can be quickly grown in a laboratory. Interestingly, the majority of human genes have homologs in *C. elegans*. A comparative proteomics study has shown that 83% of the worm proteome possesses human homologous genes [19]. *C. elegans* is therefore considered a model organism for understanding human gene function. The neural system, immune system, and digestive and reproductive systems of *C. elegans* are identical to the vertebrates which makes it an excellent model for toxicity studies as well [20–22]. *C. elegans* is ideally suited for the screening of NPs while mitigating the hurdles associated with the use of mammalian animal models, such as ethical issues, handling expertise, space requirement, and time constraints [23–25].

The pomegranate (*Punica granatum*) is a fruit-bearing deciduous shrub belonging to the family Lythraceae. Pomegranate fruits possess antioxidant and medicinal properties and are commonly used in baking, cooking, juice blends, meal garnishes, smoothies, and alcoholic beverages. Recently, pomegranate juice and peel extracts have been utilized as reducing and stabilizing agents for the synthesis of AuNPs [26–29]. Kim et al. [30] have shown that parental (F0) exposure of 10 nm size AuNPs caused reproductive toxicity in unexposed F2 generation which was gradually recovered in the unexposed F3 and F4 generations. We hypothesized that the antioxidant potential of pomegranate peel extract [31] would modify the toxicological profile of AuNPs synthesized from it. In this investigation, we studied the transgenerational effects of pomegranate peel extract synthesized gold nanoparticles (PPE-AuNPs) on the lifespan and fertility of *C. elegans* after exposing parental (F0) and three generations (F1, F2, and F3) of *C. elegans* to three different concentrations of PPE-AuNPs.

2. Materials and Methods

2.1. Synthesis of PPE-AuNPs. Pomegranate fruits were purchased from the local market. The fresh peel (50 g) obtained from a prewashed pomegranate fruit was added to 250 ml of distilled water and boiled for 25 min. The same ratio of pomegranate peel and solvent has been reported earlier for obtaining the extract [31]. The extract was filtered using a Whatman filter paper to get the aqueous fruit peel extract. The freshly prepared extract was stored in a sterile bottle and kept at 4°C for a short time to cool the extract. Pomegranate peel extract (0.9 ml) was mixed with 25 ml of 1 mM solution of chloroauric acid ($HAuCl_4$). The reacting mixture was kept for 24 h at room temperature with intermittent shaking. The color change from gold to pink indicated the synthesis of PPE-AuNPs. The synthesized nanoparticles were washed with sterile water using the sequential steps of centrifugation (17,000 g, 30 min), supernatant removal, and redispersion by vortex. Aqueous dispersions of PPE-AuNPs in the concentrations of 10, 50, and 100 μg/ml were used for *C. elegans* exposure.

2.2. Characterization of PPE-AuNPs. UV-visible spectrophotometry (Shimadzu, Japan) was used to monitor the bioreduction of $AuCl_4^-$ ions to metallic Au leading to the synthesis of PPE-AuNPs. The wavelength range from 300 nm to 800 nm was scanned for obtaining the absorption spectra of PPE-AuNPs. Scanning electron microscopy (SEM, Jeol, Japan) was used to characterize the morphology and size of the synthesized PPE-AuNPs. An energy-dispersive X-ray spectrometer (EDX, Oxford System) was used for elemental analysis. A sample for EDX analysis was prepared by sprinkling the dispersed PPE-AuNPs onto a double-sided adhesive carbon conductive tape which was then mounted on the microscopic copper stub. Photographic images were visualized on a computer screen, and the results of SEM and EDX were interpreted.

2.3. Maintenance of Caenorhabditis elegans. C. elegans (wild type, Bristol, N2) were obtained from the National Institute of Immunology, New Delhi, India. All worms were cultured in Nematode Growth Media (NGM: NaCl, 3 g/l; peptone, 2.5 g/l; agar, 17 g/l; 1 M potassium phosphate, 25 ml; 1 M $CaCl_2$, 1 ml; 1 M $MgSO_4$, 1 ml; and cholesterol, 1 ml) on agar plates. The food source was *Escherichia coli* OP50 strain. To obtain synchronized worms, gravid hermaphrodites were treated with sodium hypochlorite (5% NaOCl/1 N NaOH, 2 : 5) for 10 minutes and 1 ml aliquots of the solution were centrifuged at 2000 rpm for 2 min and washed with K-medium which consisted of 0.032 M KCl and 0.051 M NaCl [32]. *C. elegans* were allowed to mature till the fourth larval stage for further experiments. The experimental design for multigenerational toxicity assay is summarized in Figure 1.

2.4. Lifespan Assay. Worms were grown on NGM agar till they became gravid adults. The gravid adults were bleached to obtain the eggs. All the worms were grown till adult stage, which were then exposed to 25, 50, and 100 μg/ml PPE-AuNPs at 20°C for 72 h. The young adults were then treated with fluorodeoxyuridine to inhibit the development of the next progeny. The numbers of worms were similar in control and experimental plates. Scoring was done on every alternate day for live and dead worms till all the worms died. Live and dead worms were distinguished by a touch-provoke method under a dissecting microscope with the help of worm pick. Lifespan assay was performed for every generation for a multigenerational toxicity study. The lifespan of the worm was the time between the egg and the death of the worm. The experiments were conducted in three replicates.

2.5. Fertility Assay. Age-synchronized adult worms (L4 stage/P0 worms) were exposed to different concentrations (25, 50, and 100 μg/ml) of PPE-AuNPs at 20°C for 72 h. After exposure, the worms were washed with M9 buffer and a single worm was transferred to a 35 mm petri plate containing NGM medium, supplemented with *E. coli* OP50. The worms were washed and pelleted, and the progeny were counted under the dissecting microscope. For each test concentration and control, the numbers of eggs were counted for every single worm. Fertility assay was performed for every subsequent generation to study multigenerational toxicity. The experiments were conducted in three replicates.

The L4 stage worms were considered parent generation (F0). Parental worms were exposed to different concentrations of PPE-AuNPs. For reproductive toxicity studies, one exposed worm was transferred to a 35 mm petri dish to determine the brood size. The rest of the worms were transferred to 60 mm MGM plates to obtain the eggs by an alkali bleach method. The worms were collected and washed thrice with distilled water. The washed worms were placed in NGM plates, and the next generation was produced. The second-generation worms were grown till the L4 stage to produce the first filial generation (F1) which were exposed to the same concentration of PPE-AuNPs and for the same duration as conducted in F0. A single worm was isolated for reproductive

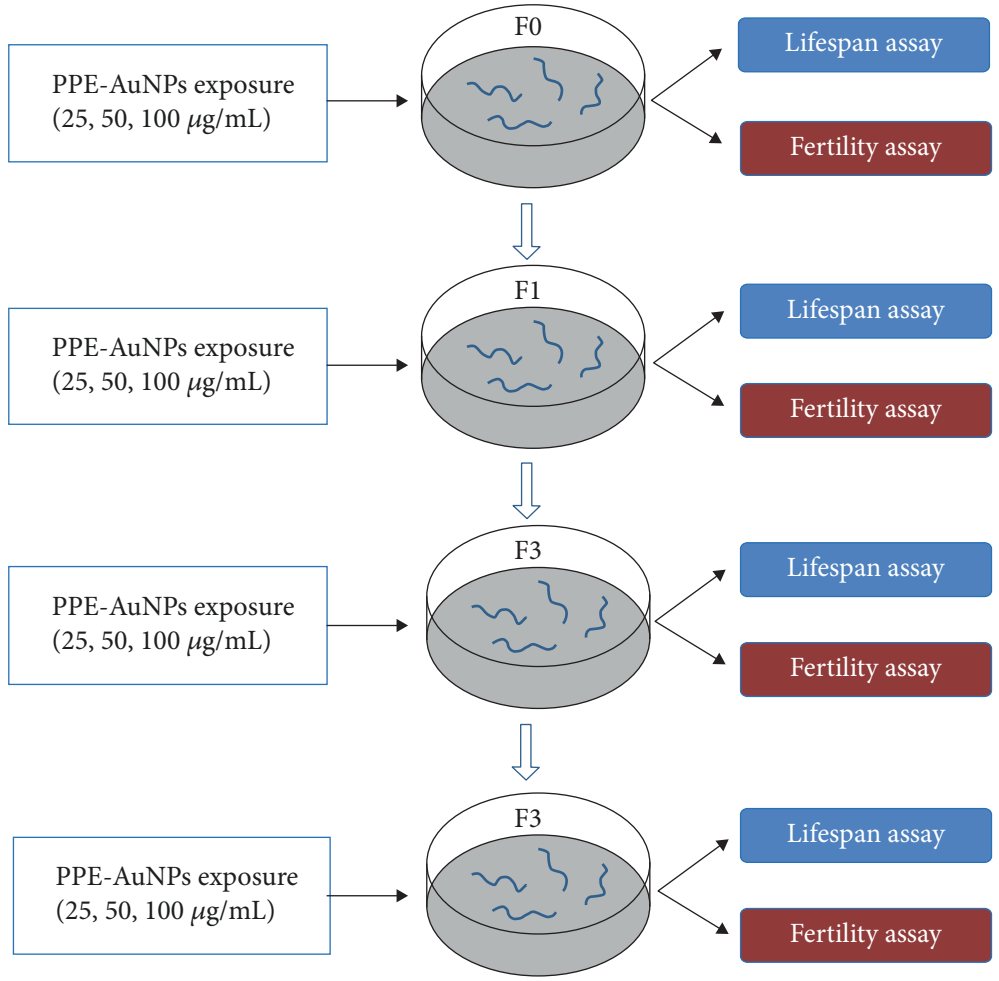

Figure 1: Schematic representation of study protocol for testing the effect of PPE-AuNPs on lifespan and fertility in *C. elegans*.

toxicity studies while the rest of the worms were allowed to grow till the L4 stage to produce the second filial generation (F2). The same protocol was followed for the third filial generation (F3).

2.6. Statistical Analysis. The data were analyzed by one-way analysis of variance (ANOVA) followed by Tukey's test using SPSS package. P values < 0.05 were considered statistically significant.

3. Results

3.1. Synthesis and Characterization of PPE-AuNPs. The appearance of pink color following the mixing of pomegranate extract with the solution of chloroauric acid indicated the formation of PPE-AuNPs. The UV-visible spectra of the reaction mixture showed the absorption peak at 540 nm with a maximal intensity at 24 h, indicating the time course of PPE-AuNP synthesis (Figure 2(a)). The Energy Dispersive X-ray (EDX) analysis of PPE-AuNPs showed the presence of the elemental peaks of carbon, oxygen, magnesium, and gold (Figure 2(b)). The presence of peak at 2 keV on spectrum confirmed the formation of gold nanoparticles. Small amounts of other elements including carbon, oxygen, and magnesium also appeared due to their occurrence in plant extract (Figure 2(b)). SEM image showed the morphology of PPE-AuNPs to be round with an average particle diameter of 11.0 ± 1.5 nm (Figure 2(c)).

3.2. Multigenerational Effect of PPE-AuNPs on C. elegans Lifespan. The average lifespan of unexposed *C. elegans* in the parental generation (F0) was 17 days which was dose-dependently reduced after exposure of PPE-AuNPs; however, this decrease in lifespan was statistically insignificant (Figure 3). Similar trends were observed in subsequent F1, F2, and F3 generations while the exposure of different concentrations of PPE-AuNPs did not cause any significant change in the lifespan of *C. elegans* (Figure 3).

3.3. Multigenerational Effect of PPE-AuNPs on C. elegans Fertility. The fertility assay in terms of the number of eggs showed that the parental generation (F0) unexposed C. elegans laid 195 ± 5 eggs which were significantly reduced following the exposure of 100 μg/ml PPE-AuNPs (Figure 4). Although the low (10 μg/ml) and medium (50 μg/ml) concentrations of PPE-AuNPs slightly reduced the fertility of F0 nematodes, this effect was statistically nonsignificant. However, all the concentrations of PPE-

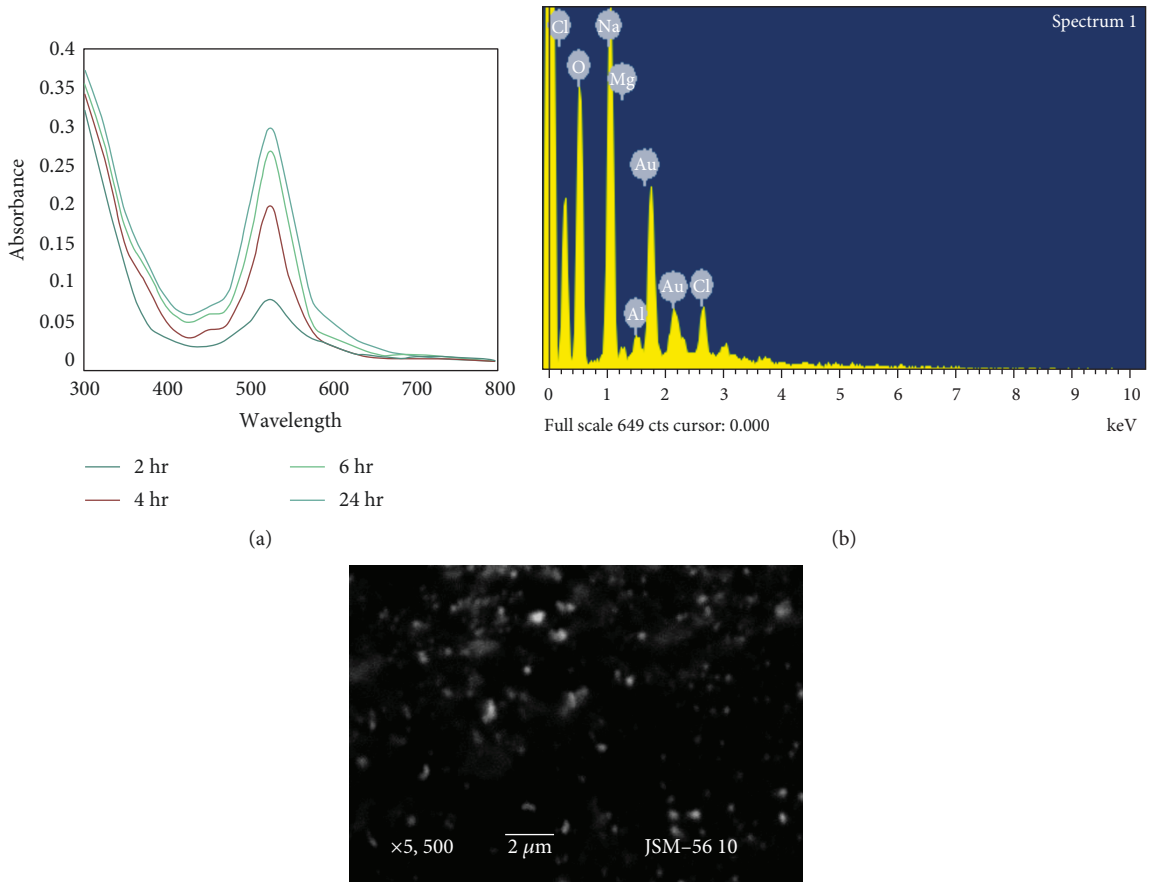

Figure 2: Characterization of PPE-AuNPs: (a) UV-visible spectra showing the increasing yield of PPE-AuNPs with time. (b) EDX analysis of PPE-AuNPs. (c) SEM image showing the morphology and size of PPE-AuNPs.

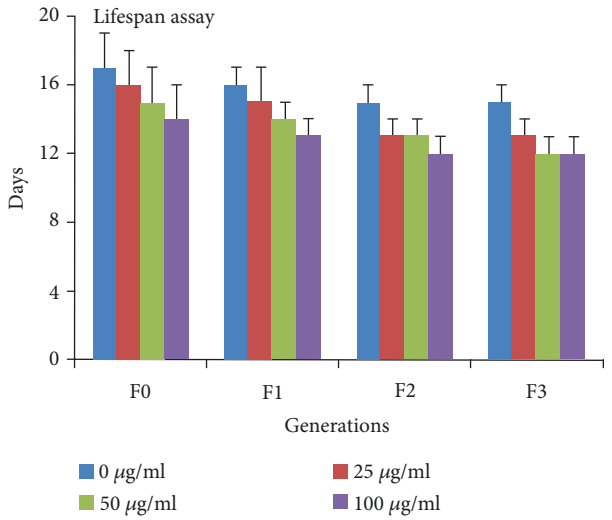

Figure 3: Multigenerational effect of different doses of PPE-AuNPs on the lifespan of *C. elegans*.

AuNPs significantly reduced the fertility of *C. elegans* in the F2 and F3 generations (Figure 4). The severity of reproductive toxicity of PPE-AuNPs in *C. elegans* was directly related to generations, while F0 nematodes were the least sensitive, and F3 nematodes were highly sensitive to the adverse effects of PPE-AuNPs on the fertility of *C. elegans* (Figure 4).

4. Discussion

In this study, we used pomegranate (*Punica granatum*) peel extract for the synthesis of AuNPs using a "green synthesis" approach. The production of AuNPs involves the reduction of a solution of chloroaurate ions ($AuCl_4^-$) with a reducing agent. Sodium borohydride is commonly used as a reducing agent in the synthesis of AuNPs; however, it is an environmental contaminant and highly toxic to biological systems [33]. Therefore, phytochemicals like epigallocatechin [34] and mangiferin [35] have been utilized for the green synthesis of AuNPs. The reducing agent used in this study was the pomegranate peel extract (PPE) to synthesize AuNPs. Earlier studies have demonstrated the presence of gallic acid in PPE, which results in the formation of larger AuNPs when compared to other plant extracts [27]. Pomegranate extract contains ellagic acid which is responsible for its antioxidant properties. Other phenolic compounds like anthocynanins enhance the antioxidant properties of ellagic acid. The presence of the hydroxyl and carboxyl groups in plant organic

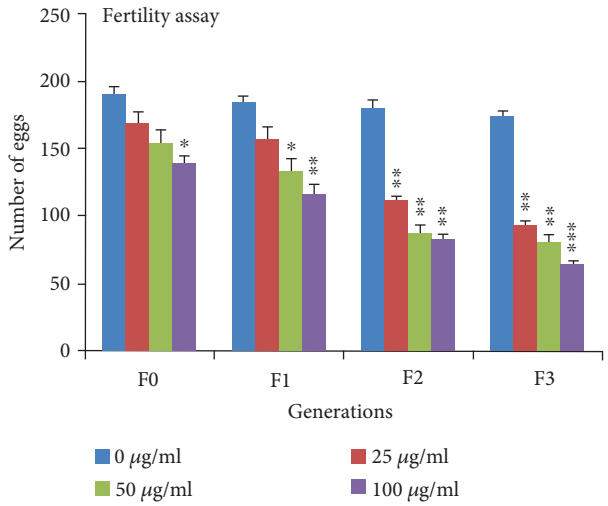

FIGURE 4: Multigenerational effect of different doses of PPE-AuNPs on the fertility of *C. elegans*. $^{*}P < 0.05$, $^{**}P < 0.01$, and $^{***}P < 0.001$ versus the control (0 μg/ml) group.

compounds helps them to chelate metal ions and act as antioxidants. The interaction of metal salts with ellagic acid found in the peel extract causes esterification of the carboxyl and hydroxyl groups of ellagic acid. This leads to the loss of hydrogen from the orthophenolic hydroxyl group resulting in a semiquinone structure. Therefore, due to its easier electron-losing ability, ellagic acid can easily form H^+ radical which reduces gold salt to AuNPs [36].

The concentrations of PPE-AuNPs used in this study (10-100 μg/ml) did not demonstrate any antibacterial activity against *E. coli*, which was used as food for *C. elegans*. Elia et al. [27] have shown that AuNPs synthesized using plant extract did not exhibit any measurable adverse effect on the growth of intestinal L-cells. The minimum inhibitory concentrations (MIC) of PPE-AuNPs against various pathogenic bacteria have been reported as follows: *C. albicans* (310 μg/ml), *A. flavus* (340 μg/ml), *S. aureus* (330 μg/ml), *S. typhi* (370 μg/ml), and *V. cholera* (410 μg/ml) [28].

The exposure of PPE-AuNPs to *C. elegans* had no significant effect on the lifespan of the nematode in the parental as well as three subsequent generations studied (Figure 3). Kim et al. [30] have also demonstrated that feeding of *C. elegans* with *E. coli* dosed with AuNPs did not show any significant effect on the survival of nematodes. On the other hand, a previous study has reported toxicogenomic effects of AuNPs on *C. elegans* by activating some biological pathways [37]. The cellular uptake and toxicity of nanoparticles mainly depend on their size, shape, and surface chemistry [38–40]. Wang et al. [41] used the *C. elegans* model to understand whether the "nanoscale" size is the determining factor for the nanomaterials to induce autophagy. They used four types of similar sized nanomaterials including silicon nanoparticles (SiNP), CdTe quantum dots, carbon dots, and AuNPs. They observed that unlike other nanomaterials tested, no autophagosome formation was detected in *C. elegans* with SiNP exposure, suggesting that the "nanoscale" size is not the determining factor for the nanomaterials to induce autophagy in *C. elegans* [41]. A recent microarray study showed that developmental changes in *C. elegans* following mercaptoundecanoic acid-coated AuNPs were related to differential gene expression in clec-174 (involved in cellular defense), cut-3 and fil-1 (both involved in body morphogenesis), dpy-14 (expressed in embryonic neurons), and mtl-1 (functions in metal detoxification and homeostasis) genes [42].

The most striking finding of this study is the reproductive toxicity of PPE-AuNPs that showed dose-dependent as well as transgeneration cumulative effects (Figure 4). Kim et al. [30] were the first to conduct a multigenerational study of AuNPs in *C. elegans* and revealed that reproduction rate was clearly affected in the F2 generation but then gradually recovered in the F3 and F4 generations, suggesting that just one exposure to the F0 generation can induce the adverse effects on subsequent generations. Moon et al. [43] demonstrated that continuous AuNP exposure to *C. elegans* impaired reproduction from F2 to F4, whereas intermittent exposure caused more pronounced effects on F3 worms, which may have resulted from damage during the convalescence period up through F2. It has been shown earlier that nanoparticles, which are able to permeate the gonad, can be transferred to the next generation [44]. Gold nanoparticles functionalized with lectin found in the tubers of the Winter Aconite (*Eranthis hyemalis*) plant delayed the onset of reproduction and reduced fecundity for L4 stage, preadult *C. elegans* [45].

Gonzalez-Moragas et al. [25] observed that citrate-stabilized 11 nm AuNPs (100 μg/ml) induced a significant decrease in the survival as well as reproductive output as compared to control *C. elegans*. However, the decreases in survival and brood size were not statistically significant in case of larger (150 nm) AuNPs. Other investigators also reported that smaller size nanoparticles (<10 nm) were more toxic to *C. elegans* than their larger counterparts (>50 nm) [46, 47]. The higher toxicity of small sized AuNPs was attributed to their higher uptake as the worms ingested smaller AuNPs about 500 times more than the larger AuNPs [25]. The above literature indicates that small size AuNPs are more toxic for the survival of *C. elegans* [25] whereas the PPE-AuNPs of the same size and in the same dosage are comparatively safe (Figure 3).

In conclusion, exposure of 11 nm PPE-AuNPs did not cause any significant change in the lifespan of *C. elegans*; however, it significantly and dose-dependently impaired the fertility of nematodes. The reproductive toxicity of PPE-AuNPs in *C. elegans* was found to increase in subsequent generations in the following order: F0<F1<F2<F3. The transgeneration flow of toxicity may be attributed to the transfer of abnormal germ cells from one generation to another. The findings of this study are of particular relevance for understanding the safety and biocompatibility of AuNPs, as strict regulatory guidelines and high cost restrict the use of laboratory animals, especially during the pilot and initial screening studies. *C. elegans* could serve as a model organism for testing the reproductive toxicity of many other toxicants including a wide range of nanomaterials.

Data Availability

The data used to support the findings of this study are available from the corresponding author upon request.

Conflicts of Interest

The author(s) declare(s) that they have no conflicts of interest.

Acknowledgments

We are grateful to Dr. Arnab Mukhopadhyay and Syed Shams Tabrez from Molecular Aging Lab, National Institute of Immunology, New Delhi, for their suggestions while conducting the experiments on *C. elegans*. The authors would like to extend their sincere appreciation to the Deanship of Scientific Research at King Saud University for funding Research Group No. RGP-009.

References

[1] A. Weir, P. Westerhoff, L. Fabricius, K. Hristovski, and N. von Goetz, "Titanium dioxide nanoparticles in food and personal care products," *Environmental Science & Technology*, vol. 46, no. 4, pp. 2242–2250, 2012.

[2] K. A. Eswar, J. Rouhi, F. S. Husairi et al., "Hydrothermal growth of flower-like ZnO nanostructures on porous silicon substrate," *Journal of Molecular Structure*, vol. 1074, pp. 140–143, 2014.

[3] S. H. Kang, M. Nafiujjaman, M. Nurunnabi et al., "Hybrid photoactive nanomaterial composed of gold nanoparticles, pheophorbide-A and hyaluronic acid as a targeted bimodal phototherapy," *Macromolecular Research*, vol. 23, no. 5, pp. 474–484, 2015.

[4] Z. Khatun, M. Nurunnabi, M. Nafiujjaman et al., "A hyaluronic acid nanogel for photo–chemo theranostics of lung cancer with simultaneous light-responsive controlled release of doxorubicin," *Nanoscale*, vol. 7, no. 24, pp. 10680–10689, 2015.

[5] M. Nafiujjaman, H. A. Khan, and Y. K. Lee, "Peptide-influenced graphene quantum dots on iron oxide nanoparticles for dual imaging of lung cancer cells," *Journal of Nanoscience and Nanotechnology*, vol. 17, no. 3, pp. 1704–1711, 2017.

[6] M. Nafiujjaman, M. Nurunnabi, S. H. Kang, G. R. Reeck, H. A. Khan, and Y. K. Lee, "Ternary graphene quantum dot–polydopamine–Mn_3O_4 nanoparticles for optical imaging guided photodynamic therapy and T_1-weighted magnetic resonance imaging," *Journal of Materials Chemistry B*, vol. 3, no. 28, pp. 5815–5823, 2015.

[7] M. Nurunnabi, K. Parvez, M. Nafiujjaman et al., "Bioapplication of graphene oxide derivatives: drug/gene delivery, imaging, polymeric modification, toxicology, therapeutics and challenges," *RSC Advances*, vol. 5, no. 52, pp. 42141–42161, 2015.

[8] H. A. Khan and R. Shanker, "Toxicity of nanomaterials," *BioMed Research International*, vol. 2015, Article ID 521014, 2 pages, 2015.

[9] P. Khare, M. Sonane, Y. Nagar et al., "Size dependent toxicity of zinc oxide nano-particles in soil nematode *Caenorhabditis elegans*," *Nanotoxicology*, vol. 9, no. 4, pp. 423–432, 2015.

[10] N. Elahi, M. Kamali, and M. H. Baghersad, "Recent biomedical applications of gold nanoparticles: a review," *Talanta*, vol. 184, pp. 537–556, 2018.

[11] P. M. Tiwari, K. Vig, V. A. Dennis, and S. R. Singh, "Functionalized gold nanoparticles and their biomedical applications," *Nanomaterials*, vol. 1, no. 1, pp. 31–63, 2011.

[12] H. A. Khan, M. A. K. Abdelhalim, A. S. Alhomida, and M. S. al-Ayed, "Effects of naked gold nanoparticles on proinflammatory cytokines mRNA expression in rat liver and kidney," *BioMed Research International*, vol. 2013, Article ID 590730, 6 pages, 2013.

[13] H. A. Khan, K. E. Ibrahim, A. Khan, S. H. Alrokayan, and A. S. Alhomida, "Immunostaining of proinflammatory cytokines in renal cortex and medulla of rats exposed to gold nanoparticles," *Histology and Histopathology*, vol. 32, no. 6, pp. 597–607, 2017.

[14] H. A. Khan, K. E. Ibrahim, A. Khan, S. H. Alrokayan, A. S. Alhomida, and Y. K. Lee, "Comparative evaluation of immunohistochemistry and real-time PCR for measuring proinflammatory cytokines gene expression in livers of rats treated with gold nanoparticles," *Experimental and Toxicologic Pathology*, vol. 68, no. 7, pp. 381–390, 2016.

[15] H. A. Khan, M. A. K. Abdelhalim, A. S. Alhomida, and M. S. al Ayed, "Transient increase in IL-1β, IL-6 and TNF-α gene expression in rat liver exposed to gold nanoparticles," *Genetics and Molecular Research*, vol. 12, no. 4, pp. 5851–5857, 2013.

[16] K. E. Ibrahim, M. G. Al-Mutary, A. O. Bakhiet, and H. A. Khan, "Histopathology of the liver, kidney, and spleen of mice exposed to gold nanoparticles," *Molecules*, vol. 23, no. 8, p. 1848, 2018.

[17] H. A. Khan, S. Alamery, K. E. Ibrahim et al., "Size and time-dependent induction of proinflammatory cytokines expression in brains of mice treated with gold nanoparticles," *Saudi Journal of Biological Sciences*, vol. 26, no. 3, pp. 625–631, 2019.

[18] K. E. Ibrahim, A. O. Bakhiet, M. E. Awadalla, and H. A. Khan, "A priming dose protects against gold nanoparticles-induced proinflammatory cytokines mRNA expression in mice," *Nanomedicine (London, England)*, vol. 13, no. 3, pp. 313–323, 2018.

[19] C. H. Lai, C. Y. Chou, L. Y. Ch'ang, C. S. Liu, and W. Lin, "Identification of novel human genes evolutionarily conserved in *Caenorhabditis elegans* by comparative proteomics," *Genome Research*, vol. 10, no. 5, pp. 703–713, 2000.

[20] R. D. Handy, G. Cornelis, T. Fernandes et al., "Ecotoxicity test methods for engineered nanomaterials: practical experiences and recommendations from the bench," *Environmental Toxicology and Chemistry*, vol. 31, no. 1, pp. 15–31, 2012.

[21] P. R. Hunt, "The *C. elegans* model in toxicity testing," *Journal of Applied Toxicology*, vol. 37, no. 1, pp. 50–59, 2017.

[22] E. K. Marsh and R. C. May, "*Caenorhabditis elegans*, a model organism for investigating immunity," *Applied and Environmental Microbiology*, vol. 78, no. 7, pp. 2075–2081, 2012.

[23] T. Wu, H. Xu, X. Liang, and M. Tang, "*Caenorhabditis elegans* as a complete model organism for biosafety assessments of nanoparticles," *Chemosphere*, vol. 221, pp. 708–726, 2019.

[24] L. Gonzalez-Moragas, A. Roig, and A. Laromaine, "*C. elegans* as a tool for in vivo nanoparticle assessment," *Advances in Colloid and Interface Science*, vol. 219, pp. 10–26, 2015.

[25] L. Gonzalez-Moragas, P. Berto, C. Vilches et al., "In vivo testing of gold nanoparticles using the *Caenorhabditis elegans* model organism," *Acta Biomaterialia*, vol. 53, pp. 598–609, 2017.

[26] J. Gubitosa, V. Rizzi, A. Lopedota et al., "One pot environmental friendly synthesis of gold nanoparticles using *Punica granatum* juice: a novel antioxidant agent for future dermatological and cosmetic applications," *Journal of Colloid and Interface Science*, vol. 521, pp. 50–61, 2018.

[27] P. Elia, R. Zach, S. Hazan, S. Kolusheva, Z. Porat, and Y. Zeiri, "Green synthesis of gold nanoparticles using plant extracts as reducing agents," *International Journal of Nanomedicine*, vol. 9, pp. 4007–4021, 2014.

[28] S. Lokina, R. Suresh, K. Giribabu, A. Stephen, R. Lakshmi Sundaram, and V. Narayanan, "Spectroscopic investigations, antimicrobial, and cytotoxic activity of green synthesized gold nanoparticles," *Spectrochimica Acta Part A: Molecular and Biomolecular Spectroscopy*, vol. 129, pp. 484–490, 2014.

[29] M. Ganeshkumar, M. Sathishkumar, T. Ponrasu, M. G. Dinesh, and L. Suguna, "Spontaneous ultra fast synthesis of gold nanoparticles using *Punica granatum* for cancer targeted drug delivery," *Colloids and Surfaces B: Biointerfaces*, vol. 106, pp. 208–216, 2013.

[30] S. W. Kim, J. I. Kwak, and Y. J. An, "Multigenerational study of gold nanoparticles in *Caenorhabditis elegans*: transgenerational effect of maternal exposure," *Environmental Science & Technology*, vol. 47, no. 10, pp. 5393–5399, 2013.

[31] S. Malviya, Arvind, A. Jha, and N. Hettiarachchy, "Antioxidant and antibacterial potential of pomegranate peel extracts," *Journal of Food Science and Technology*, vol. 51, no. 12, pp. 4132–4137, 2014.

[32] P. L. Williams and D. B. Dusenbery, "Aquatic toxicity testing using the nematode, *Caenorhabditis elegans*," *Environmental Toxicology and Chemistry*, vol. 9, no. 10, pp. 1285–1290, 1990.

[33] L. Freitas de Freitas, G. Varca, J. dos Santos Batista, and A. Benévolo Lugão, "An overview of the synthesis of gold nanoparticles using radiation technologies," *Nanomaterials*, vol. 8, no. 11, p. 939, 2018.

[34] S. K. Nune, N. Chanda, R. Shukla et al., "Green nanotechnology from tea: phytochemicals in tea as building blocks for production of biocompatible gold nanoparticles," *Journal of Materials Chemistry*, vol. 19, no. 19, pp. 2912–2920, 2009.

[35] A. Y. Al-Yasiri, M. Khoobchandani, C. S. Cutler et al., "Mangiferin functionalized radioactive gold nanoparticles (MGF-^{198}AuNPs) in prostate tumor therapy: green nanotechnology for production, in vivo tumor retention and evaluation of therapeutic efficacy," *Dalton Transactions*, vol. 46, no. 42, pp. 14561–14571, 2017.

[36] N. Ahmad, S. Sharma, and R. Rai, "Rapid green synthesis of silver and gold nanoparticles using peels of Punica granatum," *Advanced Materials Letters*, vol. 3, no. 5, pp. 376–380, 2012.

[37] O. V. Tsyusko, J. M. Unrine, D. Spurgeon et al., "Toxicogenomic responses of the model organism Caenorhabditis elegans to gold nanoparticles," *Environmental Science & Technology*, vol. 46, no. 7, pp. 4115–4124, 2012.

[38] X. Ma, Y. Wu, S. Jin et al., "Gold nanoparticles induce autophagosome accumulation through size-dependent nanoparticle uptake and lysosome impairment," *ACS Nano*, vol. 5, no. 11, pp. 8629–8639, 2011.

[39] S. Jin, X. Ma, H. Ma et al., "Surface chemistry-mediated penetration and gold nanorod thermotherapy in multicellular tumor spheroids," *Nanoscale*, vol. 5, no. 1, pp. 143–146, 2013.

[40] A. Albanese, P. S. Tang, and W. C. W. Chan, "The effect of nanoparticle size, shape, and surface chemistry on biological systems," *Annual Review of Biomedical Engineering*, vol. 14, no. 1, pp. 1–16, 2012.

[41] Q. Wang, Y. Zhou, R. Fu et al., "Distinct autophagy-inducing abilities of similar-sized nanoparticles in cell culture and live *C. elegans*," *Nanoscale*, vol. 10, no. 48, pp. 23059–23069, 2018.

[42] C. C. Hu, G. H. Wu, S. F. Lai et al., "Toxic effects of size-tunable gold nanoparticles on *Caenorhabditis elegans* development and gene regulation," *Scientific Reports*, vol. 8, no. 1, article 15245, 2018.

[43] J. Moon, J. I. Kwak, S. W. Kim, and Y. J. An, "Multigenerational effects of gold nanoparticles in *Caenorhabditis elegans*: continuous versus intermittent exposures," *Environmental Pollution*, vol. 220, Part A, pp. 46–52, 2017.

[44] N. Mohan, C. S. Chen, H. H. Hsieh, Y. C. Wu, and H. C. Chang, "In vivo imaging and toxicity assessments of fluorescent nanodiamonds in *Caenorhabditis elegans*," *Nano Letters*, vol. 10, no. 9, pp. 3692–3699, 2010.

[45] J. Djafari, M. T. McConnell, H. M. Santos et al., "Synthesis of gold functionalised nanoparticles with the *Eranthis hyemalis* lectin and preliminary toxicological studies on *Caenorhabditis elegans*," *Materials*, vol. 11, no. 8, p. 1363, 2018.

[46] Q. Wu, W. Wang, Y. Li et al., "Small sizes of TiO_2-NPs exhibit adverse effects at predicted environmental relevant concentrations on nematodes in a modified chronic toxicity assay system," *Journal of Hazardous Materials*, vol. 243, pp. 161–168, 2012.

[47] S. Gupta, T. Kushwah, A. Vishwakarma, and S. Yadav, "Optimization of ZnO-NPs to investigate their safe application by assessing their effect on soil nematode *Caenorhabditis elegans*," *Nanoscale Research Letters*, vol. 10, no. 1, 2015.

Hindawi
Journal of Nanomaterials
Volume 2019, Article ID 2458312, 12 pages
https://doi.org/10.1155/2019/2458312

Research Article

Eggshell-Derived Nanohydroxyapatite Adsorbent for Defluoridation of Drinking Water from Bofo of Ethiopia

Kifle Workeneh, Enyew Amare Zereffa, Toshome Abdo Segne, and Rajalakshmanan Eswaramoorthy

Department of Applied Chemistry, School of Applied Natural Science, Adama Science and Technology University, Adama P.O. 1888, Ethiopia

Correspondence should be addressed to Enyew Amare Zereffa; enyewama@yahoo.com and Rajalakshmanan Eswaramoorthy; rajalakshmanan.e@gmail.com

Received 25 March 2019; Revised 3 June 2019; Accepted 1 July 2019; Published 26 August 2019

Guest Editor: Nirupam Aich

Fluoride has become a notable toxicological environmental hazard worldwide because it is often found in groundwater. In the present study, hydroxyapatite adsorbent was synthesized from eggshell waste to remove fluoride from aqueous solution. XRD, FT-IR, and TGA techniques were used to characterize the prepared adsorbent. Batch adsorption studies were performed to examine the adsorption capacity of hydroxyapatite such as the effect of the initial pH of the solution, contact time, adsorbent dose, and initial fluoride concentration. The fluoride ion-selective electrode was used to determine the fluoride removal efficiency. 98.8% of fluoride was removed at pH 3.0, but at pH ~7.0, 85% of fluoride was removed; it shows that the fluoride adsorption is pH dependent. The adsorption isotherm studies (Langmuir and Freundlich models) and the experimental results for the removal of fluoride showed that the Langmuir model was more favorable and the reaction followed pseudo-second-order kinetics. In real water samples, the prepared hydroxyapatite derived from eggshell exhibited 81% removal efficiency. Our results indicate that eggshell waste-derived hydroxyapatite may be an alternative source for defluoridation in developing countries.

1. Introduction

Water is an essential element in human life which may be adulterated by industrial wastes and natural causes. It is estimated that poor quality of drinking water causes 80% of diseases worldwide. It has been reported that 65% of endemic fluorosis is caused by fluoride-contaminated drinking water [1, 2]. Fluoride is vital for mineralization of hard tissues in humans; however, it is harmful when the concentration is higher than 1.5 mg/L. Excess fluoride ions (>1.5 mg/L) are strongly attracted to cationic calcium present in bones and teeth that results in skeletal and dental fluorosis [3, 4]. World Health Organization (WHO) standards suggest that the concentration range of fluoride should be within 1.0 to1.5 ppm in drinking water. However, it has been reported that 11 million individuals living in the Rift Valley region of Ethiopia are highly vulnerable to fluoride-related problems as they rely on drinking water sources having high fluoride concentrations (33 mg/L) [5]. Therefore, developing a cost-effective fluoride removal technique is paramount in developing countries like Ethiopia. Currently, a range of techniques has been used for fluoride removal that includes precipitation, membrane filtration, ion exchange/adsorption, and distillation. However, these fluoride removal techniques have their own drawbacks such as poor removal capacities, lack of selectivity, adverse effects on water quality, production of high volumes of sludge, and complex procedures. Hence, it is critical to develop a cost-effective strategy to remove the surfeit fluoride from the drinking water.

Recently, the adsorption method is shown to be effective in the removal of fluoride even at low concentrations, and additionally, it has low maintenance cost [6–9]. Consequently, a range of low-cost materials has been investigated for their excess fluoride removal efficiency from drinking water. However, all these materials showed poor fluoride adsorption capability and are not enough for wide application. Because

of economic reasons, bone char has been commonly used as adsorbent for defluoridation of drinking water in developing countries [5, 6, 10]. However, challenges on obtaining high-quality bone char materials and hygiene-related issues limited their usage on a large scale worldwide. Recently, several researchers have investigated a range of calcium-based adsorbent materials, of which synthetic hydroxyapatite has been the promising candidate due to its identical chemical composition with bone, nontoxicity, and specifically high fluoride removal capability [11–17]. Recently, researches indicate that HA has better defluoridation capability and the defluoridation efficiency is greatly size dependent on synthetic hydroxyapatite [13, 18, 19]. Traditionally, the preparation of synthetic HA uses any of the following methods such as wet precipitation methods, sol-gel technique, hydrothermal technique, or low-temperature synthesis.

Among them, the wet chemical precipitation method has shown to be advantageous over other methods due to its cost-effective simple procedure [12]. In addition, the main advantage of this method is that it is eco-friendly and water is the only by-product. In general, HA can be synthesized either from biowastes like coral and seashell or from calcium and phosphate source precursors [12, 20, 21]. Eggshells are a naturally occurring calcium source. Daily, a large number of eggshells are left without use and produce waste. More importantly, eggshell supports microbial production that leads to environmental pollution. As per our understanding, only a limited number of researchers have used eggshells for preparing synthetic HA [22–25]. Therefore, in this study, we aimed to synthesize hydroxyapatite from eggshell through wet chemical precipitation and tested for its defluoridation capacity. The removal efficiency of the HA obtained from eggshell was compared with that of commercial HA to assure that eggshell-derived HA powder is a low-cost adsorbent that has the potential to remove excess fluoride from drinking water. In addition, various operating parameters that may influence the adsorption process such as pH, initial concentration of adsorbate, and the amount of adsorbent (HA) used were studied.

2. Materials and Methods

Chicken eggshells were collected from local restaurants in Adama city. Analytical-grade chemicals and reagents were purchased from Addis Ababa (NEWAY PLC, Chemicals). All test solutions were prepared with deionized water.

2.1. Synthesis of Hydroxyapatite. Hydroxyapatite powder was synthesized from eggshell waste and phosphoric acid through wet chemical precipitation in two phases. In phase I, the surface of the eggshells was washed three times with distilled water and the internal thin layer of the shell was removed to decrease the collagens. The cleaned raw shells were boiled in distilled water for 1 hr at 100°C to remove impurities and organic matter. The eggshell was dried in an oven at 80°C for 3 hours in order to crush and grind using a pestle and mortar to obtain a powder. The eggshell residue was sieved with a 150 μm size sieve and calcined in a furnace at 850°C for 2 hr on the ceramic crucible to obtain a fine powder. The prepared powder was analyzed by TGA and XRD to confirm the presence of calcium oxide.

In phase II, a stoichiometric amount of calcined eggshell powder (calcium oxide) and 0.3 M H_3PO_4 (to obtain the Ca/P mole ratio equal to 1.67) was added and dispersed in distilled water in a 500 mL beaker. Analytical-grade phosphoric acid was diluted to 0.3 M and added dropwise into the suspension at room temperature by monitoring the pH with a pH meter until the pH reaches 8.5. The solution was subjected to aging treatment for 12 hr at room temperature followed by stirring on a magnetic stirrer for 30 minutes without heating and left for an extra 10 hr for precipitate formation. The precipitate was washed and filtered using a filter (Whitman # 1) paper. Finally, the precipitate obtained was dried in an oven at 80°C for 3 hr and calcined (900°C) in a furnace on a ceramic crucible for 2 hr to obtain the hydroxyapatite (HA) powder. The synthesized HA powder was stored in a dry place and taken for further characterization.

2.2. Thermogravimetric Analysis (TGA). TGA analysis was used (Shimadzu DTG-60 Plus instrument) for the determination of the calcination temperatures. The prepared eggshell and synthesized HA powders were sieved with a 50 μm size sieve, and 10 mg of each sample was weighed on an electronic mass balance and placed in the alumina crucible for TGA/DTA analysis under an air atmosphere at a heating rate of 10°C/minute.

2.3. XRD Analysis. The HA samples were grounded using a marble mortar and pestle before distributing 100 mg of the ground sample powder over a 10 mm diameter. The prepared HA samples were analyzed by XRD using a CuKα monochromatic beam (wavelength = 0.154056 nm) produced at 40 kV and 30 mA. The XRD spectrum was recorded from 10° to 80° with 2θ angles.

2.4. Phase Identification. For the phase identification step, the X-ray diffraction patterns were directly compared to the files to HA from the Joint Committee Powder Diffraction Standards (JCPDS, card no. 09-432) as was supplied by the International Centre for Diffraction Data (ICDD).

2.5. Crystal Size. Scherrer's formula was used to determine the crystal size from the XRD pattern. As per this equation, a single crystal dimension (nm) can be calculated from the peak broadening.

$$D = \left(\frac{K\alpha}{\text{FWHM}}\right)\theta. \quad (1)$$

In the above equation, D is the crystal size (nm), K is the Scherrer constant (0.9 for hexagonal HA), α is the wavelength of the monochromatic X-ray beam (0.15418 nm), and FWHM is the experimental full width at half maximum intensity of the diffraction peak under the consideration peak; θ is the diffraction angle (°).

2.6. Fourier Transform Infrared (FT-IR) Spectroscopy. Fourier transform infrared spectroscopy (FT-IR) was handled by a Spectrum 65 FT-IR (PerkinElmer). Sample preparation was

done by mixing 2 mg of each sample with 300 mg of potassium bromide (KBr), compressed to form a pellet and then placed on a specimen holder; the spectrum was recorded from 400 to 4000 cm^{-1}.

2.7. Sample Preparation of Synthesized HA for the Defluoridation Test. After characterization of the synthesized HA, four samples of the powder were accurately weighed on an electronic mass balance for the defluoridation test. The samples have constant intervals of 1 g, 3 g, 5 g, and 7 g.

2.8. Preparation of Stock Solution for the Defluoridation Test. Fluoride stock solution was prepared by dissolving 2.21 g of sodium fluoride in 1000 mL of distilled water in a plastic standard flask. Equal intervals of fluoride solutions of 5, 10, 15, and 20 mg/L fluoride were prepared by serial dilution from the stock solution for the defluoridation test.

2.9. Preparation of the Raw Water Sample for the Defluoridation Test. Six samples (30 mL) of groundwater (raw water) were donated from Bofo and Serenity sites under the supervision of OSHO Lab Technical for the practical defluoridation test. Three samples from Bofo located at East Shewa, Lome district, and three samples from Serenity located at East Shew around Meki town were carefully measured with the graduated cylinder and kept in a 50 mL plastic beaker until their fluoride concentration was determined. The fluoride concentrations of water samples were 8.3 and 10.5 mg/L, respectively, and both are above the WHO guideline. The defluoridation test was done with 1, 3, and 5 g doses of synthesized HA powder by using the same procedure for optimizations.

2.10. Preparation of TISAB (Total Ionic Strength Adjustment Buffer). TISAB is essential in ion-selective electrode measurements because it masks minor changes made in the ionic strength of the solution and hence increases the accuracy of the reading. 7 g trisodium citrate ($Na_2C_6H_2O_7$), 56 g sodium chloride (NaCl), and 2 g EDTA are dissolved into 500 mL of double-distilled water. After the solution was dissolved, 57 g of glacial acetic acid is added into it, and finally, 5 M sodium hydroxide was added until the pH reached 5.3, then transferred to a 1000 mL volumetric flask, and brought up to the mark using double-distilled water.

2.11. Calibration of the Electrode. 20 mL of fluoride solution with different fluoride ion concentrations was prepared in constant intervals, and 2 mL of TISAB was added to each solution. The potential (E in mV) versus the logarithm of concentration (log c) in mg/L was plotted. The slope of the graph and R^2 were calculated to check the accuracy of the measurement. The prepared concentrations of 2.5, 5, 7.5, and 10 mg/L of fluoride were used for calibration.

2.12. Fluoride Determination Technique. A fluoride ion-selective electrode was used to determine the fluoride ion concentration. For this test, the HA powders were separately added on to 30 mL of the known concentration of fluoride water (5, 10, 15, and 20 mg/L) in a 50 mL plastic beaker. To eliminate the interference effect of complex ions in the solution and to maintain ionic strength and the pH, 2 mL of total ionic strength adjustment buffer (TISAB) solution (10 : 1 volumetric ratio) was added. In this way, the effect of various parameters like contact time, pH, adsorbent dose, and initial fluoride concentration was obtained by changing a parameter and keeping the other parameters constant. Finally, the equilibrium fluoride concentration (residual) for each test was determined using a pH meter in combination with a fluoride-selective electrode, and the pH was measured with a pH meter. The electrode was calibrated prior to each experiment.

2.13. Defluoridation Test. All experiments were conducted using 30 mL of fluoride solution (10 mg/L) taken in four different 50 mL plastic beakers. 1 g, 3 g, 5 g, and 7 g HA samples were added in this solution for different contact times. Then, the solution was stirred for 1 minute at 25°C to reach equilibrium on a homogenous solution. Each sample was taken at a specified time interval for their contact times 1 hr, 3 hr, 5 hr, 7 hr, 11 hr, and 24 hr and filtered with a Whitman filter paper (no. 1) before analysis. The fluoride-selective electrode reads the electrovolt in terms of a millivolt. The millivolt was converted into mg/L of residual fluoride concentration using predetermined calibration slop by Microsoft Excel. The percentage of adsorption efficiency and the fluoride removal capacity (mg of fluoride ion adsorbed per gram of adsorbent) at a given contact time for the HA adsorbent was calculated using the following:

$$\text{Percentage removal} = \frac{[C_o - C_t]}{C_o} \times 100,$$
$$\text{Adsorption capacity} = \frac{[C_o - C_t]}{m} \times V. \quad (2)$$

In the above equation, C_o and C_t are the initial and final fluoride concentrations, respectively, m is the mass of the adsorbent HA, and V is the volume of the solution.

2.14. Optimization of Different Parameters. In this study, the effect of major parameters like adsorbent dose, initial fluoride concentration, contact time, and pH was optimized to investigate the maximum defluoridation efficiency of the synthesized natural hydroxyapatite (HA) from the eggshell.

2.14.1. Effect of Adsorbent Dosage. Experimental examinations were carried at different concentrations of 1, 3, 5, and 7 g of adsorbent in 10 mg/L of fluoride initial concentration at pH 3.

2.14.2. Effect of Contact Time. Residual anionic fluoride concentration was measured at different contact times of adsorption, 1, 3, 5, 7, 11, and 24 hours, with 5 g of adsorbent (HA) to study the effect of contact time. Other parameters like pH, the concentration of the solution, and HA dosage remain constant.

2.14.3. Effect of Initial Fluoride Concentration. To study the effect of initial fluoride concentration, experiments were conducted at various fluoride concentrations (5, 10, 15, and

Table 1: Dimensionless separation factors (R_L).

Concentration (mg/L)	5	10	15	20
R_L	0.235	0.136	0.095	0.073

20 mg/L) at a constant temperature, pH (pH 3), adsorbent dose (5 g), and contact time (5 hr).

2.14.4. Effect of pH. To investigate the effect of pH on defluoridation, the test solutions containing the optimized concentration of fluoride were changed to pH values of 3, 5, 7, and 9 using HCl (1 N) and NaOH (1 N) and the adsorbent mass remained constant through acidic, neutral, and basic media. Then, the determined 5 g HA was added in into each test solution separately and stirred for 1 minute to reach equilibrium. Residual F^- ion concentrations were evaluated in each experiment after 5 hr contact time. Finally, pH versus percentage removal graph was plotted to explain the adsorption performance of the adsorbent HA at each pH.

2.15. Adsorption Isotherm Models. The relationship between the amounts of substances sorbed at a constant temperature and its concentration equilibrium solution is called adsorption isotherm. The frequently used adsorption isotherm models for surface average analysis are Langmuir and Freundlich isotherms.

2.15.1. Langmuir Adsorption Isotherm. The Langmuir isotherm model is widely used to quantify the amount adsorbed on the adsorbent as a function of concentration at a given temperature. Theoretically, the adsorbent has a limited number of available sites for the adsorbate. Therefore, beyond saturation value, no further adsorption can occur. The linear form of the Langmuir is as follows:

$$\frac{C_e}{q_e} = \frac{C_e}{q_e} + \frac{1}{b}. \tag{3}$$

The Langmuir isotherm can be expressed by a dimensionless separation factor or equilibrium parameter, R_L, which is defined by

$$R_L = \frac{1}{1 + C_{ob}}. \tag{4}$$

The value of R_L indicates the type of isotherm which is either favorable ($0 < R_L < 1$), unfavorable ($R_L > 1$), or irreversible ($R_L = 0$) (Tables 1 and 2).

2.15.2. Freundlich Adsorption Isotherm. The Freundlich isotherm equation takes into account repulsive interactions between adsorbed solute particles and also accounts for surface heterogeneities. The logarithm form of the Freundlich isotherm is given as follows:

$$\text{Log}q_e = \frac{1}{n} \log C_e + \log \text{kf}. \tag{5}$$

Table 2: Kinetic data obtained by varying the contact time using a constant adsorbent dose of 5 g HA, pH = 3, and 10 mg/g of fluoride concentration.

Time (hr)	Residual fluoride	q_t (mg/g)	t/q_t	$\ln(q_e - q_t)$	$\ln q_t$
1	0.15	0.0591	16.92047	-8.1117	-2.82855
3	0.12	0.0592	58.67567	-8.5171	-2.8265
5	0.10	0.0594	84.17508	∞	-2.8234
7	0.11	0.0593	118.04384	-9.2103	-2.8251
9	0.11	0.0592	151.77065	-9.2103	-1.8251
11	0.13	0.0592	185.81081	-8.5171	-2.8268
24	0.13	0.0592	405.40545	-8.5171	-2.8268

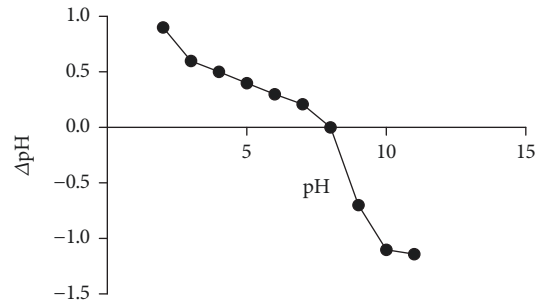

Figure 1: Plot of ΔpH vs. final pH of the adsorbent to determine the point of zero charges.

Finally, the applicability of two adsorption isotherms (Langmuir and Freundlich) can be compared by evaluating the multiple regression correlation coefficients, R^2 (Table 2).

2.16. pH at the Potential of Point of Zero Charges (pH_{pzc}) Determination. The isoelectric point or point of zero charges (pH_{pzc}) were determined by using the reported method [26]. Ten NaCl (0.1 M) solutions with an initial pH range of 2–11 were prepared in duplicate. Each duplicate was added with 2 g of HA and mixed for 0.5 hr. Then, the adsorbent was separated from the solutions by filtration. The final pH values of the 10 solutions were measured by a pH meter and therefore calculation of ΔpH (ΔpH = final pH − initial pH). A graph of final pH values plotted against ΔpH is shown in Figure 1. The pH_{pzc} (point of zero charges) of the adsorbent was determined from the plotted graph (Table 3).

2.17. Kinetics of Adsorption. It is very important to know the rate at which the adsorption process takes place and the factors that control the rate of the process; for this purpose, the kinetics of the process were evaluated. The adsorption kinetic studies describe the rate of uptake of the adsorbate molecule; in this case, fluoride ion onto adsorbent, the rate depends on the physicochemical characteristics of the adsorbate and adsorbent, pH, temperature, and concentration. To describe the adsorption kinetic behavior, the following models are used.

Table 3: ΔpH vs. final pH of the adsorbent perfumed on 2 g HA, 10 mg/L of fluoride concentration, and 5 hr contact time.

Initial pH	2	3	4	5	6	7	8	9	10	11
Final pH	2.90	3.60	4.50	5.40	6.30	7.21	7.90	8.30	8.90	9.86
Change in pH	0.90	0.60	0.50	0.40	0.30	0.21	0	-0.7	-1.1	-1.14

Table 4: Adsorption kinetic parameter for pseudo-first-order kinetics.

Pseudo-first-order kinetics	Intercept	K_1	R^2	q_e
	-8.634	0.005	0.0089	-0.1602

Table 5: Adsorption kinetic parameter for pseudo-second-order kinetics.

Pseudo-second-order kinetics	Intercept	K_2	R^2	q_e
	2.1152	134.048	0.999	0.0596

2.17.1. Pseudo-First-Order Equation. The pseudo-first-order differential equation is generally expressed as follows [27]:

$$\frac{dq}{dt} = K_1 (q_e - q_t). \tag{6}$$

In the above equation, q_e and q_t refer to the amount of fluoride ion adsorbed per unit mass of the adsorbate at equilibrium time and any time (mg/g), respectively. K_1 is the rate constant of pseudo-first-order adsorption. Integrating equation (6) by applying the boundary conditions $q_e = 0$ at $t = 0$ and $q_t = q$ to obtain the following linear equation t at $t = t$ gives

$$\frac{\text{Log}q_e}{q_e - q_t} = \frac{K_1 t}{2.303}. \tag{7}$$

Equation (7) can be rearranged and described by ln.

$$\ln (q_e - q_t) = \ln q_e - K_1 t. \tag{8}$$

The rate constant K_1 and equilibrium adsorption capacity q_e can be predicted from the slope and intercept, respectively, of the linear plots of $\log (q_e - q_t)$ versus t (Table 4).

2.17.2. Pseudo-Second-Order Equation. The rate of a pseudo-second-order differential equation is given as follows [28, 29]:

$$\frac{dq_t}{dt} K_2 (q_e - q_t)^2, \tag{9}$$

where K_2 is the rate constant of the pseudo-second-order equation (g/mg·min.) and q_e is the equilibrium adsorption capacity (mg/g). By applying the boundary conditions $q_t = 0$ at $t = 0$ and $q_t = q_t$ at $t = t$ on equation (9) and rearranging, the following linearized equation is obtained:

$$\frac{t}{q_t} = \frac{t}{q_t} + \frac{1}{K^2 {q_e}^2}. \tag{10}$$

The values of q_t and K^2 can be determined experimentally from the slope and intercept, respectively, of the plots of t/q_t versus t (Table 5).

3. Results and Discussion

3.1. Characterization of the Calcium Precursor Material (Eggshell Powder). The calcium precursor used for the HA synthesis was derived from the decomposition of eggshell. The complete calcium precursor decomposition temperature was obtained from the TGA/DTA result. The thermogravimetric analysis (TGA) of the eggshell powder was carried out between room temperature and 1000°C in order to determine the thermal stability and the decomposition temperature of eggshell powder. The TGA result revealed that a significant mass loss was observed between the temperatures 600 and 800°C, probably due to the removal of impurities, and the eggshell residue was stable above 800°C as indicated in Figure 2. XRD diffraction graph of calcined eggshell residue at 850°C is shown in Figure 3. The diffraction peaks at 34.078°, 37.123°, 54.351°, and 63.613° corresponding to (111), (200), (220), and (311) planes, respectively, shown on the graph are in good agreement with the reported standard values of CaO [30].

3.2. Characterization of HA Powder. TGA/DTA experiments were done to determine the calcination temperature for the formation of pure-phase hydroxyapatite synthesized from calcined eggshell residue and phosphoric acid. As illustrated in Figure 4, the result revealed that the material is stable or has no significant mass loss above 900°C. The XRD pattern of HA powder obtained after calcination at 900°C is shown in Figure 5. According to the figure, there is no peak attributable to possible impurities, which indicates that the final product is highly pure HA according to the ICDD powder diffraction file (pdf number 009-0432). All possible peaks can be indexed to the pure hexagonal phase of HA (P63mc) without secondary phases such as α-TCP (alpha-tricalcium phosphate) and β-TCP (beta-tricalcium phosphate). This confirmed the successful synthesis of pure-phase HA via the chemical precipitation from calcined eggshell residue. The crystallite size was calculated using Scherer's formula from the XRD pattern. The calculated single crystallite sizes were D1 = 50.5, D2 = 45.2, and D3 = 48.7 nm, and the average crystal size obtained was 48.13 nm. The FT-IR spectrum shows band 3444 cm^{-1} of the OH^- bond stretching (Figure 6). The intensified peak in the region between 1414 and 1040 cm^{-1} is attributed to the phosphate group. The

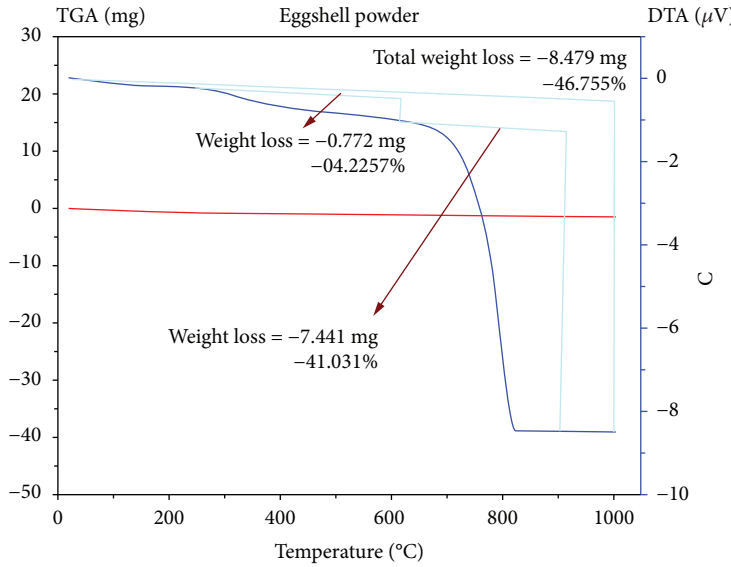

Figure 2: TGA/DTA result of eggshell powder.

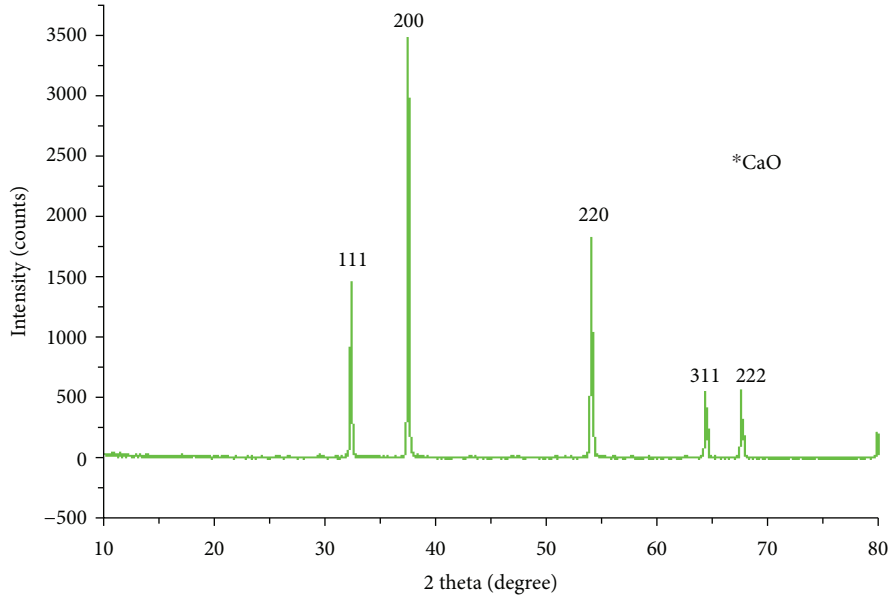

Figure 3: XRD pattern of calcinated eggshell at 850°C.

band at 595 cm^{-1} belongs to the phosphate group. These peaks confirm that the phosphate group occupies two sites in the crystal lattice [11, 31].

3.3. Defluoridation Efficacy of HA on Prepared Fluoride Solution

3.3.1. Determination of the Adsorbent Dose (HA). The concentration range was selected based on the preliminary test results at room temperature. The experiment was conducted on different masses of adsorbent at 1 g 3 g, 5 g, and 7 g in 10 mg/L of the initial fluoride concentration with 5 hr contact time at pH 3. As described in Figure 7, the fluoride removal efficiency is directly proportional to the adsorbent dose up to 5 g because of a large number of fluoride-binding site availability. As identified, the equilibrium was fully established at a 5 g dose with high fluoride removal of about 99%. When the initial fluoride concentration is 10 mg, the equilibrium fluoride concentration falls within the WHO limit and there is no significant change on the efficiency beyond this 5 g adsorbent dose. Therefore, for further adsorption experimentation, 5 g of HA was considered as an ideal dose. The adsorption versus percentage removal of fluoride is given in Figure 7. The experimental result of different HA doses exhibited increases with adsorbent dosage, until it is equal to 5 g, then decreases, when the dosage is increased to 7 g. The results

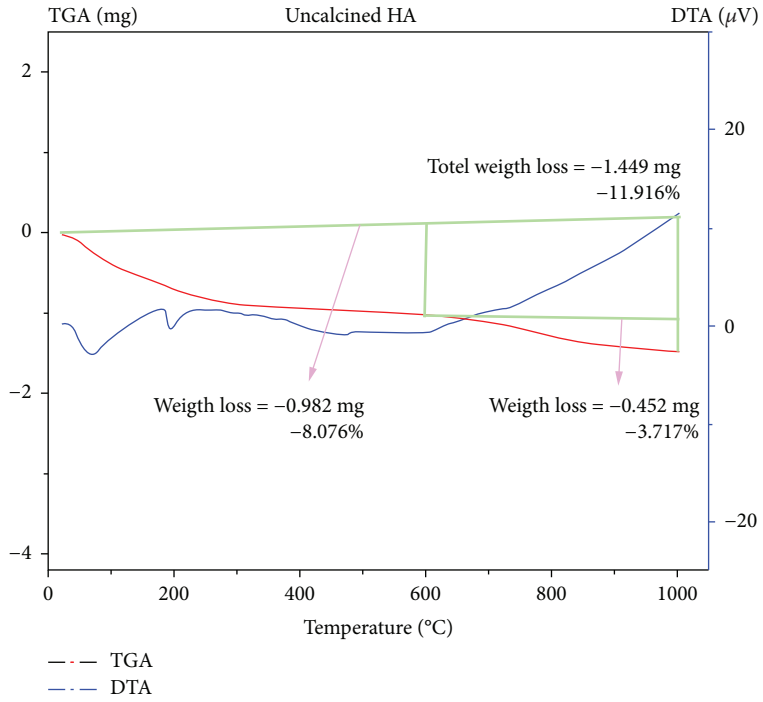

Figure 4: TGA/DTA pattern for the synthesized HA.

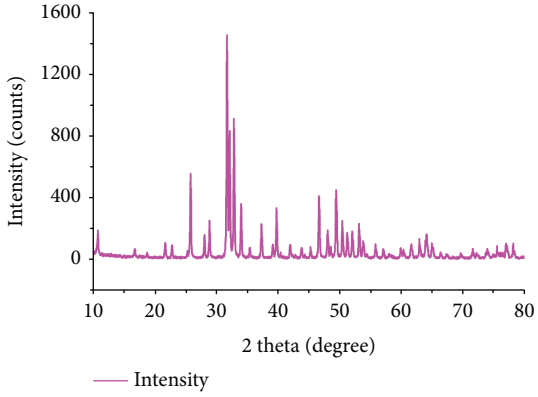

Figure 5: XRD pattern of HA powder calcined at 900°C.

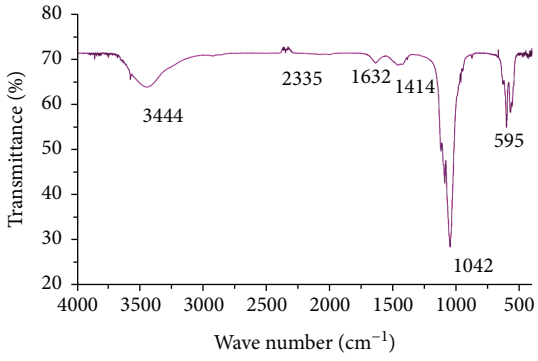

Figure 6: FT-IR patterns of calcinated HA powder.

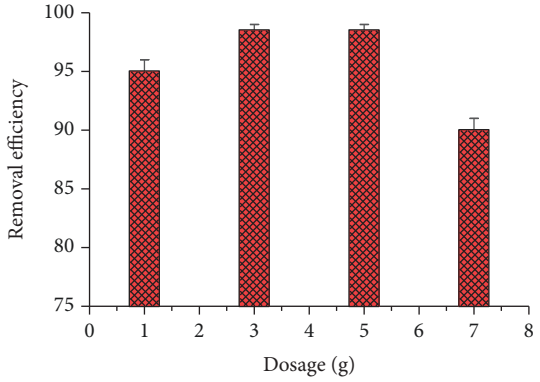

Figure 7: Investigation of the optimum dose test using 10 mg/L initial fluoride concentration, pH 3, and contact time of 5 hr.

show that an increase in adsorbent dosage results in increasing of fluoride removal efficiency because of the increased availability of fluoride-binding sites. The decrease in removal at a 7 g dose is due to the depletion of fluoride in the solution with an increasing dose of the adsorbent.

3.3.2. Determination of Contact Time. To determine the effect of contact time on adsorption of fluoride on hydroxyapatite, batch experiments were carried with different contact times (1 hr, 3 hr, 5 hr, 7 hr, 9 hr, and 11 hr) under constant dosage (5 g, 10 g/L fluoride concentration) and pH (pH 3) at room temperature. As shown in Figure 8, rapid fluoride removal was observed at the initial stage until reaching equilibrium time (5 hours) with a high removal efficiency of about 99%.

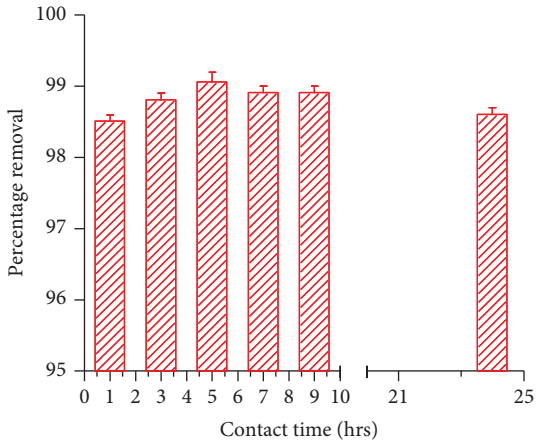

Figure 8: Fluoride removal efficiency as a function of contact time at 5 g of the HA dose, pH = 3, and initial concentration of 10 mg/L.

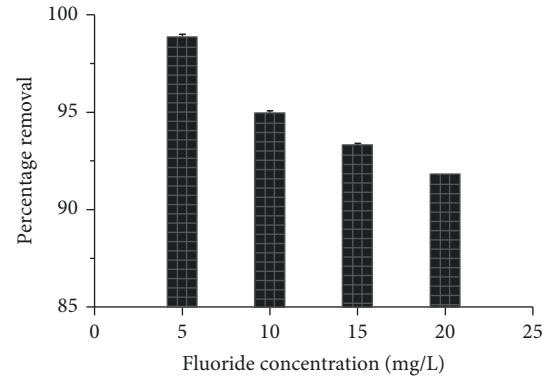

Figure 9: The effect of initial fluoride concentration on percentage removal of fluoride using 5 g adsorbent, 5 hr contact time, and pH = 3.

This is because a high number of active sites at the initial stage lead to high diffusion of fluoride towards the adsorbent surface, as shown in the figure after the equilibrium time slowly desorbed from the surface of the adsorbent to the solution. Therefore, this parameter determines the rate of mass transfer from the solution to the surface of the adsorbent, and the data were used to study the kinetic study of batch adsorption. This trend was also reported by other studies on defluoridation processes [11, 18]. This is due to the faster saturation of the active sites with time. This implies that the adsorbent has a specific number of active sites, which eventually are saturated after prolonged exposure to fluoride solution. After saturation of the active sites, no further adsorption is carried out on the residual fluoride concentration (Figure 8).

3.3.3. Determination of Initial Fluoride Concentration. For this test, the initial concentration of fluoride is selected randomly with 5 increments from 5 to 20 mg/L. The effects of other parameters remain constant, and the adsorbent dose was 5 g with 30 mL solution. The results indicate that the initial fluoride concentration has an influence on the removal capacity of the adsorbent (Figure 9). For a given mass of HA, the fluoride removal capacity decreases with increasing initial concentration because of the increased diffusion of fluoride to adsorption sites and utilization of less active sites of the adsorbent. The optimized result is selected as 10 mg/L which encountered 95% removal efficiency, and the residual fluoride concentration was 0.5 which satisfied the optimum WHO guideline for drinking water.

3.3.4. The Effect of pH on Percentage Removal of Fluoride. The adsorption process is controlled by the pH of the adsorbate solution. To make inclusive all the 3 media, the pH range was deliberately selected from 3 to 9. The effect of pH was investigated by varying the pH from 3 to 9 with 2 increments. As illustrated in Figure 10(a), the maximum defluoridation was achieved at pH 3 which is 98.8%. A decrease in the fluoride removal extent of the adsorbent was observed at increasing pH. The main reason behind the maximum defluoridation at low pH values may be because of the presence of a large number of H^+ ions at these pH values. This leads to neutralization of the OH^- ions on the adsorbed surface and hence reduction of the hindrance to the diffusion of fluoride ions. Therefore, pH is determinant to drinking water, and hence, the optimum removal efficiency for this adsorbent HA was 85% observed on pH = 7.

3.4. Synthesized HA on Raw Water Defluoridation. Samples of water were collected from two different locations of the Oromia region, East Showa district, near Adama city. Sample 1 is from Bofo around the Bati Lome District and sample 2 from around Maki Town; the secured groundwater had fluoride ion concentration of 8.3 mg/L and 10.5 mg/L, respectively, which is still more than the permissible limit of WHO. After adsorption, the fluoride ion concentration of the two samples was measured and it was found that the fluoride ion concentration was decreased significantly in adsorbent doses of 1 g, 3 g, and 5 g, at a temperature of 25°C, rotation speed of 400 rpm for 1 minute steering time, 5 h contact time, and optimum pH = 7 adjusted by a drop of 1 M NaOH. The HA adsorbent almost had good removal efficiency for field samples on the comparable condition to the result obtained on the fluoride solution test. In this paper, it was observed that on the two sites, the synthesized HA material shows fluoride removal efficiencies of 81.92 and 82. 85% for Bofo and Maki, respectively, upon addition of a 5 g dose and at pH 7. The synthesized HA from eggshell waste shows comparable fluoride removal efficiency values to the commercial HA (Figure 10(b)). The final pH of the treated water was found in the range of 7.5 to 8.

3.5. Experimental Result on Adsorption Isotherm. In this investigation, the data based on the optimized fluoride concentration were interpreted in Table 6. As can be observed from the table, $R^2 = 0.97$ is less than one, and hence, the adsorption favors the Langmuir adsorption isotherm model. To determine whether the adsorption favors the Langmuir or the Freundlich model, we can apply the comparison of R^2 or R_L favoring Langmuir's $(0 < R_L < 1)$, unfavorable $(R_L > 1)$, or irreversible $(R_L = 0)$ [32, 33]. Therefore, as we can observe

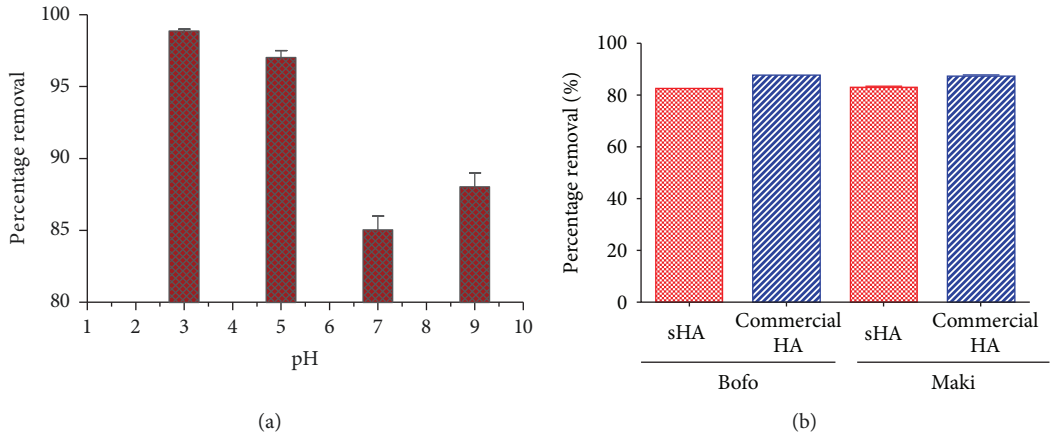

Figure 10: (a) The effect of pH on the percentage removal of fluoride at 5 g adsorbent and 5 hr. (b) Fluoride removal efficiency of synthesized HA (sHA) and commercial HA on raw water samples from Bofo and Maki (5 g dose, 5 hr contact time, and pH 7).

Table 6: Langmuir's adsorption isotherm data for concentration versus adsorption capacity.

C_o (mg/L)	C_e	q_e	log C_e	log q_e	C_e/q_e
5	0.25	0.0285	-0.6020	-1.5451	8.7719
10	0.50	0.0570	-0.3010	-1.2441	8.7719
15	0.96	0.0842	-0.0177	-1.0746	11.4014
20	1.6	0.1104	-0.2041	-0.9570	14.4927

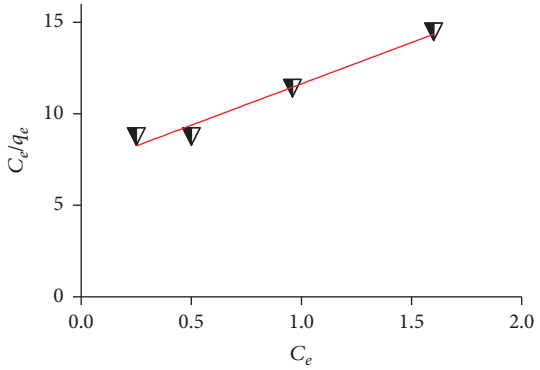

Figure 11: Linearized Langmuir adsorption isotherm for fluoride adsorption.

from the R^2 value, which is 0.96 which is less than one, the adsorption isothermal obeys Langmuir's model (Figure 11). The value of correlation coefficients ($R^2 = 0.9657$) for the Langmuir isotherm is higher in comparison to that obtained for the Freundlich isotherm. For the Freundlich model, the value of correlation coefficient (R^2) was 0.763 (Figure 12). The maximum adsorption capacity of the adsorbent for the Langmuir isotherm is greater than that for the Freundlich model (Tables 1 and 7). Hence, it can be concluded that the Langmuir isotherm model is more suitable for adsorption of fluoride ions than the Freundlich isotherm on the basis of the experimental study.

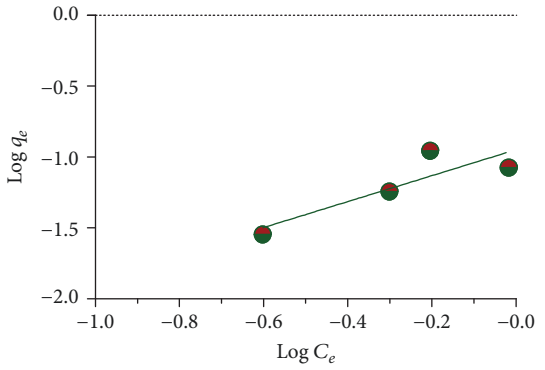

Figure 12: Freundlich isotherm graph of adsorption fluoride by HA.

Table 7: Langmuir and Freundlich isotherm model parameters describing the HA fluoride adsorption at a constant adsorbent dose of 5 g, contact time of 5 hr, and pH = 3.

Parameter	Langmuir model	Parameter	Freundlich model
q (mg/g)	0.2212	kf	0.3879
b (L/mg)	0.6349	$1/n$	0.914
R^2	0.9657	R^2	0.763

3.6. Adsorption Kinetic Models. In the present study, the kinetics of defluoridation was carried out to study the behavior of the synthesized hydroxyapatite Table 2.

3.6.1. Pseudo First-Order Kinetic Model. The different parameters of pseudo-first- and pseudo-second-order kinetics are given in Tables 4 and 5, respectively.

$$\log (q_e - q_t) = \log q_e - \frac{K_1}{2.303} t. \quad (11)$$

For kinetic studies, 5 g of HA would be contacted with 30 mL of fluoride solution having a fluoride concentration

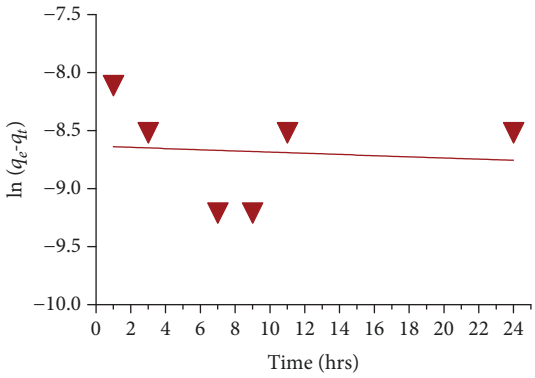

Figure 13: Pseudo-first-order kinetic result.

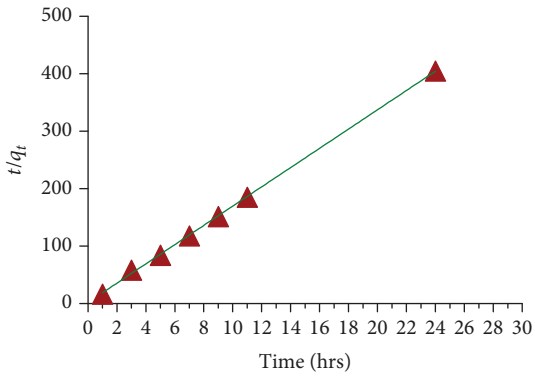

Figure 14: Pseudo-second-order kinetic result.

of 10 g, at a pH of 3, and shaken at 200 rpm and room temperature (Table 4). In the true first order, log q_e should be equal to the intercept as it can be observed from the graphs (Figure 13). Lower correlation coefficients are obtained indicating that the adsorption of fluoride ion on the adsorbent hydroxyapatite does not follow the pseudo-first-order kinetics.

3.6.2. Pseudo-Second-Order Kinetic Model. From the result of adsorption kinetic first-order and second-order data, it is possible to summarize the adsorption behavior of the adsorbents prepared (Table 5). The correlation coefficient (R^2) was found to be 0.0089 and 0.999 for pseudo-first-order kinetics and pseudo-second-order kinetics, respectively. The value of R^2 for pseudo-second-order kinetics approaches to one (Figure 14). The experimental equilibrium adsorption capacity and the calculated capacity are close to the R^2 value of 0.999 [34]. This indicated that it is unity and the adequate linear fitting of the plots confirmed that the adsorption of fluoride ions using the synthesized hydroxyapatite followed pseudo-second-order kinetics [15, 18].

3.7. pH at the Potential of Point of Zero Charge (pH_{pzc}) Determinations. pH_{pzc} is the pH value at the point where the net surface charge of the adsorbent is 0. pH_{pzc} values for the synthesized HA powder at an optimized operational parameter are around 7.90 (Table 3). In general, the pH values of the adsorbents fall in the acidic to the slightly neutral region. The net surface charge of the adsorbents under pH_{pzc} is positive, while it is negative when above pH_{pzc} (Figure 1). Therefore, determination of the pH_{pzc} value helps to identify the working pH value for adsorption studies. Hence, the adsorbent percent removal capacity increases below the pH_{pzc} value [29, 35].

4. Conclusion

In the present investigation, pure-phase hydroxyapatite was successfully synthesized from chicken eggshell through the wet precipitation method for defluoridation of water by adsorption. The main advantage of this eco-friendly method is that water is the only by-product. The XRD result revealed that the synthesized HA powder was pure phase with a hexagonal structure. The prepared HA (adsorbent) was applied to the real water samples under ideal conditions and found to be effective with 81% fluoride removal efficiency. Our results show that eggshell waste-derived hydroxyapatite may be an alternative source for defluoridation in developing countries. Additionally, natural raw water contains ions that compact with fluoride for adsorption such as HCO_3^-, $SO4^{2-}$, and Cl^-. The effect of these coions should be investigated so that it helps to selectively use the adsorbent in preference to other ions.

Data Availability

The data used to support the findings of this study are available from the corresponding authors upon request.

Conflicts of Interest

The authors declare that they have no conflicts of interest.

Authors' Contributions

The study and the first draft writing were conducted by Kifle Workeneh, and the supervision and edition were done by Prof. Rajalakshmanan Eswaramoorthy. The coauthors Enyew Amare Zereffa and Toshome Abdo Segne participated in analyzing the results and drafting the manuscript.

Acknowledgments

The authors are grateful to the management of Adama Science and Technology University for providing the financial support towards this research work.

References

[1] H. J. Mosha, "Endemic dental fluorosis and the possibilities of defluoridation and fluoridation of water supplies in Tanzania," *Odonto-Stomatologie Tropicale*, vol. 7, no. 2, pp. 89–96, 1984.

[2] S. V. Walvekar and B. A. Qureshi, "Endemic fluorosis and partial defluoridation of water supplies - a public health concern in Kenya," *Community Dentistry and Oral Epidemiology*, vol. 10, no. 3, pp. 156–160, 1982.

[3] M. M. Emamjomeh and M. Sivakumar, "An empirical model for defluoridation by batch monopolar electrocoagulation/-flotation (ECF) process," *Journal of Hazardous Materials*, vol. 131, no. 1-3, pp. 118–125, 2006.

[4] E. Y. Wong and M. K. Stenstrom, "Onsite defluoridation system for drinking water treatment using calcium carbonate," *Journal of Environmental Management*, vol. 216, pp. 270–274, 2018.

[5] A. W. Wagutu, R. Machunda, and Y. A. C. Jande, "Crustacean derived calcium phosphate systems: application in defluoridation of drinking water in East African Rift Valley," *Journal of Hazardous Materials*, vol. 347, pp. 95–105, 2018.

[6] S. Chatterjee, S. Jha, and S. De, "Novel carbonized bone meal for defluoridation of groundwater: batch and column study," *Journal of Environmental Science and Health, Part A: Toxic/Hazardous Substances and Environmental Engineering*, vol. 53, no. 9, pp. 832–846, 2018.

[7] K. S. Hashim, A. Shaw, R. Al Khaddar, M. Ortoneda Pedrola, and D. Phipps, "Defluoridation of drinking water using a new flow column-electrocoagulation reactor (FCER) - experimental, statistical, and economic approach," *Journal of Environmental Management*, vol. 197, pp. 80–88, 2017.

[8] P. Loganathan, S. Vigneswaran, J. Kandasamy, and R. Naidu, "Defluoridation of drinking water using adsorption processes," *Journal of Hazardous Materials*, vol. 248-249, pp. 1–19, 2013.

[9] V. K. Gupta, I. Ali, and V. K. Saini, "Defluoridation of wastewaters using waste carbon slurry," *Water Research*, vol. 41, no. 15, pp. 3307–3316, 2007.

[10] H. Herath, T. Kawakami, and M. Tafu, "The extremely high adsorption capacity of fluoride by chicken bone char (CBC) in defluoridation of drinking water in relation to its finer particle size for better human health," *Healthcare*, vol. 6, no. 4, p. 123, 2018.

[11] Y. Xia, X. Huang, W. Li, Y. Zhang, and Z. Li, "Facile defluoridation of drinking water by forming shell@fluorapatite nanoarray during boiling egg shell," *Journal of Hazardous Materials*, vol. 361, pp. 321–328, 2019.

[12] D. Mehta, P. Mondal, V. K. Saharan, and S. George, "Synthesis of hydroxyapatite nanorods for application in water defluoridation and optimization of process variables: advantage of ultrasonication with precipitation method over conventional method," *Ultrasonics Sonochemistry*, vol. 37, pp. 56–70, 2017.

[13] C. M. Kanno, R. L. Sanders, S. M. Flynn, G. Lessard, and S. C. B. Myneni, "Novel apatite-based sorbent for defluoridation: synthesis and sorption characteristics of nano-microcrystalline hydroxyapatite-coated-limestone," *Environmental Science & Technology*, vol. 48, no. 10, pp. 5798–5807, 2014.

[14] L. Feng, W. Xu, T. Liu, and J. Liu, "Heat regeneration of hydroxyapatite/attapulgite composite beads for defluoridation of drinking water," *Journal of Hazardous Materials*, vol. 221-222, pp. 228–235, 2012.

[15] C. S. Sundaram, N. Viswanathan, and S. Meenakshi, "Defluoridation chemistry of synthetic hydroxyapatite at nano scale: equilibrium and kinetic studies," *Journal of Hazardous Materials*, vol. 155, no. 1-2, pp. 206–215, 2008.

[16] M. J. Larsen and E. I. F. Pearce, "Defluoridation of drinking water by boiling with brushite and calcite," *Caries Research*, vol. 36, no. 5, pp. 341–346, 2002.

[17] B. Ying, X. Li, and Z. Cong, *Wei Sheng Yan Jiu*, vol. 30, no. 6, pp. 326–328, 2001, Study on the defluoridation of drinking water with synthetic hydroxyapatite.

[18] Q. Tang, T. Duan, P. Li, P. Zhang, and D. Wu, "Enhanced defluoridation capacity from aqueous media via hydroxyapatite decorated with carbon nanotube," *Frontiers in Chemistry*, vol. 6, p. 104, 2018.

[19] K. Pandi and N. Viswanathan, "Enhanced defluoridation and facile separation of magnetic nano-hydroxyapatite/alginate composite," *International Journal of Biological Macromolecules*, vol. 80, pp. 341–349, 2015.

[20] X. Li, D. Zheng, and B. Ying, "Manufacture of hydroxyapatite as a defluoridator and the mechanism of defluoridation for drinking water," *Wei Sheng Yan Jiu*, vol. 31, no. 2, pp. 136–138, 2002.

[21] B. Ying, X. Li, D. Zheng, and J. Gao, "Optimizing the synthesis of hydroxyapatite as a method for the defluoridation of drinking water," *Wei Sheng Yan Jiu*, vol. 30, no. 4, pp. 244–246, 2001.

[22] A. C. Ferro and M. Guedes, "Mechanochemical synthesis of hydroxyapatite using cuttlefish bone and chicken eggshell as calcium precursors," *Materials Science & Engineering, C: Materials for Biological Applications*, vol. 97, pp. 124–140, 2019.

[23] V. H. Ingole, K. Hany Hussein, A. A. Kashale et al., "Ultrasound-assisted green economic synthesis of hydroxyapatite nanoparticles using eggshell biowaste and study of mechanical and biological properties for orthopedic applications," *Journal of Biomedical Materials Research Part A*, vol. 105, no. 11, pp. 2935–2947, 2017.

[24] S. K. Padmanabhan, L. Salvatore, F. Gervaso et al., "Synthesis and characterization of collagen scaffolds reinforced by eggshell derived hydroxyapatite for tissue engineering," *Journal of Nanoscience and Nanotechnology*, vol. 15, no. 1, pp. 504–509, 2015.

[25] D. Siva Rama Krishna, A. Siddharthan, S. K. Seshadri, and T. S. Sampath Kumar, "A novel route for synthesis of nanocrystalline hydroxyapatite from eggshell waste," *Journal of Materials Science: Materials in Medicine*, vol. 18, no. 9, pp. 1735–1743, 2007.

[26] S. Alemu, E. Mulugeta, F. Zewge, and B. S. Chandravanshi, "Water defluoridation by aluminium oxide-manganese oxide composite material," *Environmental Technology*, vol. 35, no. 15, pp. 1893–1903, 2014.

[27] S. Muthu Prabhu and S. Meenakshi, "Defluoridation of water using dicarboxylic acids mediated chitosan-polyaniline/-zirconium biopolymeric complex," *International Journal of Biological Macromolecules*, vol. 85, pp. 16–22, 2016.

[28] V. Dhongde, K. L. Wasewar, and B. S. De, "Development of nanohybrid adsorbent for defluoridation from aqueous systems," *Chemosphere*, vol. 188, pp. 354–366, 2017.

[29] K. Parashar, N. Ballav, S. Debnath, K. Pillay, and A. Maity, "Hydrous ZrO_2 decorated polyaniline nanofibres: synthesis, characterization and application as an efficient adsorbent for water defluoridation," *Journal of Colloid and Interface Science*, vol. 508, pp. 342–358, 2017.

[30] L. M. Correia, R. M. A. Saboya, N. de Sousa Campelo et al., "Characterization of calcium oxide catalysts from natural sources and their application in the transesterification of sunflower oil," *Bioresource Technology*, vol. 151, pp. 207–213, 2014.

[31] M. A. C. Teixeira, C. Piccirillo, D. M. Tobaldi et al., "Effect of preparation and processing conditions on UV absorbing properties of hydroxyapatite-Fe_2O_3 sunscreen," *Materials Science & Engineering C*, vol. 71, pp. 141–149, 2017.

[32] S. Mukherjee, S. Dutta, S. Ray, and G. Halder, "A comparative study on defluoridation capabilities of biosorbents: isotherm, kinetics, thermodynamics, cost estimation, and eco-toxicological study," *Environmental Science and Pollution Research International*, vol. 25, no. 18, pp. 17473–17489, 2018.

[33] S. Gogoi, S. K. Nath, S. Bordoloi, and R. K. Dutta, "Fluoride removal from groundwater by limestone treatment in presence of phosphoric acid," *Journal of Environmental Management*, vol. 152, pp. 132–139, 2015.

[34] Y.-S. Ho, "Review of second-order models for adsorption systems," *Journal of Hazardous Materials*, vol. 136, no. 3, pp. 681–689, 2006.

[35] A. A. Izuagie, W. M. Gitari, and J. R. Gumbo, "Synthesis and performance evaluation of Al/Fe oxide coated diatomaceous earth in groundwater defluoridation: towards fluorosis mitigation," *Journal of Environmental Science and Health, Part A: Toxic/Hazardous Substances & Environmental Engineering*, vol. 51, no. 10, pp. 810–824, 2016.

Hindawi
Journal of Nanomaterials
Volume 2019, Article ID 4576135, 12 pages
https://doi.org/10.1155/2019/4576135

Research Article

A Green and Facile Approach for Synthesis of Starch-Pectin Magnetite Nanoparticles and Application by Removal of Methylene Blue from Textile Effluent

Mih Venasius Nsom,[1] **Ekane Peter Etape**,[1] **Josepha Foba Tendo**,[1] **Beckley Victorine Namond**,[1] **Paul T. Chongwain**,[1] **Mbom Divine Yufanyi**,[2] **and Nzegge William**[1]

[1]*Faculty of Science, Department of Chemistry, University of Buea, Cameroon*
[2]*Faculty of Science, Department of Chemistry, University of Bamenda, Cameroon*

Correspondence should be addressed to Mih Venasius Nsom; mihvenasius1@gmail.com

Received 9 March 2019; Revised 14 June 2019; Accepted 17 July 2019; Published 19 August 2019

Guest Editor: Soubantika Palchoudhury

Pectin-starch magnetite hybrid nanoparticles were fabricated, characterized, and evaluated as potential absorbents for methylene blue dye based on recycling water from the textile industry. The nanocomposite adsorbent was synthesized with the iron salt coprecipitation method, and the precipitates obtained were sponge-like. The effects of a pectin : starch ratio in the absorbent and the amount of methylene blue adsorbed were investigated. The nanocomposites obtained were characterized using a Fourier-transform infrared spectroscopy (FTIR), before and after methylene blue adsorption. Fourier-transform infrared spectroscopy (FTIR) spectra provided the evidence that the starch-pectin iron oxide hybrid nanoparticles were successfully synthesized. It also indicated that the hybrid nanoparticles actually absorbed the methylene blue dye from the effluent. PXRD results showed that the synthesized hybrid composite adopted the spinel microstructure of Fe_3O_4 though the crystallinity of the composite decreased with an increase in the pectin : starch ratio. Furthermore, calculations based on PXRD showed that the synthesized powders were nanoparticles. The amount of adsorbed dye by hybrid adsorbent increased with an increase in the starch : pectin ratio, and the increase was better observed at a low polymer concentration of 18%. The amount of adsorbed dye by hybrid adsorbent was high at high pH and low at low pH value which attested to the ion exchange and electrostatic force mechanism during the adsorption process. Finally, the capacity of the absorbent decreased with an increase in temperature.

1. Introduction

Day-to-day human activities (domestic and industrial) influence the flow, storage, and quality of available fresh water. Industries have a large potential to cause lake, stream, and river pollution. The nature of pollution varies from one industry to another and from one plant to another [1]. Dye-containing wastewaters from the textile industry are an important cause of severe pollution problems worldwide [1]. Effluents containing dyes are usually coloured, and the breakdown products of dyes are toxic as well as carcinogenic or mutagenic by virtue of the presence of benzidine, naphthalene, and other aromatic compounds [1]. High concentrations of textile dyes in water bodies reduce the reoxygenation capacity of the receiving water and cut off sunlight thereby upsetting biological activities such as photosynthesis in aquatic organisms. Toxicity and mutagenicity of synthetic dyes have increasingly become a major occupational hazard and challenge with regard to their use and safety in the textile industry [2]. Textile printing and dyeing industries such as Cotonniere Industrielle du Cameroun (CICAM) in Douala, Cameroon, are water-intensive and require large volumes of freshwater at various steps of printing which lead to the release of large volume of wastewater. The wastewater, if treated, can be recycled into the industries and the neighboring communities. The effluents from the wastewater usually

contain suspended solids such as azoic, indigo and aniline, bleaching agents, salts, acids/alkalis, and heavy metals and have a high biological oxygen demand (BOD) and chemical oxygen demand (COD) [3]. The first contaminant to be recognized in such wastewater is colour. The presence of small amounts of dyes in water is very visible and undesirable. Thus, the decolourisation of wastewater is a major environmental concern because dyes prevent light penetration and reduce photosynthetic activities of water plants. Methylene blue is one of the commonly used dyes. On inhalation, it can give rise to short periods of rapid or difficult breathing while ingestion through the mouth produces a burning sensation and may cause nausea, vomiting, diarrhoea, and gastritis [4]. Many physicochemical methods such as adsorption, irradiation-oxidation, precipitation, and ion exchange have been used for the removal of dyes from wastewater.

Among all these physicochemical methods, adsorption is known to be the most popular technique due to the ease of operation, the comparable low-cost of application, and the high-quality of the treated effluents especially for well-designed sorption processes [5].

Activated carbon is widely used as an adsorbent (because of its high performance) for the removal of dyes from industrial wastewater [6]. However, commercially available activated carbon is very expensive, and the high cost of the method of dye removal from wastewater is a major problem to developing countries. There is therefore the need for the development of adsorbents which exhibit good adsorption capacities from locally available low-cost materials. Agricultural waste materials are cheaper and represent renewable sources [4] which have proven to be useful alternative adsorbents to high-priced commercial activated carbon. Chemical modifications have been made on some of these agricultural waste adsorbents to enhance their adsorption capacities and consequential usefulness in the treatment of wastewater [7]. Biopolymers extracted from various sources of biomass including agricultural waste have also been investigated intensively. Alginates, chitosan, and pectin have all been shown to have variable adsorption capacities [8, 9]. Their adsorption abilities are attributed to hydroxyl and carboxylate groups. These biopolymers are however highly biodegradable and do not have adequate strength and physical stability required for good adsorption. Starch is a biopolymer with hydroxyl functional groups only, and no data is available on its adsorption capacity. It can be extracted from agricultural waste in large quantities using low-cost methods. A common approach to improve the mechanical, chemical, and physical performance of biopolymers is to incorporate oxide particles which also have adsorption properties. Traditional oxides used as adsorbents include alumina, silica, and aluminosilicates [7, 10]. Recently, magnetic oxide adsorbents have attracted a lot of interest because of the possibility of using magnetic fields to facilitate the separation of adsorbent from treated waters [6]. The most important oxide particles in this regard are the superparamagnetic magnetite, maghemite, and hematite nanoparticles. However, iron-oxide nanoparticles are easily oxidised and difficult to handle. This problem has been overcome by coating the particles with more stable polymer sheaths. Biopolymers are particularly interesting because of their biocompatibility, biodegradability, and nontoxicity [11].

Chitosan, a natural polysaccharide with many useful characteristics such as hydrophilicity, antibacterial properties, and affinity for heavy metal ions, has been used to show that the covalent attachment of carboxymethylchitosan at the surface of magnetite nanoparticles through the carboxylate function makes it efficient in the fast removal of Co^{2+} and Cu^{2+} ions from aqueous solutions [12]. Coating improves the surface properties and increases stability of adsorbents. Pectin-coated iron oxide magnetic nanocomposite has been tested and proven to be an effective adsorbent for Cu (II) removal [5]. The coated iron oxide magnetic nanocomposite has been considered competent for removing different types of contaminants from water because of their high sorption, fast removal capabilities, and easy isolation methods in an aqueous medium. The nanomaterials are preferred because they have the adsorption properties of pectin and magnetic properties of iron oxide. Coprecipitation followed by its encapsulation with pectin and cross-linking with calcium ions has been employed to produce pectin-coated iron oxide magnetic nanostructured hybrid [13]. A binding method using glutaraldehyde and adipic acid has been used to synthesize pectin-iron oxide magnetic nanocomposite, and the adsorption behavior of the pectin-iron oxide magnetic adsorbent has been investigated for the removal of methylene blue from aqueous solution [5, 14]. Iron oxide-based composites are of particular interest because of the possibility to synthesize large quantities of superparamagnetic hybrid nanoparticles using a one-step facile synthetic method. Their superparamagnetism offers the possibility of using them for targeted delivery of active molecules as well as adsorbents because of the ease of separation under the influence of a magnetic field. However, low-cost ecofriendly treatment solutions that use biomass as adsorbents are of special interest. In Cameroon, there are both small and large scale operations that make use of dyes and need low cost effective adsorbents to clean their operations. Our interest in replacing either partially or wholly the pectin in the pectin-iron oxide with starch is to respond to this need. Starch is a waste product obtained from processing staple food such as cassava. Starch has the –OH functional group but not the –COOH (found in pectin), and no work has been done with a starch hybrid matrix. Our investigation seeks to establish and understand the effect of replacing pectin with starch on the structure of the nanocomposite and adsorption capacity.

2. Experimental Details

2.1. Chemicals. Hydrated ferrous chloride ($FeCl_2{\cdot}XH_2O$) from Loba Chemie PVT. LTD, Mumbai (India), hydrated ferric chloride ($FeCl_3{\cdot}6H_2O$) from J.T. Baker Chemical CO, Phillipsburb, N.J., ammonia solution from Fisons science equipment, hydrochloric acid and pectin (D-galacturonic acid) from Sigma-Aldrich, starch (native) from the Douala market, and methylene blue from Merck were of analytical grade and used without further purification.

Table 1: Variation of pectin (P) to starch (S) ratios.

Final polymer conc. (%)	P : S	Volume of pectin used (mL)	Volume of starch used (mL)	Total volume of P/S mix	Volume of Fe^{3+}/Fe^{2+} used (mL)	Volume of ammonia added (mL)	Code
0.18	1 : 2	100	200	300	60	120	MV001_NP
0.18	1 : 4	50	200	250	50	110	MV002_NP
0.18	1 : 9	30	270	300	60	120	MV003_NP
0.86	1 : 2	100	200	300	60	140	MV004_NP
0.86	1 : 4	50	200	250	50	110	MV005_NP
0.86	1 : 9	30	270	300	60	120	MV006_NP
0.86	1 : 0	20	—	20	4	50	MV007_NP

2.2. Methodology. The synthesis of the Fe_3O_4-starch-pectin-nano-hybrid composites was carried out at room temperature without purging as is usually the case with the synthesis of iron oxide nanocomposites. Methylene blue was chosen as a model dye due to its well-known characteristics such as its relative stability compared with other dyes and strong adsorption onto solids. The use of ammonia solution was for amidation of the pectin and to cause deesterification reaction at the polymer esterified group during the coprecipitation of iron ions so as to provide more binding sites for magnetite nanocomposites. The method used in this study involved the coprecipitation of two iron salts $FeCl_3{\cdot}6H_2O$ and $FeCl_2{\cdot}4H_2O$, both prepared in HCl, with the consequent addition of NH_4OH solution with vigorous stirring at room temperature [14]. The shift of the initially orange colour of the solution to black indicated the formation of magnetite particles and the reaction is illustrated in equation (1).

$$2FeCl_3(s) + FeCl_2(s) + 8NH_3(aq) + 4H_2O(s) \rightarrow Fe_3O_4(s) + 8NH_4Cl(s) \quad (1)$$

The synthesis of Fe_3O_4 using the coprecipitation method in the presence of starch/pectin mixture is expected to initiate the covalent linkage instantaneously which should prevent further particle growth, resulting in starch/pectin-coated ferrite composites with a closer control over a particle size.

2.3. Synthesis of Starch-Pectin Magnetite Nanohybrid Composites. A 10% (*w*/*v*) pectin solution was prepared by dissolving 6 g of pectin powder into hot distilled water at 60°C while stirring to ensure complete dissolution. The volume of the solution was made up to 60 mL. From the 10% pectin solution, 9 mL was measured into 500 mL volumetric flask and made up to the mark with distilled water to give a concentration of 0.18% pectin solution while a 0.86% pectin solution was prepared by measuring 17.2 mL of the 10% pectin solution into a volumetric flask and diluting with distilled water to 200 mL. A 10% (*w*/*v*) starch solution was prepared by dissolving 10 g of powder starch in 100 mL of hot distilled water at 60°C while stirring to ensure homogeneity. A 0.18% starch solution was prepared by diluting with distilled water, 13.5 mL of the 10% (w/v) starch solution to 750 mL in a capacity flask, while a 0.86% starch solution was prepared by diluting with distilled water, 51.6 mL of the 10% (w/v) starch to 750 mL in another flask. The Fe^{3+}/Fe^{2+} mixture was prepared by dissolving 31.2 g of ferric chloride in 75 ml of hot distilled water at 60°C acidified with HCl to pH 4 and stirred till complete dissolution. The solution was filtered, 12 g of ferrous chloride was added to the filtrate, and the solution was diluted to 200 mL using distilled water. 10% (*v*/*v*) ammonia solution was prepared by measuring 67.6 mL of 33% NH_3 solution into a volumetric flask and diluted with distilled water to 250 mL. Table 1 summarizes how the ratios of pectin to starch were varied.

2.4. Characterization Techniques. In order to establish the various functional groups present and the possible alterations after synthesis and methylene blue adsorption, FTIR spectra were recorded in the middle infrared (4500 cm^{-1} to 500 cm^{-1}) on Shimadzu Prestige 21 with a resolution of 4 cm^{-1} in the absorbance mode for 8 to 128 scans at room temperature. The ASCI data were plotted using OriginLab 7.0 software while the TGA were carried out using a Pyris 6 Perkin-Elmer TGA 4000-Thermal Analyzer under nitrogen atmosphere with a flow rate of 20 mL/min and temperature range of 10°C to 900°C at an increase rate of 10°C/min. The determination of the microstructure was carried out by powder X-ray diffraction measurements (PXRD). The PXRD patterns of composite were recorded on a Philips PWO4 Xpert pro X-ray diffractometer. The X-ray source was Cu-Kα with a voltage of 40 kV and a current of 30 mA. The measurement was in the scanning range of 0–80 at a scanning speed of 50 s^{-1}.

The concentrations of methylene blue solutions were analyzed by measuring their absorbance at 662 nm on a Perkin-Elmer UV/Vis spectrophotometer. This wavelength corresponds to the maximum absorption peak of the methylene blue monomer [15].

3. Results and Discussion

3.1. Appearances and Texture of Composites. The physical appearances of the synthesized composites are shown in Table 2, and the results indicated that the rigidity of the composites increased with an increase in the polymer concentration which may be attributed to intermolecular hydrogen bonds. This in effect reduces the stability of the nanopowders and a consequent reduction in the efficiency due size effect.

Table 2: Appearances of the composites synthesized.

Code	Visual inspection and other remarks on composites
MV001_NP, MV002_NP, MV003_NP	Black, loose, easy to crush, and gradually turns brownish on exposure to air
MV004_NP	Black, most gelling, strong, very difficult to crush, and remains black even after exposure to air
MV005_NP, MV006_NP	Gelling, strong, difficult to crush, and remains black even after exposure to air
MV007_NP	Gelling, strong, very difficult to crush, and remains black even after exposure to air

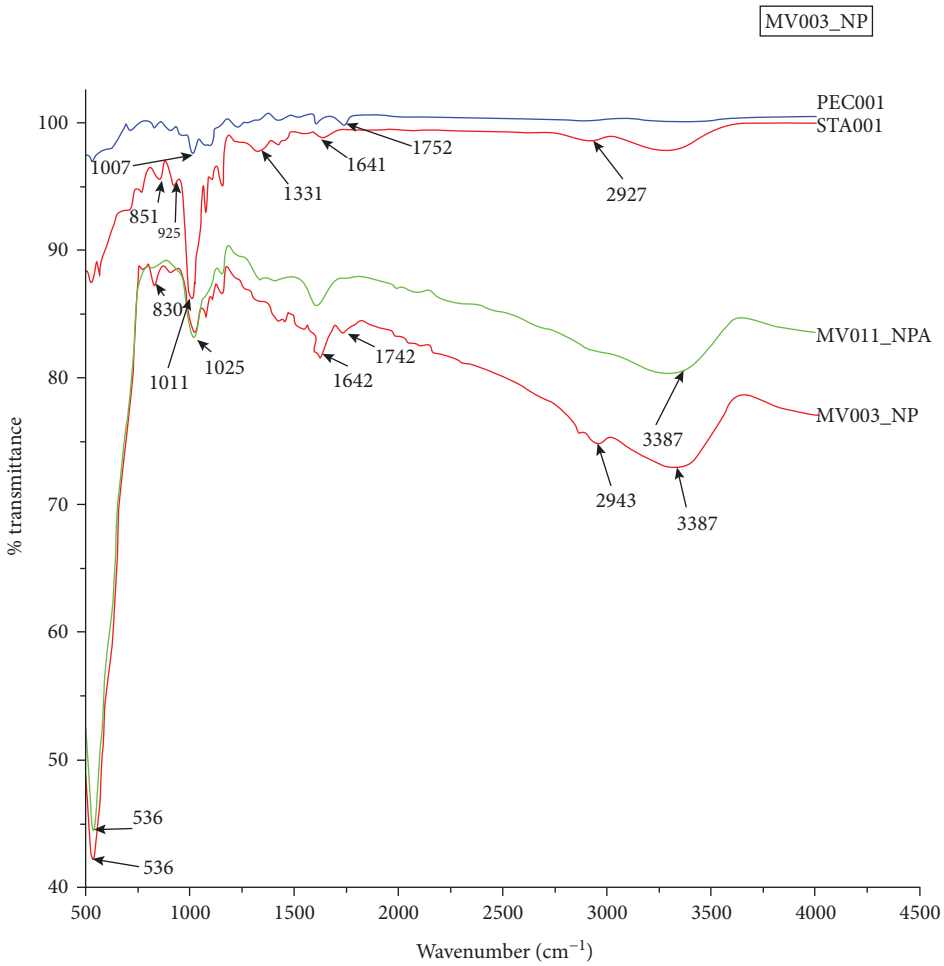

Figure 1: FT-IR spectrum of MV003_NP (composites with a starch/pectin ratio of 1 : 9 at polymer concentration of 0.18%) hybrid composites before (MV003_NP) and after (MV011_NP) adsorption.

3.2. PXRD. The PXRD patterns of the synthesized samples are shown in Figure 1. The samples MV002_NP and MV003_NP showed a diffraction peak at $2\theta = 30.2^{\circ}$, 35.5°, 43.1°, 57.0°, and 62.4° which were assigned to (220), (311), (400), (511), and (440) lattice planes of the cubic structure. Among the peaks, the diffraction at the angle $2\theta = 35.5^{\circ}$ could be attributed to Fe_3O_4, face-centered cubic structure which matched with JCPDS card no. 85 1436/JCPDS card no. 19-0629. The only crystalline peak that expressed itself in samples MV001_NP, MV004_NP, MV005_NP, and MV006_NP was the 2θ, 35.5°. This indicated that the crystallinity of the samples reduced with an increase in the polymer concentration which modified the microstructure of the iron oxide by making it more amorphous. This also indicated that there was the formation of an inverse spinel structure with a pure magnetite phase which persisted even in the presence of starch particles. The absence of any other peak demonstrated the homogeneity of the iron oxide phase.

The crystallite sizes of the composite particles were determined using Debye-Scherrer's equation which measures the size of particles according to broadening of the most intense peak (311) in the PXRD profile shown in Figure 2.

$$D = \frac{k\lambda}{\beta \cos \theta}, \tag{2}$$

where k is a dimensionless shape factor, λ is the X-ray wavelength, β is the line broadening at half the maximum intensity (FWHM), and θ is the Bragg angle.

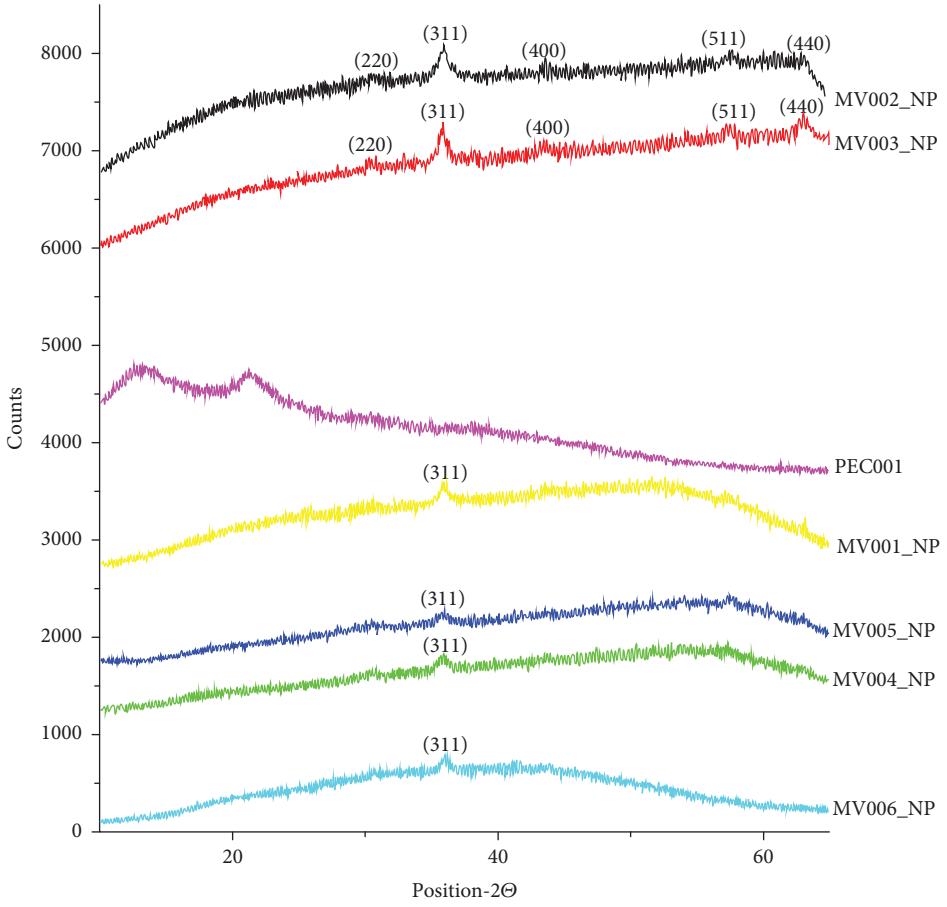

Figure 2: PXRD profiles for pectin (PEC001), composites with a starch/pectin ratio of 1 : 2, 1 : 4, and 1 : 9 at polymer concentration of 0.18% (MV001_NP, MV002_NP, and MV003_NP, respectively) and composites with a starch/pectin ratio of 1 : 2, 1 : 4, and 1 : 9 at polymer concentration of 0.86% (MV004_NP, MV005_NP, and MV006_NP, respectively).

Crystal sizes of the synthesized samples (magnetite Fe3O4) as shown in Table 3 indicated that the average particle sizes were all in the nanorange.

3.3. Fourier-Transformed Infrared (FT-IR) Spectrum Characterization. The FT-IR observed and assigned peaks are represented in Table 4 while the profiles of MV001_NP, MV002_NP, MV003_NP, MV004_NP, MV005_NP, and MV006_NP (hybrid composites before adsorption) and MV009_PN, MV010_NP, MV011_NP, MV012_NP, MV013_NP, and MV014_NP (hybrid composites after adsorption) are shown in (Figures 1, 3–7).

The spectra of PEC001 and STA001 represent the profiles of pectin and starch samples, respectively. Pectin shows peaks at 3309 cm^{-1} and 2951 cm^{-1} attributed to secondary hydroxyl groups while the one at 1750 cm^{-1} is a characteristic peak of pectin, associated with the carbonyl of the esterified pendant group [16]. The intense peak at 1011 cm^{-1} (for both PEC001 and STA001) is attributed to the glycosidic bond linking two galacturonic sugar units together. The peak at 1089 cm^{-1} is associated with the C-O stretched of secondary alcohols while the peak at 1386 cm^{-1} is assigned to the C-H bend of methyl groups. Comparison between the FTIR profiles of PEC001 (Pectin), STA001 (starch), and hybrid composites (MV001_NP, MV002_NP, MV003_NP, MV004_NP, MV005_NP, and MV006_NP) indicated the presence of new peaks at 552 cm^{-1}, 1593 cm^{-1}, and 1426 cm^{-1}. The peak at 552 cm^{-1} was attributed to the Fe-O bond vibration of Fe_3O_4 while those at 1593 cm^{-1} and 1426 cm^{-1} were attributed to the symmetric and asymmetric carboxylate-metal (COO-Fe) linkage. No changes in intensity and position of the peak at 552 cm^{-1} were recorded in the various samples which was an indication that the Fe-O bond of Fe_3O_4 was not affected during the adsorption process. The great reduction in the intensity of the peak at 1011 cm^{-1} attributed to the formation of the composites indicated that there was some interaction

Table 3: Average particle sizes.

Sample	Size (nm)
MV001_NP	10.6
MV002_NP	9.1
MV003_NP	10.2
MV004_NP	9.8
MV005_NP	9.8
MV006_NP	10.7

Table 4: Observed and assigned peaks with references indicated.

Observed peak (cm^{-1})	Assignment	Reference
1737	C=O (characteristic peak of pectin esterified pendant group)	[14]
536	Fe-O bond vibration of Fe_3O_4	[17]
1404	-CH bending of CH_2 groups	[18]
1594	Asymmetric v(C=O) vibration	[19]
2938	-CH stretching of CH_2 group vibration	[18]
1325	-CH_2 scissoring	[18]
1389 1579-1594	Symmetric and asymmetric stretching of carboxylate-metal (-COO-Fe)	[14, 19]
1074-1142	v(C-O) of -CH-OH in aliphatic cyclic secondary alcohols	[18]
1641	v(C=O) stretching vibration peak	[18]
1010-1017	C-O-C glycosidic bond linking monosaccharaides in starch and galacturonic acid in pectin	[14]
1626 and 3150	Presence of hydroxyl groups on the surface of nanoparticles	[19]

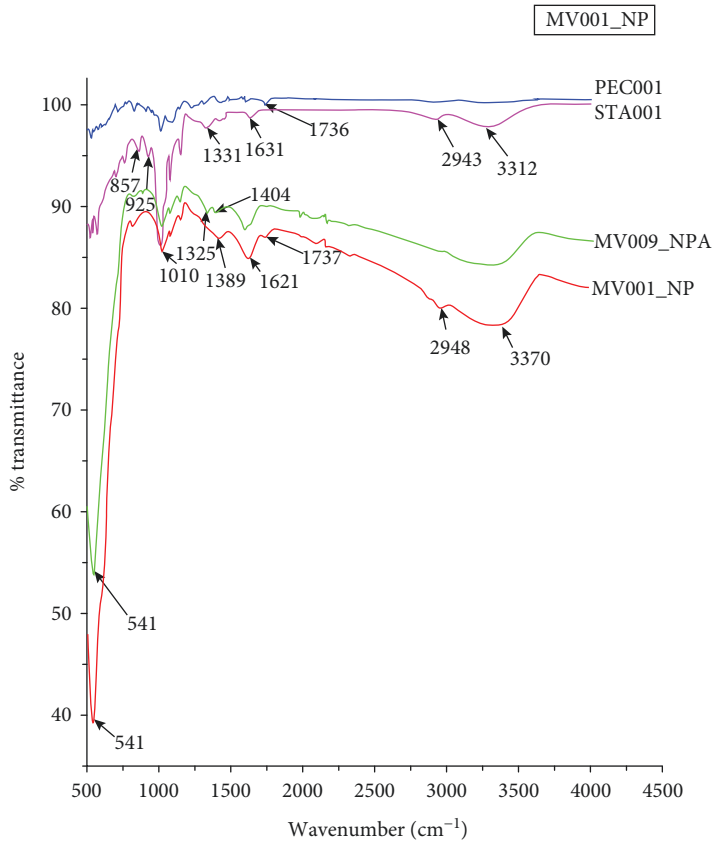

Figure 3: FT-IR spectrum of MV001_NP (composites with a starch/pectin ratio of 1 : 2 at polymer concentration of 0.18%) hybrid composites before (MV001_NP) and after (MP009_NP) adsorption.

at the level of the glycosidic bond while the reduction in peak intensity at 1742 cm^{-1}, absent in some spectra, is probably due to deesterification of the ester group along the pectin polymeric chain. The other reduction in peak intensity at 1011 cm^{-1} in all the spectra indicated an interaction of the atoms involved in the glycosidic bond with atoms of the dye.

After methylene blue adsorption, a new peak appeared at 1340 cm^{-1} and could be attributed to the Fe–S vibration which brought about the reduction in the peak intensity at 1426 cm^{-1}. Comparison between the FTIR profiles of MV001_NP, MV002_NP, and MV003_NP and hybrid composites before adsorption (MV004_NP, MV005_NP, and MV006_NP) on the one hand and hybrid composites after adsorption (MV009_PN, MP009_NP, MV010_NP, MV011_NP, MV012_NP, MV013_NP, and MV014_NP) on the other hand, as shown in Figures 1, 3–7, indicated broadening of the band with a peak at 3299 cm^{-1}. This change could be attributed to intermolecular hydrogen bonding between

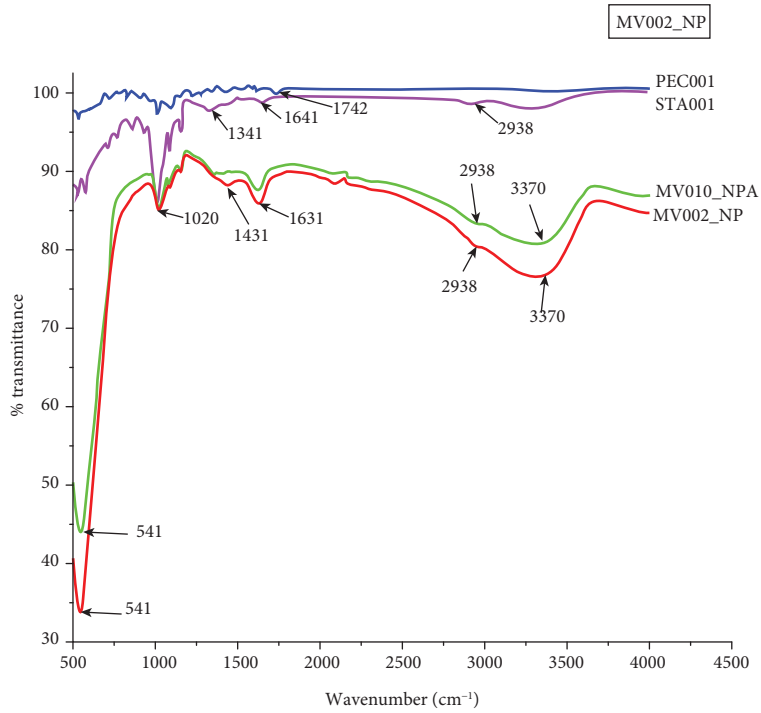

Figure 4: FT-IR spectrum of MV002_NP (composites with a starch/pectin ratio of 1 : 4 at polymer concentration of 0.18%) hybrid composites before (MN002_NP) and after (MV010_NP) adsorption.

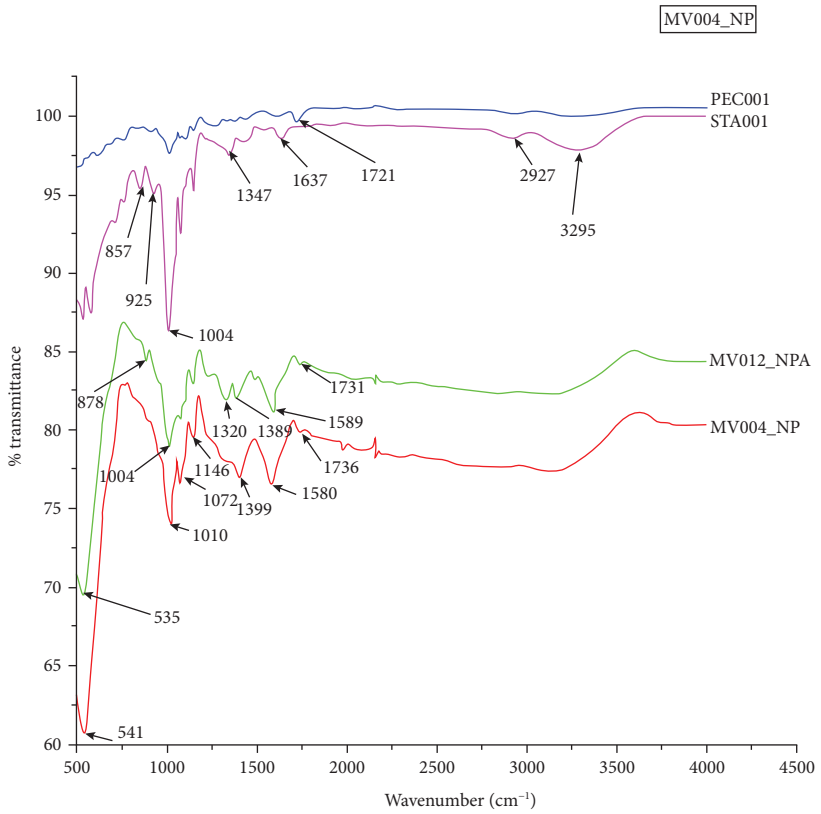

Figure 5: FT-IR spectrum of MV004_NP (composites with a starch/pectin ratio of 1 : 2 at polymer concentration of 0.86%) hybrid composites before (MV004_NP) and after (MV012_NP) adsorption.

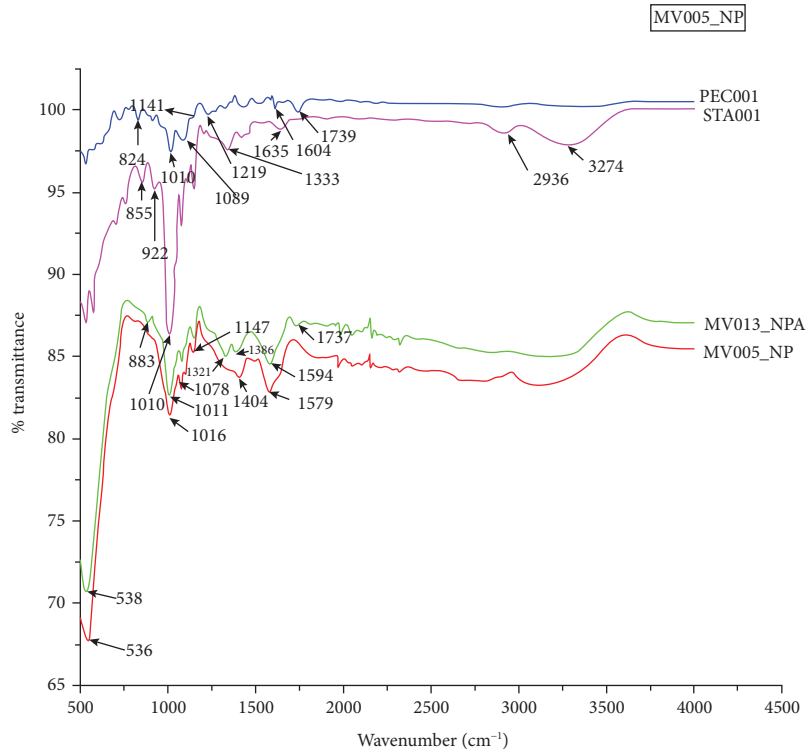

Figure 6: FT-IR spectrum of MV005_NP (composites with a starch/pectin ratio of 1 : 4 of polymer concentration of 0.86%) hybrid composites before (MV005_NP) and after (MV013_NP) adsorption.

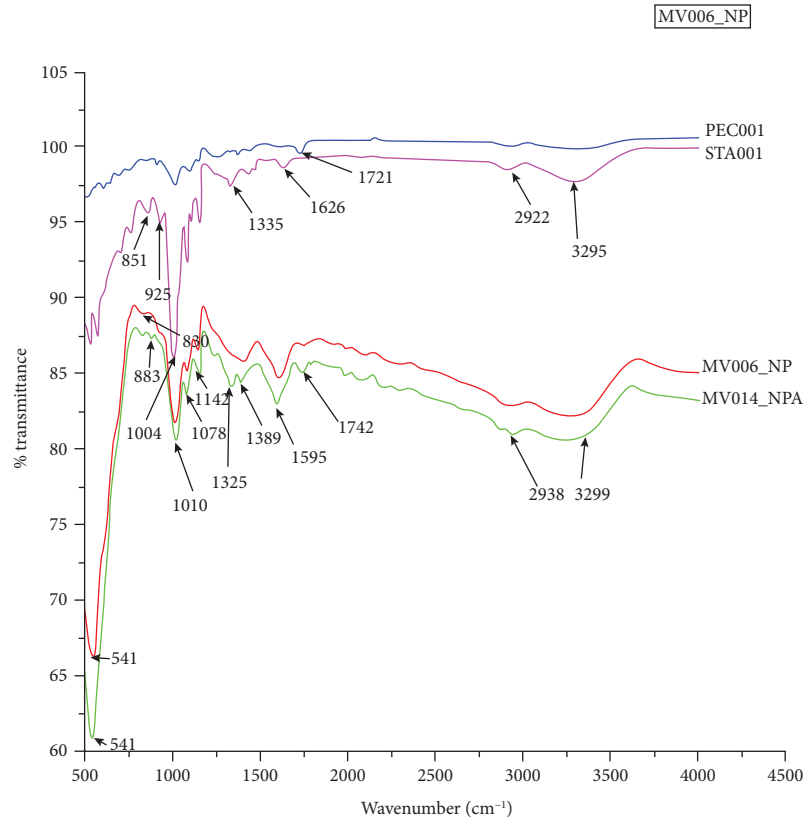

Figure 7: FT-IR spectrum of MV006_NP (composites with a starch/pectin ratio of 1 : 9 of polymer concentration of 0.86%) hybrid composites before (MV006_NP) and after (MV014_NP) adsorption.

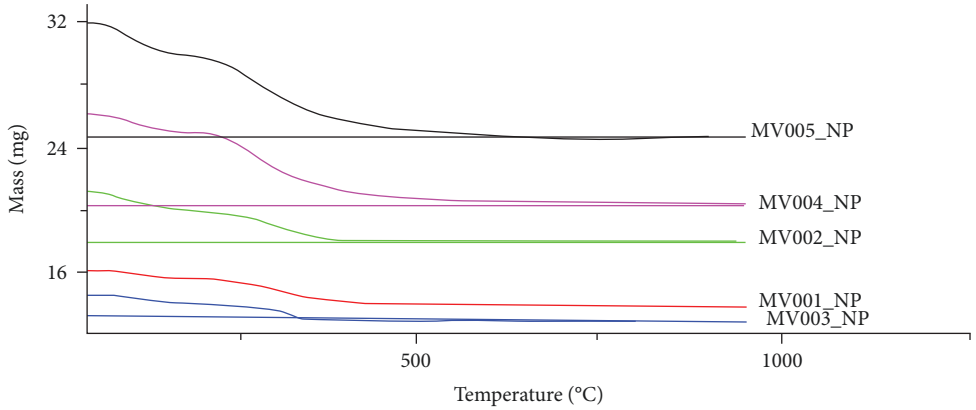

Figure 8: TGA profiles of samples (composites with a starch/pectin ratio of polymer concentration).

Table 5: Decomposition temperature and weight loss percentages.

Sample	First weight loss portion (%)	Second Wt. loss (%)	Residual Wt. (%)	Decomposition temp. (°C)
MV001_NP	2.56	9.19	88.25	375
MV002_NP	5.58	8.85	85.57	375
MV003_NP	3.44	7.64	88.92	375
MV004_NP	5.27	16.81	77.92	525
MV005_NP	7.48	15.86	76.66	525

neighboring hybrid composite and newly introduced methylene blue molecules.

The level broadening varies with the pectin : starch ratio in the hybrid composite but was indifferent to the polymer : - oxide ratio. This suggests that the adsorbent efficiency of the NPs was a function of the pectin : starch ratio in the hybrid composite.

3.4. Thermogravimetric Analysis. The TGA profiles of the hybrid pectin-starch magnetite shown in Figure 8 and weight loss percentages in Table 5 reveal two weight loss portions. The first portion at a temperature of about 102°C and corresponding to the range 2.5 - 7.5% is attributed to water of crystallization. The second weight loss portion which occurs between 250°C and 550°C corresponds to the decomposition of the hybrid with the breakage of the glycosidic bonds. The final percentage by weight of the residue which varies with the polymer concentration corresponds to iron oxide (magnetite (Fe_3O_4)) nanoparticles.

3.5. The Influence of Polymer/Oxide and Pectin/Starch Ratios and Amount of Oxide on Methylene Blue Adsorption. The variation of methylene adsorption against polymer/oxide and pectin/starch ratios and amount of oxide is shown in Table 6. The results indicated that neither the polymer : oxide ratio nor the amount of oxide present in the hybrid composite had a direct effect on the amount of methylene blue dye adsorbed. Instead, the amount of dye adsorbed by the adsorbent complex is a function of the pectin : starch ratio in the hybrid composite.

3.6. The Influence of a Pectin/Starch Ratio on Methylene Blue Adsorption. The influence of a pectin : starch ratio on methylene blue adsorption for all the samples is shown in Tables 7 and 8 and represented in Figure 9.The results revealed that the percentage of methylene blue adsorbed increased with an increase in the pectin/starch ratio. The efficiency of the absorbent reached maximum at a pectin/starch ratio of 0.50 at ambient temperature while the increase in the polymer concentration decreased the efficiency of the adsorbent which could be accounted for by the shielding effect of the constituent polymer atoms on the pores on the adsorbent.

For either polymer concentrations, 0.18 and 0.86, it was observed that a certain minimum amount of pectin was needed to maximize the adsorption of methylene blue by the adsorbents which was an indication that pectin was acting as a stabilizing agent. To determine the percentage of the dye adsorbed, the following equation was used:

$$\%\ \text{of methylene blue adsorbed} = \frac{C_o - C_f}{C_o} \times 100, \quad (3)$$

where C_o and C_f represent the initial and C_o equilibrium concentrations, respectively.

To further evaluate the percentage of methylene blue adsorbed by the pectin/starch hybrid magnetite nanocomposite, work was done with larger batches of sample and the results obtained are as presented in Table 8. These results conformed to those obtained using smaller quantities as shown in Table 7.

3.7. Influence of pH on Composite Adsorption of Methylene Blue. The results for raising the pH from 6 to 8 for MV006_NP are as shown in Table 9 and Figure 10. The

Table 6: Showing polymer/oxide and pectin/starch ratios, amount of oxide, and methylene blue adsorption.

Code	Polymer : oxide ratio	Pectin : starch ratio	Amount of Fe_3O_4 in hybrid	Methylene blue adsorption
MV001_NP	0.11	0.35	0.06	90.3
MV002_NP	0.11	0.22	0.08	44.7
MV003_NP	0.09	0.25	0.06	48.3
MV004_NP	0.22	0.48	0.09	83.3
MV005_NP	0.21	0.52	0.11	97.1

Table 7: Methylene blue adsorption by the starch-pectin magnetite nanocomposites MV001_NP, MV002_NP, MV003_NP, MV004_NP, MV005_NP, MV006_NP, and MV007_NP.

Sample	Concentration of polymer	P : S ratio	C_o	C_f	% of dye removed	% S.D.	% error
MV001_NP	0.18	0.36	25	2.43	90.3	1.53	1.70
MV002_NP	0.18	0.20	25	13.82	44.7	6.08	13.6
MV003_NP	0.18	0.22	25	12.92	48.3	3.97	8.22
MV004_NP	0.86	0.47	25	4.18	83.3	1.24	1.50
MV005_NP	0.86	0.52	25	0.72	97.1	1.04	1.07
MV006_NP	0.86	0.45	25	4.09	83.6	1.88	2.25
MV007_NP	0.86	1	25	0.31	98.7	0.64	0.65

Table 8: Results of batch trials done with larger amounts of adsorbents in larger volumes of dye solution.

Sample	Concentration of polymer	P : S ratio	C_o	C_f	% of dye removed	% S.D.	% error
MV001_NP	0.18	0.36	25	2.50	90.0	0.34	0.37
MV002_NP	0.18	0.20	25	12.04	51.8	0.25	0.49
MV003_NP	0.18	0.22	25	11.55	53.8	0.12	0.21
MV004_NP	0.86	0.47	25	4.45	82.2	0.45	0.55
MV005_NP	0.86	0.52	25	0.54	97.8	0.25	0.26
MV006_NP	0.86	0.45	25	04.66	81.3	0.33	0.41

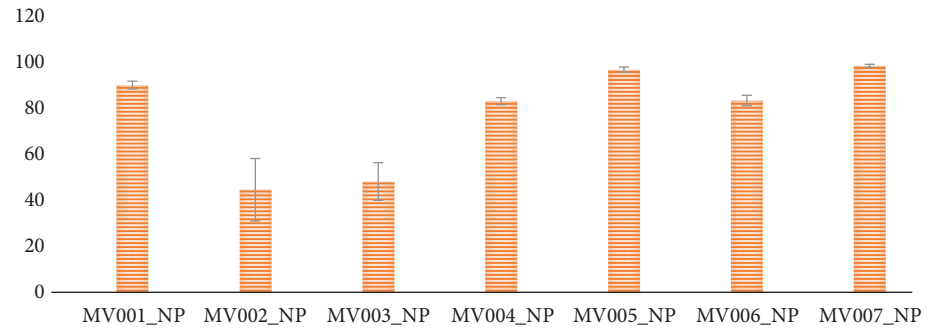

Figure 9: Bar charts showing methylene blue adsorption for various test samples.

Table 9: Influence of pH on composite adsorption of methylene blue.

Sample	pH	Standard deviation (S.D.)	Initial concentration of dye	Final concentration of dye	% adsorption of dye	% S.D.	% error
1	8	0.002	25	2.798	88.81	0.28	0.31
2	6	0.011	25	4.096	83.60	0.33	0.41

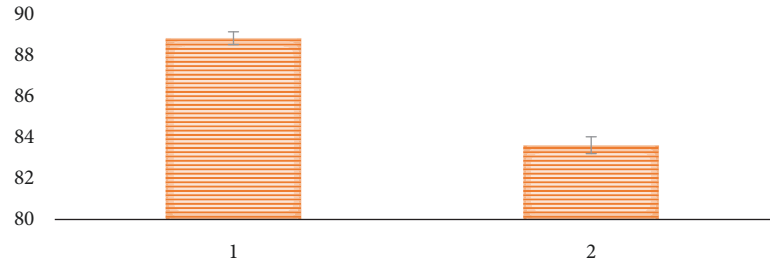

Figure 10: Bar charts showing the influence of pH on % methylene dye adsorption.

adsorption capacity of the samples increased from 83.6% to 88.81% as the pH increased from 6 to 8. Blue 1 and 2 had 100 mL of 25 mg/L of methylene blue +0.5 g of the MV006_NP sample. Methylene blue is a cationic dye, and less sorption at lower pH may be attributed to the competition of H^+ ions with methylene blue ions at sorption sites. Increasing solution pH increased the number of hydroxyl groups, thus increasing the number of negatively charged sites and enlarging the attraction between dye and adsorbent surface. Also, a net positive charge decrease with increasing pH value leads to a decrease in the repulsion between the adsorbent surface and the dye, thus improving the adsorption capacity. This means that at a higher H^+ ion concentration, the adsorbent surface becomes more positively charged, thus reducing the attraction between the adsorbent and the methylene blue ions. In contrast, as the pH increased, more negatively charged surface becomes available, thus facilitating greater dye ion uptake.

3.8. Influence of Temperature Pyrolysis on Methylene Blue Adsorption of Composite. Portions of a sample (MV002) previously heated to 60°C and 180°C were crushed and also used for the adsorption of methylene blue. The results obtained are displayed in Table 10. This was done in order to determine the effect of heat treatment on the adsorption capacity of composites.

Figure 11 shows the influence of temperature pyrolysis on methylene blue adsorption of the composite. It was noticed that the adsorption decreased with an increase in temperature. This can be explained by the fact that the nanomagnetite hybrid composite becomes unstable indicating that the critical coagulation concentration of the hybrid spinel magnetite nanoparticles correlates positively with the surface area. This is indicative of the fact that it is the surface chemistry rather than the bulk property that is dominant in the hybrid. However, the hybrid agglomerate with an increase in temperature by so reducing the effective adsorption capacity of the adsorbent.

4. Conclusion

Single molecular pectin-starch magnetite nanoparticles have been synthesized. The efficiency of the magnetite nanoparticle in removing methylene blue dye from an aqueous solution has been investigated. Results indicate that adsorption is pH and temperature dependent. The efficiency of the

Table 10: Influence of temperature pyrolysis on methylene blue adsorption of composite.

Sample	Initial conc. of dye	Final conc. of dye	% absorbance	% S.D.	% error
MV002_NP (60°C)	25	13.832	44.70	6.08	13.60
MV002 (180°C)	25	12.11	36.94	0.37	1.00

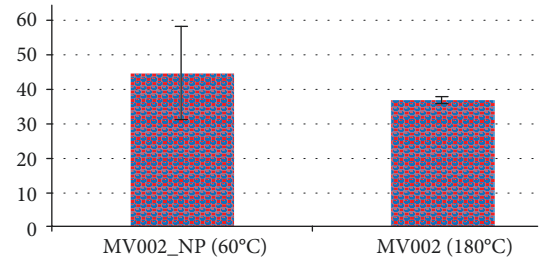

Figure 11: Bar charts showing the influence of temperature pyrolysis on methylene blue adsorption of composite.

absorbent increased with temperature though the hybrid decomposes to the magnetite at temperatures between 250°C and 550°C.

The developed pectin-starch magnetite hybrid not only has demonstrated higher adsorption efficiency especially at a low polymer concentration and starch-pectin ratio of 0.50 at ambient temperature but also has shown additional benefits like ease of synthesis, easy recovery, absence of secondary pollutants, cost-effectiveness, and environmental friendliness. It can be concluded to be a promising advanced adsorbent in environmental pollution cleanup.

Data Availability

All data used to support the findings of this study are included within the article.

Conflicts of Interest

There is no conflict of interest.

References

[1] Z. Carmen and S. Daniela, *Textile Organic Dyes Characteristics, Polluting Effects and Separation/Elimination Procedures from Industrial Effluents – A Critical Overview*, IntechOpen, 2012.

[2] A. P. Wanyama, B. Kiremire, J. E. S. Murumu, and H. Tumusiime, "Toxicological characterization of crude dye extracts derived from Albizia coriaria, Morinda lucida and V itellaria paradoxa selected dye - yielding plants in Uganda," *International Journal of Natural Products Research*, vol. 1, no. 2, pp. 16–20, 2012.

[3] S. Sharma, Kalpana, Arti et al., "Toxicity Assessment of Textile Dye Wastewater Using Swiss Albino Rats," *Australasian Journal of Ecotoxicology*, vol. 13, pp. 81–85, 2007.

[4] E. O. Oyelude and U. R. Owusu, "Adsorption of methylene blue from aqueous solution using acid modified *Calotropis Procera* leaf powder," *Journal of Applied Science and Environmental Sanitation*, vol. 6, no. 4, pp. 477–484, 2011.

[5] J.-L. Gong, X.-Y. Wang, G.-M. Zeng et al., "Copper (II) removal by pectin–iron oxide magnetic nanocomposite adsorbent," *Chemical Engineering Journal*, vol. 185-186, pp. 100–107, 2012.

[6] H. Tavallali and A. Daneshyar, "Modified iron oxide nanoparticles as solid phase extractor for spectrophotometric determination and separation of muroxide," *International Journal of ChemTech Research*, vol. 4, no. 3, pp. 1170–1173, 2012.

[7] A. O. Okewale, B. R. Etuk, and P. K. Igbokwe, "Comparative studies on some starchy adsorbents for the uptake of water from ethanol – water mixtures," *International Journal of Engineering & Technology*, vol. 11, no. 5, 2010.

[8] A. Tiwari and P. Kathane, *Superparamagnetic PVA-alginate microspheres as adsorbent for Cu^{2+} ions removal from aqueous systems*, International Science Congress Association, 2013.

[9] Y. Habibi, L. A. Lucia, and O. J. Rojas, "Cellulose nanocrystals: "chemistry, self-assembly, and applications"," *Chemical Reviews*, vol. 110, no. 6, pp. 3479–3500, 2010.

[10] S. Lin, C. C. Akoh, and A. E. Reynolds, "Determination of optimal conditions for selected adsorbent combinations to recover used frying oils," *Journal of the American Oil Chemists' Society*, vol. 76, no. 6, pp. 739–744, 1999.

[11] D. Le Corre, J. Bras, and A. Dufresne, "Starch nanoparticles: a review," *Biomacromolecules*, vol. 11, no. 5, pp. 1139–1153, 2010.

[12] J. Fresnais, M. Yan, J. Courtois, T. Bostelmann, A. Bée, and J.-F. Berret, "Poly(acrylic acid)-coated iron oxide nanoparticles: quantitative evaluation of the coating properties and applications for the removal of a pollutant dye," *Journal of Colloid and Interface Science*, vol. 395, pp. 24–30, 2013.

[13] S. F. Chin, S. C. Pang, and C. H. Tan, "Green synthesis of magnetite nanoparticles (via thermal decomposition method) with controllable size and shape," *Journal of Materials and Environmental Science*, vol. 2, no. 3, pp. 299–302, 2011.

[14] F.-T. J. Ngenefeme, N. J. Eko, Y. D. Mbom, N. D. Tantoh, and K. W. M. Rui, "A one pot green synthesis and characterisation of iron oxide-pectin hybrid nanocomposite," *Open Journal of Composite Materials*, vol. 3, no. 2, pp. 30–37, 2013.

[15] C. Kaewprasit, E. Hequet, N. Abidi, and J. P. Gourmont, *The Journal of Cotton Science*, vol. 2, pp. 164–173, 1998.

[16] B. Min, J. Lim, S. Ko, K.-G. Lee, S. H. Lee, and S. Lee, *Bioresource Technology*, vol. 102, no. 4, pp. 3855–3860, 2011.

[17] J. Sun, S. Zhou, P. Hou et al., "Synthesis and characterization of biocompatible Fe_3O_4 nanoparticles," *Journal of Biomedical Materials Research Part A*, vol. 80A, no. 2, pp. 333–341, 2007.

[18] R. K. Mishra, A. Anis, S. Mondal, M. Dutt, and A. K. Banthia, "Reparation and characterization of amidated pectin based polymer electrolyte membranes," *Chinese Journal of Polymer Science*, vol. 27, no. 5, pp. 639–646, 2009.

[19] M. Timko, P. Kop£anský, M. Antalik et al., "Magnetism - Magnetic properties of matter Poznan," in *European Conference of Physics and Magnetism*, Poland, 2011.

Hindawi
Journal of Nanomaterials
Volume 2019, Article ID 6890572, 11 pages
https://doi.org/10.1155/2019/6890572

Research Article

Increased Plant Growth with Hematite Nanoparticle Fertilizer Drop and Determining Nanoparticle Uptake in Plants Using Multimodal Approach

Armel Boutchuen,[1] Dell Zimmerman,[1] Nirupam Aich,[2] Arvid Mohammad Masud,[2] Abdollah Arabshahi,[3] and Soubantika Palchoudhury[1]

[1]*Department of Civil and Chemical Engineering, University of Tennessee at Chattanooga, Chattanooga, Tennessee 37403, USA*
[2]*Department of Civil, Structural, and Environmental Engineering, University of Buffalo, Buffalo, New York 14260, USA*
[3]*SimCenter, University of Tennessee at Chattanooga, Chattanooga, Tennessee 37403, USA*

Correspondence should be addressed to Soubantika Palchoudhury; soubantika-palchoudhury@utc.edu

Received 22 February 2019; Accepted 16 May 2019; Published 9 June 2019

Academic Editor: Paulo Cesar Morais

There is an emerging scientific interest in the use of nanoparticle fertilizers for enhanced agricultural and bioenergy crop production to meet the growing food and energy demands of the world. The objective of designing the nanoparticle fertilizers is to effectively deliver the required nutrients for the plants without adding large quantities of fertilizer to the environment. However, most reports on nanoparticle fertilizers so far, involved the addition of nanoparticles to the hydroponic system or the soil. In this study, we report a new modified seed presoak strategy using a drop of Fe-enriching hematite nanoparticle dispersion to enhance plant growth and production in four different legume species, i.e., chickpea, green gram, black bean, and red bean. The hematite nanoparticle fertilizer drop promoted a 230-830% increase in plant growth with green gram showing the highest increase, based on our prolonged and statistically reliable growth studies. In general, we observed an increase in the survival span of plants, a twofold increase in fruit production per plant, nearly two times faster fruit production, and healthy second-generation plants with the nanoparticle treatment; however, there were slight species-specific variations. We used a novel multimodal material characterization approach combining three techniques, hyperspectral imaging, Fourier transform infrared spectroscopy (FTIR), and inductively coupled plasma optical emission spectroscopy (ICP-OES), to evaluate the internalization and transport of the nanoparticle fertilizer within the plants. Our results indicated that the hematite nanoparticles were transported through the roots and stems and were localized in the leaves after 10 days of growth in pots of soil. Therefore, the modified seed presoaking method using a drop of hematite nanoparticle will be highly attractive in enhancing plant growth and health, while minimizing environmental impacts.

1. Introduction

Iron (Fe) is a key element for several cellular reactions in plants such as respiration and the formation of chlorophyll required for photosynthesis. Plants have adopted a mechanism to acquire this essential nutrient from the soil using the apoplastic pathway through the roots, but limited Fe is available in some soil types or in soils with excessive agricultural use [1, 2]. Fe deficiency is known to cause chlorosis in plants [3]. Therefore, Fe-enriching fertilizers are required to ensure optimum Fe delivery to the plants. Recently, there has been a thrust to develop innovative fertilizer formulations like nanoparticle (NP) fertilizers because conventional fertilizers are required in large quantities owing to their slower absorption by the plants [4–6]. The NP fertilizers can facilitate tunable delivery of the required nutrients to the plants. Therefore, NP fertilizers are seen as highly promising candidates for enhanced production of agricultural and bioenergy crops to meet the growing food and energy demands of the world population [5, 7–9].

Recently, Yuan et al. demonstrated a concentration-specific role of Fe NPs in promoting growth in *Capsicum annuum* plants [10]. The Fe NPs increased growth in these plants through reorganization of the leaf, increasing chloroplast per grana stacking, and regulating the vascular tissues within the leaf and stem. Raju et al. reported the role of Fe NPs in increasing the radical length and biomass of green gram sprouts during germination [11]. In the study by Srivastava et al., iron pyrite NPs induced a marked increase in the growth of spinach sprouts [12]. Iron pyrite NPs also facilitated a denser network of roots and a significantly (~2.5 times) higher yield in both chili and marigold plants [13]. These NPs served as a suitable equivalent of nitrogen, phosphorus, and potash fertilizer for the production of rice, a staple food crop [14]. Li et al. demonstrated the stimulated root growth of peanut plants under the influence of Fe NPs [15]. In addition to Fe NPs, iron oxide NPs have also been adopted as Fe-enriching fertilizers to replenish Fe content in plants as they are inherently nontoxic. For example, Jeyasubramanian et al. showed that hematite NPs boosted the growth rate of spinach plants in a slightly acidic hydroponic system via conversion to Fe^{2+} ions [16]. Ren et al. reported increased physiological activity of green gram plants with iron oxide (γ-Fe_2O_3, maghemite) NPs. The NPs translocated through the plant roots to the stem and leaves in this case [17]. In another study, Ghafariyan et al. demonstrated that iron oxide NPs were absorbed and translocated within the soybean plants under hydroponic conditions. The iron oxide NPs boosted chlorophyll production in these plants without showing any toxic impact [18]. Zhu et al. also reported the absence of any toxic impact of iron oxide NPs in pumpkin plants during a prolonged period of exposure [19]. These studies demonstrate the immense potential of iron oxide NPs as Fe-enriching fertilizers and chlorosis treatment agents for agricultural and bioenergy crops. However, most of these methods involved the direct addition of the NP fertilizer to the soil or the hydroponic system, which is less attractive in terms of environmental sustainability. Studies have shown stress response and reduction of amino acids in plants with excess addition of NP fertilizers [20]. There is a need for a new environmental-friendly strategy that increases plant growth with a minimum quantity of the fertilizer while also minimizing the addition of fertilizer to the environment. Recently, we reported a seed presoak strategy where soaking the embryonic seeds of legumes in liquid dispersions of iron oxide NPs showed enhanced root growth by 88-366%, but more than 4 mL of NPs were required for each seed [21]. Minimizing the quantity of NP dispersions required would make the seed presoak strategy more effective for practical applications.

We also need to understand the pathway of internalization, interaction, and translocation of the NP fertilizer within the plant both for risk assessment and for synthesizing high-efficiency NP fertilizers [1, 22–24]. Most plant-NP interaction studies to date have focused on the physiological aspects as it is challenging to find a material characterization method capable of detecting the low concentrations of NPs uptaken within the complex biological matrix of plants [25]. Imaging techniques like optical and electron microscopy have been traditionally used to detect NPs within the plant cells [15, 21, 26, 27]. However, optical microscopy cannot resolve objects less than 250 nm apart due to the diffraction limit of visible light even though it is rapid and requires negligible sample preparation. Electron microscopy can easily resolve nanoscale objects, but the required sample preparation stages such as staining, ultrathin sectioning, sputter-coating, and labeling increase artifacts in the images. Recently, darkfield hyperspectral imaging has emerged as a highly promising visualization tool to both detect and map the localization of NPs within complex microenvironments [28]. The charge-dependent uptake and mobility of Au NPs by the roots of *Arabidopsis thaliana* could be demonstrated using this technique [29]. When combined with an elemental analysis technique like X-ray tomography or mass spectroscopy, hyperspectral imaging provided further reliable insights into plant-NP interactions [29, 30]. Another method requiring minimum sample preparation is FTIR, which has also proven useful in understanding the plant-NP interactions via chemical composition analysis in several reports.

In the present study, we investigated the effectiveness of an Fe-enriching hematite (α-Fe_2O_3) NP fertilizer to boost plant growth and production using four different species of legumes as model plants (i.e., chickpea, green gram, black beans, and red beans). The plants were grown in same-sized pots filled with the same soil type to keep all growth conditions the same other than the NP treatment. A new "modified seed presoak" strategy was investigated to minimize the quantity of NP fertilizer required and to prevent the addition of NPs directly to the soil. Two different concentrations of the hematite NP fertilizer were used to investigate the Fe concentration-dependent growth trend in the plants. Another objective of this study was to develop a multimodal material characterization strategy combining hyperspectral imaging, FTIR, and ICP-OES for gaining insights into the internalization, transport, and localization of the NP fertilizer within the plants. This improved seed presoaking method with one drop of the NP fertilizer will be highly beneficial in promoting enhanced agricultural production in nutrient-deficient environments in a cost-effective and sustainable fashion. The multimodal material characterization strategy will be significant both in understanding the mechanism of plant-NP interactions and risk assessment of the new NP fertilizers.

2. Materials and Methods

2.1. Materials. All reagents were used as purchased. The reagents for NP synthesis included iron (III) acetylacetonate ($Fe(acac)_3$, 99%, Alfa Aesar), polyvinylpyrrolidone (PVP, Mw 10 kDa, TCI, Thermo Fisher Scientific), polyethyleneimine (PEI, Mw 60 kDa, 50% aq, Alfa Aesar), triethylene glycol ($C_6H_{14}O_4$, TREG, 99%, Acros Organics), and deionized water (DI, Thermo Fisher Scientific). Potting soil, pots, and seeds of chickpea (*Cicer arientinum*), green gram or mung bean (*Vigna radiata*), and black and red beans (*Phaseolus vulgaris*) were purchased from local grocery stores in Chattanooga, Tennessee, USA, for plant growth experiments.

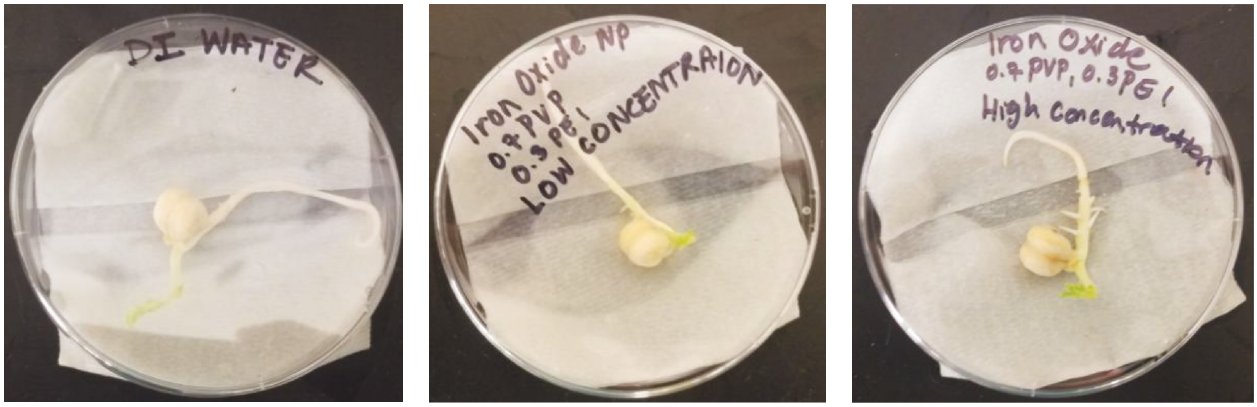

(a) (b) (c)

Figure 1: Images of chickpea seeds treated with a drop of (a) DI water, (b) a drop of low concentration NP fertilizer suspension (0.022 gL^{-1} Fe), and (c) a drop of high concentration NP fertilizer suspension (1.1 gL^{-1} Fe), immediately before planting on day 7.

2.2. Hematite NP Synthesis and Characterization. Hematite (α-Fe_2O_3) NPs were synthesized using a highly reproducible modified polyol synthesis method developed and reported in our earlier studies [21, 31]. In a typical synthesis conducted on a Schlenk line, the $Fe(acac)_3$ iron precursor (2 mmol) was added to a PVP/PEI (PVP, 0.7 g and PEI, 0.3 g) ligand mixture in the solvent, TREG. The reactant mixture was heated at 290°C for 1 h on a heating mantle with magnetic stirring (Thermo Fisher Scientific) under an inert atmosphere to form the hematite NP product. The NPs were cleaned with DI water three times via centrifugation at 14000 rpm (Thermo Fisher Scientific). Transmission electron microscopy and X-ray diffraction characterization of these hematite NPs were reported in our earlier studies [21].

2.3. Hematite NP Growth Dispersion Synthesis and Characterization. Finally, the precipitant hematite NPs were dispersed in DI water via sonication (Branson 1800, room temperature) for 15 min to obtain the target concentrations for use in subsequent plant growth studies. Two NP growth suspensions for plants were prepared with two different hematite NP concentrations, i.e., low NP concentration (0.022 gL^{-1} Fe), and high NP concentration (1.1 gL^{-1} Fe), while DI water without the addition of hematite NPs was used as a control.

The hydrodynamic diameter and zeta potential of the hematite NPs in the growth suspensions were analyzed on a Litesizer 500 Particle Analyzer (Anton Paar), prior to use as fertilizer drop for the legumes. Mean hydrodynamic diameter was reported based on an average of five consecutive runs. Zeta potential measurements were conducted at 25°C using omega cuvettes and reported as an average of five analyses (Figures S1a-b, SI).

2.4. Plant Growth Experiments Using Hematite NP Drop. Four different varieties of legumes, i.e., chickpea or *Cicer arientinum*, green gram or *Vigna radiata*, black beans and red beans or *Phaseolus vulgaris*, of varying seed sizes were used as test plants for our plant growth studies to investigate the general effectiveness of the NP fertilizer. A "modified seed presoak" method was developed to enhance the growth of legumes using a drop of α-Fe_2O_3 NP growth suspension. First, the seeds were cleaned with 75% ethanol and DI water and dried with filter paper for use in the plant growth experiments. In this modified presoak method, each legume seed was placed on a wet paper towel inside a sterilized petri dish (Thermo Fisher Scientific), prior to the addition of one drop of α-Fe_2O_3 NP growth suspension. A set of three petri dishes with the same seed type was prepared for adding three different growth suspensions, i.e., one drop of DI water reference, one drop of a low concentration of hematite NPs (0.022 gL^{-1} Fe), and one drop of a high concentration of hematite NPs (1.1 gL^{-1} Fe), to investigate the applicability of the NP fertilizer in enhancing plant growth. The petri dishes were then loosely closed with lids to retain airflow for the growing seeds. Roots were observed from these seeds within 2-4 days, following which the shoots sprouted. Figure 1 and Figure S2 (SI) show the three sets of seeds for chickpea, green gram, black bean, and red bean immediately before planting. A summary of the experimental parameters used for our plant growth study is presented in Table 1. The three seeds of the same legume species treated with a drop of DI water, a drop of a low concentration of NPs, and a drop of a high concentration of NPs were planted in the same pot as soon as shoots were seen at around day 7. The pot was placed indoor near a window to ensure a controlled environment and access to sunlight. The growth of each plant was subsequently monitored each day by measuring the length of the shoot using a Vernier caliper for a total period of 60-100 days, depending on the species. The experiment was repeated six times for each legume species to ensure statistical reliability. Error bars for the average plant height were reported based on a 95% Student's *t*-distribution.

The NP-treated plants from all legume species except the chickpea produced fruit pods. Seeds were collected from the mature pods and cleaned with 75% ethanol and DI water. These seeds from NP-treated green gram, black bean, and red bean plants were planted in pots of soil and placed near a window, similar to the first generation plants. The second-generation seeds were planted on the same day after collection from the seed pods, without any NP treatment. The growth of the second-generation plants were then

Table 1: Summary of key experimental conditions used to investigate legume growth with hematite NP fertilizer.

Type of legume seeds Germination condition: seeds placed in moist paper towel inside a nearly covered petri dish	Type of suspension used for seed presoaking	No. of seeds tested	Potting conditions	Total time of plant growth monitoring (days)
Green gram Seed size: 4.76 ± 0.2 mm	Reference suspension: DI water (0 gL^{-1} Fe), 1 drop	6	Soil Seeds potted after 7 days of germination Plant placed indoor in sunlight beside the window	60
	Low-concentration suspension: hematite NP fertilizer (0.022 gL^{-1} Fe), 1 drop	6	Soil Seeds potted after 7 days of germination Plant placed indoor in sunlight beside the window	60
	High-concentration suspension: hematite NP fertilizer (1.1 gL^{-1} Fe), 1 drop	6	Soil Seeds potted after 7 days of germination Plant placed indoor in sunlight beside the window	60
Black bean Seed size: 8.50 ± 0.7 mm	Reference suspension: DI water (0 gL^{-1} Fe), 1 drop	6	Soil Seeds potted after 7 days of germination Plant placed indoor in sunlight beside the window	60
	Low-concentration suspension: hematite NP fertilizer (0.022 gL^{-1} Fe), 1 drop	6	Soil Seeds potted after 7 days of germination Plant placed indoor in sunlight beside the window	60
	High-concentration suspension: hematite NP fertilizer (1.1 gL^{-1} Fe), 1 drop	6	Soil Seeds potted after 7 days of germination Plant placed indoor in sunlight beside the window	60
Chickpea Seed size: 9.21 ± 0.7 mm	Reference suspension: DI water (0 gL^{-1} Fe), 1 drop	6	Soil Seeds potted after 7 days of germination Plant placed indoor in sunlight beside the window	100
	Low-concentration suspension: hematite NP fertilizer (0.022 gL^{-1} Fe), 1 drop	6	Soil Seeds potted after 7 days of germination Plant placed indoor in sunlight beside the window	100
	High-concentration suspension: hematite NP fertilizer (1.1 gL^{-1} Fe), 1 drop	6	Soil Seeds potted after 7 days of germination Plant placed indoor in sunlight beside the window	100
Red bean Seed size: 16.82 ± 0.7 mm	Reference suspension: DI water (0 gL^{-1} Fe), 1 drop	6	Soil Seeds potted after 7 days of germination Plant placed indoor in sunlight beside the window	60
	Low-concentration suspension: hematite NP fertilizer (0.022 gL^{-1} Fe), 1 drop	6	Soil Seeds potted after 7 days of germination Plant placed indoor in sunlight beside the window	60
	High-concentration suspension: hematite NP fertilizer (1.1 gL^{-1} Fe), 1 drop	6	Soil Seeds potted after 7 days of germination Plant placed indoor in sunlight beside the window	60

monitored to assess any adverse effect of the NP fertilizer on the next generation of plants.

2.5. Evaluating Plant Uptake of Hematite NPs

2.5.1. Fourier Transform Infrared Spectroscopy. The surface functional groups of the shoot and leaf samples from legumes grown by seed presoaking with hematite NP drops (Figure S1c, SI) were analyzed using a Bruker Alpha Fourier transform infrared (FTIR) spectrometer equipped with attenuated total reflectance (ATR) capability to better understand the role of NP fertilizers in promoting plant growth. Samples for FTIR measurements were prepared by cutting a 2 mm piece of the shoot and leaf from the potted plants after 10 days of growth. FTIR measurements conducted over a range of 400-4000 cm^{-1} were reported as an average of three consecutive measurements for reliability.

2.5.2. Hyperspectral Imaging. The leaf samples from the legume plants as collected were further characterized via CytoViva hyperspectral imaging to investigate the accumulation of the NP fertilizer within the leaf. For hyperspectral imaging, the leaf samples were placed on a standard 1 mm glass slide and covered with a glass cover slip for viewing (Figure S3, SI). The sample images were further analyzed by generating a spectral library from the images and filtering the library against respective images of hematite NP and control leaf samples from plants grown without NP treatment to eliminate false positive signals. The remaining spectral library was then mapped to determine the location of NPs within the leaf samples.

2.5.3. ICP-OES Measurements. Acid digestion of the plant leaves for ICP-OES analysis was carried out following an established protocol [32]. Leaves were collected from all the four species of potted plants after 10 days of growth, except for the green gram plant without NP treatment because the plant did not survive that long. The leaves were air dried at 70°C in an oven for 24 hours. Acid digestion was carried out with 100 mg of dried leaves for all the species. 5 mL of HNO_3 was added to 100 mg of each dried sample (from a specific plant type without or with NP treatment) in a glass vial, and the mixture was left unaltered for 24 hours to allow the reaction to take place. The acidified sample was then heated at 120°C on a hot plate for 1 hour. Four additions of 2 mL H_2O_2 were made after every 15 minutes within a 1-hour period. The digested sample turned colorless at the end of 1 hour and confirmed the completion of the digestion process. The sample was then completely air dried in an oven at 80°C for 48 hours. The dried sample was cooled and dissolved in 3 mL of 10% HCl (*v*/*v*) for 2 hours. This solution was diluted five times with DI water and was used as the stock solution for the ICP-OES measurement.

An iCAP 6000 ICP-OES (Thermo Fisher Scientific) was used to determine the iron content in the plant leaves. A high-purity Argon (Ar) gas was employed as a plasma, auxiliary (0.5 L/min), and nebulizing gas. Before operating with the sample, the ICP-OES was purged with Ar gas for 1 hour. The power of the radio frequency (R.F.) was kept at 1150 W. The sample pump rate was fixed at 50 rpm with a stabilization time of 5 seconds. For iron content determination, the measurements were observed at the most sensitive emission wavelength of 259.9 nm. A standard calibration curve (1-5 ppm) for the known iron concentration was prepared ($R^2 = 0.999$). The end solution from the digestion step was used in ICP-OES to measure the unknown iron concentration by comparing its spectra with that from the calibration curve.

3. Results and Discussion

Iron is an essential element for the generation of chlorophyll in plants. Iron is added in the form of soil fertilizers or chelated compounds in soil-less cultivation to facilitate iron uptake for enhanced production of agricultural and bioenergy crops. Agricultural research facilities and commercial units are investigating innovative formulations of Fe fertilizers such as the Fe micronutrient containing iron and phosphates [33–35]. The two major targets in designing these fertilizers are to significantly increase the plant growth or production and to minimize the addition of excess fertilizers to the soil for environmental sustainability. In this study, we designed a "modified seed presoak" strategy to apply the minimum possible quantity of Fe fertilizer for enhanced plant growth. In this method, the seed was placed on a wet paper towel inside a nearly covered petri dish for germination and one drop of the fertilizer suspension was added to the seed once. The germinated seeds were potted in soil after 7 days. Using this modified seed presoak method, we investigated the role of our new hematite NP fertilizer on the shoot growth of four different species of legumes (e.g., chickpea or *Cicer arientinum*, green gram or *Vigna radiata*, and black beans and red beans or *Phaseolus vulgaris*). Each species of legume seed was treated with a drop of hematite NP fertilizer suspension of three different concentrations: reference suspension (DI water, 0 gL^{-1} Fe), low concentration (0.022 gL^{-1} Fe), and high concentration (1.1 gL^{-1} Fe). Figure 2 shows a schematic representation of the improved seed presoak strategy used in this study to promote enhanced plant growth and production.

The shoot length of each potted legume plant was measured every day for a maximum period of 100 days to determine the efficacy and concentration-dependent effect of the synthesized hematite NP fertilizer on plant growth enhancement. The growth experiments were repeated six times with a new set of seeds for each legume species to predict statistically reliable growth trends. Figure 3 shows representative images of the different legume plants treated with different NP suspensions at the end of the growth study and also the corresponding time-dependent plant growth plots.

As seen from the images, all three chickpea plants showed healthy growth, but the growth height of plants treated with a drop of high-concentration hematite NP fertilizer was 230% higher than the control DI water plant. The chickpea plants treated with a drop of low-concentration hematite NP fertilizer also grew 206% higher than the control DI water plant. Growth heights were reported based on the final height of the plant achieved before the plant death. In addition, the NP fertilizer-treated chickpea plants showed a higher

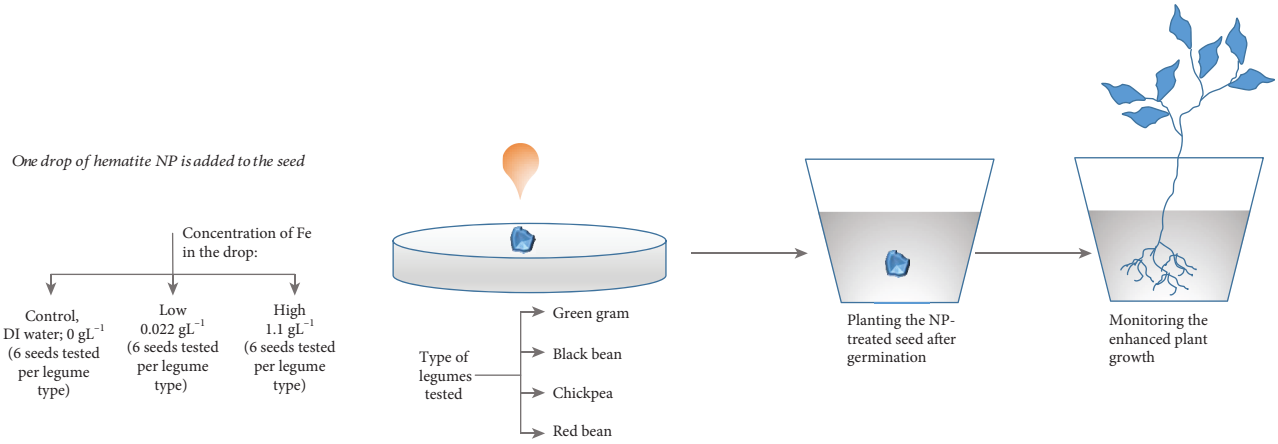

Figure 2: Schematic of the modified seed presoak method with hematite NP fertilizer.

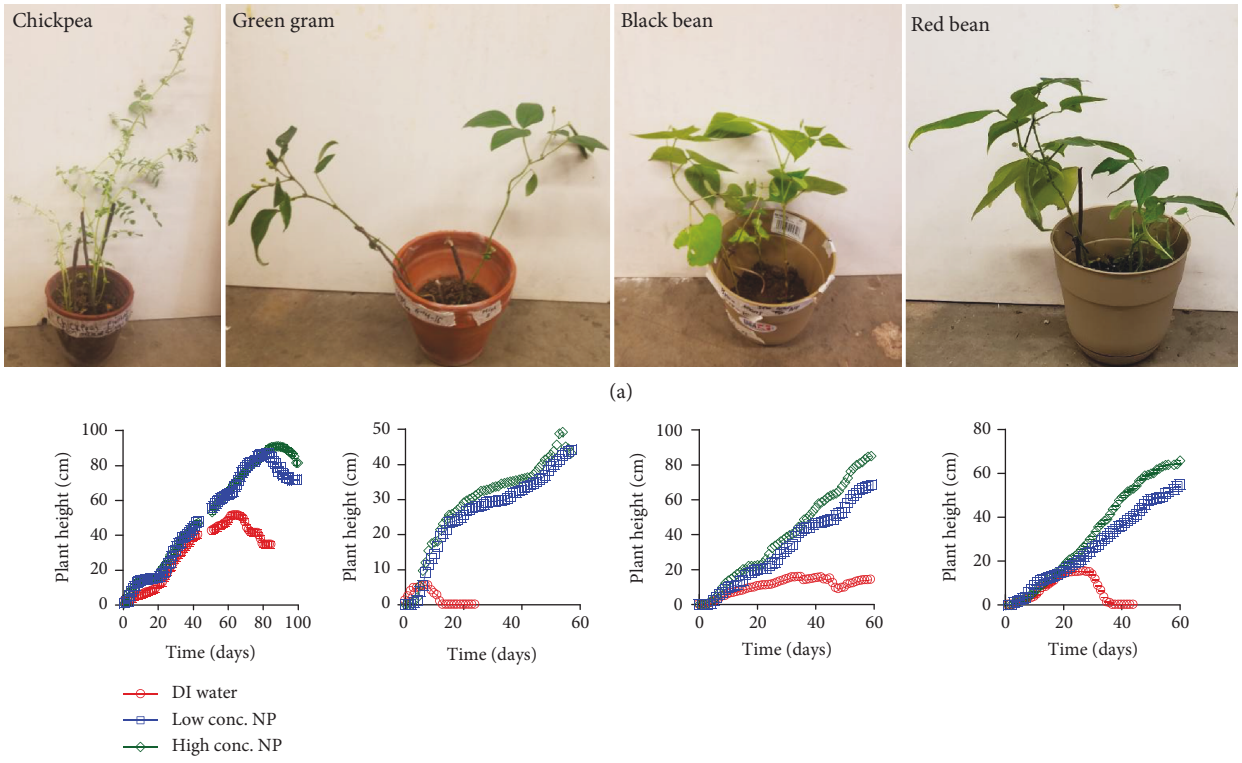

Figure 3: Effect of the hematite NP fertilizer delivered via a modified seed presoak method on the growth of different legumes. (a) Images of plants taken on day 30 of growth after transferring the seeds to potted soil and (b) plots showing comparative time-dependent growth of the plants treated with control DI water, a low concentration of NPs, and a high concentration of NPs. Error bars on the plots are reported based on 95% normalized distribution.

survival time than the control DI water plants by 15 days. The DI water chickpea plant held an increasing growth trend for 72% of its total life span. In comparison, the hematite NP-treated plants showed an increasing growth for 82-85% of their life span, suggesting a healthier growth and vitality as compared to the DI water plant. We observed a difference in morphology of the leaves for chickpea plants treated with DI water, low-concentration NP fertilizer, and high-concentration NP fertilizer, which may suggest a possible dominance of a more stable genetic structure for the NP-treated plants (Figure S4, SI) [10, 36]. However, the leaf structures are currently under further detailed investigation and further proof through genetic and molecular level analyses is required, which is not within the scope of this work. The Fe-enriching hematite NP fertilizer significantly boosted the growth of green gram plants as the seeds treated with low and high concentrations of the fertilizer grew 830% and 700% more than the control DI water plant. The NP fertilizer-treated green gram plants were stronger with a 5-fold higher survival span compared to the control

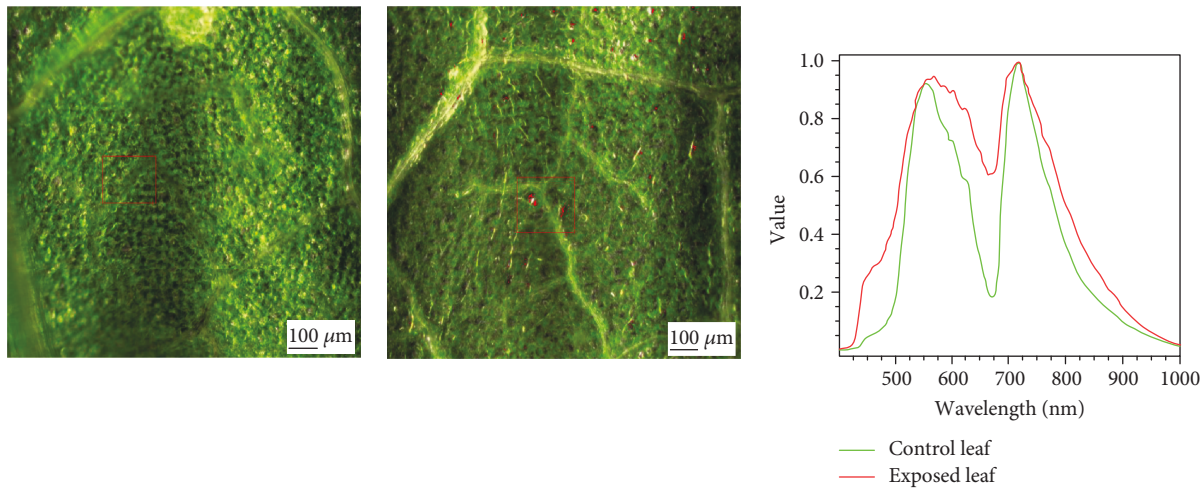

FIGURE 4: Hyperspectral imaging of black bean leaf samples. (a) Image of control DI water-treated leaf. (b) Image of leaf from a plant treated with a high concentration of hematite NPs (1.1 gL^{-1} Fe); the red dots indicate the localization of NPs. (c) Comparative spectral plots of leaves from control and NP-treated plants.

plant. These green gram plants produced pods after 18 days, two times faster than other literature reports on regular plants [37]. Images of the healthy second-generation plants from the NP fertilizer-treated green gram seeds are included in the SI (Figure S5). In the case of black beans, the plants grown with a drop of high-concentration hematite NP fertilizer showed the highest growth. The Fe-enriching hematite NP fertilizer significantly boosted the growth rate of black bean plants, even though the beans are richer in Fe content compared to the other legume species tested in this study [38]. Black bean plants treated with high- and low-concentration NP fertilizers grew 588% and 453% higher than the control plants, respectively. Growth percentages were reported based on the last day of measurement for the black bean plants. They also produced more seed pods than the control plants, and healthy second-generation plants were observed for the NP-treated black bean plants (Figure S5, SI) [39]. However, the survival span of the black bean plants was not affected by the NP fertilizer. This could be due to the high iron content in the beans [38]. The Fe-enriching NP fertilizer treatment increased the growth of red bean plants by 425% and 350% for high and low fertilizer concentrations, respectively, as compared to the control plant. Fruit production per plant increased twofold with NP treatment for the red bean plants, and healthy second-generation plants were observed (Figure S5, SI). In brief, the key insights from our growth studies was that the modified seed presoak method with the hematite NP fertilizer increased the growth of legumes by 230–830%, increased survival time of most legume species, enhanced fruit production per plant except for chickpeas, facilitated faster fruit production, and produced healthy second-generation plants. The highest impact in growth with the NPs was observed for the green gram plants.

These results indicated the strong potential of hematite NPs to serve as a leading Fe-enriching fertilizer for enhanced agricultural production. However, understanding the method of uptake and interaction of these NPs with the plants is important both for practical applicability and safety. It is difficult to determine NP interactions in complex biological media like plants via a single independent material characterization technique due to the low concentrations of NPs encountered in the plant tissues, interference from plant tissues, and the similarity of the NPs to naturally occurring NPs or metal ions. Electron microscopy is traditionally used to visualize NPs within the plants, but the sample preparation required for this method increases the probability of artifacts in the images. Therefore, we chose hyperspectral imaging (CytoViva), a minimally invasive and enhanced darkfield imaging technique requiring negligible sample preparation to investigate the uptake of hematite NPs in the legumes [29, 40]. The enhanced darkfield illumination technology in this method minimized light loss and enabled scatter from the sample to be detected without source illumination interference. Figures 4(a) and 4(b) show representative hyperspectral images of control and NP-treated black bean leaves used for visually mapping the localization of the hematite NP fertilizer. The spectral signature of the NP fertilizer was collected as a reference for comparison. A spectral library was created from the image of the NP-treated leaf and filtered against the control image to generate the comparative map (Figure 4(c)). The peak around 475 nm and the shoulder at 600-650 nm indicated the presence of hematite NPs in the leaves of legumes treated with the NP fertilizer. The localization of hematite NPs within the leaf is marked in red in Figure 4(b). The images and spectra from chickpea leaves and the raw hematite NP fertilizer are presented in the SI for further confirmation of our conclusion (Figures S6 and S7). It should be noted that though hyperspectral imaging has been reported earlier in detecting NPs within animal tissues, the use of this technique for plant samples is relatively new [29].

We used FTIR with ATR as a second noninvasive characterization technique requiring minimum sample preparation

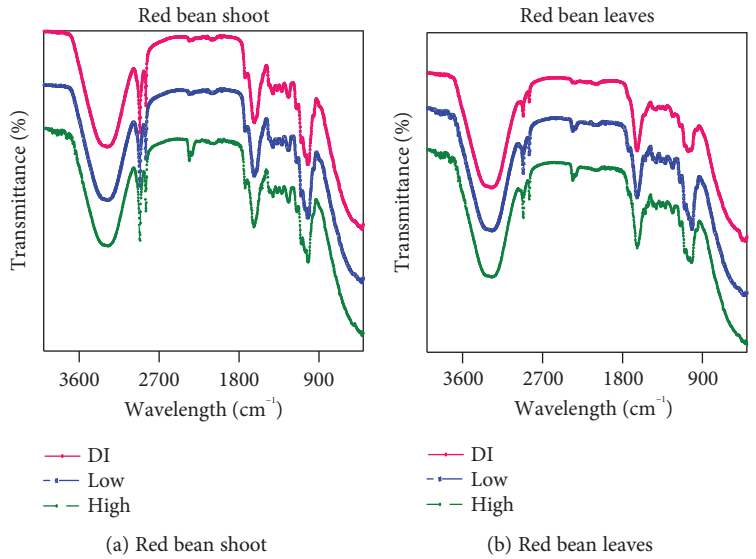

(a) Red bean shoot (b) Red bean leaves

Figure 5: FTIR plots of stem and leaf samples from red bean plants grown from seeds treated with DI water, a drop of a low concentration of NPs, and a drop of a high concentration of NPs. Samples were taken after 10 days of growth in soil.

to further understand the uptake and translocation of the NP fertilizer within the legumes [16, 21]. The chemical composition of the shoot and leaves of the legumes grown from seeds presoaked in DI water, low-concentration NP fertilizer, and high-concentration NP fertilizer were investigated using an FTIR spectrometer. Figure 5 shows the representative FTIR plots from red bean leaves after 10 days of plant growth. The FTIR spectrum of the hematite NP fertilizer is presented in the SI (Figure S1c). Typically, the shoot and leaf exhibit characteristic peaks between 3500 and 3000 cm^{-1} representative of O-H and N-H groups, 3000 and 2800 cm^{-1} due to CH_3 and CH_2 stretching, 1800 and 1200 cm^{-1} attributed to C=O stretch, 1738 cm^{-1} attributed to membrane lipids and cell wall, 1656 cm^{-1} due to amide I, 1563 cm^{-1} from amide II, 1513 cm^{-1} attributed to lignin, 1235 and 1153 cm^{-1} due to carbonyl stretch in esters and amide III, and 1100 and 1000 cm^{-1} in the fingerprint region owing to cellulose [21, 41]. All these regions were visible in the FTIR spectra of all our shoot and leaf samples. The shoots of red bean plants treated with the high-concentration hematite NP fertilizer showed additional bands at 2345 and 2365 cm^{-1}, similar to the C-N triple-bond peaks in the FTIR spectrum of hematite NPs shown in Figure S1c (SI). This data suggested the internalization of the NP fertilizer by the plants treated with high concentrations of the fertilizer. The peaks at 2345 and 2365 cm^{-1} were absent in the shoot samples of both the plants treated with a low NP concentration and those treated with DI water, indicating the absence of NPs in the stem of these plants after 10 days growth. However, the leaves of plants treated with both low and high concentrations of NPs showed these two additional peaks. This suggested the translocation of the NP fertilizer from the roots through the stem to the leaves. The NP fertilizer localized in the leaves within 10 days of growth in plants treated with a low concentration of NPs. After 10 days of growth, the hematite NPs were being transported through the shoots with some accumulation within the leaves for the plants treated with a high concentration of NPs. FTIR plots for the other legume samples were included in the SI (Figure S8). Therefore, the coupled hyperspectral imaging and FTIR characterization method provided significant insights into the transport of the NP fertilizer through the legume plants. The difference in the rate of transport of the NPs within the plants could account for the enhanced growth rate in the NP-treated plants, based on our FTIR results.

The ICP-OES measurements confirmed the presence of iron in the plant leaves; however, it indicated the absence of any dose-dependent relationship between the iron content in plant leaves and hematite NP dosing (Figure 6). The results did not suggest any significant difference in the iron content among the three different dose conditions (control, low NP concentration, and high NP concentration) for each species of legumes. Previous studies involving iron NPs in the soil matrix after seed germination have reported a dose-dependent relationship between the iron NP dosage and iron content within different parts of the plant [10, 16, 42]. However, when applied as only seed treatment, Srivastava et al. found no significant difference in iron content in spinach plant leaves with a different iron pyrite (FeS_2) NP dosing [12, 43]. Our study also confirms the absence of a significant dose-dependent iron content relationship when applying NPs in a "modified seed presoak" strategy. Hematite NPs facilitating enzymatic activity during germination, through surface chemistry rather than uptake, can be attributed as one of the reasons. These surface-mediated processes can contribute to the overall growth of the plants. Additionally, plants dosed with higher hematite NP loading exhibited higher and faster growth resulting in more chlorophyll production utilizing more iron content. This can also offset the added iron input for plants with NP dosing compared to the controls.

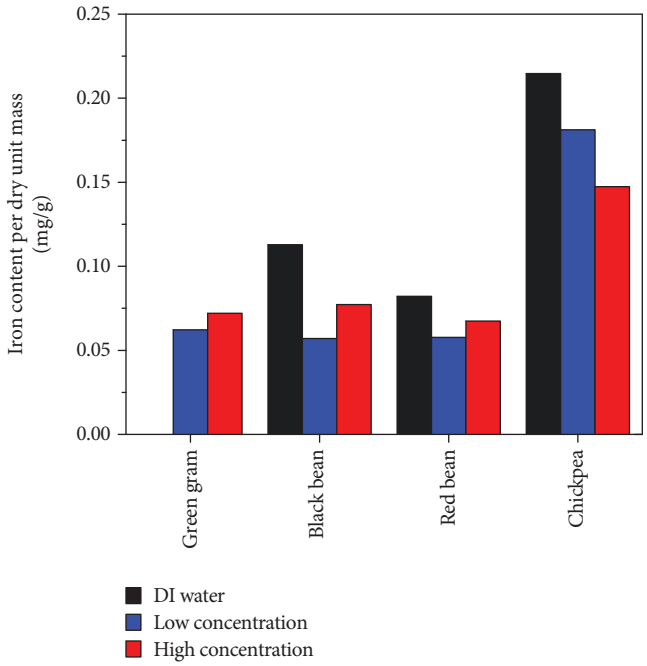

Figure 6: Different iron content in four different legumes with different hematite NP loading.

4. Conclusion

In summary, we reported a new seed presoak method using just a drop of hematite NP fertilizer to significantly increase plant growth in legumes by 230-830%, depending on the species. Though the growth trend varied between different species of legumes, in general, the seeds treated with a high concentration of the NPs (1.1 gL^{-1} Fe) showed the fastest growth compared to those soaked in a low concentration of the NPs (0.022 gL^{-1} Fe) and control DI water. The NP-treated plants exhibited twofold faster initial fruit production, two times more fruits per plant, and a longer life span compared to the control plants, in general. They produced healthy second-generation plants.

We also reported a minimally invasive material characterization strategy coupling hyperspectral imaging and FTIR to determine the internalization and transport of the NP fertilizer within the plants, while minimizing artifacts from sample preparation. The hematite NPs were transported through the shoot and localized in the leaves of the legumes. The ICP-OES measurements showed the presence of iron in the plant leaves; however, no correlation was found between the iron content in the leaves and input hematite NP fertilizer concentrations. This indicates that seed presoaking with hematite NPs actually led to more effective iron utilization which resulted in improved growth and faster fruit productions in the tested plants.

A primary advantage of our strategy is that the NP fertilizer was added in minimum quantity to a moist paper towel as a presoak solution for the seed. No NPs or additional ingredients were added to the soil. Therefore, our Fe-enriching NP fertilizer could drastically increase the production rate and life span of plants with minimum impact on the environment. The hematite NP fertilizer and the reported strategy will be highly beneficial in enhancing the production of bioenergy crops.

Data Availability

The .xls data used to support the findings of this study are available from the corresponding author upon request.

Conflicts of Interest

The authors declare no conflicts of interest.

Acknowledgments

The authors acknowledge that the research reported in this publication was supported by the University of Tennessee Chattanooga's internal grants (2018 Center of Excellence for Applied Computational Science competition and 2018 Student SEARCH grant). The authors also acknowledge Mr. Kaan Alp for help with plant growth experiments.

Supplementary Materials

The supplementary materials include the following: hydrodynamic size plot; zeta potential plot and FTIR characterization of hematite NPs; images showing difference in chickpea leaves for NP-treated plants; images of second-generation green gram, black bean, and red bean plants; photo demonstrating hyperspectral imaging of leaf samples without any special sample preparation; hyperspectral images and map for hematite NPs; hyperspectral images and mapping for chickpea leaf samples; and FTIR characterization of shoot and leaves of legumes. *(Supplementary Materials)*

References

[1] H. Roschzttardtz, G. Conéjéro, F. Divol et al., "New insights into Fe localization in plant tissues," *Frontiers in Plant Science*, vol. 4, p. 350, 2013.

[2] J. Morrissey and M. L. Guerinot, "Iron uptake and transport in plants: the good, the bad, and the ionome," *Chemical Reviews*, vol. 109, no. 10, pp. 4553–4567, 2009.

[3] C. A. Price and E. F. Carell, "Control by iron of chlorophyll formation and growth in *Euglena gracilis*," *Plant Physiology*, vol. 39, no. 5, pp. 862–868, 1964.

[4] R. Raliya, V. Saharan, C. Dimkpa, and P. Biswas, "Nanofertilizer for precision and sustainable agriculture: current state and future perspectives," *Journal of Agricultural and Food Chemistry*, vol. 66, no. 26, pp. 6487–6503, 2018.

[5] N. Kottegoda, C. Sandaruwan, G. Priyadarshana et al., "Urea-hydroxyapatite nanohybrids for slow release of nitrogen," *ACS Nano*, vol. 11, no. 2, pp. 1214–1221, 2017.

[6] P. K. Rai, V. Kumar, S. Lee et al., "Nanoparticle-plant interaction: implications in energy, environment, and agriculture," *Environment International*, vol. 119, pp. 1–19, 2018.

[7] M. Rui, C. Ma, Y. Hao et al., "Iron oxide nanoparticles as a potential iron fertilizer for peanut (*Arachis hypogaea*)," *Frontiers in Plant Science*, vol. 7, p. 815, 2016.

[8] A. Karny, A. Zinger, A. Kajal, J. Shainsky-Roitman, and A. Schroeder, "Therapeutic nanoparticles penetrate leaves and deliver nutrients to agricultural crops," *Scientific Reports*, vol. 8, no. 1, article 7589, 2018.

[9] D.-Y. Kim, A. Kadam, S. Shinde, R. G. Saratale, J. Patra, and G. Ghodake, "Recent developments in nanotechnology transforming the agricultural sector: a transition replete with opportunities," *Journal of the Science of Food and Agriculture*, vol. 98, no. 3, pp. 849–864, 2018.

[10] J. Yuan, Y. Chen, H. Li et al., "New insights into the cellular responses to iron nanoparticles in *Capsicum annuum*," *Scientific Reports*, vol. 8, no. 1, article 3228, 2018.

[11] D. Raju, S. R. Beedu, and U. J. Mehta, "Biogenic green synthesis of monodispersed gum kondagogu (*Cochlospermum gossypium*) iron nanocomposite material and its application in germination and growth of mung bean (*Vigna radiata*) as a plant model," *IET Nanobiotechnology*, vol. 10, no. 3, pp. 141–146, 2016.

[12] G. Srivastava, C. K. Das, A. Das et al., "Seed treatment with iron pyrite (FeS_2) nanoparticles increases the production of spinach," *RSC Advances*, vol. 4, no. 102, pp. 58495–58504, 2014.

[13] H. Jangir, C. K. Das, J. Kumar et al., "Nano pyrite (FeS_2) root priming enhances chilli and marigold production in nutrients-deficient soil: a nano strategy for fertiliser tuning," *Applied Nanoscience*, vol. 9, no. 3, pp. 327–340, 2019.

[14] C. K. Das, H. Jangir, J. Kumar et al., "Nano-pyrite seed dressing: a sustainable design for NPK equivalent rice production," *Nanotechnology for Environmental Engineering*, vol. 3, no. 1, p. 14, 2018.

[15] X. Li, Y. Yang, B. Gao, and M. Zhang, "Stimulation of peanut seedling development and growth by zero-valent iron nanoparticles at low concentrations," *PLoS One*, vol. 10, no. 4, article e0122884, 2015.

[16] K. Jeyasubramanian, U. U. Gopalakrishnan Thoppey, G. S. Hikku, N. Selvakumar, A. Subramania, and K. Krishnamoorthy, "Enhancement in growth rate and productivity of spinach grown in hydroponics with iron oxide nanoparticles," *RSC Advances*, vol. 6, no. 19, pp. 15451–15459, 2016.

[17] H. X. Ren, L. Liu, C. Liu et al., "Physiological investigation of magnetic iron oxide nanoparticles towards Chinese mung bean," *Journal of Biomedical Nanotechnology*, vol. 7, no. 5, pp. 677–684, 2011.

[18] M. H. Ghafariyan, M. J. Malakouti, M. R. Dadpour, P. Stroeve, and M. Mahmoudi, "Effects of magnetite nanoparticles on soybean chlorophyll," *Environmental Science & Technology*, vol. 47, no. 18, pp. 10645–10652, 2013.

[19] H. Zhu, J. Han, J. Q. Xiao, and Y. Jin, "Uptake, translocation, and accumulation of manufactured iron oxide nanoparticles by pumpkin plants," *Journal of Environmental Monitoring*, vol. 10, no. 6, pp. 713–717, 2008.

[20] M. Rui, C. Ma, J. C. White et al., "Metal oxide nanoparticles alter peanut (*Arachis hypogaea* L.) physiological response and reduce nutritional quality: a life cycle study," *Environmental Science: Nano*, vol. 5, no. 9, pp. 2088–2102, 2018.

[21] S. Palchoudhury, K. L. Jungjohann, L. Weerasena et al., "Enhanced legume root growth with pre-soaking in α-Fe_2O_3 nanoparticle fertilizer," *RSC Advances*, vol. 8, no. 43, pp. 24075–24083, 2018.

[22] L. Grillet, S. Mari, and W. Schmidt, "Iron in seeds—loading pathways and subcellular localization," *Frontiers in Plant Science*, vol. 4, p. 535, 2014.

[23] J. P. Stegemeier, B. P. Colman, F. Schwab, M. R. Wiesner, and G. V. Lowry, "Uptake and distribution of silver in the aquatic plant *Landoltia punctata* (duckweed) exposed to silver and silver sulfide nanoparticles," *Environmental Science & Technology*, vol. 51, no. 9, pp. 4936–4943, 2017.

[24] X. Gui, Y. Deng, Y. Rui et al., "Response difference of transgenic and conventional rice (*Oryza sativa*) to nanoparticles (γFe_2O_3)," *Environmental Science and Pollution Research*, vol. 22, no. 22, pp. 17716–17723, 2015.

[25] J. Lv, P. Christie, and S. Zhang, "Uptake, translocation, and transformation of metal-based nanoparticles in plants: recent advances and methodological challenges," *Environmental Science: Nano*, vol. 6, no. 1, pp. 41–59, 2019.

[26] A. Milewska-Hendel, M. Zubko, J. Karcz, D. Stroz, and E. Kurczynska, "Fate of neutral-charged gold nanoparticles in the roots of the *Hordeum vulgare* L. cultivar Karat," *Scientific Reports*, vol. 7, no. 1, article 3014, 2017.

[27] L. van Nhan, C. Ma, Y. Rui et al., "The effects of Fe_2O_3 nanoparticles on physiology and insecticide activity in non-transgenic and Bt-transgenic cotton," *Frontiers in Plant Science*, vol. 6, article 1263, 2016.

[28] M. Mortimer, A. Gogos, N. Bartolomé, A. Kahru, T. D. Bucheli, and V. I. Slaveykova, "Potential of hyperspectral imaging microscopy for semi-quantitative analysis of nanoparticle uptake by protozoa," *Environmental Science & Technology*, vol. 48, no. 15, pp. 8760–8767, 2014.

[29] A. Avellan, F. Schwab, A. Masion et al., "Nanoparticle uptake in plants: gold nanomaterial localized in roots of *Arabidopsis thaliana* by X-ray computed nanotomography and hyperspectral imaging," *Environmental Science & Technology*, vol. 51, no. 15, pp. 8682–8691, 2017.

[30] R. Sekine, K. L. Moore, M. Matzke et al., "Complementary imaging of silver nanoparticle interactions with green algae: dark-field microscopy, electron microscopy, and nanoscale secondary ion mass spectrometry," *ACS Nano*, vol. 11, no. 11, pp. 10894–10902, 2017.

[31] S. Palchoudhury and J. R. Lead, "A facile and cost-effective method for separation of oil-water mixtures using polymer-coated iron oxide nanoparticles," *Environmental Science & Technology*, vol. 48, no. 24, article 14558, 14563 pages, 2014.

[32] A. Pequerul, C. Perez, P. Madero, J. Val, and E. Monge, "A rapid wet digestion method for plant analysis," in *Optimization of Plant Nutrition*, Springer, 1993.

[33] F. Yunta, M. di Foggia, V. Bellido-Díaz et al., "Blood meal-based compound. Good choice as iron fertilizer for organic farming," *Journal of Agricultural and Food Chemistry*, vol. 61, no. 17, pp. 3995–4003, 2013.

[34] M. D. Frost, J. C. Cole, and J. M. Dole, "Fertilizer source affects iron, manganese, and zinc leaching, nutrient distribution, and geranium growth," *Journal of Plant Nutrition*, vol. 26, no. 2, pp. 315–329, 2003.

[35] G. A. Achari and M. Kowshik, "Recent developments on nanotechnology in agriculture: plant mineral nutrition, health, and interactions with soil microflora," *Journal of Agricultural and Food Chemistry*, vol. 66, no. 33, pp. 8647–8661, 2018.

[36] R. P. S. Pundir, M. H. Mengesha, and K. N. Reddy, "Leaf types and their genetics in chickpea (*Cicer arietinum* L.)," *Euphytica*, vol. 45, no. 3, pp. 197–200, 1990.

[37] J. Iqbal, M. Ahsan, M. Saleem, and A. Ali, "Appraisal of gene action for indeterminate growth in mungbean (*Vigna radiata* (L.) wilczek)," *Frontiers in Plant Science*, vol. 6, p. 665, 2015.

[38] N. Petry, E. Boy, J. Wirth, and R. Hurrell, "Review: the potential of the common bean (*Phaseolus vulgaris*) as a vehicle for iron biofortification," *Nutrients*, vol. 7, no. 2, pp. 1144–1173, 2015.

[39] C. Miles, K. Atterberry, and B. Brouwer, "Performance of Northwest Washington heirloom dry bean varieties in organic production," *Agronomy*, vol. 5, no. 4, pp. 491–505, 2015.

[40] A. Moghimi, C. Yang, M. E. Miller, S. F. Kianian, and P. M. Marchetto, "A novel approach to assess salt stress tolerance in wheat using hyperspectral imaging," *Frontiers in Plant Science*, vol. 9, article 1182, 2018.

[41] A. Ertani, O. Francioso, E. Ferrari, M. Schiavon, and S. Nardi, "Spectroscopic-chemical fingerprint and biostimulant activity of a protein-based product in solid form," *Molecules*, vol. 23, no. 5, p. 1031, 2018.

[42] M. Mohammadi, N. Majnoun Hoseini, M. R. Chaichi, H. Alipour, M. Dashtaki, and S. Safikhani, "Influence of nano-iron oxide and zinc sulfate on physiological characteristics of peppermint," *Communications in Soil Science and Plant Analysis*, vol. 49, no. 18, pp. 2315–2326, 2018.

[43] G. Srivastava, A. Das, T. S. Kusurkar et al., "Iron pyrite, a potential photovoltaic material, increases plant biomass upon seed pretreatment," *Materials Express*, vol. 4, no. 1, pp. 23–31, 2014.

Hindawi
Journal of Nanomaterials
Volume 2019, Article ID 6061275, 15 pages
https://doi.org/10.1155/2019/6061275

Research Article

Metal-Organic Framework MIL-101: Synthesis and Photocatalytic Degradation of Remazol Black B Dye

Pham Dinh Du,[1] **Huynh Thi Minh Thanh**,[2,3] **Thuy Chau To**,[1] **Ho Sy Thang**,[4] **Mai Xuan Tinh**,[3] **Tran Ngoc Tuyen**,[3] **Tran Thai Hoa**,[3] **and Dinh Quang Khieu**[3]

[1]*Faculty of Natural Science, Thu Dau Mot University, 820000, Vietnam*
[2]*Department of Chemistry, Quy Nhon University, 59000, Vietnam*
[3]*University of Sciences, Hue University, 530000, Vietnam*
[4]*Dong Thap University, 870000, Vietnam*

Correspondence should be addressed to Dinh Quang Khieu; dqkhieu@hueuni.edu.vn

Received 20 January 2019; Revised 2 April 2019; Accepted 28 April 2019; Published 14 May 2019

Guest Editor: Soubantika Palchoudhury

In the present paper, the synthesis of metal-organic framework MIL-101 and its application in the photocatalytic degradation of Remazol Black B (RBB) dye have been demonstrated. The obtained samples were characterized by X-ray diffraction (XRD), transmission electron microscope (TEM), X-ray photoelectron spectroscopy (XPS), and nitrogen adsorption/desorption isotherms at 77 K. It was found that MIL-101 synthesized under optimal conditions exhibited high crystallinity and specific surface area (3360 $m^2 \cdot g^{-1}$). The obtained MIL-101 possessed high stability in water for 14 days and several solvents (benzene, ethanol, and water at boiling temperature). Its catalytic activities were evaluated by measuring the degradation of RBB in an aqueous solution under UV radiation. The findings show that MIL-101 was a heterogeneous photocatalyst in the degradation reaction of RBB. The mechanism of photocatalysis was considered to be achieved by the electron transfer from photoexcited organic ligands to metallic clusters in MIL-101. The kinetics of photocatalytic degradation reaction were analyzed by using the initial rate method and Langmuir-Hinshelwood model. The MIL-101 photocatalyst exhibited excellent catalytic recyclability and stability and can be a potential catalyst for the treatment of organic pollutants in aqueous solutions.

1. Introduction

Textile and paint industries and dyestuff manufacturing release a considerable amount of wastewater with dyes. This has raised serious environmental concerns all over the world; thus, their removal is of interest to many scientists [1]. Dyes are difficult to treat along with municipal waste treatment operations due to their complicated chemical structures. Remazol Black B (RBB) is a popular diazo reactive dye and used widely in textile industries [2]. Various processes for eliminating RBB from aqueous solutions including adsorption, electrochemistry, and biosorption have been reported. Thi Thanh et al. [3] reported the efficient removal of RBB using iron-containing zeolite imidazole framework-8 (Fe-ZIF-8). Fe-ZIF-8 possessed high stability. After three cycles, the degradation yield was reduced slightly—95% compared to the initial catalyst. Soloman et al. [2] reported the degradation of hydrolyzed Remazol Black using the electrochemical approach. Brazilian pine-fruit shells (*Araucaria angustifolia*) in natural form are efficient adsorbents for the removal of RBB dye from aqueous effluents [4]. Biosorption of an azo dye by growing fungi (*Aspergillus flavus*) was reported in which the removal of chemical oxygen demand (COD) was found to be 90% at 100 $mg \cdot L^{-1}$ initial concentration of dye [5]. The introduction of iron to ZIF-8 significantly enhanced the photocatalytic degradation of RBB Fe-ZIF-8 under visible light [6].

Metal-organic frameworks (MOFs) are porous materials formed *via* strong metal-ligand bonds between metal cations and organic linkers [7, 8]. MOFs have many applications in gas storage [9–15], separation [16, 17], and heterogeneous catalysis [18–21]. MIL-101 is a member of the

large family of MOFs with the largest Langmuir surface area ($4500\,m^2 \cdot g^{-1}$), pore size (29–34 Å), and cell volume (702.000 Å). It was first reported by Férey et al. in 2005 [22], who synthesized it from HF-$Cr(NO_3)_3$-1,4-dicarboxylic acid- (H_2BDC-) H_2O. Since the discovery of large-pore MIL-101, several groups have tried to synthesize MIL-101 for gas adsorption. However, it is hard to obtain crystalline MIL-101 with a high BET surface of more than $3200\,m^2 \cdot g^{-1}$ [18] because of the presence of H_2BDC residue or inorganic impurities in the pores as well as outside the pores. In the synthesis of MIL-101, it is complicated to remove most of the nonreacted H_2BDC present both outside and within the pores of MIL-101. Yang et al. [13] used various alkalis, such as potassium hydroxide (KOH), tetramethylammonium hydroxide (TMAOH), triethylamine ($(C_2H_5)_3N$), dimethylamine (C_2H_7N), methylamine (CH_5N), and ammonia (NH_3), to avoid recrystallization of H_2BDC. The TMAOH-$Cr(NO_3)_3$-H_2BDC-H_2O system was found to be suitable for obtaining MIL-101 with high surface properties. Hong et al. [18] reported a separation process in which huge amounts of H_2BDC were separated with a fritted glass filter, and then excess dissolution was done with a hot solvent (ethanol or N,N-dimethyl-formamide (NH_4F)).

The heterogeneous photocatalysis is one of the highly effective methods used for the treatment of a wide variety of organic pollutants owing to its ability to degrade the pollutants completely. Photocatalytic degradation is usually conducted for dissolved compounds in water, at mild temperature and pressure conditions, using UV radiation and photocatalytic semiconductors without any requirement of expensive oxidants. The use of metal-organic frameworks (MOFs) as photocatalysts is a new field of application for this material. Recently, some MOF materials such as MOF-5 [23–25], MIL-125 [26], and MIL-53(M) (M = Fe, Al, and Cr) [27] have been applied successfully in the decolorization of various dyes in aqueous solutions. Owing to its excellent porosities (high specific surface area, large pore volume, and uniform pores), MIL-101 is a good candidate in catalysis [28] and has been found to be a great candidate for many other applications [16, 17, 29–32]. Several papers have reported visible-light photocatalytic activity of modified MIL-101, e.g., N-$K_2Ti_4O_9$/MIL-101 composite [33] and $Bi_{25}FeO_{40}$/MIL-101/PTH [34]. To the best of our knowledge, no attention has ever been paid to the study of the photocatalytic properties of pure MIL-101 to date.

In the present paper, we focused on an $Cr(NO_3)_3$-H_2BDC-H_2O system and analyzed the effect of different conditions on the synthesis of MIL-101 and monitored the hydrothermal stability of MIL-101 in various solvents and conditions. Photocatalytic degradation of RBB was also investigated.

2. Experimental

2.1. Materials. Chromium(III) nitrate nonahydrate ($Cr(NO_3)_3 \cdot 9H_2O$; 99%), benzene-1,4-dicarboxylic acid ($C_6H_4(COOH)_2$; >98%) (denoted as H_2BDC), and hydrogen fluoride (HF; 40%) were purchased from Merck, Germany. Remazol Black B ($C_{26}H_{21}N_5Na_4O_{19}S_6$, molecular weight = 991.82) (denoted as RBB) was procured from the Thuy Duong Textile Company (Hue city, Vietnam). The structure of RBB is shown in Scheme 1.

Ferrous ammonium sulfate ($Fe(NH_4)_2(SO_4)_2 6H_2O$; >98%), potassium dichromate ($K_2Cr_2O_7$; >99%), ferrous sulfate heptahydrate ($FeSO_4 \cdot 7H_2O$; >99%), silver sulfate (Ag_2SO_4; >99%), conc. H_2SO_4 (98%), and mercuric sulfate ($HgSO_4$; >98%) were supplied from Merck, Germany, and used to measure the COD of samples.

2.2. MIL-101 Synthesis. MIL-101 was synthesized according to an earlier report with some modifications [22]. The mixture of reactants including H_2BDC, $Cr(NO_3)_3$, HF, and H_2O was heated in a Teflon-lined stainless steel autoclave at 200°C for 8 h. The resulting green solid material was filtered using a 0.2 μm membrane and then extracted in ethanol with Soxhlet equipment for 12 h to remove residual amount of H_2BDC still present in the product. The effects of the molar ratio of chromium nitrate and water to H_2BDC on the formation of MIL-101 were also monitored. With a fixed water volume of 100 mL, the composition of the synthesized gel was calculated at the following molar ratio:

(i) For the study on the effect of the molar ratio of Cr/H_2BDC, the molar composition of a reactant mixture of $H_2BDC : Cr(NO_3)_3 \cdot 9H_2O : HF : H_2O = 1.00 : x : 0.25 : 265$, with $x = 0.5, 0.75, 1.00, 1.25, 1.50$, and 1.75. The samples were denoted as M-0.5, M-0.75, M-1.00, M-1.25, M-1.50, and M-1.75

(ii) For the study on the effect of the ratio of H_2O/H_2BDC, the molar composition of a reactant mixture of $H_2BDC : Cr(NO_3)_3 \cdot 9H_2O : HF : H_2O = 1.00 : 1.25 : 0.25 : y$, with $y = 200, 265, 350, 400, 500$, and 700. The samples were denoted as M-200, M-265, M-350, M-400, M-500, and M-700

2.3. Photocatalytic Performance. The photocatalytic degradation of RBB was measured at ambient conditions using a set of home-made equipment. The source of UV light was UV-B313 30 W ($\lambda = 310$ nm).

The photocatalytic experiments were performed in a 1000 mL beaker containing 500 mL of aqueous suspensions of 10–50 ppm RBB and a 0.25 mg catalyst. The beaker was kept at 25°C with a thermostat. The UV lamp was focused on the beaker at 15 cm distance. All of the experiments were performed under natural pH conditions (around 7–7.5) unless specified otherwise. Then, 3 mL of the mixture was withdrawn at certain time intervals and centrifuged to remove the MIL-101 solid. The RBB concentration was monitored by means of spectroscopy at the maximum wavelength ($\lambda = 600$ nm). The experiments were replicated three times.

The chemical oxygen demand (COD) of the RBB solution was measured by the ASTM method [35]. The sample was oxidized by the boiling mixture of chromic and sulfuric acids. The sample was refluxed in a strongly acidic solution with a known excess of potassium dichromate ($K_2Cr_2O_7$). After digestion, the remaining unreduced $K_2Cr_2O_7$ was titrated with ferrous ammonium sulfate to determine the amount of $K_2Cr_2O_7$ consumed and the oxidizable matter

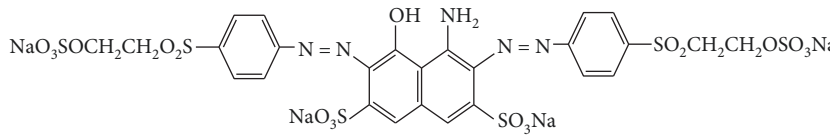

Scheme 1: Structure of RBB.

was calculated in terms of the oxygen equivalent. The samples were analyzed in duplicate to yield reliable data.

X-ray diffraction (XRD) was carried on a D8 ADVANCE system (Bruker, Germany) (Hanoi city, Vietnam). Cu Kα radiation ($\lambda = 1.5406$ Å) was the light source with applied voltage of 35 kV and current of 40 mA. Transmission electron microscopy (TEM) was carried out using a JEOL JEM-2100F microscope (Hanoi city, Vietnam). Nitrogen adsorption/desorption isotherm measurements were conducted using a Micromeritics 2020 volumetric adsorption analyzer system (Hanoi city, Vietnam). The samples were pretreated by heating under vacuum at 150°C for 3 h. The BET (Brunauer–Emmett–Teller) model was used to calculate the specific surface area using adsorption data in the relative range 0–0.24. Total volume was obtained from the nitrogen volume adsorbed at a relative pressure of 0.99. The X-ray photoelectron spectroscopy (XPS) was conducted using a Shimadzu Kratos AXIS Ultra DLD spectrometer (Japan). Peak fitting was performed by CasaXPS software. The absorbance of RBB, methyl orange (MO), and methylene blue (MB) was measured at $\lambda_{max} = 600$ nm, 464 nm, and 664 nm, respectively, using a Lambda 25 Spectrophotometer, PerkinElmer, Singapore (Hue city, Vietnam).

3. Results and Discussion

3.1. Synthesis of MIL-101 and Its Stability under Different Conditions. The XRD patterns of the MIL-101 samples synthesized with different Cr/H_2BDC molar ratios of 0.50, 0.75, 0.85, 1.00, 1.25, and 1.75 are shown in Figure 1(a). From the figure, it is found that the diffraction at a small angle of about 1.7° characterizing the mesoporous structure of MIL-101 was obtained depending on the Cr/H_2BDC ratio. At a low Cr/H_2BDC ratio, the diffraction at such a small angle was not observed. However, when the Cr/H_2BDC ratio was increased to a level such as M-1.25, M-1.5, or M-1.75, the XRD patterns were similar to the patterns of MIL-101 as reported earlier [22], in which sharp and strong diffraction at 2θ of around 1.7° was clearly observed. Therefore, a Cr/H_2BDC ratio larger than 1.25 could provide MIL-101 with high crystallinity. The textural properties of MIL-101 samples synthesized at different ratios of Cr/H_2BDC were investigated by the N_2 adsorption-desorption isotherms at 77 K as shown in Figure 1(b). The isothermal curves are of type IV, with pore-filling steps at $p/p^0 \approx 0.2$ and $p/p^0 \approx 0.3$, characteristic of the presence of two types of narrow mesopores [18]. The parameters characterizing the textural properties of the obtained MIL-101 samples are displayed in Table 1. The specific surface area tends to increase with the increase in the molar ratio of Cr/H_2BDC and reaches the highest value at the ratio of 1.25 and then decreases when this ratio continues to rise.

The morphologies of MIL-101 samples synthesized with different molar ratios of Cr/H_2BDC were observed by TEM images (Figure 2). It can be seen that the particles have an octahedron shape with different sizes, in the range of 230-570 nm, depending on the molar ratios of Cr/H_2BDC. The values of standard deviation (SD)/mean (4%-9%) were less than 10% in all cases indicating that particle size distributions were normal. The size of particles reaches a minimum at the Cr/H_2BDC ratio of 1.25 (M-1.25) (see Table 1). In fact, the effect of the Cr/H_2BDC ratio on the MIL-101 particle size was not clear as the Cr/H_2BDC ratio was between 0.75 and 1.25. The particle size increased significantly as the Cr/H_2BDC ratio is larger than 1.25. On the contrary, crystallite sizes obtained from the Scherrer equation (using (375) diffraction) was within 34.1 and 45.8 nm and they appeared to be less affected by the Cr/H_2BDC ratio. These results implied that particles consisted of several crystals. Based on the specific surface area and morphology, the suitable Cr/H_2BDC molar ratio for the synthesis of MIL-101 was found to be 1.25.

Figure 3(a) displays the XRD results of MIL-101 samples synthesized with different molar ratios of H_2O/H_2BDC. The results show that the amount of water in the composition of reactants has a considerable effect on the structure of MIL-101. All the samples with an increase in molar ratios of H_2O/H_2BDC from 200 to 700 provided the characteristic diffractions of MIL-101. However, the peak at 2θ of about 1.7° characterizing the mesoporous structure did not appear for the samples having a high water content (M-500, M-700), while the same was observed clearly for the samples having a lower water content with molar ratios of H_2O/H_2BDC from 200 to 400. In addition, at a high water content in the reactant mixtures, a lower peak intensity was observed. Therefore, the water content in the reactant mixtures not only affected the structure of materials but also reduced their crystallinity.

The isotherms of nitrogen adsorption/desorption and texture properties of MIL-101 synthesized with different molar ratios of H_2O/H_2BDC are illustrated in Figure 3(b) and Table 2. It was found that the specific surface area increased steadily when the molar ratio of H_2O/H_2BDC increased and peaked at the molar ratio of 350, but after that, it decreased when this ratio was increased. The water content in the reactant mixtures had a significant effect on the particle size of MIL-101 but had less effect on crystallite size. It can be seen in Figure 4 and Table 2 that the particle size decreased slightly with the increase in water content while crystallite sizes around 26.8–31.8 nm seemed to be

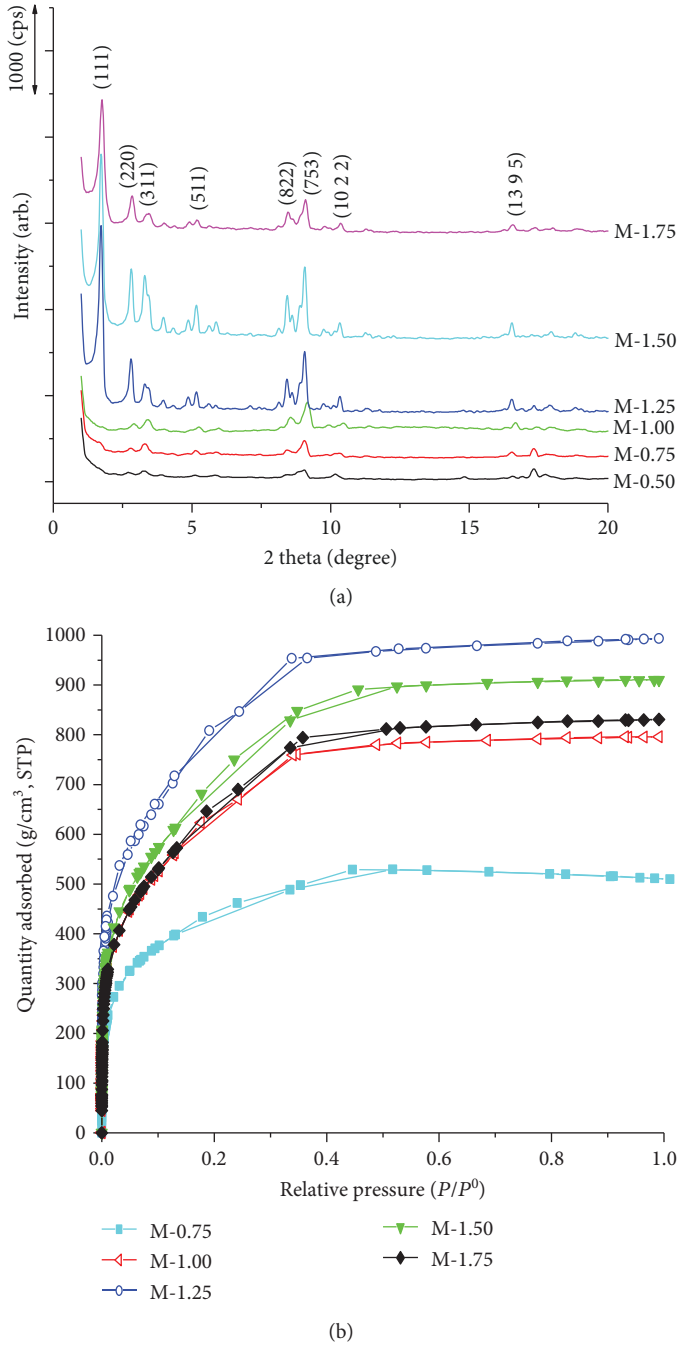

Figure 1: (a) XRD patterns and (b) nitrogen adsorption/desorption isotherms of MIL-101 synthesized using different molar ratios of Cr/H_2BDC.

unchangeable. A large amount of water resulted in irregular shapes and formation of the needle-shaped crystals of terephthalate acid. It can be inferred that a high water content probably reduced the crystal growth rates [36]. Therefore, a perfect MIL-101 crystal could not be achieved at high water contents in the reactant mixture, and the most perfect MIL-101 crystal was observed in the M350 sample.

As mentioned previously, a larger amount of nonreacted H_2BDC is present in MIL-101, resulting in a decrease in its surface area and pore volume. The previous studies are focused on the purification using hot ethanol, water, or fluoride–anion exchange using aqueous NH_4F solutions [18, 22, 32]. In the present work, we proposed the Soxhlet extraction using ethanol solvent to purify the H_2BDC. Table 3 shows the specific surface area and porous volume of the present MIL-101 material compared to some previous studies. The surface area and porous volume of MIL-101 synthesized in this study are smaller than those reported by Férey et al. [22] but much higher than recent studies. The proposed purification is time-consuming but is capable for completely

Table 1: Textural properties of MIL-101 samples synthesized using different molar ratios of Cr/H_2BDC.

Samples	S_{BET} ($m^2 \cdot g^{-1}$)	$S_{Langmuir}$ ($m^2 \cdot g^{-1}$)	V_{pore} ($cm^3 \cdot g^{-1}$)	Particle size* M ± SD (nm)	Crystallite size** (nm)
M-0.75	1582	2426	0.79	231.5 ± 20.1	34.1
M-1.00	2328	3833	1.23	376 ± 15.4	29.3
M-1.25	2946	4776	1.53	216 ± 20.3	43.7
M-1.50	2642	4354	1.41	522 ± 20.0	45.8
M–1.75	2414	4057	1.28	573 ± 27.2	34.6

*Mean value (M) of particle size counted from 100 particles. SD: standard deviation. **Crystallite size calculated from the Scherrer equation using diffraction (753).

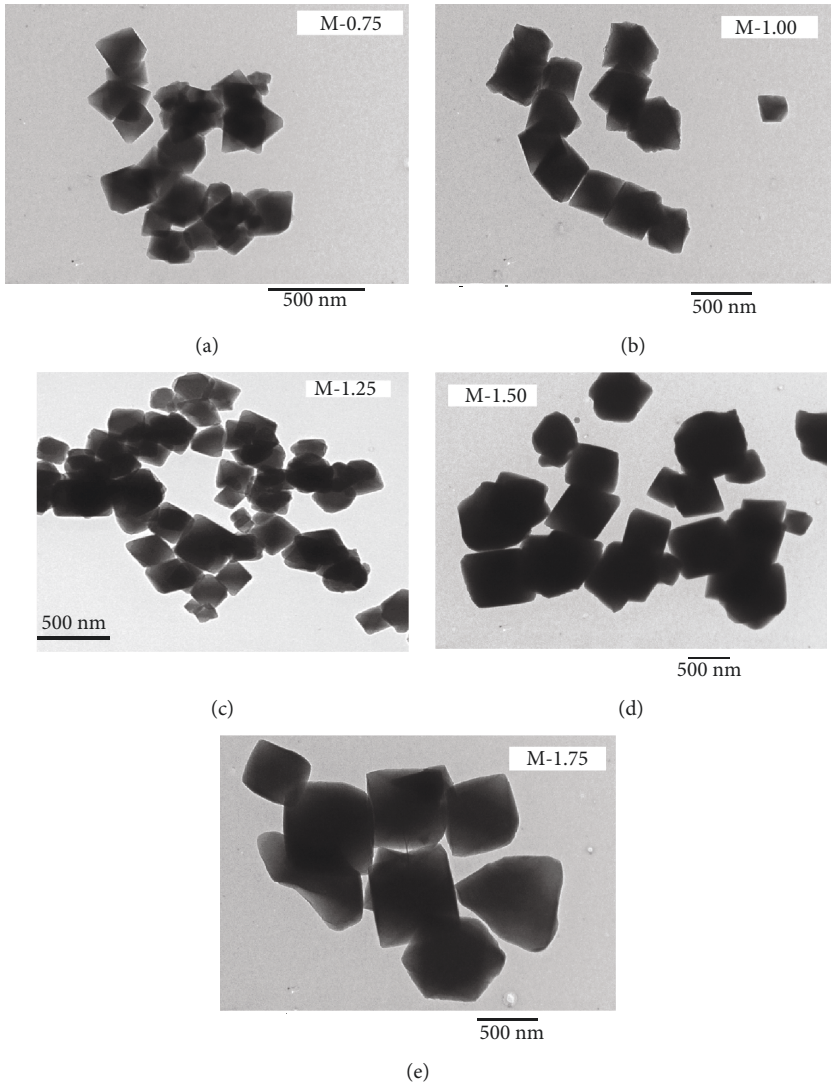

Figure 2: TEM images of MIL-101 synthesized using different molar ratios of Cr/H_2BDC.

removing H_2BDC, making the obtained MIL-101 have a high specific surface area.

The results of stability testing of MIL-101 under ambient conditions over several days are given in Figures 5(a) and 5(b). Generally, the main characteristic peaks of MIL-101 could be observed in all XRD patterns. The peak at a small angle (2θ is about 1.7°) was not present in the samples exposed to ambient conditions for 15 to 30 days without drying before XRD measurements (Figure 5(a)). It is worth noting that this peak was observed clearly in the dried sample,

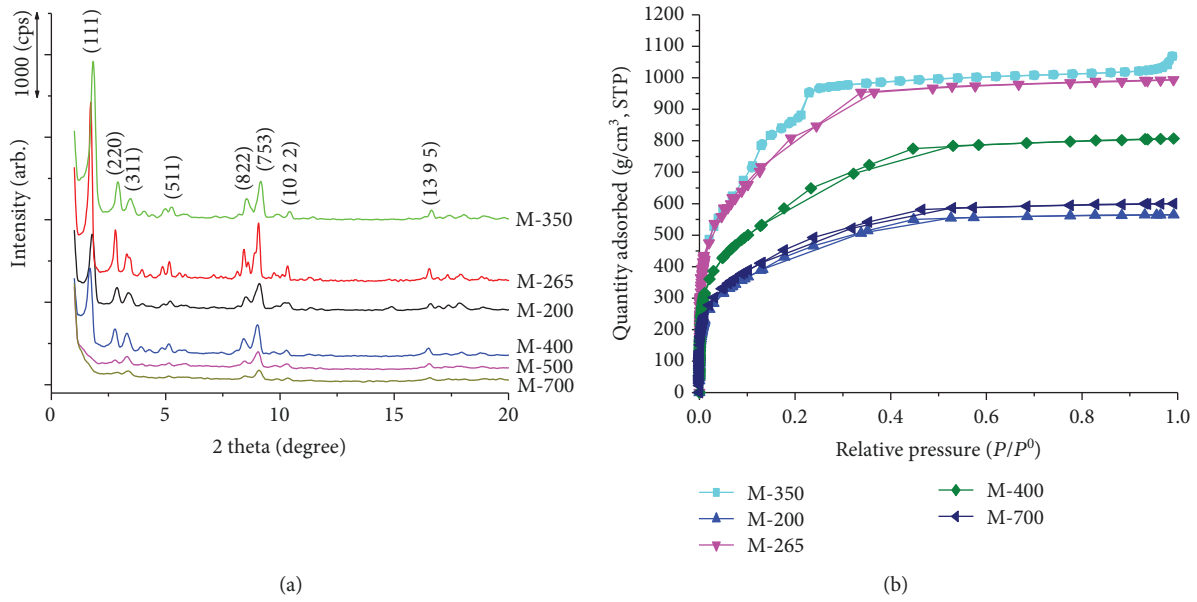

Figure 3: (a) XRD patterns and (b) isotherms of nitrogen adsorption/desorption of MIL-101 synthesized using different molar ratios of H_2O/H_2BDC.

Table 2: Textural properties of MIL-101 samples synthesized using different molar ratios of H_2O/H_2BDC.

Samples	S_{BET} ($m^2 \cdot g^{-1}$)	$S_{Langmuir}$ ($m^2 \cdot g^{-1}$)	V_{pore} ($cm^3 \cdot g^{-1}$)	Particle size* M ± SD (nm)	Crystallite size** (nm)
M-200	1618	2570	0.87	530.5 ± 78.2	26.8
M-265	2946	4776	1.53	520.3 ± 53.4	30.4
M-350	3360	5059	1.44	490.3 ± 19.4	31.8
M-400	2274	3664	1.25	250 ± 35	31.4
M-700	1708	2701	0.93	137 ± 25	30.0

*The mean value (M) of 50 particles counted from TEM images. SD: standard deviation. **Crystallite size calculated from the Scherrer equation using diffraction (753).

although it was exposed to ambient conditions up to a year (Figure 5(b)). The peak at a small angle characteristic of a mesoporous structure seems to be unstable under moistened air. This explains why this peak which diffracted at 1.7° has been reported in some studies [22], while not in others [13, 15, 18]. The reason is not clear, but it could be possible that water in the moistened air blocks some of the pores resulting in the disappearance of the characteristic diffraction of the mesoporous structure at around 1.7°. Therefore, this peak was observed after the drying process to remove water vapor from the material structure.

The stability of MIL-101 material in water at room temperature is illustrated in Figure 5(c). The results indicate that the characteristic diffractions of MIL-101 were obtained in all patterns. Notably, the characteristic diffraction of the mesoporous structure at around 1.7° still remained stable after the sample had been soaked in water for several days.

The stability of MIL-101 material in several solvents at boiling temperature for 8 h is shown in Figure 5(d). The results of XRD indicate that MIL-101 material was still stable after being soaked in boiling water continuously for 8 h, which is in good agreement with that reported by Hong et al. [18]. Moreover, the characteristic diffraction of MIL-101 still appeared with high intensity suggesting that its structure did not collapse after soaking in ethanol and benzene at boiling temperature for 8 h. In contrast, the MOFs that are used mostly, such as MOF-177 and MOF-5, have relatively high thermal and chemical stabilities; they are known to be unstable and to easily decompose in the presence of moisture [38, 39]. Therefore, MIL-101 is rather stable in both polar and nonpolar solvents at high temperatures, which makes MIL-101 an attractive candidate for various applications and catalysts.

Lin et al. [40] used X-ray absorption near edge structure (XANES) spectroscopy for characterizing the oxidation state of Cr in the MIL-101 catalyst and found that the chromium atom is in the divalent (Cr(II)) state in the MIL-101 crystals although the source of initial Cr is Cr(III) in $Cr(NO_3)_3$. In the present paper, the surface composition of the MIL-101 sample was analyzed by XPS (Figure 6(a)) and the spectra corresponding to C_{1s} and Cr_{2p} were collected. The binding energy values of 587 eV for Cr2p1/2 and 576 eV for

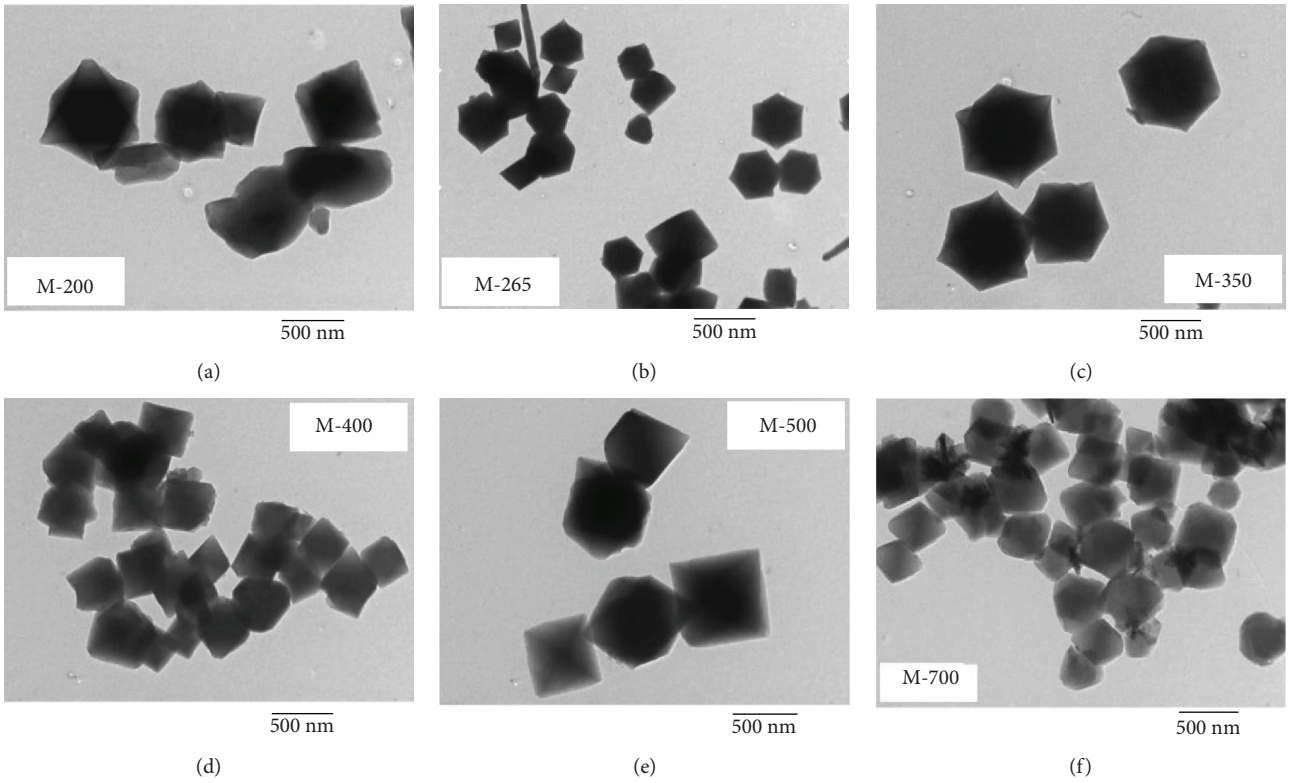

Figure 4: TEM images of MIL-101 synthesized using different molar ratios of H_2O/H_2BDC.

Cr2p3/2 (Figure 6(b)) are typically assigned to Cr^{3+} [41]. It could be inferred that the oxidation state Cr(III) of the chromium in MIL-101 does not change during its synthesis.

Figure 7(a) shows the DR-UV-Vis spectrum of MIL-101. There are three absorption peaks at 275, 425, and 610 nm. The absorption band at the UV region could be contributed by the electron transfer $n \rightarrow \pi^*$ in terephthalic acid. The absorption bands in the visible region should be related to the electron transfer in orbital 3d. The energy gaps based on Tauc's plot were found to be 1.75, 2.27, and 3.74 eV (Figure 7(b)). Since the oxidation state of chromium in MIL-101 is 3+, it was believed that here the electron shift occurs in the $3d^3$ orbital of Cr^{3+} under the action of the terephthalate ligand field.

In order to analyze this electron transfer, the Tanabe-Sugano d^3 diagram was used (Figure 8) and, according to which, spin-allowed transition was as follows:

$$\begin{aligned} &4A_{2g} \rightarrow 4T_{2g} \\ &4A_{2g} \rightarrow 4T_{1g} \\ &4A_{2g} \rightarrow 4T_{1g}\,(P) \end{aligned} \quad (1)$$

In Tauc's plot (Figure 7), three energy levels could be seen to be excited corresponding to the wave number: $\nu_1 = 14104.37$ (cm^{-1}), $\nu_2 = 18281.54$ (cm^{-1}), and $\nu_3 = 30120.48$ (cm^{-1}). Since the ratio $\nu_2/\nu_1 = 18282.54/14104.37$ was found as 1.3, this ratio corresponded to $\Delta_o/B = 36$ based on the Tanabe-Sugano diagram of the d^3 system (Δ is the ligand field splitting parameter). Considering $\Delta_o/B = 36$, the value of E/B for the spin-allowed transition was determined to be $\nu_1/B = 36$, $\nu_2/B = 46$, and $\nu_3/B = 76$.

Since ν_1 was 14104.37 cm^{-1}, the value of B calculated from the first spin-allowed transition was 391.8 cm^{-1} and Δ was calculated as 14104.37 cm^{-1} from the ratio $\Delta/B = 36$.

It is worth noting that the Racah B parameter in MIL-101 is 391.8 cm^{-1} while that in free Cr^{3+} is 1030 cm^{-1} [42]. Thus, a reduction of about 62% in the Racah B parameter of MIL-101 compared to Cr_2O_3 indicates a strong influence of the terephthalate ligand. Figure 8 presents three spin-enabled electrons in the Tanabe-Sugano diagram of the d^3 system corresponding to the three excited energy levels as follows:

(i) $4A_{2g} \rightarrow 4T_{2g}$ with energy transfer of 1.75 eV corresponds to a wavelength of 709 nm

(ii) $4A2g \rightarrow 4T_{1g}$ with energy transfer of 2.27 eV corresponds to a wavelength of 547 nm

(iii) $4A2g \rightarrow 4T_{1g}$ (P) with energy transfer 3.74 eV corresponds to a wavelength of 332 nm

MIL-101 is constituted from the trimer units (Cr_3O_{16}), which are made up of CrO_6 clusters, wherein a central chromium atom is surrounded by 6 oxygen atoms [18, 22]. As suggested by Bordiga et al. [43] for MOF-5, it is supposed that Cr_3O_{16} clusters in MIL-101, which behave as quantum dots surrounded by six terephthalate ligands, could act as light-absorbing antennae ($h\nu$) then transferring it to Cr_3O_{16}

Table 3: Comparison of the porosity of the present MIL-101 and the results published.

S_{BET} ($m^2 \cdot g^{-1}$)	$S_{Langmuir}$ ($m^2 \cdot g^{-1}$)	V ($cm^3 \cdot g^{-1}$)	Method/purification	References
3360	5059	1.4	Hydrothermal method/Soxhlet extraction using ethanol solvent	The present work
4100	5900	2.0	Hydrothermal method/ethanol and DMF	[22]
4230	—	2.2	Hydrothermal method/double filtration with glass and paper filters, water, ethanol, and NH_4F	[18]
2345	3674	1.3	Microwave-assisted hydrothermal method/ethanol	[32]
3054	4443	2.	Microwave-assisted hydrothermal method/ethanol and DMF	[37]
3197	4546	1.7	Solvothermal process/TMAOH ($(CH_3)_4NOH$)	[13]
2220	—	1.1	Hydrothermal method/ethanol and DMF	[20]
2674	—	1.4	Hydrothermal method/ethanol and DMF	[9]
3360	4792	1.8	Microwave-assisted hydrothermal method/water, ethanol, and NH_4F	[15]

DMF: N,N-dimethylformamide.

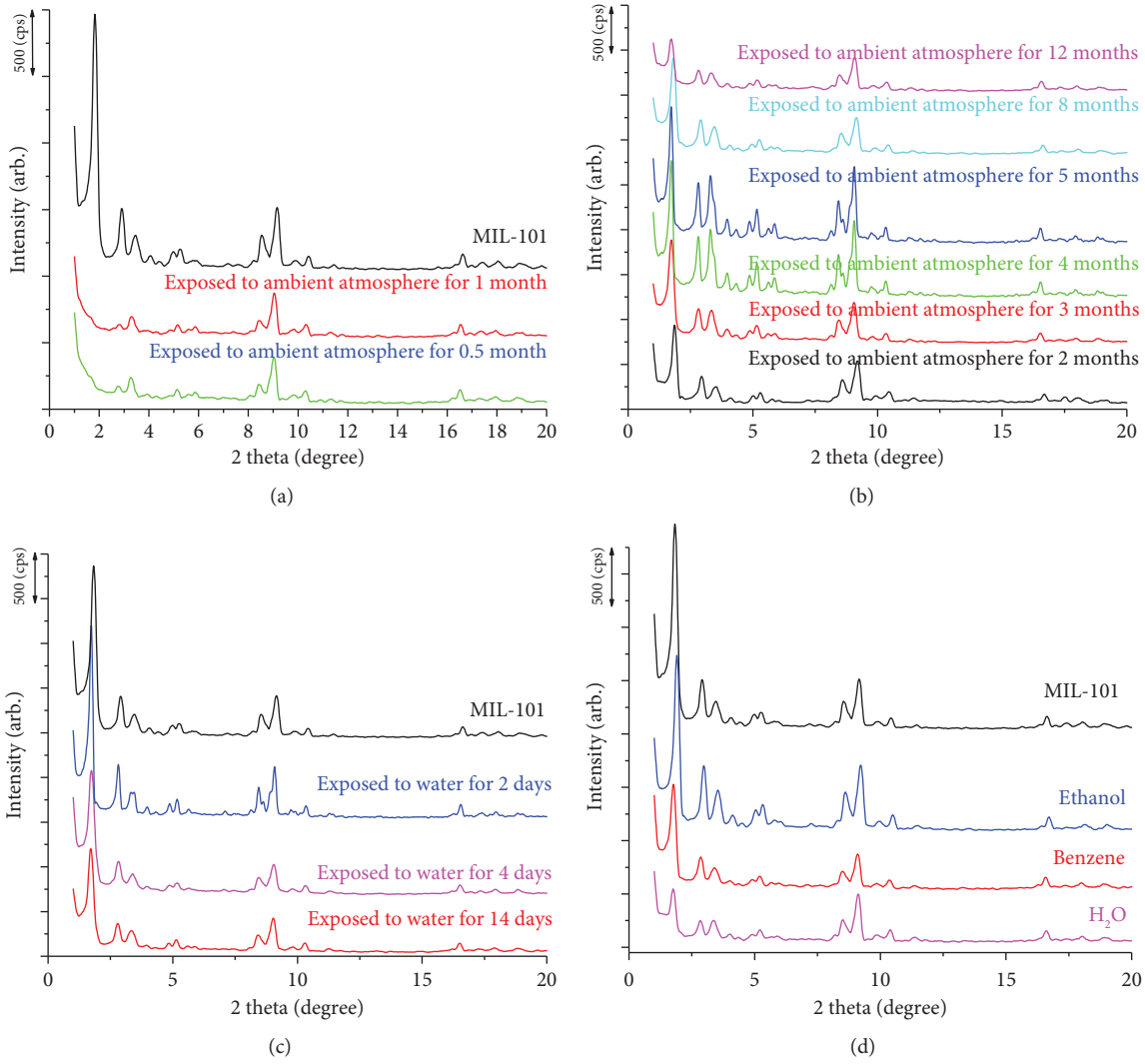

Figure 5: XRD patterns of MIL-101 exposed to ambient atmosphere for several months: (a) MIL-101 sample tested without drying; (b) MIL-101 sample dried at 100°C for 12 h before testing; (c) MIL-101 exposed to water for several days; (d) MIL-101 exposed to several solvents at boiling temperature.

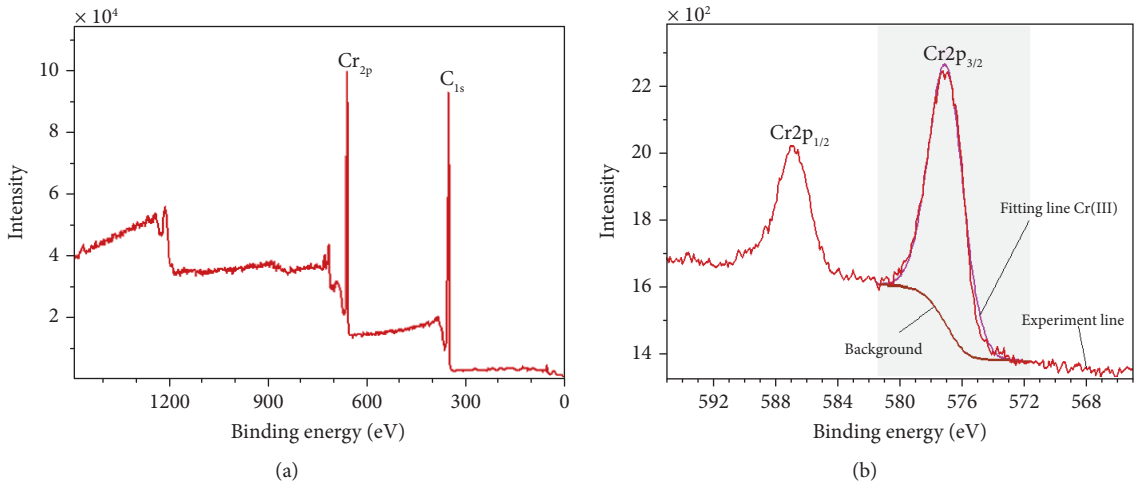

Figure 6: XPS spectra for the MIL-101 (a) and the binding energy of Cr2p (b).

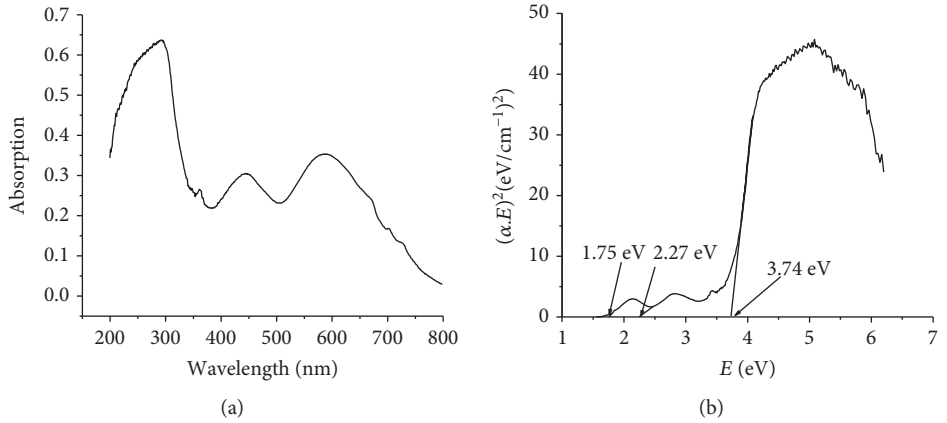

Figure 7: (a) DR-UV-Vis spectrum; (b) Tauc's plot of MIL-101.

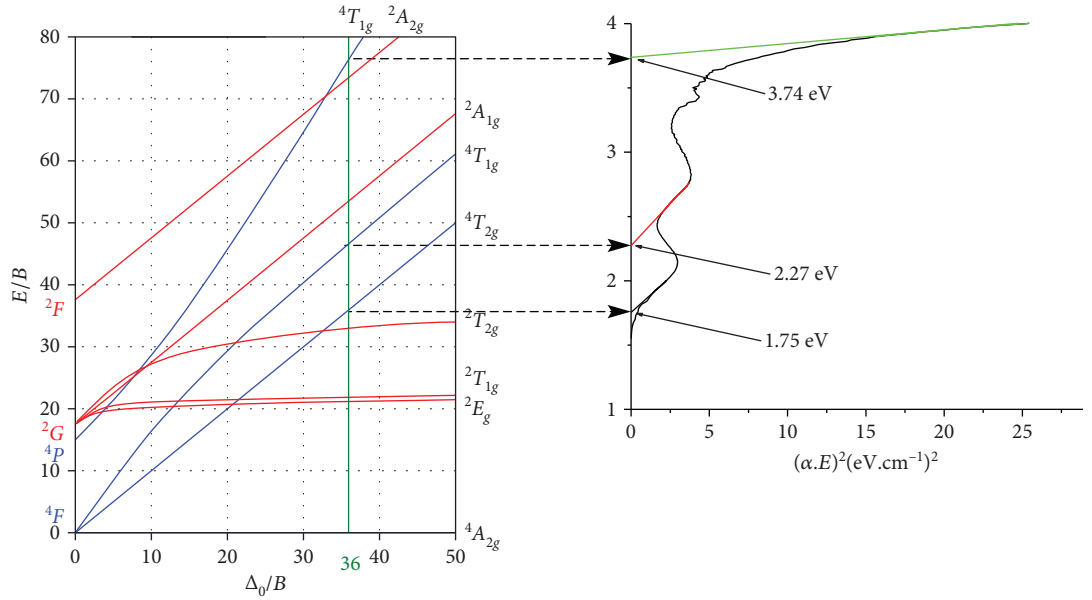

Figure 8: The electron shift corresponding to the three excited energy levels in MIL-101.

clusters to irradiate the photons ($h\nu'$) as can be observed in Figure 9. The photocatalysis of MIL-101 was considered to be achieved by the electron transfer from photoexcited organic ligands to metallic clusters in MIL-101, which was termed as a ligand-to-cluster charge transfer [23, 25].

3.2. Photocatalytic Activity of MIL-101. Adsorption is one of the important aspects of photocatalysis. Hence, in most cases, the dark adsorption is often conducted to obtain an adsorption-desorption equilibrium before UV is irradiated. In the present case, that procedure could not be carried out because the dye molecules were adsorbed quickly on the MIL-101 surface and prevented the UV light from stimulating the MIL-101 catalyst, so that the UV light was irradiated at the same time as the catalyst was introduced as shown in Figure 10. Figure 10(a) shows the decolorization kinetics for RBB dye under different conditions. It was found that the color of the RBB solution with MIL-101 catalyst but without UV irradiation was decolorized around 43% within only 15 min and then stayed constant due to saturated adsorption while the RBB color was removed completely under UV irradiation/MIL-101 catalysis after 45 min. These experiments demonstrated that the decolorization of the solution was due to the photocatalytic effect rather than adsorption.

The kinetics of decolorization of RBB on MIL-101 added with 0.01 g $Cr(NO_3)_3$ or Cr_2O_3 are shown in Figure 10(b). It was found that the Cr^{3+} ion or Cr_2O_3 did not affect decolorization. It could be inferred that the Cr^{3+} ion or Cr_2O_3 does not exhibit photocatalytic activity in this condition. In addition, the decolorization of RBB was not observed if UV was irradiated in the absence of MIL-101 suggesting that RBB was stable and did not undergo photolysis. A leaching experiment was also conducted in which the MIL-101 catalyst was filtered by centrifugation after 5 min of irradiation. The decolorization of dye was stopped despite the fact that UV light irradiation was still maintained. This indicates that there is no leaching of the active species, into the reaction solution, from the homogeneous catalyst. The above experimental results confirmed that MIL-101 was a heterogeneous catalyst in the degradation reaction of RBB.

The influence of the initial concentration of RBB on the photocatalytic decolorization rate in the presence of MIL-101 is shown in Figure 11. The results exhibited that when the dye concentration increased in the range of 10 ppm to 50 ppm, an increase in the decolorization rate was observed.

The generalized rate equation for decolorization of dye can be written as

$$r = -\frac{dC}{dt} = k \cdot C^n, \tag{2}$$

where C is the concentration of dye at time t (the reaction time), k is the kinetic rate constant, n is the order of the reaction, and r is the reaction rate.

In this paper, the initial rate method was used to determine k and n [44, 45].

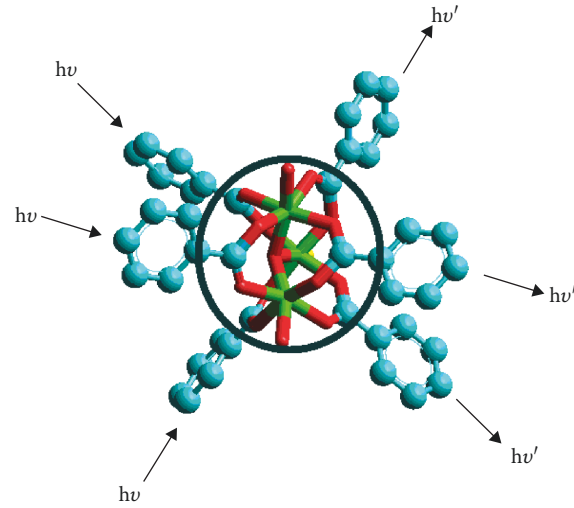

Figure 9: The Cr_3O_{16} cluster of MIL-101 (Cr (green rods), O (red rods), and benzene ring (blue ring)).

The instantaneous reaction rate was calculated from the following equation:

$$r_{\text{in}} = -\frac{dC}{dt}. \tag{3}$$

Integrating equation (3) for the boundary conditions $t \to 0$, then $C \to C_0$ gives

$$C_t = -r_{\text{in}} \cdot t + C_0, \tag{4}$$

where C_0 and C_t are the initial concentration and the concentration at time t, respectively. The instantaneous rate (r_{in}) is determined from the plot of concentration versus time at time t. The initial rate (r_0) of a reaction is the instantaneous rate at the start of the reaction (when $t = 0$). The initial rate is equal to the negative slope of the curve of reactant concentration versus time at $t = 0$. From the slopes of the plots of C_t against t at C_0 ($t = 0$), the values of r_0 corresponding to each initial concentration C_0 was obtained as shown in Figure 12(a).

On the other hand, the initial rate for a reaction can be written as

$$r_0 = k_i \cdot C_0^n, \tag{5}$$

where k_i is the overall observed rate constant for the reaction and n is the order of the reaction with respect to the concentration. The linearization of equation (5) by taking natural logarithms on both sizes yields

$$\ln r_0 = \ln k_i + n \cdot \ln C_0. \tag{6}$$

Therefore, the plot of the $\ln r_0$ against $\ln C_0$ gives a straight line with a slope corresponding to n and the intercept on the ordinate gives $\ln k_i$ (Figure 12(a)). From the plot of $\ln r_{\text{Ao}}$ against $\ln C_{\text{Ao}}$, the slope, $n = 0.604$, and $k = 1.156$

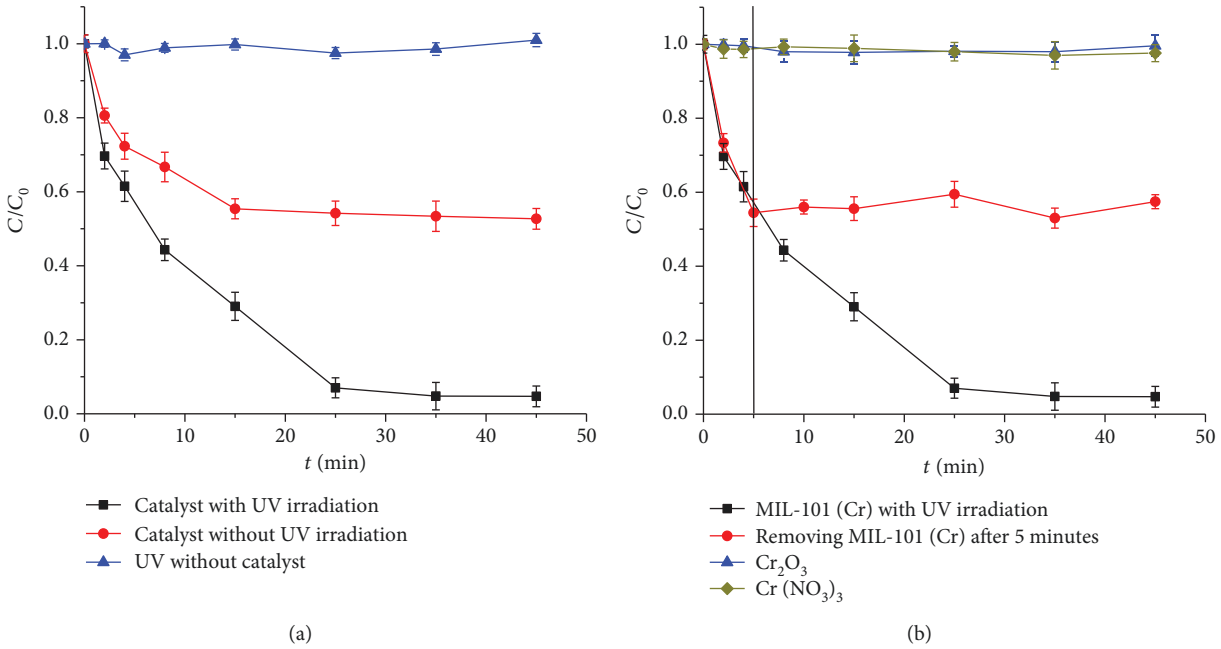

FIGURE 10: (a) The time dependence on decolorization efficiency of the RBB dye with or without MIL-101 catalyst; (b) leaching experiments.

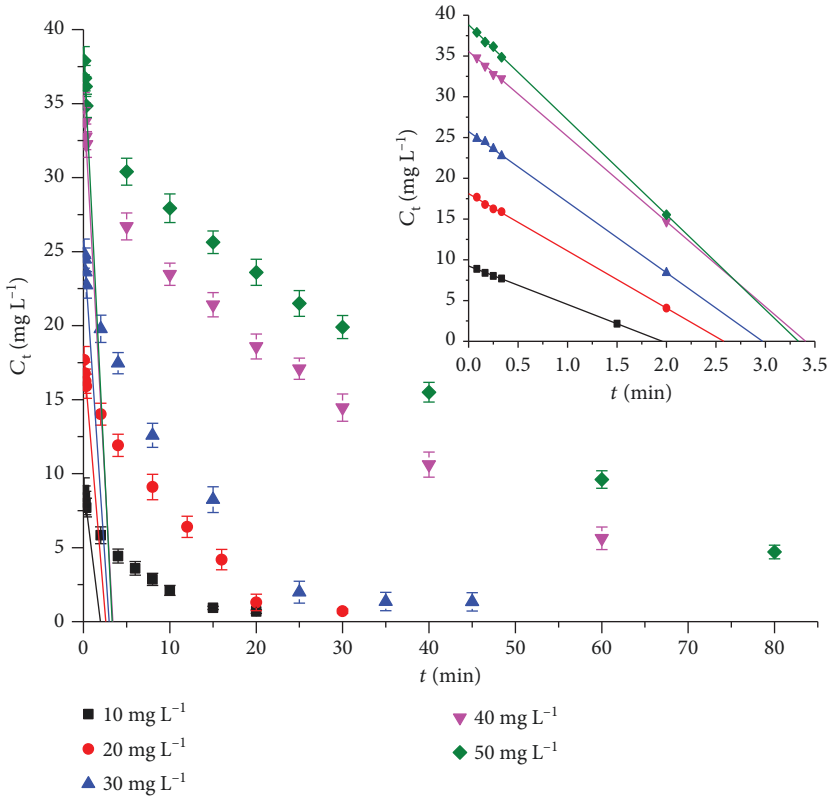

FIGURE 11: The plots of C_t against t (time) and tangent lines at C_0; the inset presents extrapolated tangent lines.

were calculated, and the plot has an excellent correlation coefficient ($r^2 = 0.998$, $p \leq 0.001$). The reaction order of photocatalytic degradation is unity in some cases [27, 46]. In the present paper, the value of n less than unity could be due to the contribution of both adsorption and photocatalytic reaction.

The Langmuir-Hinshelwood (L-H) equation is widely used in studying the kinetics of photocatalytic reaction

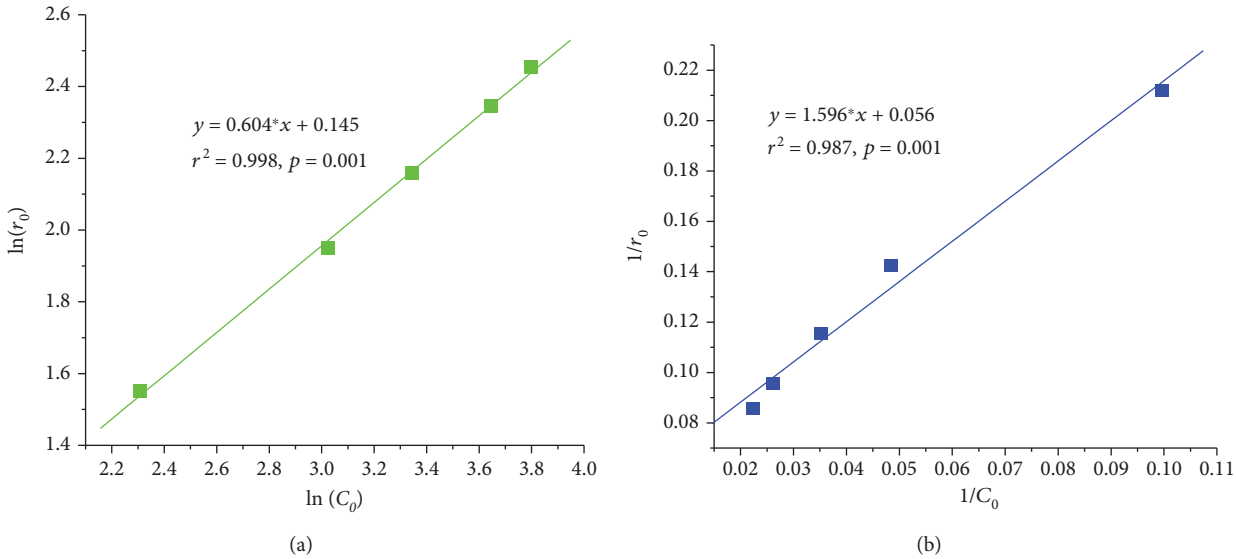

Figure 12: (a) Initial rate plot for RBB to determine the overall rate order; (b) a plot of the Langmuir-Hinshelwood model.

[46, 47]. In this model, the reaction rate depends on the percentage of the surface coverage, θ, by the following equation:

$$r_0 = k_T \cdot \theta = -\frac{dC}{dt} = \frac{k_T \cdot K_{LH} \cdot C_0}{1 + K_{LH} \cdot C_0}, \quad (7)$$

where K_{LH} is the Langmuir-Hinshelwood adsorption equilibrium constant ($L \cdot mg^{-1}$) and k_T is the reaction rate constant ($mg \cdot L^{-1} \cdot min^{-1}$). Equation (7) can be written in the linear form as

$$\frac{1}{r_0} = \frac{1 + K_{LH} \cdot C_0}{k_T \cdot K_{LH} \cdot C_0} = \frac{1}{k_T \cdot K_{LH} \cdot C_0} + \frac{1}{k_T}. \quad (8)$$

The plot of $1/r_0$ against $1/C_0$ (Figure 12(b)) gives a straight line with a good correlation ($r^2 = 0.987$, $p = 0.001$); the values of k_T and K_{LH} were 17.857 $mg \cdot L^{-1} \cdot min^{-1}$ and 0.035 $L \cdot mg^{-1}$, respectively. Akpan and Hameed [46] compared the adsorption and reaction rate relying on the ratio of $k_T : K_{LH}$. However, this comparison seems to be unclear because the units of k_T and K_{LH} are not similar.

The complete degradation of dyes with a cost-effective process is important for industrial applications. UV-Vis spectra are shown in Figure 13(a). The absorbance band at 310 nm was contributed by the $\pi \rightarrow \pi^*$ transition of the double bond in the aromatic ring. The absorbance band at 600 nm was assigned to $n \rightarrow \pi^*$ due to the double bond conjugation of N=N and C=C in the aromatic ring. The absorption peak decreased significantly with an increase in the irradiation time and disappeared after 45 min of irradiation. The chemical oxygen demand (COD) test is shown in Figure 13(b). The COD decreased from an initial value of 86.4 $mg \cdot L^{-1}$ to around 10.0 $mg \cdot L^{-1}$ after 80 min. The results indicate that RBB molecules were degraded into fragments and, subsequently, were completed with minerals.

The photochemical degradation mechanism of RBB dye on MIL-101 can be interpreted by the semiconductor theory [25]. As proved earlier, MIL-101 was photoexcited leading to the electron transitions in the $3d^3$ orbital, followed by the formation of an electron (e^-) and hole (h^+) pair on the surface of the catalyst. The high oxidation potential of the hole (h^+) in the catalyst either permitted the direct oxidation of the dye or reacted with water molecules or hydroxyl ions (OH^-) to generate hydroxyl radicals ($^{\cdot}OH$). These hydroxyl radicals oxidized the surface adsorbed organic molecules. On the other hand, the photogenerated electrons (e^-) reduced the dye or reacted with the O_2 adsorbed on the MIL-101 surface or dissolved in water forming a radical anion ($^{\cdot}O_2^-$). This strong oxidation could degrade RBB. According to this, the photochemical degradation reactions of RBB on MIL-101 can be expressed as follows:

$$\begin{aligned}
&(\text{MIL-101}) + h\nu(\text{MIL-101}) \left(e^- + h^+\right) \\
&h^+ + \text{dye} \rightarrow \text{RBB}^{\cdot} \rightarrow \text{degradation products} \\
&h^+ + H_2O \rightarrow H^+ + {}^{\cdot}OH \\
&h^+ + OH^- \rightarrow {}^{\cdot}OH \\
&{}^{\cdot}OH + \text{RBB}^{\cdot} \rightarrow \text{degradation products} \\
&e^- + O_2 \rightarrow {}^{\cdot}O_2^- \\
&{}^{\cdot}O_2^- + \text{RBB} \rightarrow \text{degradation products}
\end{aligned} \quad (9)$$

The reusability of the catalyst is an important concern in the application of heterogeneous catalysis. After the experiment, the MIL-101 material was collected by centrifugation and washed with water and ethanol for three times to remove RBB completely and dried at 120°C for 15 h and then reused. The photocatalytic degradation efficiency of MIL-101 after four cycles of usage was decreased slightly

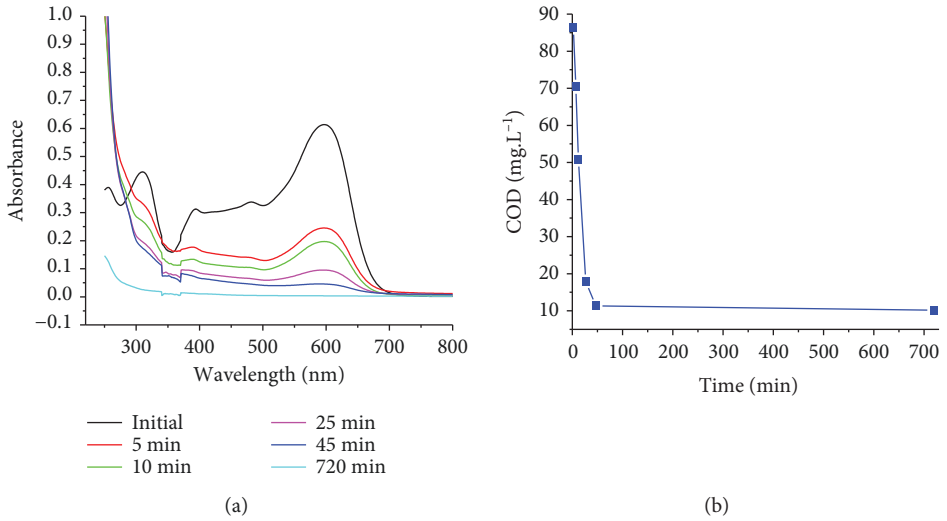

Figure 13: The UV-Vis spectrum (a) and the chemical oxygen demand (COD) test (b) of the RBB dye and RBB degradation over MIL-101(Cr) under UV irradiation.

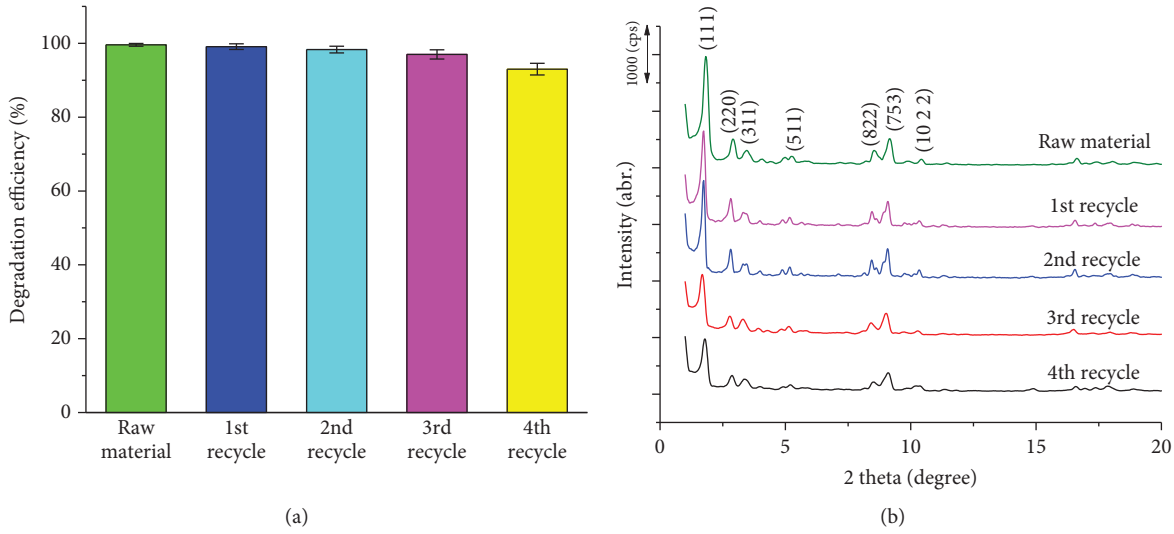

Figure 14: (a) The RBB degradation efficiency of the MIL-101 photocatalyst for the fourth cycle; (b) XRD patterns of MIL-101 and used MIL-101 ($V = 450$ mL; $C_0 = 90\ \text{mg} \cdot \text{L}^{-1}$, UV-irradiation time: 45 min).

(only 5%) (Figure 14(a)). The XRD patterns of the recycled MIL-101 catalysts were unchanged (Figure 14(b)). It can be concluded that the MIL-101 photocatalyst exhibited excellent catalytic recyclability and stability in the tested conditions. It can be inferred that MIL-101 can be a potential catalyst for the treatment of organic pollutants in aqueous solutions.

4. Conclusions

The suitable molar ratios of Cr/H_2BDC and H_2O/H_2BDC for the synthesis of MIL-101 with a large surface area and high crystallinity were 1.25 and 350, respectively. High water content in the synthesized gel significantly reduced particle size and crystallinity. MIL-101 can be exposed to ambient conditions for several months. The characteristic XRD diffraction pattern at 1.7° can be observed in the samples stored in dry conditions, whereas this diffraction disappeared when the samples were stored in moistened conditions. MIL-101 is stable in water, benzene, and toluene even at boiling point for several hours. MIL-101 exhibited excellent photodegradation of RBB in the UV region. The kinetics of the photocatalytic degradation reaction was fitted well with the Langmuir-Hinshelwood (L-H) equation. The initial rate method yielded the order of the reaction and the initial reaction rate constant to be 0.604 and 1.156 $[(\text{mg}\cdot\text{L}^{-1})^{0.396}\cdot\text{min}^{-1}]$, respectively.

Data Availability

The data used to support the findings of this study are available from the corresponding author upon request.

Conflicts of Interest

The authors declare that they have no conflict of interest.

Acknowledgments

This research was sponsored by Hue University under Decision No. 1208/QĐ-DHH.

References

[1] F. P. van der Zee and S. Villaverde, "Combined anaerobic–aerobic treatment of azo dyes—a short review of bioreactor studies," *Water Research*, vol. 39, no. 8, pp. 1425–1440, 2005.

[2] P. A. Soloman, C. A. Basha, M. Velan, V. Ramamurthi, K. Koteeswaran, and N. Balasubramanian, "Electrochemical degradation of Remazol Black B dye effluent," *Clean - Soil, Air, Water*, vol. 37, no. 11, pp. 889–900, 2009.

[3] M. Thi Thanh, T. Vinh Thien, V. Thi Thanh Chau, P. Dinh Du, N. Phi Hung, and D. Quang Khieu, "Synthesis of iron doped zeolite imidazolate framework-8 and its Remazol deep black RGB dye adsorption ability," *Journal of Chemistry*, vol. 2017, 18 pages, 2017.

[4] N. F. Cardoso, R. B. Pinto, E. C. Lima et al., "Removal of Remazol Black B textile dye from aqueous solution by adsorption," *Desalination*, vol. 269, no. 1-3, pp. 92–103, 2011.

[5] V. P. Ranjusha, R. Pundir, K. Kumar, M. G. Dastidar, and T. R. Sreekrishnan, "Biosorption of Remazol Black B dye (azo dye) by the growing Aspergillus flavus," *Journal of Environmental Science and Health, Part A*, vol. 45, no. 10, pp. 1256–1263, 2010.

[6] M. T. Thanh, T. V. Thien, P. D. Du, N. P. Hung, and D. Q. Khieu, "Iron doped zeolitic imidazolate framework (Fe-ZIF-8): synthesis and photocatalytic degradation of RDB dye in Fe-ZIF-8," *Journal of Porous Materials*, vol. 25, no. 3, pp. 857–869, 2018.

[7] C. Janiak and J. K. Vieth, "MOFs, MILs and more: concepts, properties and applications for porous coordination networks (PCNs)," *New Journal of Chemistry*, vol. 34, no. 11, pp. 2366–2388, 2010.

[8] O. M. Yaghi, M. O'Keeffe, N. W. Ockwig, H. K. Chae, M. Eddaoudi, and J. Kim, "Reticular synthesis and the design of new materials," *Nature*, vol. 423, no. 6941, pp. 705–714, 2003.

[9] P. Chowdhury, C. Bikkina, and S. Gumma, "Gas adsorption properties of the chromium-based metal organic framework MIL-101," *Journal of Physical Chemistry C*, vol. 113, no. 16, pp. 6616–6621, 2009.

[10] L. Hamon, C. Serre, T. Devic et al., "Comparative study of hydrogen sulfide adsorption in the MIL-53(Al, Cr, Fe), MIL-47(V), MIL-100(Cr), and MIL-101(Cr) metal-organic frameworks at room temperature," *Journal of the American Chemical Society*, vol. 131, no. 25, pp. 8775–8777, 2009.

[11] Y. Li and R. T. Yang, "Hydrogen storage in metal-organic and covalent-organic frameworks by spillover," *AICHE Journal*, vol. 54, no. 1, pp. 269–279, 2008.

[12] P. L. Llewellyn, S. Bourrelly, C. Serre et al., "High uptakes of CO2 and CH4 in mesoporous metal—organic frameworks MIL-100 and MIL-101," *Langmuir*, vol. 24, no. 14, pp. 7245–7250, 2008.

[13] J. Yang, Q. Zhao, J. Li, and J. Dong, "Synthesis of metal-organic framework MIL-101 in TMAOH-$Cr(NO_3)_3$-H_2BDC-H_2O and its hydrogen-storage behavior," *Microporous and Mesoporous Materials*, vol. 130, no. 1-3, pp. 174–179, 2010.

[14] K. Yang, Q. Sun, F. Xue, and D. Lin, "Adsorption of volatile organic compounds by metal-organic frameworks MIL-101: influence of molecular size and shape," *Journal of Hazardous Materials*, vol. 195, pp. 124–131, 2011.

[15] Z. Zhang, S. Huang, S. Xian, H. Xi, and Z. Li, "Adsorption equilibrium and kinetics of CO_2 on chromium terephthalate MIL-101," *Energy & Fuels*, vol. 25, no. 2, pp. 835–842, 2011.

[16] R. Kitaura, K. Seki, G. Akiyama, and S. Kitagawa, "Porous coordination-polymer crystals with gated channels specific for supercritical gases," *Angewandte Chemie International Edition*, vol. 42, no. 4, pp. 428–431, 2003.

[17] S. Ma, D. Sun, X.-S. Wang, and H.-C. Zhou, "A mesh-adjustable molecular sieve for general use in gas separation," *Angewandte Chemie International Edition*, vol. 46, no. 14, pp. 2458–2462, 2007.

[18] D. Y. Hong, Y. K. Hwang, C. Serre, G. Férey, and J. S. Chang, "Porous chromium terephthalate MIL-101 with coordinatively unsaturated sites: surface functionalization, encapsulation, sorption and catalysis," *Advanced Functional Materials*, vol. 19, no. 10, pp. 1537–1552, 2009.

[19] Y. K. Hwang, D. Y. Hong, J. S. Chang et al., "Selective sulfoxidation of aryl sulfides by coordinatively unsaturated metal centers in chromium carboxylate MIL-101," *Applied Catalysis A: General*, vol. 358, no. 2, pp. 249–253, 2009.

[20] N. Maksimchuk, M. Timofeeva, M. Melgunov et al., "Heterogeneous selective oxidation catalysts based on coordination polymer MIL-101 and transition metal-substituted polyoxometalates," *Journal of Catalysis*, vol. 257, no. 2, pp. 315–323, 2008.

[21] Z. Saedi, S. Tangestaninejad, M. Moghadam, V. Mirkhani, and I. Mohammadpoor-Baltork, "MIL-101 metal-organic framework: a highly efficient heterogeneous catalyst for oxidative cleavage of alkenes with H_2O_2," *Catalysis Communications*, vol. 17, pp. 18–22, 2012.

[22] G. Férey, C. Mellot-Draznieks, C. Serre et al., "A chromium terephthalate-based solid with unusually large pore volumes and surface area," *Science*, vol. 309, no. 5743, pp. 2040–2042, 2005.

[23] J. Gascon, M. D. Hernández-Alonso, A. R. Almeida, G. P. M. van Klink, F. Kapteijn, and G. Mul, "Isoreticular MOFs as efficient photocatalysts with tunable band gap: an operando FTIR study of the photoinduced oxidation of propylene," *ChemSusChem*, vol. 1, no. 12, pp. 981–983, 2008.

[24] C. G. Silva, A. Corma, and H. García, "Metal–organic frameworks as semiconductors," *Journal of Materials Chemistry*, vol. 20, no. 16, pp. 3141–3156, 2010.

[25] F. X. Llabre, A. Corma, H. Garcia, D. Valencia, and C. De Vera, "Applications for metal-organic frameworks (MOFs) as quantum dot semiconductors," *Journal of Physical Chemistry C*, vol. 111, pp. 80–85, 2006.

[26] Q. Xu, Y. Wang, G. Jin et al., "Photooxidation assisted sensitive detection of trace Mn^{2+}in tea by NH_2-MIL-125 (Ti) modified carbon paste electrode," *Sensors and Actuators B: Chemical*, vol. 201, pp. 274–280, 2014.

[27] J. J. Du, Y. P. Yuan, J. X. Sun et al., "New photocatalysts based on MIL-53 metal-organic frameworks for the decolorization of methylene blue dye," *Journal of Hazardous Materials*, vol. 190, no. 1-3, pp. 945–951, 2011.

[28] N. V. Maksimchuk, K. A. Kovalenko, V. P. Fedin, and O. A. Kholdeeva, "Heterogeneous selective oxidation of alkenes to α,β-unsaturated ketones over coordination polymer MIL-101," *Advanced Synthesis and Catalysis*, vol. 352, no. 17, pp. 2943–2948, 2010.

[29] S. J. Lee, J. W. Yoon, Y. K. Seo et al., "Effect of purification conditions on gas storage and separations in a chromium-based metal-organic framework MIL-101," *Microporous and Mesoporous Materials*, vol. 193, pp. 160–165, 2014.

[30] D. Liu, Y. S. Lin, Z. Li, and H. Xi, "Adsorption and separation of CH_4/H_2 in MIL-101s by molecular simulation study," *Chemical Engineering Science*, vol. 98, pp. 246–254, 2013.

[31] Q. Liu, L. Ning, S. Zheng, M. Tao, Y. Shi, and Y. He, "Adsorption of carbon dioxide by MIL-101(Cr): regeneration conditions and influence of flue gas contaminants," *Scientific Reports*, vol. 3, no. 1, 2013.

[32] M. S. El-Shall, V. Abdelsayed, A. E. R. S. Khder, H. M. A. Hassan, H. M. El-Kaderi, and T. E. Reich, "Metallic and bimetallic nanocatalysts incorporated into highly porous coordination polymer MIL-101," *Journal of Materials Chemistry*, vol. 19, no. 41, pp. 7625–7631, 2009.

[33] Y. Xu, Q. Chen, H. Yang et al., "Enhanced photodegradation of rhodamine B under visible light by N-$K_2Ti_4O_9$/MIL-101 composite," *Materials Science in Semiconductor Processing*, vol. 36, pp. 115–123, 2015.

[34] M. Lv, H. Yang, Y. Xu, Q. Chen, X. Liu, and F. Wei, "Improving the visible light photocatalytic activities of $Bi_{25}FeO_{40}$/MIL-101/PTH via polythiophene wrapping," *Journal of Environmental Chemical Engineering*, vol. 3, no. 2, pp. 1003–1008, 2015.

[35] L. S. Clesceri, A. E. Greenberg, and R. R. Trussell, *Standard Methods for the Examination of Water and Wastewater*, American Public Health Association, 20th edition, 1998.

[36] N. A. Khan, I. J. Kang, H. Y. Seok, and S. H. Jhung, "Facile synthesis of nano-sized metal-organic frameworks, chromium-benzenedicarboxylate, MIL-101," *Chemical Engineering Journal*, vol. 166, no. 3, pp. 1152–1157, 2011.

[37] Z. Zhao, X. Li, S. Huang, Q. Xia, and Z. Li, "Adsorption and diffusion of benzene on chromium-based metal organic framework MIL-101 synthesized by microwave irradiation," *Industrial and Engineering Chemistry Research*, vol. 50, no. 4, pp. 2254–2261, 2011.

[38] B. Panella and M. Hirscher, "Hydrogen physisorption in metal-organic porous crystals," *Advanced Materials*, vol. 17, no. 5, pp. 538–541, 2005.

[39] Y. Li and R. T. Yang, "Gas adsorption and storage in metal –organic framework MOF-177," *Langmuir*, vol. 23, no. 26, pp. 12937–12944, 2007.

[40] K. S. Lin, A. K. Adhikari, Y. H. Su, C. L. Chiang, and K. Dehvari, "Structural characterization of chromium atoms in MIL-101 metal organic frameworks using XANES/EXAFS spectroscopy," *Chinese Journal of Physics*, vol. 50, pp. 322–342, 2012.

[41] T. Van Vu, H. Kosslick, A. Schulz et al., "Selective hydroformylation of olefins over the rhodium supported large porous metal–organic framework MIL-101," *Applied Catalysis A: General*, vol. 468, pp. 410–417, 2013.

[42] Q. Wei, "Investigations of the optical and EPR spectra for Cr^{3+} ions in diammonium hexaaqua magnesium sulphate single crystal," *Acta Physica Polonica A*, vol. 118, no. 4, pp. 670–672, 2010.

[43] S. Bordiga, C. Lamberti, G. Ricchiardi et al., "Electronic and vibrational properties of a MOF-5 metal–organic framework: ZnO quantum dot behaviour," *Chemical Communications*, vol. 5, pp. 2300-2301, 2004.

[44] C. Galindo, P. Jacques, and A. Kalt, "Photooxidation of the phenylazonaphthol AO_{20} on TIO_2: kinetic and mechanistic investigations," *Chemosphere*, vol. 45, no. 6-7, pp. 997–1005, 2001.

[45] S. Khezrianjoo, "Langmuir-Hinshelwood kinetic expression for the photocatalytic degradation of metanil yellow aqueous solutions by ZnO catalyst," *Chemical Science*, vol. 85, pp. 1–7, 2012.

[46] U. G. Akpan and B. H. Hameed, "Photocatalytic degradation of 2,4-dichlorophenoxyacetic acid by Ca–Ce–W–TiO_2 composite photocatalyst," *Chemical Engineering Journal*, vol. 173, no. 2, pp. 369–375, 2011.

[47] M. Saquib and M. Muneer, "TiO_2/mediated photocatalytic degradation of a triphenylmethane dye (gentian violet), in aqueous suspensions," *Dyes and Pigments*, vol. 56, no. 1, pp. 37–49, 2003.

Hindawi
Journal of Nanomaterials
Volume 2019, Article ID 5942194, 31 pages
https://doi.org/10.1155/2019/5942194

Review Article

Metaloxide Nanomaterials and Nanocomposites of Ecological Purpose

Tetiana A. Dontsova, Svitlana V. Nahirniak, and Ihor M. Astrelin

Department of Inorganic Substances, Water Purification, and General Chemical Technology, National Technical University of Ukraine "Igor Sikorsky Kyiv Polytechnic Institute", Kyiv 03056, Ukraine

Correspondence should be addressed to Tetiana A. Dontsova; dontsova@xtf.kpi.ua

Received 28 November 2018; Revised 3 March 2019; Accepted 14 March 2019; Published 30 April 2019

Guest Editor: Ziyou Zhou

The features of the properties and creation of nanocomposite metal oxide materials, especially TiO_2, ZnO, SnO_2, ZrO_2, and Fe_3O_4, and their applications for ecology are considered in the article. It is shown that nanomaterials based on them are very promising for use in the ecological direction, especially as sorbents, photocatalysts, and sensitive layers of gas sensors. The crystallochemical characteristics, surface structure, and surface phenomena that occur when they enter the water and air environment are given for these metal oxides, and it is shown that they play a significant role in obtaining the sorption and catalytic characteristics of these nanomaterials. Particular attention is paid to the dispersion and morphology of metal oxide particles by which their physical and chemical properties can be controlled. Synthesis methods of metal oxide nanomaterials and ways for creating of nanocomposites based on them are characterized, and it is noted that there are many methods for obtaining individual nanoparticles of metal oxides with certain properties. The main task is the correct selection and testing of parameters. The prospects for the production of metal oxide nanocomposites and their application for environmental applications are noted, which will lead to a fundamentally new class of materials and new environmental technologies with their participation.

1. Introduction

Nanomaterials based on metal oxides (nanostructured and nanodispersed) are a diverse class of materials in terms of electronic structure and physical, chemical, and electromagnetic properties [1]. The application of metal oxide nanomaterials and nanocomposites based on them is becoming increasingly popular in applied ecology, especially where they can be used as adsorbents and photocatalysts as well as a material for the manufacture of environmental monitoring devices. Adsorption materials based on nanosized metal oxides have a large specific surface area, high capacity, fast kinetics, and specific affinity for various contaminants [2–5]. The use of nanostructured metal oxides in photocatalytic processes allows the oxidation of organic compounds that are not decomposed biochemically, and the pretreatment of aqueous solutions by their use is considered to be the most promising [2, 6, 7]. Metal oxide nanostructures used in environmental monitoring as sensitive layers of chemoresistive gas sensors are characterized by high values of the sensory signal due to the large specific surface area; hence, a higher adsorption capacity [8–10].

Consequently, nanosized metal oxide materials are of considerable interest because of significant advantages over bulk analogues and, of course, because they have great prospects for obtaining new types of adsorbents, photocatalysts, and sensitive layers of gas sensors based on them. However, nanostructured and nanodispersed oxides also have a significant drawback—their application can lead to environmental pollution with nanoparticles. In this case, it is promising to create metal-oxide nanocomposites—an extremely interesting type of nanomaterial due to their properties—that may exceed the properties of its individual phases by order. The use of the latter will prevent the loss of metal oxide nanoparticles due to the stabilization of the nanoparticles in the composite's matrix, which will also positively affect the separation process after the completion of the processes of sorption and photocatalysis [4]. In addition, nanocomposites due to their

structure have special, sometimes unique, physical and chemical properties, and they can be applied in a wide variety of fields, including the production of new materials for use in the fields of medicine, energy, and ecology.

The purpose of this work is to consider the features and potential use of the metal oxide nanomaterials and nanocomposites based on TiO_2, ZnO, SnO_2, ZrO_2, and Fe_3O_4 for environmental applications. The crystallochemical structures of selected metal oxides, the features of their surface structure, and their possible surface phenomena in water and air environments are considered in the article. Their physical, chemical, sorptive, and photocatalytic properties are also provided for an understanding of their more efficient usage. We also reviewed what we considered the most promising synthesis methods of individual oxides in terms of ease of implementation, and the existing approaches for the creation of nanocomposite metal oxide materials of ecological direction in the literature are presented.

2. Crystallochemical Characteristics of Metal Oxides and Their Surface Structure

2.1. Crystallochemical Structures of TiO_2, ZnO, SnO_2, ZrO_2, and Fe_3O_4. In nature, TiO_2 exists in three different crystalline structures: rutile, anatase, and brookite. In all modifications, the structural unit of the TiO_2 crystalline lattice is the distorted TiO_6 octahedra, joined together by common vertices or ribs, i.e., each Ti^{4+} ion is surrounded by six O^{2-} ions, and each O^{2-} ion is surrounded by three Ti^{4+} ions. Octahedra are arranged in such a way that each oxygen ion belongs to three octahedra [11]. In rutile, the octahedra of TiO_6 are connected with two adjacent octahedra along the edges in the (001) plane, resulting in longitudinal bands in the crystal lattice. In anatase, the octahedra of TiO_6 are connected along the edges lying in the (001) and (100) planes. Thus, each octahedron has four common ribs with neighbors that form zigzag chains. There are 4 common ribs for one octahedron in anatase and 2 in rutile. Hence, the elementary cell of anatase consists of four TiO_2 molecules, while that of rutile consists of only two (see Figure 1).

At atmospheric pressure and temperature, anatase is less dense and less stable than rutile. In the brookite structure, each octahedron of TiO_6 has two common ribs with its neighbors and also forms zigzag chains. The Ti–O bond lengths in these structures are 0.195-0.198, 0.194-0.197, and 0.187-0.204 nm for rutile, anatase, and brookite, respectively [12]. The parameters and some characteristics of all of the TiO_2 modifications are shown in Table 1.

When heated, both anatase and brookite irreversibly transform into rutile. The temperature transition depends on many factors, including impurities, the obtainment method, the precursor type, and the size of the final crystal. Also, the direct obtainment of the particular phase can be realized by adjusting the finite particle size [13].

Zinc oxide crystallizes in three modifications: hexagonal wurtzite, cubic sphalerite, and cubic modification of the NaCl type, which is rare. Only the hexagonal wurtsite is thermodynamically stable under normal conditions. Cubic sphalerite can be obtained when growing ZnO on the substrates with a cubic lattice. ZnO with the NaCl structure is obtained at relatively high pressures [14].

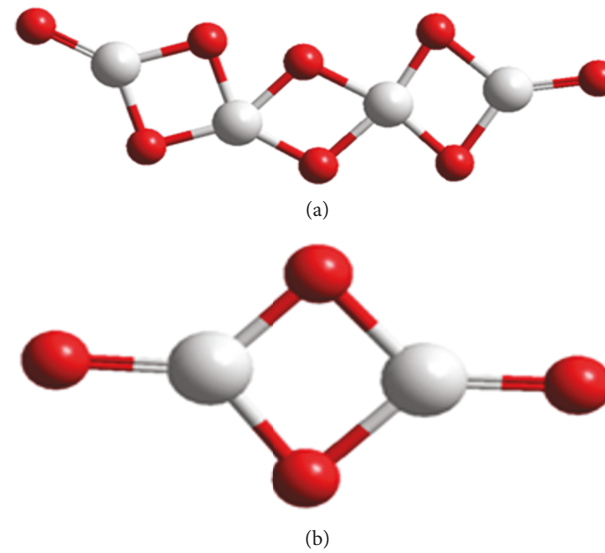

Figure 1: Elementary cells of rutile (a) and anatase (b): titanium—white; oxygen—red.

The wurtsite structure is obtained from the hexagonal close-packed lattice consisting of two interpenetrating packed hexagonal Bravais lattices based on the positions (0 0 0) and $(a/2\sqrt{3}a/c\ c/2)$. In the ideal tetrahedral surroundings, the constants a and c are correlated with each other as $c/a = \sqrt{8/13}$. In real structures, there are deviations from this relationship. The ZnO structure can be described as the series of alternating planes composed of tetrahedrally coordinated O^{2-} and Zn^{2+} arranged one on top of another along the c axis. O^{2-} and Zn^{2+} form the tetrahedral unit, and the whole structure is devoid of central symmetry (see Figure 2). [15].

SnO_2 has only one stable phase, the mineral form of which is known as cassiterite. Tin (IV) oxide crystallizes in the tetragonal structure of rutile, the parameters and characteristics of which are given in Table 1. In the rutile structure, tin atoms are located at the center and surrounded by six oxygen atoms, which are located at the corners of the almost regular octahedron. Atoms of oxygen are surrounded by three tin atoms, which form an equilateral triangle. The length of the Sn–O bond is 0.209-0.216 nm [16, 17].

ZrO_2 also exists in three crystalline modifications (see Figure 3): monoclinic, tetragonal, and cubic. The cubic ZrO_2 has a fluorite structure, in the crystal lattice of which each zirconium atom has eight bonds with oxygen atoms. Thus, zirconium atoms form face-centered cubic lattices with oxygen atoms occupying the position in tetrahedral interstices. Consequently, the elementary cell of cubic ZrO_2 contains one zirconium atom and two atoms of oxygen; the length of the Zr–O bond is 0.221 nm [18, 19].

The tetragonal ZrO_2 can be considered as a slightly distorted cubic structure (see Figure 3(b)). In the crystalline tetragonal structure of ZrO_2, zirconium atoms are also bound to eight oxygen atoms—four neighboring oxygen atoms are located at the tetrahedron plane with a Zr–O bond length of 0.207 nm, while the other oxygen atoms are located at a

Table 1: Parameters of TiO_2, ZnO, SnO_2, ZrO_2, and Fe_3O_4 crystalline lattices and some of their characteristics [11, 14–16, 19, 23].

Phase	Space group	Lattice parameters (nm)	Volumetric density (g/cm^3)	Band gap (eV)
TiO_2 tetragonal (rutile)	P4/mnm	$a = 0.4585$, $c = 0.2953$	4.3	3.0
TiO_2 tetragonal (anatase)	I4/amd	$a = 0.3784$, $c = 0.9515$	3.9	3.2
TiO_2 rhombic (brookite)	Pbca	$a = 0.9184$, $b = 0.5447$, $c = 0.5145$	4.1	3.3
ZnO hexagonal	$P6_3mc$	$a = 0.3249$, $c = 0.5206$	5.6	3.4
SnO_2 tetragonal (cassiterite)	$P4_2/nmm$	$a = 0.4738$, $c = 0.3188$	7.0	3.6
ZrO_2 monoclinic (baddeleyite)	$P2_1/c$	$a = 0.5169$, $b = 0.5232$, $c = 0.5341$	5.6	5.8
ZrO_2 tetragonal	$P4_2/nmc$	$a = 0.514$, $b = 0.527$, $a/c = 1.02$ (at 1523 K)	6.1	5.8
ZrO_2 cubic	Fm/3m	$a = 0.5256$ (at 2603 K)	6.3	6.1
Fe_3O_4 cubic (magnetite)	Fd/3m	$a = 0.8396$	5.2	~2

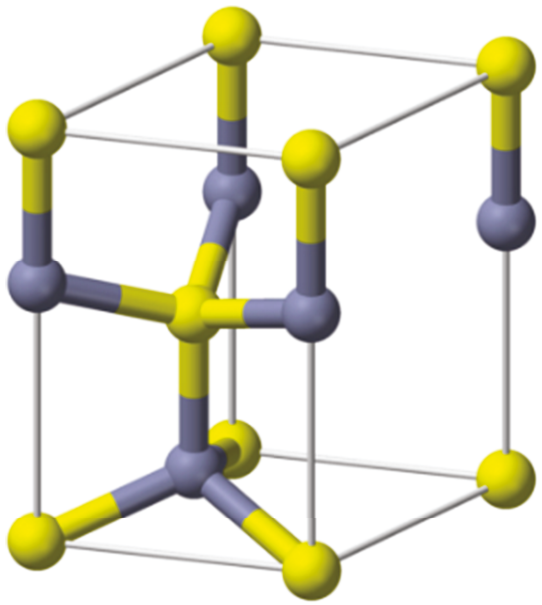

Figure 2: Elementary cell of wurtzite: zinc—violet; oxygen—yellow.

90° angle to the tetrahedron plane at a distance of 0.246 nm from the zirconium atoms [19, 20]. The monoclinic ZrO_2 is formed by further distortion of the tetragonal structure (see Figure 3(c)). It is even less symmetric and is represented by 12 atoms of an elementary cell and more complex geometric structures. In the monoclinic ZrO_2, zirconium atoms have seven bonds with oxygen. In the space, the oxygen atoms form angles of 134.5° and 109.5°. Consequently, the atoms of oxygen are not in the same plane. In the crystalline structure of the monoclinic ZrO_2, the interatomic distances of Zr–O vary considerably; however, they have average values of 0.207 nm and 0.221 nm [20, 21]. Some structural characteristics of ZrO_2 are given in Table 1.

The monoclinic ZrO_2 modification is the most stable, and transition to it occurs during cooling from 1273 K to 923 K. On the contrary, during heating, the monoclinic phase is transformed into a tetragonal modification, starting at 1093 K. At the same time, the tetragonal modification exists even up to 1443 K [22]. Consequently, the tetragonal ZrO_2 modification is unstable and can be stabilized by using dopants (usually rare earth oxides, calcium, magnesium, and iron). Cubic ZrO_2 has the highest strength and density. However, the like tetragonal modification, it is also unstable. To stabilize the cubic modification, the same dopants for the tetragonal modification are used; however, larger amounts are used.

Magnetite belongs to the class of spinel, which has the general formula AB_2O_4, where A and B are cations of divalent and trivalent metals, respectively. The structure of spinel is based on the face-centered cubic lattice with oxygen atoms, in which 1/8 tetrahedral and 1/2 octahedral positions are occupied. Magnetite has the structure of an inverse spinel, in which the elementary cell contains 32 oxygen anions with 64 tetrahedral and 32 octahedral cavities, where the Fe (III) ions are randomly distributed between the octahedral and tetrahedral positions, and the Fe (II) ions are found only in the octahedral positions [23, 24]. The parameters of the magnetite crystalline lattice and some of its characteristics are presented in Table 1.

2.2. Features of the Metal Oxide Surface Structure. The surface of metal oxides plays a major role in adsorption processes, heterogeneous (photo)catalysis, detection of molecules in the gas environment, etc., since in these cases all molecular and chemical processes occur on the surface of metal oxide crystals. The surface is considered as the transition region from the crystal volume to the environment that is in contact with the atmosphere, which leads to the formation of oxide layers, depositions on the surface, or penetration into the water vapor, carbon atoms, and other chemical compounds. Therefore, the actual surfaces of the crystals are too complicated to study, so it is usually assumed that they are atomically clean and smooth surfaces, which are considered as simplified models of real systems.

To a certain extent, they are similar to bulk crystals in terms of their structural properties and reactivity surfaces; however, there are a number of differences that can fundamentally distinguish their surface from that of bulk crystals. These consist of the arrangement of atoms and ions, which is different from the location found in bulk crystals; the ionic mobility of the particles on the surface; the number and nature of defects and dislocations; the presence of surface groups with different chemical compositions on them; the

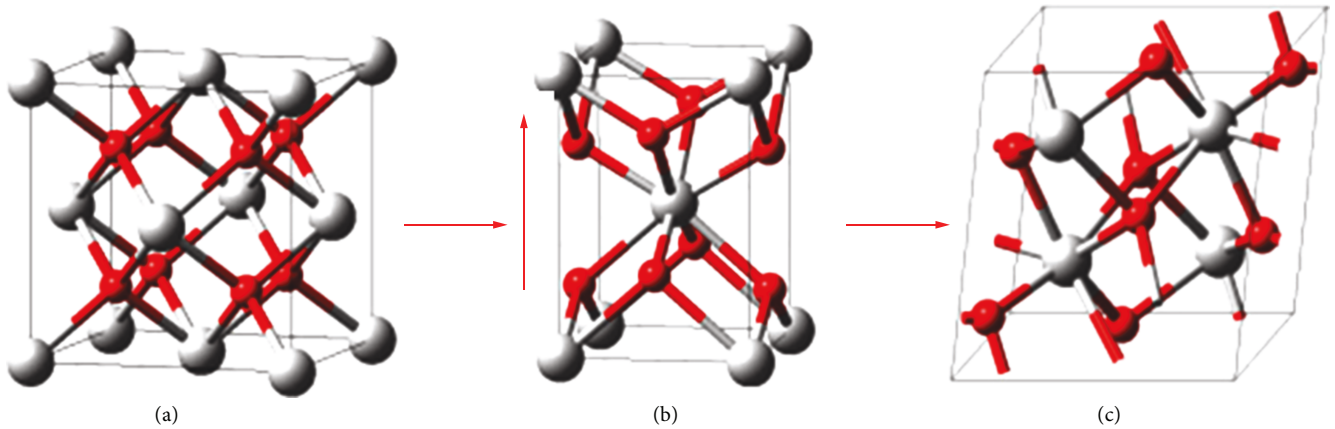

Figure 3: Distortion of ZrO_2 crystalline lattices: cubic (a), tetragonal (b), and monoclinic (c).

ability of the surface for adsorptive concentration of matter from adjacent volumetric phases; and the wider set of possible structures corresponding to this solid material than in the volume [25]. Also, chemical bond types that are unique or rarely encountered can be realized on the surface. This is due to the following factors: the presence of the phase separation boundary, which sharply differs in electrical and chemical properties; the reduction of symmetry on the surface, which facilitates the appearance of attenuated, intermediate, and deformed bonds; the presence of defects in the structure, as well as mechanical stresses, resulting in the redistribution of electronic density; and finally, the incomplete saturation of bonds in the surface structures [25]. So, proceeding from this, the surface is the special state of matter with its chemistry.

Many papers were preoccupied in both experimental and theoretical studies of the surface structure and its influence on the TiO_2 properties [11, 26–48]. The results of these studies indicate that the definition of the surface structure of TiO_2 and defects on it is rather the complex issue, especially because of the presence of Magneli phases, which for TiO_2 fluctuates between Ti_2O_3 and TiO_2 [44, 45]. In addition, titanium (IV) oxide is characterized by a variety of TiO_2 crystalline structures; hence, in the first place, the structure of its surface will be determined by the phase composition.

The main building unit of titanium (IV) oxide structures is Ti_2O_4 or Ti_4O_8. In all three structures of titanium (IV) oxide, the scaling is carried out by the multiplication of octahedra for the triple-coordinated oxygen atom $O^{(3)}$. The features of the structure of bulk crystals of rutile and anatase and the most thermodynamically stable faces (110) and (101) are shown in Figures 4(a) and 4(b).

From Figure 4, it is evident that both surfaces have six and five times coordinated atoms of titanium $Ti^{(6)}$ and $Ti^{(5)}$, and triple- and double-coordinated atoms of oxygen $O^{(3)}$ and $O^{(2)}$ [42, 46–48]. The presence or absence of the latter (the so-called bridge oxygen atoms) can change the electronic structure of the bulk material and the surface energy of the faces; hence, the finite properties of TiO_2.

The ZnO surface is studied by examining faces $(10\bar{1}0)$ and $(11\bar{2}0)$ [49]. At the same time, the physical and chemical properties of ZnO are primarily affected by their own defects caused by the absence or presence of zinc or oxygen in the lattice [50]. Therefore, in the case of ZnO, the surface structure and its properties primarily depend on its stoichiometry.

The surface of zinc oxide is the most studied $(10\bar{1}0)$ (see Figure 5). In the stoichiometric ZnO, the shortening of the Zn–O bond from 0.198 nm to 0.183 nm is observed due to the surface relaxation on this face. As a result, a slight transformation occurs, in which the surface zinc "gets involved" inside the structure, and oxygen "appears" above the surface. In the case of the nonstoichiometric zinc oxide, everything is more complicated; as a result, the surface may have fundamentally different properties.

In the SnO_2 single crystals, low-index facets (110) and (101) are the most developed. The surface (110) is the most theoretically [51–57] and experimentally [58–70]studied. The surface structure and the presence of these or other facets to a decisive extent depend on the methods and conditions of SnO_2 synthesis, which in turn affects the concentration of oxygen on the surface in the lattice. The production of SnO_2 crystals in the absence of oxygen leads to the formation of the oxygen-depleted (110) face.

The face (101) in the SnO_2 single crystal has been studied only recently [71–75]. In this case, the double valence of tin contributes to the formation of different charges on this face: Sn^{2+} or Sn^{4+}. The transition from one charge to another on this face is easily accomplished through the peculiarity of atomic stacking in this crystallographic direction. The structure of the (101) surface is shown on Figure 6. It can be seen that atomic stacking along this direction can be described as the three-layer O–Sn–O, the boundary of which is oxygen (see Figure 6(a)); that is, with such a sequence, tin retains its valence for Sn^{4+}. When removing the oxygen layer, the surface of the crystal is already ending with the layer of tin (see Figure 6(b)); as a result, the transformation of Sn(IV) into Sn(II) can easily take place [76]. Thus, the addition or removal of the surface oxygen layer by simply treating it at ambient conditions or in vacuum, can convert the tin surface from Sn(IV) to Sn(II) or vice versa. For the face (110), such easy conversion is not observed; therefore, on this face tin exists only in the form of Sn(IV) [71, 76].

In the environment, the pure ZrO_2 phase has the monoclonal structure of the baddeleyite m-ZrO_2 [77, 78], in

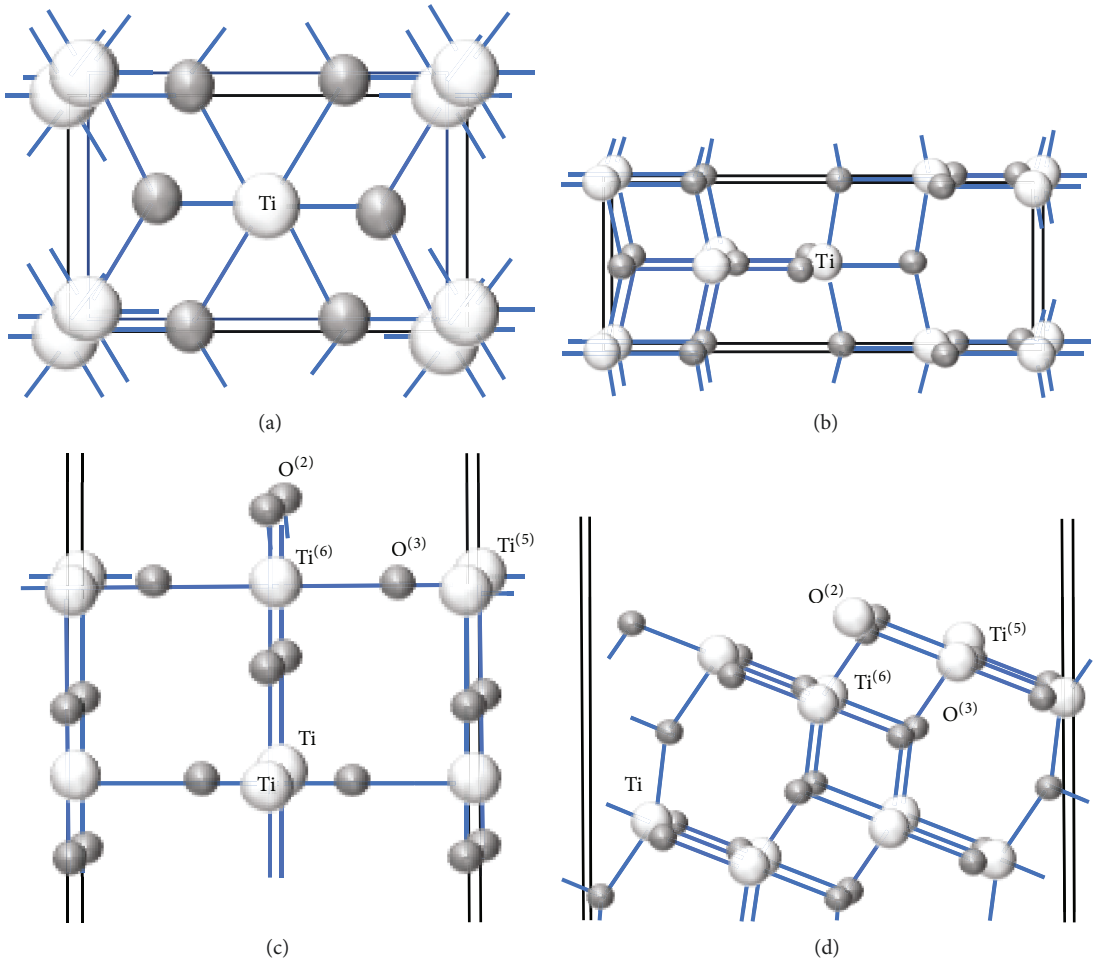

FIGURE 4: The structure of the bulk structures of rutile (a) and anatase (b) and faces (110) and (101) of rutile (c) and anatase (d), respectively.

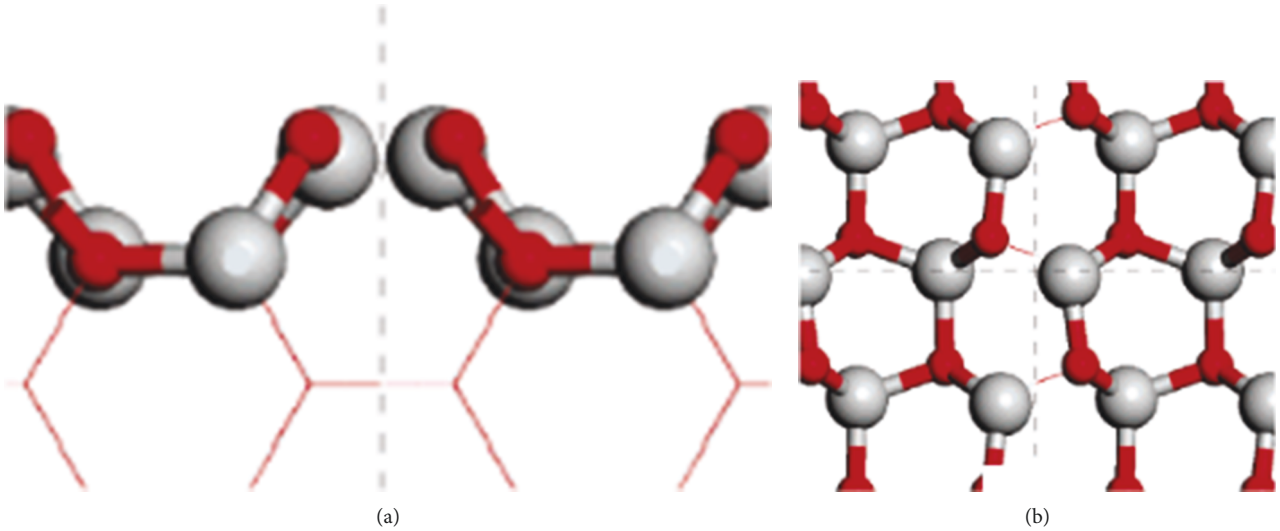

FIGURE 5: The structure of the stoichiometric $(10\bar{1}0)$ surface: (a) side view and (b) top view [49].

which zirconium is in a distorted sevenfold coordination, and oxygen atoms are four times or three times coordinated (see Figures 7(a)–7)c)). At approximately 1400 K, m-ZrO_2 is transformed into the tetragonal structure (t-ZrO_2), where zirconia is surrounded by eight anions but with two different Zr–O distances. The ideal eightfold coordination with the transformation of t-ZrO_2 into the cubic structure of the fluorite type (c-ZrO_2) is achieved at 2600 K [79–81].

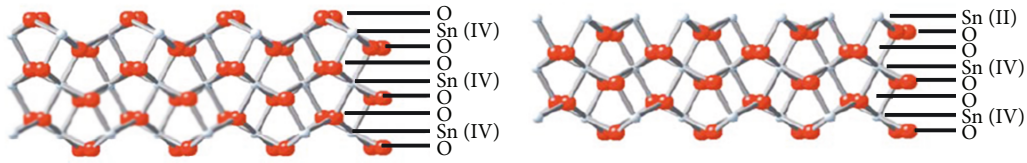

(a) (b)

FIGURE 6: Structure of the (101) facet of three layers on the SnO_2 surface (cross-section) (a) with the existing boundary oxygen layer (110) and (b) without it.

Experimental studies of ZrO_2 polycrystalline samples have shown that only a few crystal faces with low indices are open, especially the face (101), which is the most stable (see Figures 7(d) and 7(e)), and (001) [77, 82–85]. Theoretical studies have confirmed the discovered fact. Figures 7(d) and 7(e) show three outer layers where dashed lines allocate the repeating link of one layer in the direction perpendicular to the surface. The oxygen atoms have threefold coordination on these surfaces, and there are two different types of oxygen atoms on the face (101).

The structure of magnetite is based on the tight packet of oxygen (anion of the lattice) with iron cations, occupying octahedral and tetrahedral coordinated gaps between them (see Figure 8), in which Fe (II) and Fe (III) coexist in the octahedral position. Properties of magnetite are mainly determined by this fact.

Natural and synthetic crystals of Fe_3O_4 often have octahedral crystals, in which the main facet is (111) [23]. However, depending on the synthesis conditions, it is possible to obtain other forms of magnetite particles, for example, cubes (see Figure 9), in which the main facet is (100). Consequently, the properties of magnetite can be regulated by obtaining magnetite particles of different shapes, which will have the different set of surface facets; therefore, they will differ in surface energies.

In the (100) direction, the surface of magnetite consists of layers, which alternate as follows: the first layer consists of two Fe (III) ions in the tetrahedral position, then the plane containing eight O^{2-} anions followed by two Fe (III) ions and two Fe (II) ions in the octahedral positions (see Figure 10(a)). The main defect of this face may be an excess of iron ions [23].

The direction (111) in the magnetite consists of 6 different atomic planes: iron in the tetrahedral positions of Fe_{tet1}, plane of oxygen O_1, iron in the octahedral positions of Fe_{oct1}, plane of oxygen O_2, iron in the tetrahedral positions of Fe_{tet2}, and iron in the octahedral positions of Fe_{oct2} (see Figure 10(b)). Consequently, the close location of the oxygen plane to the surface causes a strong negative charge, but the presence of iron in the tetrahedral positions of Fe_{tet1} partially neutralizes it, resulting in the formation of the polar surface on the facet (111) by Tasker type 3 surfaces [23, 24, 86, 87].

The considered structures and structural features of different surfaces of TiO_2, ZnO, SnO_2, ZrO_2, and Fe_3O_4 indicate that the control of the metal oxide properties, especially in the nanodispersed range where the surface comes to the fore, begins with the shape and size of the crystals that affect the presence of those or other facets depending on the choice of the synthesis method, the process conditions, and treatment parameters after obtaining them.

2.3. Surface Phenomena on Metal Oxides. The phenomena occurring on the surface of solids are traditionally described using several models: statistical, band, and geometric [25, 88].

The statistical model (the model of "local" interactions) is based on the chemical approach, in which surface phenomena are described through active centers belonging to the surface. The active centers in this case are the surface atoms of the lattice, centers connected with defects of an inhomogeneous surface (point defects, dislocations), and impurities on the surface. When considering the surface in the theory of the crystalline field, the surface centers are free orbitals with a high affinity to the electron or occupied orbitals with a low ionization potential. Thus, the active centers are always localized on the real surface of the solid and have certain chemical activities [25].

A band model ("hard zone" model) is based on the electronic or energy approach. In this model, the surface description is carried out through surface states, which correspond to the surface electronic energy levels. The corresponding mathematical description does not depend on the chemical nature of the adsorbate and on the details of the local chemical interaction. The description is carried out due to the energy position in the forbidden zone of the semiconductor, which changes its charge depending on the position of the Fermi level on the surface.

The geometric model is based on the geometric characteristics of the surface, and the latter is considered as the fractal structure characterized by fractional dimensionality (D) and repeatability on different scales. For example, if $D = 2$, then this is a perfectly smooth surface, and if $D = 3$, then we are talking about volumetric porous structures. The fractality of the surface has a significant effect on its properties, for example, on sorption and catalytic characteristics, etc. [88]. At a later time, all these models are taken into account more increasingly when considering the surface phenomena involving metal oxides [89–95].

The acid-base properties of metal-oxide systems, which exhibit practically all the fundamental parameters of a solid, reflect the surface reactivity in the best way. According to this, two types of acidic and basic centers, the Lewis center and the Brønsted center, can exist on the surface of the solid. The presence of acidic and alkaline centers (as well as water) on the surface will determine the chemical activity of the solid as an adsorbent, (photo)catalyst, or metal oxide semiconductor [96].

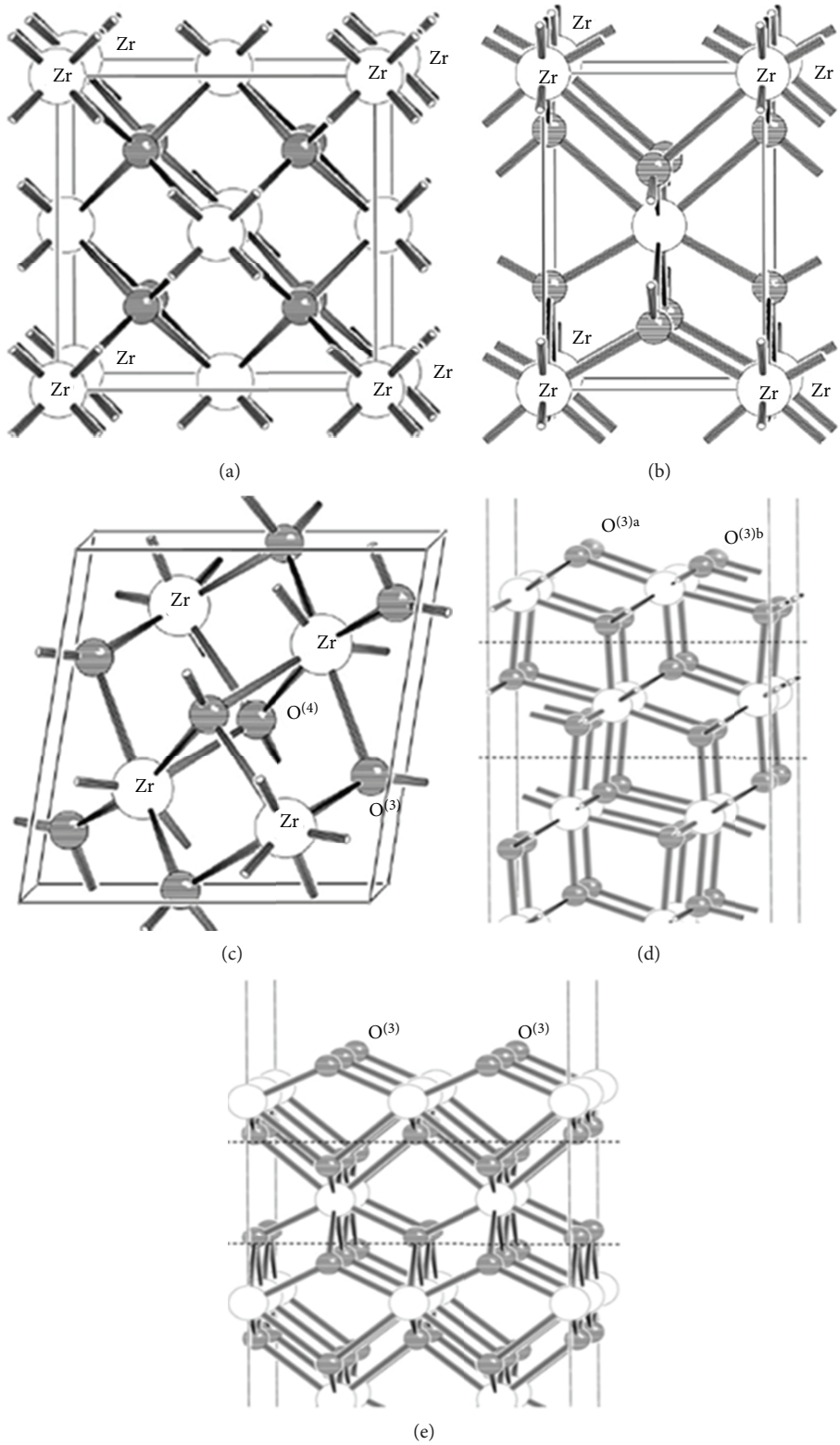

FIGURE 7: Bulk ZrO_2 crystals of various polymorphic modifications: cubic (a), tetragonal (b), and monoclinic (c). The most stable faces (101) (d) and (001) (e) on the t-ZrO_2 surface. White balls—oxygen; gray—zirconium [77].

The Lewis acid center is the vacant metal atom or the localized surface state capable of accepting an electron pair or an electron donating a molecular fragment. The alkaline Lewis centers are formed from the orbital of an oxygen atom on the surface and interact with the electron transfer to the energy level of the adsorbed molecule. Thus, any cation

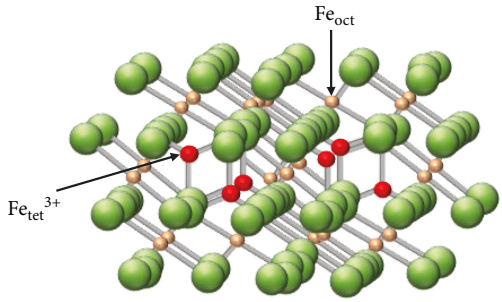

Figure 8: The structure of magnetite (green balls—oxygen, yellow balls—iron in octahedral gaps, and red balls—iron in tetrahedral gaps).

having unfilled electronic orbitals is an acid by the Lewis definition, and each of the surface anions having an undivided electron pair is an alkaline center [97].

Along with the aprotic centers (or the Lewis centers), there are proton acids and the Brønsted bases on the surface of the solid, which are the result of the interaction of water molecules and their fragments with aprotic centers. In the case of the adsorption of water molecules on one-electron surface levels formed by the homolytic dissociation mechanism, the Brønsted acids and bases of different acidic strengths can be formed, depending on which type of surface state participated in this process—the Shockley state (see Figure 11(a)) or the Tamm state (see Figure 11(b)). In the case of the interaction of water molecules with acids and bases of the Lewis centers, two types of mechanisms are possible: dissociative (see Figure 11(c)) and molecular (see Figure 11(d)). The molecular mechanism is also realized in the hydration process of the solid due to the water adsorption at the Brønsted acid and base centers by alkaline (see Figure 11(e)) and acid (see Figure 11(f)) types [97].

In the literature, the interaction of the surfaces of amphoteric metal oxides, which also include TiO_2, ZnO, SnO_2, ZrO_2, and Fe_3O_4, with water in aqueous medium, is described by a simplified mechanism [98–101]:

$$\begin{aligned} &\mathrm{MeOH} + \mathrm{H^+} \leftrightarrow \mathrm{MeOH_2^+}, \quad \text{if pH of solution} < \mathrm{pH_{pzc}},\\ &\mathrm{MeOH} + \mathrm{OH^-} \leftrightarrow \mathrm{MeO^-} + \mathrm{H_2O}, \quad \text{if pH of solution} > \mathrm{pH_{pzc}}, \end{aligned} \tag{1}$$

where pH_{pzc} is the point of zero charge.

Figure 12 shows the scheme of the interaction of the metal oxide surface with oxygen in the air.

In this case, according to studies of electron paramagnetic resonance, the adsorbed oxygen may be present on the surface of metal oxides in various chemical forms, the formation of which occurs according to the following scheme [102]:

$$\mathrm{O_{2(g)}} \rightarrow \mathrm{O_{2(ad)}} \rightarrow \mathrm{O_2^-{}_{(ad)}} \rightarrow \mathrm{O^-{}_{(ad)}} \rightarrow \mathrm{O^{2-}{}_{(ad)}} \rightarrow \mathrm{O^{2-}{}_{(lat.)}}. \tag{2}$$

The temperature dependence of the existence of this or that oxygen form was established in [103], where it is indicated that the transition from adsorbed oxygen to chemosorbed oxygen ($\mathrm{O_{2(ad)}} \rightarrow \mathrm{O_2^-{}_{(ad)}}$) occurs approximately at 423 K. The significant reduction in the conductivity of metal oxide systems at temperatures higher than 423 K was connected with this.

2.4. Properties of Metal Oxides in the Different States of Dispersion and Morphology. Metal oxides form the basis of modern diverse intellectual materials and devices due to the possibility of controlling their physical and chemical properties. Their properties depend on many chemical and structural characteristics: chemical composition, various defects, morphology, particle size, specific surface area, etc. By changing any of these characteristics, the electrical, optical, magnetic, (photo)catalytic, and sorption properties can be controlled. The unique characteristics of metal oxides make them the most diverse class of materials covering almost all aspects of material science and physics in the fields of semiconductivity, superconductivity, ferroelectricity, and magnetism [102].

The nanostructured titanium (IV) oxide has high chemical and thermal stability, and with special doping by impurity levels in an electronic structure, it is uniquely capable of the creating new functional materials on itself, especially for (photo)catalysis, sensors, adsorption, and photovoltaics. The highly dispersed doped TiO_2 for the creation of a photocatalyst that would work efficiently in the visible spectrum, as well as the components of devices for the efficient conversion of solar energy into electricity (solar cells), is of particular interest [104–109].

In the process of using nanodispersed, submicron and micron ZnO for bleaching methylene orange in aqueous solutions, the following order was revealed: nanodispersed powder (50 nm) > submicron powder (200 nm) > micron powder (1000 nm) [110]. The authors explain the fact as follows: the number of dispersed nanoparticles per volume in the reaction solution increases, and consequently, the photon absorption ability is improved; the large surface area of the nanodispersed powder contributes to the large adsorption of dye molecules on the catalyst surface; and the recombination process is reduced due to the smaller path of electrons and holes on the surface of the particles.

Tin (IV) oxide is one of the classical sensory materials that belong to the class of substances that combines high electrical conductivity and optical transparency in the visible spectral region, has chemical stability at high temperatures, etc. [111]. Therefore, materials based on SnO_2 are widely used as organic oxidation catalysts, lithium ion batteries, transparent electrodes of solar cells, various electronic and optical coatings, and as sensitive materials for metal oxide chemoresistive gas sensors.

Modifications of nanodispersed ZrO_2-based nanomaterials determine the ways of application, since each of its modifications has a number of properties inherent only for that particular modification. The monoclinic modification of ZrO_2 nanopowders is used mostly in the production of substrates for luminescent, photosensitive materials [112]; in catalysis [113, 114]; and in the production of nanomaterials

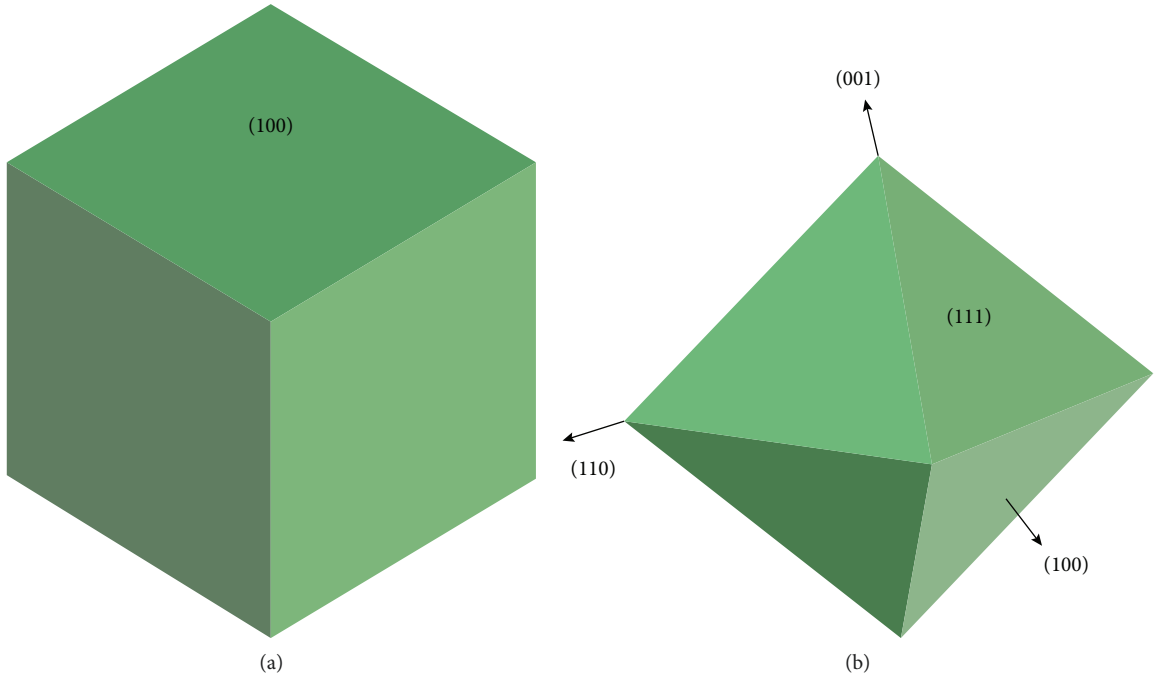

Figure 9: Magnetite particles in the form of the cube (a) and octahedron (b) [23].

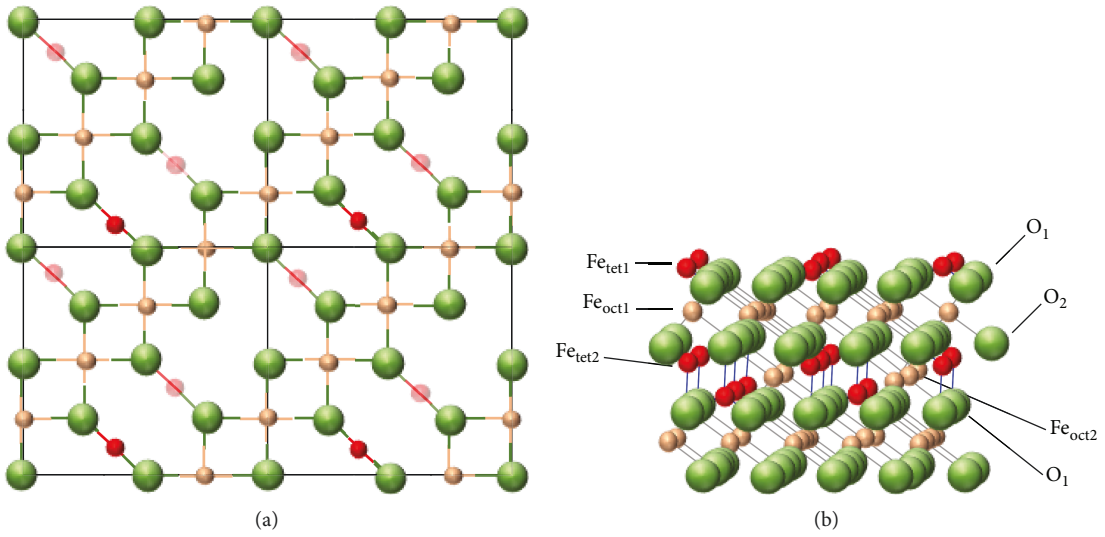

Figure 10: The structure of Fe_3O_4 surfaces: (a) the top view of the facet (100), where Fe_{tet} is red, Fe_{oct} is yellow, and oxygen is green; (b) side view of the facet [23].

based on tetragonal and cubic ZrO_2 modifications, for example, in ceramic materials, including new materials with improved performance [115]. The tetragonal modification of zirconium (IV) oxide has become widely used for bioceramics in restorative dentistry [116, 117] and in catalysis [118, 119], and its cubic modification has become widely used for chemically resistant and thermostable high-strength nanoceramics [120] and for solid electrolytes in solid oxide fuel cells [121, 122].

The constantly growing interest in the properties of nanomagnetism is due to its powerful potential for solving a wide range of tasks in material science, mineralogy, biology, and medicine [123]. At present, the application of magnetic nanoparticles is the most widely developed in biology and medicine, storage and recording of information, and in other areas of science and technology. At sizes from several to tens of nanometers, magnetic particles, especially nanomagnetic particles, reveal the special characteristic of their magnetic behavior—superparamagnetism. Recent studies have shown that the prospective application of magnetite is in sorption technology, since it has been found that it has a high sorption activity for some organic compounds, and the modification of existing sorption materials allows removing them quickly by magnetic separation [124, 125].

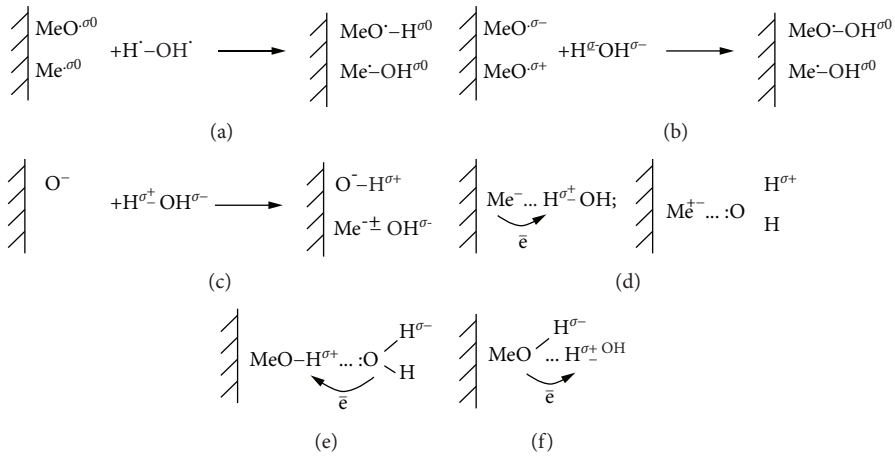

Figure 11: Mechanisms of the interaction of water with different centers on the surface of metal oxides.

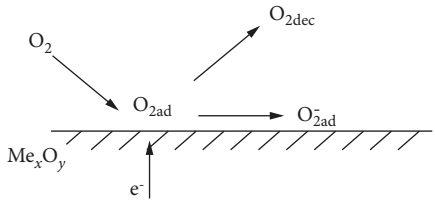

Figure 12: Schematic formation of the chemosorbed oxygen on the surface of metal oxides.

Consequently, the considered multifaceted properties of these nanostructured and nanodispersed metal oxides make these materials very promising not only for optical and electronic applications, but also for their use in environmental applications, which is the cause for the significant scientific interest in them by environmental engineering specialists.

2.5. Features of Chemical and Physical Characteristics in the Nanodispersed Range. Materials obtained from nanosized particles exhibit unusual chemical and physical properties that differ significantly from the properties of the respective bulk materials. Their study is important in modern science, because such studies are fundamental, since they allow investigating the changes in the properties of substances in the gradual transition from atomic or molecular level to condensed systems.

The peculiarities of the chemical and physical characteristics of nanoparticles related to their size are determined by the following phenomena. With a decrease of the particle size, the percentage of atoms on the surface increases. This leads to the increase in reactivity due to coordination nonsaturation. Proceeding from this and taking into account the fact that with the transition to nanoparticles the surface-to-volume ratio increases, the origin of these "unusual" properties, called "dimensional effects," becomes clear.

The influence of the particle size on the physical and chemical properties of the substance is also due to the presence of surface pressure acting on the substance. This additional pressure, which is inversely proportional to the particle size, leads to the increase in the Gibbs energy and, consequently, increases the pressure of the saturated vapor above the nanoparticles and decreases the boiling point of the liquid and the melting point of the solid phase. Other thermodynamic characteristics also change, especially the equilibrium constant and the standard electrode potentials [126]. Also, when the size of the particles decreases, the influence of the structure on the stoichiometry of the material is noticeably manifested [127]. A variation of stoichiometry leads to a significant change in the chemical and (photo)catalytic activities of the material.

For example, when the size of the titanium (IV) oxide particle diminishes, its anatase modification becomes more stable and, according to the results of studies [128–130], the anatase structure has a greater number of oxygen vacancies on the surface than the rutile structure. This results in its greater chemical and photocatalytic activities compared to rutile.

When reducing the size of ZnO particles to nanometer size, some of its physical properties undergo changes that are known today as "quantum size effects." For example, quantum confinement increases the energy gap of quasi-one-dimensional (Q1D) ZnO, which is confirmed by photoluminescence. The band gap of ZnO nanoparticles also demonstrates the same dependence [131]. In this case, ZnO can be used to create unique nanostructures that are in demand in a wide variety of applications, such as in optoelectronics, sensors, transducers, and photocatalytic and biomedical materials. From this, it follows that ZnO unambiguously has the richest family of nanostructures among all materials, which differ in both structure and properties [132].

As already mentioned, materials based on zirconium (IV) oxide have different applications depending on the phase composition. In particular, monoclinic ZrO_2 is used as a catalyst [113, 114], tetragonal ZrO_2 is used as a carrier of catalysts [118, 119], and cubic ZrO_2 is used as a solid electrolyte in fuel cells of solid oxide batteries [121, 122]. The degree of tetragonality or cubicity at normal temperatures depends on the size of the crystallites: the metastable tetragonal modification of ZrO_2 can be obtained under normal conditions if the size of the crystallites is less than 25-30 nm, and the metastable cubic ZrO_2 modification can be obtained if the crystallite size is less than 5-10 nm [133].

The change in the physical and chemical properties of SnO_2 and Fe_3O_4 in the transition to the nanoscale is achieved by varying the morphology of these nanoparticles, which determines the presence of certain facets on the surface, which differ in their surface energies [23, 76].

2.6. Sorption, (Photo)catalytic, and Sensory Properties of Metal Oxides. One of the most important properties of metal oxide nanoparticles, which has a large potential for application in various chemical and technological processes, is their high adsorption capacity in relation to pollutants in water systems, especially organic matter, which indicates the prospect of using metal oxide nanomaterials to improve the ecological state of the environment. A similar impressive adsorption capacity of metal oxide nanoparticles and other compounds to various organic compounds has been documented by many researchers [133–138]. A significant increase in catalytic activity was found in some metal oxides in the transition to the nanoparticles [138–140].

The dimensional effect is already widely used in heterogeneous catalysis. In many cases, the nanoparticles exhibit catalytic activity where the same larger particles are inactive. The explanation for these phenomena is based on the acid-alkaline properties of metal oxides, which change in the transition to the nanoscale, namely, a large number of active centers are exposed, which is connected, first of all, to the sharp increase in the specific surface area. When obtaining these metal oxides in the form of nanostructures, the percentage of coordinated-unsaturated ions, especially at the edges and angles of microcrystallites, is predicted to be large. Consequently, the physical and chemical properties of the surface in such nanoscale systems will play a decisive role in determining the scale of their application and in assessing the catalytic activity.

Controlled regulation of the functional properties of metal-oxide nanomaterials and the implementation of the dependencies of composition-structure-properties can also be accomplished by changing the phase composition, which in many respects also determines their physical and chemical characteristics.

2.6.1. TiO_2. The most important of all applications of different crystalline modifications of TiO_2 is the ecological direction, namely, in the sorption-photocatalytic processes. Along with crystalline modifications, the amorphous TiO_2 modification is also actively synthesized and studied. However, the latter has no photoactivity but has high sorption properties. At the same time, the sorption-photocatalytic properties are influenced by such parameters as the degree of crystallinity, the correlation between modifications, the distribution of particles in size and shape, the specific surface area, and the average pore size.

Among the three polymorphic modifications of titanium (IV) oxide, only rutile and anatase have an applied value. Rutile is a more thermodynamically stable structure; however, anatase is considered to be more promising as a nanomaterial of the ecological direction due to the greater photochemical activity. However, there are data in the literature on the increase of the photocatalytic activity of TiO_2-based nanomaterials when they consist of mixed phases, such as anatase and brookite or anatase and rutile [141]. Due to the denser packing of ions in crystals, rutile exceeds anatase in terms of stability, density, hardness, refractive index, and dielectric permittivity, but it is believed that it has insufficient photochemical activity [142–144]. In recent scientific publications [145, 146], there is evidence that brookite, an unstable modification of TiO_2, is characterized with the highest photocatalytic activity. Unfortunately, it is difficult to obtain this modification in pure form even in laboratory conditions.

Despite that the band gap in rutile (3.0 eV) is lower than that in anatase (3.2 eV), the latter crystalline modification still has the higher photocatalytic activity. This is explained by the fact that anatase is a semiconductor with an indirect forbidden zone, and rutile, in turn, is a semiconductor with a direct width of the forbidden zone. As a result, in anatase, electrons and holes can migrate from volume to the surface at a high rate, which leads to a low recombination rate [147]. Typically, the mixture of these modifications gives higher photocatalytic activities compared to individual modifications due to the synergistic effects that are manifested in the interfacial interaction and electron transfer [148–150]. For example, when using the mixture of anatase and rutile, the recombination of photogenerated electrons and holes decreases due to the anatase modification, and light absorption increases due to rutile.

2.6.2. ZnO. Due to the unique electrical, optical, and mechanical properties and the remarkable characteristics in electronics, optics, and photonics, ZnO can be effectively used in environmental applications, namely, as a photocatalyst and a sensor material.

As a photocatalyst, zinc oxide is already competing with the most popular catalyst based on TiO_2, which holds leading positions not without a base. Recently, however, in-depth research in the scientific literature on the ZnO-based photocatalyst for the destruction of various pollutants in aqueous solutions shows the significant promise of this oxide for use along this direction [111]. It is noted that the creation of a "suitable" ZnO architecture during synthesis will allow minimizing the loss of the electron during excitation and maximizing the absorption of photons [151–153]. Among other things, its nontoxicity and ecological purity are noted, which are very important for such materials that are used for environmental purposes [111]. Thus, by varying the morphology and particle size, it is possible to create effective photocatalysts for wastewater treatment.

Zinc oxide has proved itself as a promising sensitive material for gas sensors because of its high surface conductivity in various environments. At the same time, this parameter strongly depends on the morphology and size of ZnO particles. It is established that the use of ZnO nanowhiskers, nanowires, nanorods, and nanobelts as well as the nanoflower architecture significantly increases the surface conductivity [154, 155].

2.6.3. SnO_2. The sensitivity of sensors based on metal oxides strongly depends on the morphology of their particles [156].

In this sense, one-dimensional nanostructures such as nanowires and nanobelts are of greatest interest [157–161]. Sensors based on them are promising because of the possibility of creating sensors of ultrahigh sensitivity ppb-level sensors. The authors [162] theoretically proved and experimentally confirmed that the sensitivity of one-dimensional nanostructures is much larger than that of nanoparticles with a round shape and depends on two important parameters: (1) the particle surface-to-volume ratio and (2) the Debye radius. It has been shown that the characteristics of metal-oxide sensors strongly depend on the size and morphology of nanostructures.

2.6.4. ZrO_2. Zirconium (IV) oxide is used as the catalyst (due to the greater number of acidic centers on the surface) in the monoclinic modification [163], as the carrier for catalysts (due to the high thermal stability) in the tetragonal modification [164], and as the sorbent in the amorphous phase or at a low degree of crystallinity [165, 166].

When zirconium (IV) oxide is used as a catalyst, the acid-alkaline nature of its properties and the presence of several types of defect in the crystalline lattice and on the surface, which is one of the main factors of the reactive-catalytic activity of the surface of any oxide, play an important role. When using ZrO_2 as the carrier for catalysts, it must have sufficiently developed outer and inner surfaces. These requirements are provided to obtain zirconium (IV) oxide crystallites with a size as little as possible. One of the most unusual and promising properties of zirconium (IV) oxide particles is their sorption capacity both to anions and cations, which allows considering nanosized ZrO_2 and materials based on them as instruments for improving the ecological state of the environment. In this case, the hydrated zirconium (IV) oxide that is in the amorphous state has the highest sorption capacity [165, 166]. The specificity of ZrO_2 usage as the sorbent is that it has high selectivity to polyvalent anions (chromates, borates, sulfates, phosphates, arsenates, etc.) and can be used at high temperatures without losing its effectiveness.

The ZrO_2 cubic modification is used as an oxygen sensor. The high thermal stability of the zirconium (IV) oxide cubic modification and the ability of the sensors based on it to operate in hot, contaminated, and wet gases without any additional preparation makes ZrO_2 a promising material for the creation of sensors operating in difficult conditions. In this case, the use of ZrO_2 and materials based on it in the nanoband allows increasing the surface area of the sensor material (solid electrolyte), resulting in the receipt of high-sensitivity sensors to oxygen [167].

2.6.5. Fe_2O_3. Magnetite is considered as a promising nanomaterial for use in water purification due to its high surface-to-volume ratio, magnetic properties, and the possibility of easy surface modification and reuse [168]. Because of the listed advantages, it has enormous potential for application in the ecological direction as a sorbent, photocatalyst, and modifier. Particularly noteworthy is its magnetic properties, which contribute to the creation of more effective water purification schemes by combining adsorption with magnetic separation, which is becoming widespread in the field of water treatment [169, 170]. In addition, magnetite has a relatively lower cost, high sorption capacity, and stability [171–173]. Current applications of nanomagnetite, which are predicted in water purification, can be divided into two groups: technologies that use magnetite as the nanosorbent or the modifier for faster removal of the used sorbent (adsorption technologies) and technologies that use magnetite as the photocatalyst to destroy contaminants or convert them into less toxic forms (photocatalytic technologies) [171]. However, it can be assumed that technology based on the usage of nanomagnetite will soon be used employing both approaches at the same time.

2.7. Optical, Electrical, and Magnetic Properties. As has been shown in numerous studies [174–179], the optical, electrical, and magnetic properties of metal oxides depend on their dispersion and morphology. Thus, there is an increase in electrical resistance and permittivity observed in nanophase metal oxide systems compared to metal oxide macrosystems [180], and TiO_2 nanoparticles absorb ultraviolet light much more efficiently than micrometer-sized particles [181]. The invented phenomena are undoubtedly related to the dimensional effects.

The dimensional effects depend on the nanoparticle size: it can either be classical (the changes in properties can be explained only by the influence of the surface) or quantum (changes in the properties of the substance cannot be interpreted as ordinary surface phenomena, most often such effects are observed for very small particles, the size of which does not exceed 10 nm) dimensional effects. It is the latter that directly affects the change in the optical, electrical, and magnetic properties of substances in the transition to the nanoscale.

Quantum dimensional effects are manifested in materials that have dimensions that are comparable to one of the characteristic lengths—the free path of charge carriers, the De Broglie wavelength, the size of the magnetic domains and the exciton, etc. [182, 183].

The change in optical properties occurs in nanoparticles with a size that is much smaller than the De Broglie wavelength and does not exceed 10-15 nm. The differences in absorption spectra in these nanoparticles and in massive objects are due to the difference in their dielectric constant [184].

The increase in the electrical resistance is due to the increasing role of defects in nanoparticles and the features of the phonon spectrum. A noticeable change in the electrical resistance is observed at particle sizes of less than 100 nm [185]. In semiconductors, the approaching of particle size to 10 nm or less leads to the decrease in the band gap (Eg) to the dielectric level [186].

The magnetic properties of particles in the nanorange change significantly. In this case the ferro- and superparamagnetic properties are manifested. Superparamagnets are magnetic only when the field is applied, while ferromagnets have a constant mean magnetic moment and stronger magnetic properties [187].

The morphology also has a significant effect on the physical and chemical properties of nanoparticles. It is generally accepted that 1D nanostructures are ideal objects for

studying the phenomenon of nanosized materials and investigating the dependence of structural properties on their size and dimension for practical use [188]. It is also expected that 1D nanomaterials, with their large specific surface area and quantum retention effects, exhibiting unique properties in contrast to their bulk analogues, will play an important role in the development of optical, electrical, electrochemical, and electromechanical devices of nanoscale dimensions [189, 190]. Management of the determined size, crystallinity, and composition of 1D nanostructures can lead to the acquisition of new properties that are impossible in the case of macromaterials [190, 191].

2.8. Optical Properties. Zinc oxide and tin (IV) oxide have unique optical characteristics. ZnO and SnO_2 belong to the group of materials that are called transparent conductive oxides. These oxides are characterized by a wide band gap $Eg > 3$ eV and are highly transparent in the visible spectrum. In this regard, they are used in the manufacture of a wide range of photovoltaic devices, such as semiconductor LEDs and solar and electrochromic cells [192]. The optical properties of pure zinc oxide and tin (IV) oxide are influenced by the degree of crystallinity of the material, the presence of point defects, and tensions in the crystal structure. These parameters affect the absorption and transmittance in the visible region of the spectrum, which are important for using them as transparent conductive oxides, especially for creating transparent electrodes. The optical properties of materials based on ZnO and SnO_2 are regulated by their doping.

2.9. Electrical Properties. Among the metal oxides under consideration, TiO_2, ZnO, and SnO_2 are characterized by electronic conductivity, which has the applied value. These electrical properties are of great importance when using these oxides as photocatalysts, sensitive layers of gas sensors, solar cells, and electrochromic devices. The conductivity of these materials is carried out both on its own (internal defects) and by impurity (doped atoms) carriers. The global growth in the demand for energy-efficient and compact devices stimulates the deep interest of researchers in this class of materials. The uniqueness of materials based on TiO_2, ZnO, and SnO_2 is that they are n-type wide-gap semiconductors that can be doped to high concentrations, turning them into degenerate semiconductors, that is, metal like. The transport in these polycrystalline materials is more complicated than in corresponding single-crystal materials. However, they are preferentially used because of their special characteristics, for example, the fact that TiO_2 is characterized by a high refractive index in the visible part of the spectrum and a high chemical and thermal stability and the fact that tin (IV) oxide has the highest chemical stability, which is a prerequisite for several applications, for example, in electrochemical elements [193].

Thus, titanium (IV) oxide has the greatest practical importance in photocatalytic processes, zinc oxide is widely used both as a photocatalyst and as sensitive layers of gas sensors, and tin (IV) oxide holds the greatest potential as a sensitive layer for miniature gas sensors. It should be added that all of them are used in the listed areas, and the creation of nanocomposites based on them is considered as the most promising direction in obtaining photocatalysts and sensory layers [194].

The authors in [195] have shown that when using TiO_2 particles in the form of nanotubes for photoelectric applications, the vector charge transfer (Figure 13) is facilitated in comparison with round-shaped nanoparticles, which leads to faster kinetics and more efficient photoelectrocatalytic degradation for three different models of disperse azo dyes in aqueous solutions [196, 197].

In addition, TiO_2 nanotubes are characterized by high sorption-photocatalytic properties (see Figure 14) [198]. According to the data given in [198], the sorption properties of TiO_2 nanotubes considerably exceed the sorption properties of the commercial nanodispersed TiO_2 sample.

Due to the fact that the hexagonal structure of ZnO does not have symmetry with respect to inversion, this leads to additional piezoelectric properties in the oxide. Like most II-VI materials, ZnO predominantly has ionic bonds, which explains its strong piezoelectric properties [14].

SnO_2 is the material that combines high electrical conductivity with such functional properties as high optical transparency in the visible spectral region and chemical stability at high temperatures [199, 200]. A high sensitivity is predicted when using 1D type SnO_2 nanostructures in sensory elements due to the higher values of the specific surface area compared to the round-shaped particles. As a result of the high values of the specific surface area, a large part of the adsorbed molecules from a gas medium will be concentrated on the surface. Thus, a reaction between the target gas and the chemically active chemisorbed molecules (O^-, O^{2-}, H^+, and OH^-) on the surface of 1D structures may occur at low temperatures [201].

Among the three zirconium (IV) oxide modifications, only the cubic modification has ionic conductivity, which determines its use in such a promising direction as the production of solid oxide fuel cells [202, 203]. The versatility of the materials based on the cubic zirconia (IV) oxide is that when introducing additional atoms (Mg, La, and Y) during the ZrO_2 synthesis the latter obtained a large number of point defects in the crystalline lattice which are associated with oxygen vacancies. This fact contributes to the growth of the ionic conductivity of cubic ZrO_2 and leads to the leveling of its dielectric properties. It should be added that doping not only changes the crystalline structure of ZrO_2 but also changes its electronic structure, which also increases ionic conductivity and, besides its application in fuel cells, finds a demand for the creation of oxygen sensors [204, 205].

2.10. Magnetic Properties. The magnetic properties of nanosized magnetite depend on many factors, including the type and defects of the crystal lattice, the size and shape of the particles, the presence of impurities, and the nature of the interaction of the nanoparticle with the surrounding matrix or other nanoparticles [206]. It has been proven that reducing the size of magnetite particles leads to qualitative changes in its magnetic properties to a one-domain state and superparamagnetism [207]. The behavior

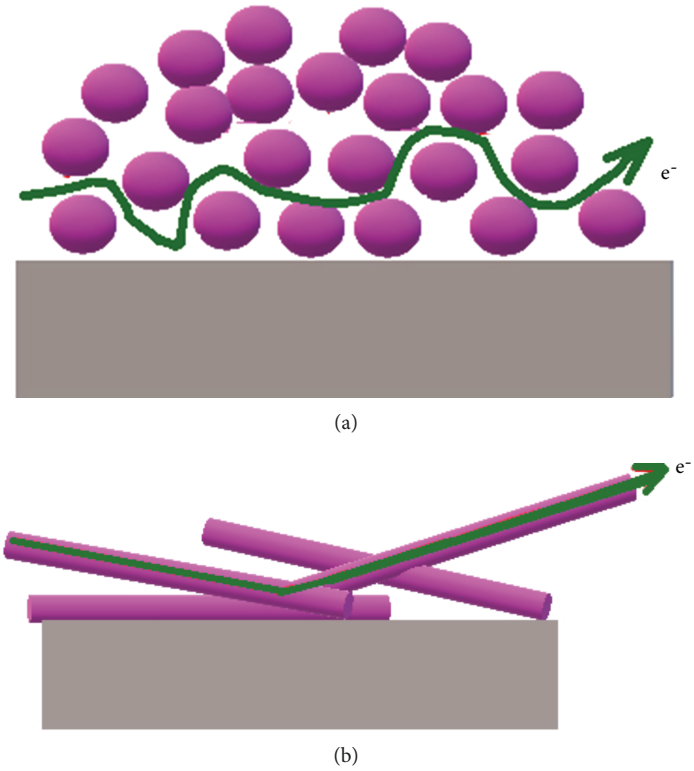

Figure 13: Nanostructured (a) and nanotube (b) photocatalytic films and the vector transport of electrons in them.

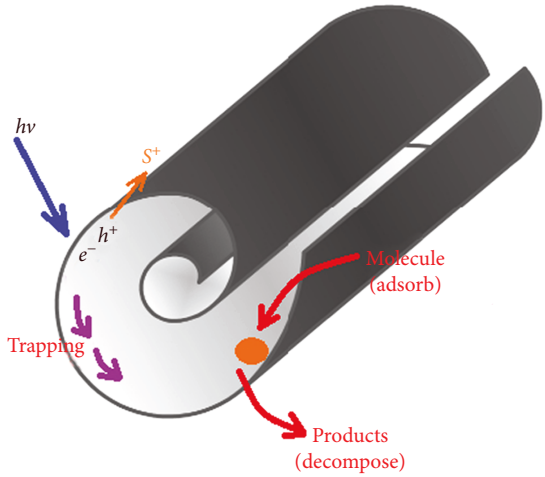

Figure 14: The TiO_2 nanotube structure and the scheme of the adsorption-photocatalytic process based on it.

of superparamagnetic substances (the size of magnetite up to 5 nm) in the external magnetic field is significantly different from ordinary paramagnets and ferromagnets. Under the influence of the external field, each separate magnetic domain takes the same direction as the external field [208]. In such systems, the losses at absorption and release of the energy of the external magnetic field are minimized, which makes them the ideal basis for magnetic resonance contrast mean in MRI studies and the magnetic modifiers of sorption materials.

Consequently, based on the considered physical, chemical, optical, electrical, sorption, photocatalytic, and magnetic properties of metal-oxide nanomaterials at various states of dispersion and morphology, the prospects and relevance of the further development of the newest effective nanomaterials based on TiO_2, ZnO, SnO_2, ZrO_2, and Fe_3O_4 for environmental applications in order to develop new environmental technologies of their use can be argued.

3. Synthesis Methods of Metal Oxide Nanomaterials and Nanocomposites Based on Them

3.1. Synthesis of Metal Oxide Nanomaterials. A synthesis method is crucial for the development of new nanomaterials, especially for the purpose of their specific applications. It affects not only the shape and size of the obtained particles but also the nanostructure, morphology, degree of crystallinity, etc., which leads to the different finite physical and chemical properties (sorption, (photo)catalytic, magnetic, and optical) of nanomaterials.

Chemical deposition, hydrothermal synthesis, sol-gel technology, gas-phase synthesis (vapor transport or CVD), template method, electrochemical synthesis, electrospinning, "green" technology, combined techniques, and others [138, 209–212] are used for obtaining metal oxide nanomaterials.

The widespread use of chemical deposition, hydrothermal synthesis, sol-gel technology, or the so-called soft chemistry methods [213] in scientific research is associated with

the relative ease of their implementation and the wide range of control parameters, such as process duration, concentration of reactants, and low temperature and pressure. In addition, to produce metal oxide products with more diverse properties, these methods can be easily combined with each other or various additional treatments can be used. For example, ultrasound or ultra-high-frequency radiation is used with the main methods of synthesis to exert influence on such properties of metal oxide nanoparticles such as size, morphology, specific surface area, and sorption capacity. Ultrasonic processing makes it possible to avoid the consolidation of formed particles and to achieve a high level of homogeneity [214, 215].

Synthesis of metal oxides from the gas phase provides a means for obtaining monocrystalline metal oxide nanoparticles of controlled and diverse morphologies with a high degree of crystallinity [216–220] with relatively high productivity, simplicity, and accessibility.

Synthesis methods of metal oxide nanoparticles, such as the electrochemical method, electrospinning method, environmental methods, or the so-called "green" technologies, are used for purely specific applications or are still in the initial stage of laboratory studies [209–212].

3.1.1. Chemical Deposition Method. The chemical deposition method is the simplest method for obtaining various substances and is based on the interaction of water-soluble or other solvents of metal compounds (usually chlorides, oxychlorides, or nitrates) with precipitators (alkali metal hydroxides, ammonia, or their oxalates). As a result, the insoluble compounds (precursors for the synthesis of nanodispersed metal oxide particles) are formed, which are subsequently washed, separated, and calcined under certain conditions to obtain the product with given properties. Even though chemical deposition is considered to be the simplest, in reality, it is a complex physicochemical process that has several stages, each of which has a significant effect on the properties of the final product [221]. By this method, it is possible to vary the properties and morphology of the resulting particles in a wide range, but the disadvantage of this method is the complexity of controlling the particle size distribution.

3.1.2. Homogeneous Deposition Method. To overcome this shortcoming, the so-called homogeneous deposition method has recently been proposed, where the precipitant and the deposited substance are in the same phase (solution) and do not interact chemically. The interaction process occurs only due to the additional chemical reaction, for example, the reaction of the carbamide hydrolysis as the mixture is heated. As a result, ammonium hydroxide is formed, which enters the deposition reaction. In this case, unlike heterogeneous deposition, the entire amount of the precipitant appears simultaneously, which prevents local supersaturation in the reaction mixture. The degree of supersaturation depends on the concentration of reagents and the heating temperature, which affects the size of the obtained particles [222]. The sediments obtained by this method are characterized by less polydispersity and greater homogeneity than in the case of the heterogeneous deposition.

3.1.3. Hydrothermal (Solvothermal) Method. The essence of the hydrothermal (solvothermal) method is to heat the aqueous (or nonaqueous) solutions of the initial reagents at a temperature above the solvent boiling point (but usually up to 573 K) in special reactors—autoclaves lined with Teflon. Processing time varies from 10 minutes to 48 hours. During the heating process, there is an increase in the pressure of saturated vapor above the solution to values greater than 0.1 MPa. Since the process is carried out in a closed system, the hydrothermal (solvothermal) method using aqueous (or nonaqueous) solutions as the reaction medium is environmentally friendly. As precursors in hydrothermal synthesis, both inorganic and organic metal salts can be used [223, 224]. At high pressure, the dissolved metal salt in water or in another solvent is converted into metal oxide, bypassing the step of converting salt into hydroxide:

$$2\mathrm{Me(NO_3)_2} + 2\mathrm{H_2O} = 2\mathrm{MeO} + 4\mathrm{HNO_3}. \quad (3)$$

A necessary condition for the course of this reaction is to carry out the process at a temperature higher than that of the area of the hydroxide existing on the P-T diagram. In addition, the properties of the reagents (solubility, diffusion rate, and reactivity) also change at elevated temperatures.

The hydrothermal (solvothermal) method allows obtaining metal oxide nanoparticles with a round shape and a size of 10 nm with a high degree of monodispersity. It was found that there was an increase of nanoparticle size with an increase of the hydrothermal process duration. The same applies to the temperature: the larger particles of the solid phase are obtained at higher temperatures [225]. Also, according to this method, particles of other morphologies can also be obtained: nanowires, nanoneedles, and nanorods with diameters of 20–150 nm and lengths of 10–300 microns [226, 227]. Thus, hydrothermal (solvothermal) synthesis is a simple, efficient, and ecological method for the chemical synthesis of metal oxides, as well as complex oxides, solid solutions, and composites [228]. In addition, the control of the main process parameters (pressure, temperature, and duration) of this method provides wide opportunities for obtaining high-quality nanoparticles of metal oxides. However, it should be noted that the method is complex in hardware design and is quite energy-consuming. Moreover, the materials used for the creation of autoclaves are subject to rigid requirements: they must be chemically inert in acid and alkaline environments at elevated temperatures and pressures.

3.1.4. Sol-Gel (Hydrolytic) Method. The sol-gel (hydrolytic) method is a universal process, which is very widely used for obtaining simple and complex metal oxides of high purity. In the typical sol-gel process, the colloidal suspension, that is, the sol, is formed by the reactions of hydrolysis and partial polymerization of precursors, which are usually inorganic metal salts or metal organic compounds, such as alcoholic metals. Full polymerization and solvent removal lead to the transition from the liquid sol to the solid gel phase. The development of nanoparticles depends on such factors as the solvent nature, pH value, solution viscosity, and

temperature. With relative simplicity and versatility of the sol-gel method, the properties of the finite material are sensitive to each stage of this process. The systematic study of the reactive parameters such as the reaction duration, temperature, concentration, and chemical composition of reagents allows controlling the size, shape, and quality of nanocrystals. Thin films of nanoparticles can be obtained by this method on the substrate area by spin-coating or dip-coating techniques [229–232]. As a result of the use of inorganic metal salts, powders with a larger particle size in comparison with the organic precursors are produced. Particles of another morphology, for example, nanofibers with an average diameter in the range of 100–300 nm and a length of more than 10 μm, can also be received by sol-gel technology.

A significant advantage of the sol-gel technology is the ability to achieve a high homogeneity of materials in the case of the synthesis of complex compounds. All precursors are in the liquid phase; their mixing is realized at the molecular level, which results in a high degree of homogeneity. Thus, it is possible to provide high-quality materials in terms of the purity, composition, and uniformity of the structure. Under certain conditions, this method can produce powders, monoliths, coatings, films, fibers, aerogels, glass, ceramics, and hybrid materials. It is also possible to synthesize both crystalline and amorphous nanopowders [233].

3.1.5. Gas Phase Synthesis Method. The gas phase synthesis method, which is based on the processes of evaporation and condensation with the passage of a chemical reaction, has recently become popular for the synthesis of metal oxide nanostructures. It is usually realized in an inert atmosphere at elevated temperatures (up to 1573 K) [234–237]. The appropriate metals and their oxides or mixtures based on them are used as precursors. This method allows receiving monocrystalline particles of various forms, such as prismatic plates, tapes, and nanowires, in diameters of 40–200 nm and in lengths from several tens to several hundreds of micrometers. In addition, this method allows obtaining monocrystals of controlled and diverse morphologies with a high degree of crystallinity [238, 239]. A feature of the CVD method is its numerous varieties, among the most popular of which is MOCVD, which is used for obtaining metal oxide powders [240].

3.1.6. Template Synthesis. Template synthesis is a process occurring under the influence of certain factors of spatial constraints—with the help of a peculiar pattern—a template that allows controlling the structure of the generated phase. Template synthesis can also be combined with methods of electrodeposition, sol-gel technology (most often), and chemical vapor deposition [241]. The method of template synthesis allows the preparation of nanoparticles of various shapes and sizes, as well as structures, for example, mesoporous structures. The disadvantages of the template method include the soft processing conditions characterized by a weak motive force of material deposition, so the process of obtaining particles by this method is quite a long-term process.

3.1.7. Electrospinning. Electrospinning is a relatively cheap and easy-to-use technology that allows synthesizing materials in the form of fibers of a certain strength and flexibility on a large scale. The method consists in the injection of precursors through stainless steel needles with the application of high voltage to produce fibrous mesh material on the collector. This technology makes it possible to obtain one-dimensional (1D) nanoscale metal oxide materials (nanofibers, nanotubes, and nanoclusters) with a required composition with the given morphology, depending on the type of the selected solvent and its viscosity, vapor pressure, and applied voltage [230, 242, 243].

3.1.8. Ecological methods. Ecological methods involve the synthesis of chemical compounds without the use of substances toxic to the environment and human health. Another advantage of such methods is their cheapness [244].

3.1.9. Green Synthesis. Green synthesis of metal oxide nanoparticles is carried out using various extracts [244, 245].

3.1.10. Combined Methods. The combination of different synthesis methods of nanoparticles allows the use of the advantages of individual methods, for example, to obtain nanocomposites with known and controlled chemical and phase composition, as well as with different and varied particle sizes [246]. Due to this, in modern practice, combined methods are gaining popularity [247]. A significant advantage of the combined methods is the possibility of obtaining both amorphous and crystalline powders with a sufficiently developed specific surface area (up to 600 m^2/g and above).

Thus, the considered methods have a high potential for obtaining nanostructured and nanodispersed metal oxides with a certain morphology and dispersion. But nowadays, the problem of the correct choice of the synthesis method of metal-oxide nanomaterials, which would allow the production of metalloxide nanomaterials with certain sorption, catalytic, surface, and structural properties, arises. In addition, it also necessary to aim to create materials with new and unique properties. This will lead to the acquisition of the newest, most effective metal-oxide nanomaterials with an ecological direction.

3.2. Creation of Nanocomposites with Metal Oxides. Certain successes have already been achieved in the synthesis of individual nanosized metal oxides, but the possibilities of synthesizing methods for the creation of nanomaterials based on the individual metal oxides, even with a certain morphology and dispersion, are limited; therefore, recently the attention of researches was focused on the creation of nanocomposites based on them. This is especially promising for nanomaterials for environmental purposes.

For example, for sorption materials a number of requirements are proposed, namely, cheapness, ease of obtaining, the possibility of reapplication, and high sorption efficiency and selectivity. It is known that one of the disadvantages of ZrO_2 as the sorbent is its high cost. To reduce the cost of such sorption materials, nanocomposites based on ZrO_2 can be created in combination with different carriers [248]. The choice of the carrier must be conditioned by

its properties, such as a developed surface, chemical inertness, and high sorption properties. The most popular carriers used today in the literature are Al_2O_3, Fe_2O_3, SiO_2, activated carbon, layered graphite, multilayer carbon nanotubes, and graphene.

The main characteristic of sorption-catalytic materials is their catalytic activity with respect to a certain list of pollutants. They should also have a large adsorption capacity in relation to the various pollutants of nature, a short time to establish the sorption equilibrium, and an ability to effectively separate from purified water to prevent a secondary contamination of the aqueous medium [3, 249, 250]. For example, TiO_2 with a particle size of about 20-30 nm will have a specific surface area of 60 m^2/g; however, after the aggregation of its particles, it can be reduced by two times or more. Obtaining nanocomposites with it and with different carriers may be one of the ways for solving this problem. As a result, the size of TiO_2 nanoparticles is stabilized on the matrix of the carrier, and the total specific surface area increases. Also, the creation and application of nanocomposites can prevent secondary contamination, and the modification of, for example, nanosized magnetite can facilitate the rapid removal of waste materials. This points to the prospect of the creation and use of nanocomposite material metal oxides.

A study on the inactivation of *Escherichia coli* shows that ZnO-TiO_2 composites exhibit high inactivation compared with ZnO and titanium (IV) oxide. The increase in the inactivation of *Escherichia coli* by ZnO-TiO_2 is explained by the separation of charge carriers in hybrid structures [251].

The analysis of literature data shows that magnetic composites based on such matrices as silica gel, activated carbon, carbon nanotubes, graphene, and clay minerals, are effective sorption materials for the extraction of heavy metals [252] and organic pollutants of a different nature [253–255]. Thus, the modification of activated carbon with a specific surface area of 430 m^2/g by nanosized magnetite results in a mesoporous composite with a specific surface area of 742 m^2/g [256], while the sorption capacities of polyethyleneimine-magnetite composites [257], silica gel-magnetite composites [258], and carbon nanotube-magnetite composites [259] containing Fe_3O_4 particles with a diameter of about 10 nm were 2-3 times higher than that of the matrix of the composites. It should be noted that the specific surface area of nanosized Fe_3O_4 is only 13 m^2/g [260].

Consequently, the advantages of creating metal oxide nanocomposites with an environmental direction can be attributed to the following factors: the ability to fix the nanodisperse state of metal oxide particles; the ability to obtain nanocomposites with certain structural-sorption characteristics and a high specific surface area; and the presence of synergistic effects in such nanocomposite materials, that is, their sorption-catalytic properties may be much better than their individual phases.

The creation of nanocomposites can be realized in different ways. In the literature, the most promising ways of creation are considered to be [3] the intercalation of nanosized particles in the porous system, deposition of nanosized particles on the inner pore surface of various rigid matrices (polymers, zeolites, and carbon materials), obtaining hybrid materials by sol-gel methods, etc.

The structures of some nanocomposites with metal oxides obtained in laboratory conditions are shown in Figure 15. As can be seen from Figure 15, the structure of composite materials can vary considerably: it is possible to obtain the numerical number of nanocomposites that will have various physical and chemical properties by varying the ratio of components, the nature of the matrix, and the synthesis method.

Proceeding from this, it can be argued that the nanocomposite era has only begun. Also, there is no information in modern literature regarding the influence of certain parameters on the final properties of composites for environmental purposes, but only a few studies with some of their types are available. Thus, carrying out systematic and comprehensive research on the synthesis and detection of the physicochemical properties of nanocomposite materials with metal oxides is the urgent and relevant issue that will allow the development of the scientific basis for the creation and use of the newest nanocomposites based on metal oxides for environmental purposes in order to improve their sorption and (photo)catalytic characteristics in comparison with the metal oxide counterparts.

4. Features of the Use of Metal Oxides and Nanocomposites Based on Them for Ecological Purposes

4.1. Nanomaterials Based on Pure Metal Oxides. As shown above, nanomaterials based on nanostructured and nanodispersed metal oxides are characterized by valuable electrical, optical, and magnetic properties. In view of this, they are used more and more in applied ecology, especially as adsorbents and photocatalysts, as well as materials used for the manufacture of environmental monitoring devices.

Adsorption materials based on nanosized metal oxides should have a large specific surface area, high capacity, fast kinetics, and specific affinity for various contaminants [3, 249, 250]. The use of nanostructured metal oxides in photocatalytic processes can permit the oxidation of organic compounds that are not decomposed biochemically, and the treatment of aqueous solutions by their use is considered to be the most promising [250]. Metalloxide nanostructures used in environmental monitoring as sensitive layers of chemoresistive gas sensors are characterized by high values of the sensory signal due to the significant specific surface area; hence, the higher adsorption capacity [8]. Consequently, nanosized metal oxide materials are of considerable interest because of their significant advantages over bulk analogues and because of the great prospects for obtaining new types of adsorbents, photocatalysts, and sensitive layers of gas sensors based on them.

Nowadays materials based on nanodispersed TiO_2 have the greatest demand as photocatalysts and disinfectants. Titanium (IV) oxide-based sorbents and photocatalysts are particularly effective in extracting a wide range of pollutants

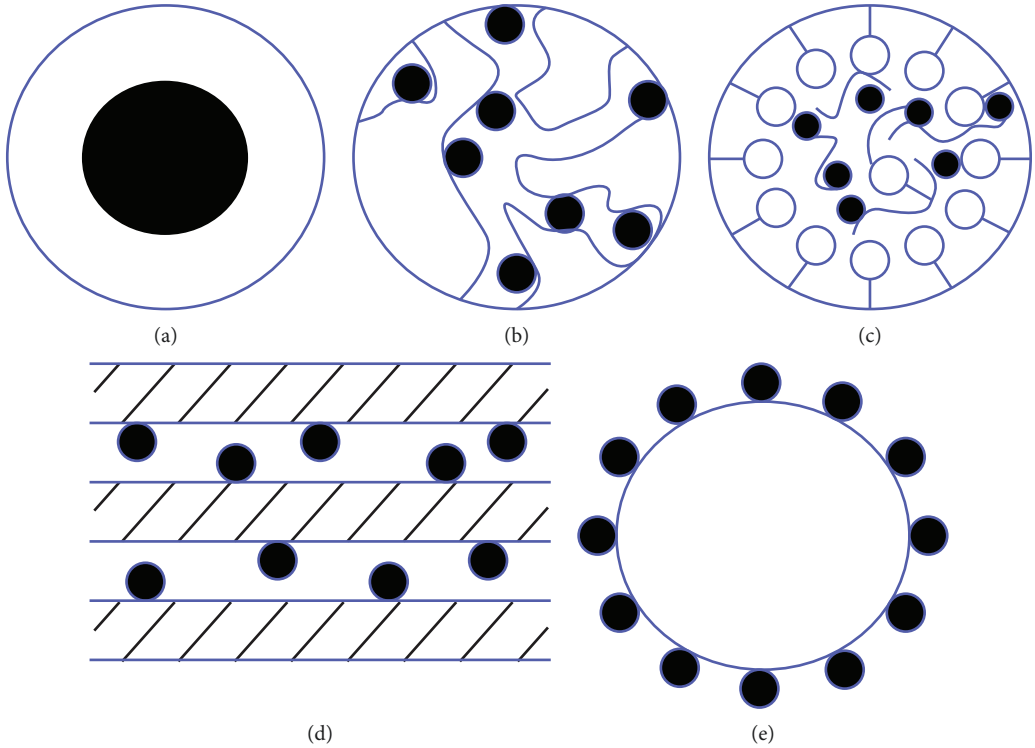

Figure 15: Nanocomposites based on nanodispersed metal oxides for environmental applications [261]: (a) core-shell structure; (b) with carbon materials and (c) with polymers; (d) surface modification of clay minerals and (e) nonporous metal oxide particles.

from water systems [262, 263]. This is evidenced by the growing number of researches devoted to this topic in the world. The mechanisms of photocatalysis involving metal oxides are presented in many studies [264–273]. At the same time, the prospects of using 1D nanostructures for photocatalytic processes, which have better transport characteristics than traditional nanoparticles, have recently been noted [274, 275].

However, unfortunately, these nanomaterials still do not have a commercial application because of their tendency to agglomerate due to the Van der Waal forces or other interactions [276], which results in a significant reduction or even the loss of the high adsorption capacity and selectivity with prolonged use. In addition, the disadvantages that limit the practical use of titanium (IV) oxide as a photocatalyst also include the high band gap, high recombination rate of electron-hole pairs, and low efficiency of the photocarrier separation [277]. It is known that the absorption of photons by particles of titanium (IV) oxide occurs only if the photon energy is greater than the energy of the forbidden band. In the case of the TiO_2 anatase modification, its surface photoactivation can be carried out exclusively under the influence of ultraviolet radiation (≤390 nm). However, only by 5% of sunlight consists of ultraviolet light (300-400 nm); therefore, the use of sunlight for the photoactivation of the pure anatase phase is not promising. The high recombination rate of the electron-hole pairs leads to the decrease in the photocatalytic efficiency of TiO_2 and, as a consequence, to the low quantum yield rate and limited photooxidation rate. The low efficiency of the photocarrier separation leads to the recombination, and therefore, to the low photocatalytic activity of photocatalysts.

One of the ways to improve the photocatalytic properties of TiO_2 is by doping or by modifying [277, 278]. This is achieved by self-doping, doping with nonmetals, doping with transition and rare-earth metals, or modifying with noble metals. As a result, the adsorption capacity and photocatalytic activity are improved. Using doping, additional energy levels are created in the structure of the zones that can be used to trap electrons or holes. As a result, the carriers are separated, which allows them to diffuse to the surface successfully. Also, as a result of doping, the desired redshift of the absorption edge can be achieved. Thus, doping can change both the electronic structure and the band gap, which ultimately leads to the optimization of the optical properties and the reduction of the massive recombination of photogenerated carriers in TiO_2. In addition, as was shown previously, the photocatalytic activity strongly depends on the set of open crystal facets, which have different levels of surface energy for the conduction band (CB) and valence band (VB), which can affect the carrier transport. The facet structure of TiO_2 particles can also be effectively modified by doping [264].

In addition to doping, for the change in the electronic properties of photocatalysts based on titanium (IV) oxide the method of ionic implantation of metals was proposed in [279], which resulted in photocatalysts that effectively absorb and work not only under ultraviolet light, but also under visible radiation (even longer than 550 nm). This, according to the authors, can be the important breakthrough in the use

of safe sunlight energy, which can shift these researches into the field of sustainable green chemistry.

In order to reduce the rate of recombination or even prevent it, the creation (excluding modifying) of nanocomposites based on titanium (IV) oxide is proposed [278, 280]. The modification of titanium (IV) oxide with noble metals (Au, Ag, Pt, and Pd) effectively increases the photocatalytic efficiency of TiO_2, but it is a very expensive process. In this composite, the metal plays a dual role as a catalyst and trap for electrons. Metal nanoparticles direct flows of photoinduced electrons and holes in opposite directions, which prevents their recombination [277]. Combining two semiconductors with the corresponding potentials of the conduction band and the valence band are considered to be a promising direction for increasing photocatalytic activity.

In recent years, a number of studies have been carried out on the formation of TiO_2-based heterostructures in conjunction with other semiconductors such as SnO_2, WO_3, Fe_2O_3, ZnO, and CdS, among which TiO_2 and SnO_2 composites are the most noteworthy. Nanocomposites of the TiO_2-SnO_2 anatase-rutile modification are characterized by the highest levels of photocatalytic activity due to the effects of the merging of SnO_2 nanoparticles and the coexistence of the phases of anatase and rutile [281, 282]. In addition, titanium (IV) oxide and tin (IV) oxide have similar ion radii (0.68 Å for Ti^{4+} and 0.71 Å for Sn^{4+}) and have similar structural (tetragonal structure of the rutile type) and electronic properties. The band gap widths of SnO_2, TiO_2 (anatase), and TiO_2(rutile) are 3.6 eV, 3.2 eV, and 3.0 eV, respectively, and the potential of the conduction band of tin (IV) oxide is approximately 0.5 V more positive than that of titanium (IV) oxide [281].

The use of ZnO-based photocatalysts for photooxidative degradation of organic pollutants in aqueous solutions looks promising and may be a good alternative of using TiO_2-based photocatalysts [283]. Its advantages include high potential efficiency, relative cheapness, high stability, nontoxicity, the absence of secondary pollution, and the possibility of decomposing harmful organic pollutants into less harmful pollutants in a relatively short time [284].

Photocatalysts based on zinc oxide synthesized by the sol-gel method show a high degree of removal (99.7%) of anionic dyes (for example, methylene orange) from aqueous solutions. The resulting photocatalyst efficiently and quickly decomposes azo dyes by the generated superoxide ions, which were the main species [285]. ZnO nanoparticles, which were obtained by the hydrothermal method, had various nanostructures, depending on the pH: nanorods, hexagonal disks, porous nanorods, and nanoflower structures. The photocatalytic activity of the obtained ZnO nanoparticles, estimated by the dye rhodamine B (RhB), was not lower than 94%. The photocatalyst had good stability for five cycles [286]. Thus, zinc oxide is an economical and environmentally friendly photocatalyst that can be used to clean wastewater contaminated with synthetic dyes.

It should be noted that photocatalysis with both TiO_2 and ZnO depends on the structural design of their particles, which are classified according to a known dimensional classification. In a zero-dimensional structure in the form of spheres, these materials have a high specific surface area and a porous structure. One-dimensional structures such as fibers or tubes may have lower recombination levels. Two-dimensional structures of titanium (IV) oxide and zinc oxide are characterized by a flat surface, high compression ratio, low turbidity, and excellent adhesion to substrates; as a result, they can be effectively used in self-cleaning glasses. The three-dimensional architectures of these materials can provide potential benefits for cleaning, separation, and storage. In general, the properties of these materials strongly depend on the dimensions of their structures; therefore, it is very important that the dimensions are taken into account before their use [287].

Despite the rather significant advantages, the use of photocatalysts based on ZnO has some problems: ZnO does not absorb the visible part of the solar spectrum and requires costly ultraviolet radiation to excite charge carriers that can recombine quickly; it is difficult to extract ZnO powder from the suspension after the photocatalytic process; ZnO has a tendency to aggregate during photocatalysis; and, most importantly, ZnO is susceptible to corrosion under the influence of ultraviolet light [111].

All these suggests that oxidative methods can solve the problem of the lack of clean water [288]. Directional modification or doping, creating the specific morphology and architecture, and attaining the required degree of crystallinity and the highest specific surface area are necessary for effective photocatalyst usage; creating metal oxide nanocomposites also looks very promising. The synthesis and characterization of porous ZnO-SnO_2 nanosheets obtained by the hydrothermal method in [289] showed the well-crystallized, porous, and well-defined morphology of the nanosheet material. The synthesized ZnO-SnO_2 nanocomposites were used as an effective photocatalyst and as a material in the manufacture of a chemical sensor. The photocatalytic degradation of the highly dangerous dye, direct blue 15, was carried out under irradiation with visible light. The synthesized nanocomposites were also used for the detection of 4-nitrophenol in an aqueous medium. The synthesized nanocomposites were highly active and highly sensitive. According to the authors, the obtained result was due to the formation of a ZnO-SnO_2 heterojunction, which effectively separates the photogenerated electron-hole pairs, and the high surface area.

The successful use of nanomaterials based on zinc oxide in electrochemical sensors is due to such properties as high specific surface area, chemical and photochemical stability, nontoxicity, electrochemical activity, and ease of synthesis. Its electrochemical activity and electronic communication features make it possible to consider ZnO-based nanomaterials as excellent candidates for electrochemical sensors [290]. However, the elevated operating temperature is still the bottleneck of widespread ZnO usage in real-time gas monitoring; thus, research to reduce the operating temperature is currently underway. To overcome this difficulty, surface modification, doping, and light activation are mainly proposed [291].

SnO_2-based nanostructures are already widely used in the creation of miniature chemoresistive gas sensors with

minimal energy consumption and high sensitivity [292]. However, the sensitivity and selectivity of SnO_2 sensors still remain as pressing questions. To increase the sensitivity of SnO_2-based nanostructures, a modification with various activating additives is necessary. Increasing the selectivity can be achieved by creating appropriate nanocomposites and obtaining information from several sensitive layers simultaneously with its subsequent mathematical processing. In this case, SnO_2-based nanostructures can be used to detect the most diverse components in the gas mixture, such as acetone, NH_3, NO_x, SO_2, H_2, CH_4, CO, CO_2, LPG, and others [293, 294].

Nanomaterials based on ZrO_2 are characterized by sufficiently high catalytic activity and sorption capacity due to the significant specific surface area of nanodispersed ZrO_2. Inorganic ion exchangers and adsorbents with ZrO_2 have certain advantages over known organic resins, since they are chemically stable even under high temperature [295]. The only drawback of sorption materials based on nanodispersed ZrO_2 is their relatively high cost.

For ecological purposes, all crystalline modifications of ZrO_2, as well as its amphoteric form, are used. Amphoteric zirconium (IV) oxide behaves as the anion exchange resin in an acidic and neutral solution and as the cation resin in an alkaline solution. The value of amphoteric ZrO_2 is that it can be successfully used in the processing of radioactive waste [296–298].

Crystalline ZrO_2 is an important material and is widely used in ceramic technology and in heterogeneous catalysis. Due to the nature of the n-type semiconductor, it has recently been considered as a photocatalyst in photochemical heterogeneous reactions. The report in the scientific literature of the energy values of the forbidden zone in the range from 3.25 to 5.1 eV, depending on the method of sample preparation, also contributed to this [299]. It is reported that nanoscale ZrO_2 of all modifications (monoclinic, tetragonal, and cubic) can be used as photocatalysts. In [300], ZrO_2 was studied as the catalyst for the photocatalytic degradation of methyl orange and the effect of all modifications was shown. It was found that the photocatalytic activity of the pure monoclinic ZrO_2 sample is higher than that of the tetragonal and cubic ZrO_2 samples under identical conditions. The authors explain the higher activity of the monoclinic ZrO_2 sample with respect to the photocatalytic degradation of methyl orange by the presence of a small amount of the oxygen-deficient zirconium oxide phase, high crystallinity, large pores, and the high density of surface hydroxyl groups.

In recent years, intensive research for the synthesis and use of nanoparticles based on ferric oxide, especially magnetite, which has magnetic properties that can be varied in a wide range due to the change in size and morphology, has begun. High surface-to-volume ratio and superparamagnetism make these ferromagnetic nanoparticles particularly attractive for use in the ecological direction [301]. In addition, magnetite nanoparticles are nontoxic, chemically inert, and biocompatible; therefore, they also have a huge potential for use in water purification.

The applications of nanoparticles based on TiO_2, ZnO, SnO_2, ZrO_2, and Fe_3O_4 in the ecological direction listed here indicate the likely prospect of creating new environmental technologies with their participation.

4.2. Nanocomposite Metal Oxide Materials. In modern literature, more and more studies on the creation of metal-oxide nanocomposites, an extremely promising type of nanomaterial, appear. Because of their structure, nanocomposites have specific, sometimes unique, physical and chemical properties and can be applied in a wide variety of fields, including engineering, medicine, and ecology as well as in the production of new materials in the construction industry.

Obtaining nanocomposites with metal oxides for water purification is considered in terms of stabilizing the latter in the matrix of the composite and their easy separation after the completion of the processes of sorption and photocatalysis. In addition, the use of individual nanodispersed metal oxides can lead to environmental contamination with nanoparticles but using them as part of nanocomposites will prevent this [3]. Nanocomposites based on nanodispersed oxides of titanium and zirconium and a carbon matrix (activated carbon, carbon nanotubes, and graphene) indeed have great potential for use in water purification [302]. Mesoporous oxides of titanium and zirconium are characterized by high values of exchange capacity and chemical and thermal resistance, and carbon materials have mechanical strength, resistance to aggressive environments, and a well-developed porous structure. It is possible to obtain fundamentally new sorption materials that will have this given set of properties by combining these phases.

In assessing the promising use of metal oxide nanocomposites based on activated carbon for sorption and photocatalytic purposes, it was noted that the increase of the sorption capacity and photocatalytic activity of organic substances is at least 2.5 times compared with those of pure metal oxides [303]. The introduction, for example, of TiO_2 in a matrix with a diverse nature increases not only the adsorption capacity but also the chemical stability of the final composite material [304].

ZnO-based nanocomposites for environmental applications are becoming increasingly popular. The most diverse composites are synthesized based on it, where both natural substances (clay minerals, chitin, and chitosan) and artificial ones (graphene, CNT, polymers, and other metal oxides) are used as a matrix [305, 306].

The creation of composites based on zinc oxide, for example, ZnO-graphene, allows obtaining photocatalytically active catalysts with respect to antibiotics in wastewater [307]. The obtained ZnO-reduced graphene oxide (rGO) nanocomposites in [308] showed more than doubled photocatalytic activity in visible light to dyes of different natures compared to pure ZnO. The photoactivity of nanocomposites is due to the smaller size of ZnO nanorods and the presence of rGO, which acts as the photosensitizer, transferring electrons to the ZnO conduction band inside the nanocomposite when illuminated by sunlight.

Obtaining mixed oxide nanocomposites with the participation of various oxides is considered very promising for the creation of effective photocatalysts/sorbents to organic pollutants. This fact is confirmed by the authors in [309], who

showed that the mixed oxide nanocomposite WO_3-ZnO is the most effective photocatalyst for the decomposition of organic pollutants in water compared to commercial ZnO.

It was established that the creation of nanocomposites based on tin (IV) oxide with other metal oxides for their usage as sensitive layers of gas sensors can increase the selectivity of the detection of certain analytes. At the same time, due to the developed surface of metal oxides and the low solubility of metal oxide additives in them, there is mainly the superficial distribution of modifiers. This leads to the purposeful change in the surface state and the creation of additional active centers, contributing to the separation of the functions of the metal oxide surface (receptor) and volume (converter) [310]. SnO_2-carbon nanotube nanocomposites exhibit high sensitivity at low power consumption; therefore, effective devices for monitoring the environment at ambient temperatures can be created based on such compositions [311–313].

For the "zirconium (IV) oxide-activated carbon nanocomposite," a synergistic effect in extracting heavy metals from aqueous solutions was found (the sorption capacity of the nanocomposite, for example, was 8 times higher than that of pure ZrO_2 and 3.15 times higher than that of activated carbon) [227]. Even the ordinary mixing of nanosized titanium oxide with activated carbon leads to the increase in the sorption capacity by 1.3 times [314].

In recent years, the development of nanocomposite magnetic sorbent materials based on minerals is also growing due to the possibility of the easy removal of clay minerals after the completion of the sorption process. The synthesis of magnetite-containing particles and their modification are considered "green" technologies, and the sorbents themselves are "green" materials [315–318], while the creation of magnetic sorbents is already offered from a variety of wastes [319]. According to the results of the studies, the modification of a clay matrix such as zeolites, bentonites, and montmorillonite clays by nanosized magnetite does not reduce the adsorption capacity [320, 321], and in some cases even increases it [124, 254].

The analysis of the relevant literary sources leads to the conclusion that studies devoted to the synthesis and use of nanocomposite metal oxide materials in the ecological direction are almost not carried out. Therefore, today this is the rather topical issue, the solution of which will lead to the creation of new technologies for obtaining and using composite nanomaterials in the recovery of the environment and catalysis.

5. Conclusions

The considered features of the properties and the creation of metal oxide nanomaterials and nanocomposites based on TiO_2, ZnO, SnO_2, ZrO_2, and Fe_3O_4 for ecological applications show the likely prospect of the development of this scientific and practical direction. It is shown that the dispersion and morphology of nanoparticles have a determining influence on the finite physical and chemical characteristics of metal oxide nanomaterials. For TiO_2, ZnO, SnO_2, ZrO_2, and Fe_3O_4, the crystallochemical characteristic, the surface structure, and the features of surface phenomena, which have a significant effect on their sorption and catalytic properties, are given. Their use as sorbents, photocatalysts, and sensitive layers of gas sensors has been substantiated. It is shown that the creation of metal-oxide composite nanomaterials, which will have better sorption and catalytic properties than their individual metal oxide nanomaterials due to the synergistic effects and special structural and adsorption characteristics, is the most promising direction. This will allow obtaining a fundamentally new class of nanomaterials for environmental purposes. Based on the analysis of modern literary sources, it is expected that the use of metal-oxide nanocomposites for environmental applications will lead to the development of new effective environmentally and economically feasible technologies.

Conflicts of Interest

The authors declare that there is no conflict of interest regarding the publication of this paper.

Acknowledgments

The authors thank the Faculty of Chemical Technology of the National Technical University of Ukraine "Igor Sikorsky Kyiv Polytechnic Institute" for support in conducting this research. The authors also thank the Postgraduate and Doctoral Studies Department of the National Technical University of Ukraine "Igor Sikorsky Kyiv Polytechnic Institute" for funding support.

References

[1] J. L. G. Fierro, Ed., *Metal Oxides: Chemistry and Application*, Taylor & Francis, CRC Press, 2006.

[2] S. R. Kumar and P. Gopinath, *Nano-Bioremediation Applications of Nanotechnology for Bioremediation*, in The Book: Remediation of Heavy Metals in the Environment, CRC Press, Boca Raton, 2016.

[3] Y. Zhang, B. Wu, H. Xu et al., "Nanomaterials-enabled water and wastewater treatment," *NanoImpact*, vol. 3-4, pp. 22–39, 2016.

[4] C. Santhosh, V. Velmurugan, G. Jacob, S. K. Jeong, A. N. Grace, and A. Bhatnagar, "Role of nanomaterials in water treatment applications: a review," *Chemical Engineering Journal*, vol. 306, pp. 1116–1137, 2016.

[5] A. A. Werkneh and E. R. Renein, *Applications of Nanotechnology and Biotechnology for Sustainable Water and Wastewater Treatment*, in The Book: Water and Wastewater Treatment Technologies, Energy, Environment, and Sustainability, Springer, Singapore, 2019.

[6] M. Cerro-Lopez and M. A. Méndez-Rojas, "Application of nanomaterials for treatment of wastewater containing pharmaceuticals," in *The Handbook of Environmental Chemistry*, vol. 66, Springer, Cham, 2017.

[7] M. Pelaez, N. T. Nolan, S. C. Pillai et al., "A review on the visible light active titanium dioxide photocatalysts for environmental applications," *Applied Catalysis B: Environmental*, vol. 125, no. 21, pp. 331–349, 2012.

[8] C. Xu, J. Tamaki, N. Miura, and N. Yamazoe, "Grain size effects on gas sensitivity of porous SnO_2-based elements," *Sensors and Actuators B: Chemical*, vol. 3, no. 2, pp. 147–155, 1991.

[9] D. R. Miller, S. A. Akbar, and P. A. Morris, "Nanoscale metal oxide-based heterojunctions for gas sensing: a review," *Sensors and Actuators B: Chemical*, vol. 204, pp. 250–272, 2014.

[10] T. A. Miller, S. D. Bakrania, C. Perez, and M. S. Wooldridge, "Nanostructured tin dioxide materials for gas sensor applications," *Functional Nanomaterials*, vol. 30, pp. 1–24, 2006.

[11] U. Diebold, "The surface science of titanium dioxide," *Surface Science Reports*, vol. 48, no. 5-8, pp. 53–229, 2003.

[12] S. M. Gupta and M. Tripathi, "A review of TiO_2 nanoparticles," *Chinese Science Bulletin*, vol. 56, no. 16, pp. 1639–1657, 2011.

[13] A. S. Barnard and P. Zapol, "Effects of particle morphology and surface hydrogenation on the phase stability of TiO_2," *Physical Review B*, vol. 70, no. 23, article 235403, p. 23, 2004.

[14] H. Morkoç and Ü. Özgür, *Zinc Oxide: Fundamentals, Materials and Device Technology*, Wiley-VCH Verlag GmbH & Co. KGaA, 2009.

[15] M. I. H. Chowdhury, M. S. Hossain, M. A. S. Azad, M. Z. Islam, and M. A. Dewan, "ZnO: material, physics and applications," *Chemphyschem*, vol. 8, no. 6, pp. 782–803, 2007.

[16] M. A. Maki-Jaskari and T. T. Rantala, "Band structure and optical parameters of the SnO_2(110) surface," *Physical Review B*, vol. 64, no. 7, article 075407, 2001.

[17] H. K. Shashikumar, M. Siddaraju, and B. N. Chethan, "Structure simulation and study of electronic and dielectric properties of tin dioxide," *Inorganic Chemistry: An Indian Journal*, vol. 10, no. 4, pp. 148–151, 2015.

[18] I. D. Muhammad, M. Awang, O. Mamat, and Z. B. Shaari, "First-principles calculations of the structural, mechanical and thermodynamics properties of cubic zirconia," *World Journal of Nano Science and Engineering*, vol. 4, no. 2, pp. 97–103, 2014.

[19] S. Banerjee and P. Mukhopadhyay, *Phase Transformations: Examples from Titanium and Zirconium Alloys*, Elsevier Ltd., 2007.

[20] R. J. Nicholls, N. Ni, S. Lozano-Perez et al., "Crystal structure of the ZrO_2 phase at zirconium/zirconium oxide interfaces," *Advanced Engineering Materials*, vol. 17, no. 2, pp. 211–215, 2015.

[21] I. Nettleship and R. Stevens, "Tetragonal zirconia polycrystal (TZP)—a review," *International Journal of High Technology Ceramics*, vol. 3, no. 1, pp. 1–32, 1987.

[22] G. Dercz, K. Prusik, and L. Pajak, "X-ray and SEM studies on zirconia powders," *Journal of Achievements in Materials and Manufacturing Engineering*, vol. 31, no. 2, pp. 408–414, 2008.

[23] G. S. Parkinson, "Iron oxide surfaces," *Surface Science Reports*, vol. 71, no. 1, pp. 272–365, 2016.

[24] K. E. Sickafus, J. M. Wills, and N. W. Grimes, "Structure of spinel," *Journal of the American Ceramic Society*, vol. 82, no. 12, pp. 3279–3292, 1999.

[25] A. W. Adamson and A. P. Gast, *Physical Chemistry of Surfaces*, Wiley-Interscience, New York, NY, USA, 6th edition, 1997.

[26] M. Ramamoorthy, R. D. King-Smith, and D. Vanderbilt, "Defects on TiO_2 (110) surfaces," *Physical Review B*, vol. 49, no. 11, pp. 7709–7715, 1994.

[27] W. C. Mackrodt, E. A. Simson, and N. M. Harrison, "An ab initio Hartree-Fock study of the electron-excess gap states in oxygen-deficient rutile TiO_2," *Surface Science*, vol. 384, no. 1–3, pp. 192–200, 1997.

[28] A. Vijay, G. Mills, and H. Metiu, "Adsorption of gold on stochiometric and reduced rutile TiO_2 (110) surfaces," *The Journal of Chemical Physics*, vol. 118, no. 14, pp. 6536–6551, 2003.

[29] J. Oviedo, M. A. San Miguel, and J. F. Sanz, "Oxygen vacancies on TiO_2 (110) from first-principles calculations," *The Journal of Chemical Physics*, vol. 121, no. 15, pp. 7427–7433, 2004.

[30] M. Menetrey, A. Markovits, and C. Minot, "Reactivity of a reduced metal oxide surface: hydrogen, water and carbon monoxide adsorption on oxygen defective rutile TiO_2(110)," *Surface Science*, vol. 524, no. 1–3, pp. 49–62, 2003.

[31] A. T. Paxton and L. Thien-Nga, "Electronic structure of reduced titanium dioxide," *Physical Review B*, vol. 57, no. 3, pp. 1579–1584, 1998.

[32] P. J. D. Lindan, N. M. Harrison, M. J. Gillan, and J. A. White, "First-principles spin-polarized calculations on the reduced and reconstructed TiO_2 (110) surface," *Physical Review B*, vol. 55, no. 23, pp. 15919–15927, 1997.

[33] M. D. Rasmussen, L. M. Molina, and B. Hammer, "Adsorption, diffusion and dissociation of molecular oxygen at defected TiO_2(110): a density functional theory study," *The Journal of Chemical Physics*, vol. 120, no. 2, pp. 988–997, 2004.

[34] X. Wu, A. Selloni, and S. K. Nayak, "First principles study of CO oxidation on TiO_2 (110): the role of surface oxygen vacancies," *The Journal of Chemical Physics*, vol. 120, no. 9, pp. 4512–4516, 2004.

[35] X. Wu, A. Selloni, M. Lazzeri, and S. K. Nayak, "Oxygen vacancy mediated adsorption and reactions of molecular oxygen on the TiO_2(110) surface," *Physical Review B*, vol. 68, no. 24, article 241402, 2003.

[36] A. Vittadini and A. Selloni, "Small gold clusters on stochiometric and defected TiO_2 anatase (101) and their interaction with CO: a density functional study," *The Journal of Chemical Physics*, vol. 117, no. 1, pp. 353–361, 2002.

[37] Y.-F. Zhang, W. Lin, Y. Li, K. N. Ding, and J. Q. Li, "A theoretical study on the electronic structures of TiO_2: effect of Hartree-Fock exchange," *The Journal of Physical Chemistry B*, vol. 109, no. 41, pp. 19270–19277, 2005.

[38] C. Di Valentin, G. Pacchioni, and A. Selloni, "Electronic structure of defect states in hydroxylated and reduced rutile TiO_2 (110) surfaces," *Physical Review Letters*, vol. 97, no. 16, article 166803, 2006.

[39] E. Cho, S. Han, H.-S. Ahn, K. R. Lee, S. K. Kim, and C. S. Hwang, "First-principles study of defects in rutile TiO_{2-x}," *Physical Review B*, vol. 73, no. 19, article 193202, 2006.

[40] C. di Valentin, G. Pacchioni, and A. Selloni, "Theory of carbon doping of titanium dioxide," *Chemistry of Materials*, vol. 17, no. 26, pp. 6656–6665, 2005.

[41] K. Hameeuw, G. Cantele, D. Ninno, F. Trani, and G. Iadonisi, "Influence of surface and subsurface defects on the behavior of the rutile TiO_2 (110) surface," *Physica Status Solidi (A)*, vol. 203, no. 9, pp. 2219–2222, 2006.

[42] M. V. Ganduglia-Pirovano, A. Hofmann, and J. Sauer, "Oxygen vacancies in transition metal and rare earth oxides: current state of understanding and remaining challenges," *Surface Science Reports*, vol. 62, no. 6, pp. 219–270, 2007.

[43] M. Ramamoorthy, D. Vanderbilt, and R. D. King-Smith, "First-principles calculations of the energetics of stoichiometric TiO_2 surfaces," *Physical Review B*, vol. 49, no. 23, pp. 16721–16727, 1994.

[44] S. Andersson, B. Collén, U. Kuylenstierna et al., "Phase analysis studies on the titanium-oxygen system," *Acta Chemica Scandinavica*, vol. 11, pp. 1641–1652, 1957.

[45] J. B. Goodenough, "Metallic oxides," *Progress in Solid State Chemistry*, vol. 5, pp. 145–399, 1972.

[46] Z. Zhang and J. T. Yates, *Defects on TiO_2-Key Pathways to Important Surface Processes*, in The Book: Defects at Oxide Surfaces, Springer, Switzerland, 2015.

[47] M. Lazzeri, A. Vittadini, and A. Selloni, "Structure and energetics of stochiometric TiO_2 anatase surfaces," *Physical Review B*, vol. 63, no. 15, article 155409, 2001.

[48] U. Diebold, N. Ruzycki, G. S. Herman, and A. Selloni, "One step towards bridging the materials gap: surface studies of TiO_2 anatase," *Catalysis Today*, vol. 85, no. 2–4, pp. 93–100, 2003.

[49] D. J. Cooke, A. Marmier, and S. C. Parker, "Surface structure of $(10\bar{1}0)$ and $(11\bar{2}0)$ surfaces of ZnO with density functional theory and atomistic simulation," *The Journal of Physical Chemistry B*, vol. 110, no. 15, pp. 7985–7991, 2006.

[50] A. Janotti and C. G. van de Walle, "Fundamentals of zinc oxide as a semiconductor," *Reports on Progress in Physics*, vol. 72, no. 12, article 126501, 2009.

[51] M. A. Maki-Jaskari and T. T. Rantala, "Theoretical study of oxygen-deficient SnO_2 (110) surfaces," *Physical Review B*, vol. 65, no. 24, article 245428, 2002.

[52] T. T. Rantala, T. S. Rantala, and V. Lantto, "Surface relaxation of the (110) face of rutile SnO_2," *Surface Science*, vol. 420, no. 1, pp. 103–109, 1999.

[53] T. T. Rantala, T. S. Rantala, and V. Lantto, "Electronic structure of SnO_2 (110) surface," *Materials Science in Semiconductor Processing*, vol. 3, no. 1–2, pp. 103–107, 2000.

[54] A. Bouzoubaa, A. Markovits, M. Calatayud, and C. Minot, "Comparison of the reduction of metal oxide surfaces: TiO_2-anatase, TiO_2-rutile and SnO_2-rutile," *Surface Science*, vol. 583, no. 1, pp. 107–117, 2005.

[55] E. A. Florianoa, L. V. A. Scalvia, J. R. Sambranoc, and V. Geraldo, "Evaluation of bulk and surfaces absorption edge energy of sol-gel-dip-coating SnO_2 Thin Films," *Materials Research*, vol. 13, no. 4, pp. 437–443, 2010.

[56] I. Manassidis, J. Goniakowski, L. N. Kantorovich, and M. J. Gillan, "The structure of the stoichiometric and reduced SnO_2 (110) surface," *Surface Science*, vol. 339, no. 3, pp. 258–271, 1995.

[57] D. F. Cox, T. B. Fryberger, and S. Semancik, "Oxygen vacancies and defect electronic states on the SnO_2 (110)-1×1 surface," *Physical Review B*, vol. 38, no. 3, pp. 2072–2083, 1988.

[58] M. Sinner-Hettenbach, M. Göthelid, J. Weissenrieder et al., "Oxygen-deficient SnO_2 (110): a STM, LEED and XPS study," *Surface Science*, vol. 477, no. 1, pp. 50–58, 2001.

[59] J. M. Themlin, R. Sporken, J. Darville, R. Caudano, J. M. Gilles, and R. L. Johnson, "Resonant-photoemission study of SnO_2: cationic origin of the defect band-gap states," *Physical Review B*, vol. 42, no. 18, pp. 11914–11925, 1990.

[60] M. Sinner-Hettenbach, M. Göthelid, T. Weiß et al., "Electronic structure of SnO_2 (110)-4×1 and sputtered SnO_2 (110) revealed by resonant photoemission," *Surface Science*, vol. 499, no. 1, pp. 85–93, 2002.

[61] J. Oviedo and M. J. Gillan, "The energetics and structure of oxygen vacancies on the SnO_2 (110) surface," *Surface Science*, vol. 467, no. 1–3, pp. 35–48, 2000.

[62] J. Oviedo and M. J. Gillan, "Reconstructions of strongly reduced SnO_2 (110) studied by first-principles methods," *Surface Science*, vol. 513, no. 1, pp. 26–36, 2002.

[63] R. G. Egdell, S. Eriksen, and W. R. Flavell, "Oxygen deficient SnO_2 (110) and TiO_2 (110): a comparative study by photoemission," *Solid State Communications*, vol. 60, no. 10, pp. 835–838, 1986.

[64] D. F. Cox, S. Semancik, and P. D. Szuromi, "Structural and electronic-properties of clean and water dosed SnO_2 (110)," *Journal of Vacuum Science & Technology A*, vol. 4, no. 3, pp. 627-628, 1986.

[65] D. F. Cox, T. B. Fryberger, J. W. Erickson, and S. Semancik, "Surface-properties of clean and gas-dosed SnO_2 (110)," *Journal of Vacuum Science & Technology A*, vol. 5, no. 4, pp. 1170-1171, 1987.

[66] E. de Frésart, J. Darville, and J. M. Gilles, "Influence of the surface reconstruction on the work function and surface conductance of (110) SnO_2," *Applications of Surface Science*, vol. 11-12, pp. 637–651, 1982.

[67] D. F. Cox and T. B. Fryberger, "Preferential isotopic labeling of lattice oxygen positions on the SnO_2 (110) surface," *Surface Science*, vol. 227, no. 1–2, pp. L105–L108, 1990.

[68] A. Atrei, E. Zanazzi, U. Bardi, and G. Rovida, "The SnO_2 (110) (4×1) structure determined by LEED intensity analysis," *Surface Science*, vol. 475, no. 1–3, pp. L223–L228, 2001.

[69] F. H. Jones, R. Dixon, J. S. Foord, R. G. Egdell, and J. B. Pethica, "The surface structure of SnO_2 (110) (4×1) revealed by scanning tunneling microscopy," *Surface Science*, vol. 376, no. 1–3, pp. 367–373, 1997.

[70] C. L. Pang, S. A. Haycock, H. Raza, P. J. Møller, and G. Thornton, "Structures of the 4×1 and 1×2 reconstructions of SnO_2 (110)," *Physical Review B*, vol. 62, no. 12, pp. R7775–R7778, 2000.

[71] M. Batzill, K. Katsiev, J. M. Burst, U. Diebold, A. M. Chaka, and B. Delley, "Gas-phase-dependent properties of SnO_2 (110), (100), and (101) single-crystal surfaces: structure, composition, and electronic properties," *Physical Review B*, vol. 72, no. 16, article 165414, 2005.

[72] M. Batzill, A. M. Chaka, and U. Diebold, "Surface oxygen chemistry of a gas-sensing material: SnO_2(101)," *Europhysics Letters*, vol. 65, no. 1, pp. 61–67, 2004.

[73] M. Batzill and U. Diebold, "The surface and materials science of tin oxide," *Progress in Surface Science*, vol. 79, no. 2-4, pp. 47–154, 2005.

[74] M. Batzill and U. Diebold, "Characterizing solid state gas responses using surface charging in photoemission: water adsorption on SnO_2(101)," *Journal of Physics: Condensed Matter*, vol. 18, no. 8, pp. L129–L134, 2006.

[75] M. Batzill, K. Katsiev, J. M. Burst et al., "Tuning surface properties of SnO_2 (101) by reduction," *Journal of Physics and Chemistry of Solids*, vol. 67, no. 9–10, pp. 1923–1929, 2006.

[76] M. Batzill, "Surface science studies of gas sensing materials: SnO_2," *Sensors*, vol. 6, no. 10, pp. 1345–1366, 2006.

[77] D. K. Smith and W. Newkirk, "The crystal structure of baddeleyite (monoclinic ZrO_2) and its relation to the polymorphism of ZrO_2," *Acta Crystallographica*, vol. 18, no. 6, pp. 983–991, 1965.

[78] F. Haase and J. Sauer, "The surface structure of sulfated zirconia: periodic ab initio study of sulfuric acid adsorbed on ZrO_2 (101) and ZrO_2 (001)," *Journal of the American Chemical Society*, vol. 120, no. 51, pp. 13503–13512, 1998.

[79] G. Teufer, "The crystal structure of tetragonal ZrO_2," *Acta Crystallographica*, vol. 15, no. 11, p. 1187, 1962.

[80] D. K. Smith and C. F. Cline, "Verification of existence of cubic zirconia at high temperature," *Journal of the American Ceramic Society*, vol. 45, no. 5, pp. 249-250, 1962.

[81] B. Akgenc and T. Cagin, "Density functional theory of cubic zirconia and 6–15 mol% doped yttria-stabilized zirconia: structural and mechanical properties," *Turkish Journal of Physics*, vol. 42, pp. 223–231, 2018.

[82] C. Morterra, G. Cerrato, L. Ferroni, A. Negro, and L. Montanaro, "Surface characterization of tetragonal ZrO_2," *Applied Surface Science*, vol. 65-66, pp. 257–264, 1993.

[83] A. Hofmann, S. J. Clark, M. Oppel, and I. Hahndorf, "Hydrogen adsorption on the tetragonal ZrO_2(101) surface: a theoretical study of an important catalytic reactant," *Physical Chemistry Chemical Physics*, vol. 4, no. 14, pp. 3500–3508, 2002.

[84] A. Christensen and E. A. Carter, "First-principles study of the surfaces of zirconia," *Physical Review B*, vol. 58, no. 12, pp. 8050–8064, 1998.

[85] A. Eichler and G. Kresse, "First-principles calculations for the surface termination of pure and yttria-doped zirconia surfaces," *Physical Review B*, vol. 69, no. 4, article 045402, 2004.

[86] P. W. Tasker, "The stability of ionic crystal surfaces," *Journal of Physics C: Solid State Physics*, vol. 12, no. 22, pp. 4977–4984, 1979.

[87] R. M. Cornell and U. Schwertmann, *The Iron Oxides: Structure, Properties, Reactions, Occurrences and Uses*, Wiley-VCH, 2003.

[88] J. C. Russ, *Fractal Surface*, Springer Science+Business Media, New York, NY, USA, 1994.

[89] C. T. Campbell and J. Sauer, "Introduction: surface chemistry of oxides," *Chemical Reviews*, vol. 113, no. 6, pp. 3859–3862, 2012.

[90] R. A. van Santen, I. Tranca, and E. J. M. Hensen, "Theory of surface chemistry and reactivity of reducible oxides," *Catalysis Today*, vol. 244, pp. 63–84, 2015.

[91] Y.-F. Geng, P. Li, J.-Z. Li, X. M. Zhang, Q. D. Zeng, and C. Wang, "STM probing the supramolecular coordination chemistry on solid surface: structure, dynamic, and reactivity," *Coordination Chemistry Reviews*, vol. 337, pp. 145–177, 2017.

[92] H. H. Kung, Ed., "Transition metal oxides: surface chemistry and catalysis," *Studies in Surface Science and Catalysis*, vol. 45, pp. 1–286, 1989.

[93] R. A. V. Santen, "Theoretical heterogeneous catalysis," *World Scientific Lecture and Course Notes in Chemistry*, vol. 5, p. 322, 1991.

[94] D. R. Mullins, "The surface chemistry of cerium oxide," *Surface Science Reports*, vol. 70, no. 1, pp. 42–85, 2015.

[95] Z. Jovanovic, D. Bajuk-Bogdanović, S. Jovanović et al., "The role of surface chemistry in the charge storage properties of graphene oxide," *Electrochimica Acta*, vol. 258, pp. 1228–1243, 2017.

[96] J. R. H. Ross, Ed., *Heterogeneous Catalysis. Fundamentals and Applications*, Elsevier, 2012.

[97] M. M. Sychev, T. S. Minakova, Y. G. Slizhov, and O. A. Shilova, *Acid-Basic Characteristics of the Surface of Solids and Control of the Properties of Materials and Composites*, Khimizdat, St. Petersburg, 2016.

[98] M. A. Islam, D. W. Morton, B. B. Johnson, B. Mainali, and M. J. Angove, "Manganese oxides and their application to metal ion and contaminant removal from wastewater," *Journal of Water Process Engineering*, vol. 26, pp. 264–280, 2018.

[99] J. Rivera-Utrilla, I. Bautista-Toledo, M. . A. Ferro-García, and C. Moreno-Castilla, "Activated carbon surface modifications by adsorption of bacteria and their effect on aqueous lead adsorption," *Journal of Chemical Technology & Biotechnology*, vol. 76, no. 12, pp. 1209–1215, 2001.

[100] A. Piscopo, D. Robert, and J. V. Weber, "Influence of pH and chloride anion on the photocatalytic degradation of organic compounds," *Applied Catalysis B: Environmental*, vol. 35, no. 2, pp. 117–124, 2001.

[101] M. Fukuta, N. Zettsu, I. Yamashita, Y. Uraoka, and H. Watanabe, "The adsorption mechanism of titanium-binding ferritin to amphoteric oxide," *Colloids and Surfaces B: Biointerfaces*, vol. 102, pp. 435–440, 2013.

[102] S. Nagirnyak, V. Lutz, T. Dontsova, and I. Astrelin, "The effect of the synthesis conditions on morphology of tin (IV) oxide obtained by vapor transport method," *Nanophysics, Nanophotonics, Surface Studies, and Applications*, vol. 183, p. 331, 2016.

[103] S.–. C. Chang, "Oxygen chemisorption on tin oxide: correlation between electrical conductivity and EPR measurements," *Journal of Vacuum Science and Technology*, vol. 17, no. 1, pp. 366–369, 1980.

[104] J. Matos, S. Miralles-Cuevas, A. Ruíz-Delgado, I. Oller, and S. Malato, "Development of TiO_2-C photocatalysts for solar treatment of polluted water," *Carbon*, vol. 122, pp. 361–373, 2017.

[105] M. Shafaee, E. K. Goharshadi, M. Mashreghi, and M. Sadeghinia, "TiO_2 nanoparticles and TiO_2@graphene quantum dots nancomposites as effective visible/solar light photocatalysts," *Journal of Photochemistry and Photobiology A: Chemistry*, vol. 357, pp. 90–102, 2018.

[106] J. Archana, S. Harish, S. Kavirajan et al., "Ultra-fast photocatalytic and dye-sensitized solar cell performances of mesoporous TiO_2 nanospheres," *Applied Surface Science*, vol. 449, pp. 729–735, 2018.

[107] Z. Shayegan, C.-S. Lee, and F. Haghighat, "TiO_2 photocatalyst for removal of volatile organic compounds in gas phase—a review," *Chemical Engineering Journal*, vol. 334, pp. 2408–2439, 2018.

[108] R. Murugan and C. Ganesh Ram, "Energy efficient drinking water purification system using TiO_2 solar reactor with traditional methods," *Materials Today: Proceedings*, vol. 5, no. 1, pp. 415–421, 2018.

[109] S. Kathirvel, H.-S. Chen, C. Su, H. H. Wang, C. Y. Li, and W. R. Li, "Preparation of smooth surface TiO_2 photoanode for high energy conversion efficiency in dye-sensitized solar cells," *Journal of Nanomaterials*, vol. 2013, Article ID 367510, 8 pages, 2013.

[110] S. G. Kumar and K. S. R. Koteswara Rao, "Zinc oxide based photocatalysis: tailoring surface-bulk structure and related interfacial charge carrier dynamics for better environmental applications," *RSC Advances*, vol. 5, no. 5, pp. 3306–3351, 2015.

[111] S. Nahirniak, T. Dontsova, and I. Astrelin, "Directional synthesis of SnO_2-based nanostructures for use in gas sensors," *Nanochemistry, Biotechnology, Nanomaterials, and Their Applications*, vol. 214, pp. 233–245, 2018.

[112] L. X. Lovisa, V. D. Araújo, R. L. Tranquilin et al., "White photoluminescence emission from ZrO_2 co-doped with Eu^{3+}, Tb^{3+} and Tm^{3+}," *Journal of Alloys and Compounds*, vol. 674, pp. 245–251, 2016.

[113] A. Zheng, S. J. Huang, Q. Wang, H. Zhang, F. Deng, and S. B. Liu, "Progress in development and application of solid-state NMR for solid acid catalysis," *Chinese Journal of Catalysis*, vol. 34, no. 3, pp. 436–491, 2013.

[114] M. C. Muñoz, S. Gallego, J. I. Beltrán, and J. Cerdá, "Adhesion at metal-ZrO_2 interfaces," *Surface Science Reports*, vol. 61, no. 7, pp. 303–344, 2006.

[115] A. Saxena, N. Singh, D. Kumar, and P. Gupta, "Effect of ceramic reinforcement on the properties of metal matrix nanocomposites," *Materials Today: Proceedings*, vol. 4, no. 4, pp. 5561–5570, 2017.

[116] G. Soon, B. Pingguan-Murphy, K. W. Lai, and S. A. Akbar, "Review of zirconia-based bioceramic: surface modification and cellular response," *Ceramics International*, vol. 42, no. 11, pp. 12543–12555, 2016.

[117] Y. L. Bruni, L. B. Garrido, and E. F. Aglietti, "Effect of high alumina cement on permeability and structure properties of ZrO_2 composites," *Ceramics International*, vol. 38, no. 3, pp. 1755–1763, 2012.

[118] M. E. Zorn, D. T. Tompkins, W. A. Zeltner, and M. A. Anderson, "Photocatalytic oxidation of acetone vapor on TiO_2/ZrO_2 thin films," *Applied Catalysis B: Environmental*, vol. 23, no. 1, pp. 1–8, 1999.

[119] K. Hayek, R. Kramer, and Z. Paál, "Metal-support boundary sites in catalysis," *Applied Catalysis A: General*, vol. 162, no. 1–2, pp. 1–15, 1997.

[120] N. I. de Azevedo Lopes, L. de Arruda Santos, and V. T. L. Buono, "Mechanical properties of nanoceramic zirconia coatings on NiTi orthodontic wires," *Advances in Science and Technology*, vol. 97, pp. 147–152, 2016.

[121] M. O. Curi, H. C. Ferraz, J. G. M. Furtado, and A. R. Secchi, "Dispersant effects on YSZ electrolyte characteristics for solid oxide fuel cells," *Ceramics International*, vol. 41, no. 5, pp. 6141–6148, 2015.

[122] S. R. Hui, J. Roller, S. Yick et al., "A brief review of the ionic conductivity enhancement for selected oxide electrolytes," *Journal of Power Sources*, vol. 172, no. 2, pp. 493–502, 2007.

[123] P. Nadoll, T. Angerer, J. L. Mauk, D. French, and J. Walshe, "The chemistry of hydrothermal magnetite: a review," *Ore Geology Reviews*, vol. 61, pp. 1–32, 2014.

[124] O. Makarchuk, T. Dontsova, A. Perekos, A. Skoblik, and Y. Svystunov, "Magnetic mineral nanocomposite sorbents for wastewater treatment," *Journal of Nanomaterials*, vol. 2017, Article ID 8579598, 7 pages, 2017.

[125] R. A. Revia and M. Zhang, "Magnetite nanoparticles for cancer diagnosis, treatment, and treatment monitoring: recent advances," *Materials Today*, vol. 19, no. 3, pp. 157–168, 2016.

[126] J. Leitner, V. Bartůněk, D. Sedmidubský, and O. Jankovský, "Thermodynamic properties of nanostructured ZnO," *Applied Materials Today*, vol. 10, pp. 1–11, 2018.

[127] J. Zheng, J. Xiao, and J.-G. Zhang, "The roles of oxygen non-stoichiometry on the electrochemical properties of oxide-based cathode materials," *Nano Today*, vol. 11, no. 5, pp. 678–694, 2016.

[128] W.-J. Yin, B. Wen, C. Zhou, A. Selloni, and L. M. Liu, "Excess electrons in reduced rutile and anatase TiO_2," *Surface Science Reports*, vol. 73, no. 2, pp. 58–82, 2018.

[129] F. Xu, "Review of analytical studies on TiO_2 nanoparticles and particle aggregation, coagulation, flocculation, sedimentation, stabilization," *Chemosphere*, vol. 212, pp. 662–677, 2018.

[130] N. Arconada, A. Durán, S. Suárez et al., "Synthesis and photocatalytic properties of dense and porous TiO_2-anatase thin films prepared by sol-gel," *Applied Catalysis B: Environmental*, vol. 86, no. 1–2, pp. 1–7, 2009.

[131] Z. Fan and J. G. Lu, "Zinc oxide nanostructures: synthesis and properties," *Journal of Nanoscience and Nanotechnology*, vol. 5, no. 10, pp. 1561–1573, 2005.

[132] Z. L. Wang, "Zinc oxide nanostructures: growth, properties and applications," *Journal of Physics: Condensed Matter*, vol. 16, pp. 829–858, 2004.

[133] L. Renuka, K. S. Anantharaju, S. C. Sharma et al., "Hollow microspheres Mg-doped ZrO_2 nanoparticles: green assisted synthesis and applications in photocatalysis and photoluminescence," *Journal of Alloys and Compounds*, vol. 672, pp. 609–622, 2016.

[134] A. Król, P. Pomastowski, K. Rafińska, V. Railean-Plugaru, and B. Buszewski, "Zinc oxide nanoparticles: synthesis, antiseptic activity and toxicity mechanism," *Advances in Colloid and Interface Science*, vol. 249, pp. 37–52, 2017.

[135] J. Zhang and A. Yu, "Nanostructured transition metal oxides as advanced anodes for lithium-ion batteries," *Science Bulletin*, vol. 60, no. 9, pp. 823–838, 2015.

[136] S. Mallakpour and E. Khadem, "Carbon nanotube-metal oxide nanocomposites: fabrication, properties and applications," *Chemical Engineering Journal*, vol. 302, pp. 344–367, 2016.

[137] T. A. Dontsova, L. M. Kulikov, and I. M. Astrelin, "Adsorption photocataltic properties of micronic and graphene (2D) nanoparticles of molybdenum dichalcogenides," *Journal of Water Chemistry and Technology*, vol. 39, no. 3, pp. 132–137, 2017.

[138] X. Carrier, S. Royer, and E. Marceau, "Chapter 2. Synthesis of metal oxide catalysts," in *Metal Oxides in Heterogeneous Catalysis*, pp. 43–103, Elsevier, 2018.

[139] K. Naseem, Z. H. Farooqi, R. Begum, and A. Irfan, "Removal of Congo red dye from aqueous medium by its catalytic reduction using sodium borohydride in the presence of various inorganic nano-catalysts: a review," *Journal of Cleaner Production*, vol. 187, pp. 296–307, 2018.

[140] S. B. Singh and P. K. Tandon, "Catalysis: a brief review on nano-catalyst," *Journal of Energy and Chemical Engineering*, vol. 2, no. 3, pp. 106–115, 2014.

[141] M. Landmann, E. Rauls, and W. G. Schmidt, "The electronic structure and optical response of rutile, anatase and brookite TiO_2," *Journal of Physics: Condensed Matter*, vol. 24, no. 19, pp. 195503–195506, 2012.

[142] N. Rahimi, R. A. Pax, and E. M. A. Gray, "Review of functional titanium oxides. I: TiO_2 and its modifications," *Progress in Solid State Chemistry*, vol. 44, no. 3, pp. 86–105, 2016.

[143] H. Zangeneh, A. A. L. Zinatizadeh, M. Habibi, M. Akia, and M. Hasnain Isa, "Photocatalytic oxidation of organic dyes

and pollutants in wastewater using different modified titanium dioxides: a comparative review," *Journal of Industrial and Engineering Chemistry*, vol. 26, pp. 1–36, 2015.

[144] M. R. D. Khaki, M. S. Shafeeyan, A. A. A. Raman, and W. M. A. W. Daud, "Application of doped photocatalysts for organic pollutant degradation—a review," *Journal of Environmental Management*, vol. 198, Part 2, pp. 78–94, 2017.

[145] J. Wen, X. Li, W. Liu, Y. Fang, J. Xie, and Y. Xu, "Photocatalysis fundamentals and surface modification of TiO_2 nanomaterials," *Chinese Journal of Catalysis*, vol. 36, no. 12, pp. 2049–2070, 2015.

[146] Y. Liu, L. Tian, X. Tan, X. Li, and X. Chen, "Synthesis, properties, and applications of black titanium dioxide nanomaterials," *Science Bulletin*, vol. 62, no. 6, pp. 431–441, 2017.

[147] K. Fischer, A. Gawel, D. Rosen et al., "Low-temperature synthesis of anatase/rutile/brookite TiO_2 nanoparticles on a polymer membrane for photocatalysis," *Catalysts*, vol. 7, no. 7, p. 209, 2017.

[148] Y. Liao and W. Que, "Preparation and photocatalytic activity of TiO_2 nanotube powders derived by a rapid anodization process," *Journal of Alloys and Compounds*, vol. 505, no. 1, pp. 243–248, 2010.

[149] J. Yu and B. Wang, "Effect of calcination temperature on morphology and photoelectrochemical properties of anodized titanium dioxide nanotube arrays," *Applied Catalysis B: Environmental*, vol. 94, no. 3-4, pp. 295–302, 2010.

[150] S.-J. Kim, E. G. Lee, S. D. Park et al., "Photocatalytic effects of rutile phase TiO_2 ultrafine powder with high specific surface area obtained by a homogeneous precipitation process at low temperatures," *Journal of Sol-Gel Science and Technology*, vol. 22, no. 1/2, pp. 63–74, 2001.

[151] M. I. H. Chowdhury, M. S. Hossain, M. A. S. Azad et al., "Photocatalytic degradation of methyl orange under UV using ZnO as catalyst," *International Journal of Scientific & Engineering Research*, vol. 9, no. 6, pp. 1646–1649, 2018.

[152] N. A. Yusoff, S.-A. Ong, L.-N. Ho, Y. S. Wong, and W. F. Khalik, "Degradation of phenol through solar-photocatalytic treatment by zinc oxide in aqueous solution," *Desalination and Water Treatment*, vol. 54, pp. 1–8, 2014.

[153] A. Akyol and M. Bayramoğlu, "Photocatalytic degradation of Remazol Red F3B using ZnO catalyst," *Journal of Hazardous Materials*, vol. 124, no. 1–3, pp. 241–246, 2005.

[154] L. Zhu and W. Zeng, "Room-temperature gas sensing of ZnO-based gas sensor: a review," *Sensors and Actuators A: Physical*, vol. 267, pp. 242–261, 2017.

[155] P. Struk, T. Pustelny, K. Gołaszewska, M. A. Borysiewicz, and A. Piotrowska, "Gas sensors based on ZnO structures," *Acta Physica Polonica A*, vol. 124, no. 3, pp. 567–569, 2013.

[156] L. Li, T. Zhai, Y. Bando, and D. Golberg, "Recent progress of one-dimensional ZnO nanostructured solar cells," *Nano Energy*, vol. 1, no. 1, pp. 91–106, 2012.

[157] P. Yang, H. Yan, S. Mao et al., "Controlled growth of ZnO nanowires and their optical properties," *Advanced Functional Materials*, vol. 12, no. 5, pp. 323–331, 2002.

[158] C. M. Lieber and Z. L. Wang, "Functional nanowires," *MRS Bulletin*, vol. 32, no. 2, pp. 99–108, 2007.

[159] X. Fang, Y. Bando, U. K. Gautam, C. Ye, and D. Golberg, "Inorganic semiconductor nanostructures and their field-emission applications," *Journal of Materials Chemistry*, vol. 18, no. 5, pp. 509–522, 2008.

[160] Y. Wang, M. Wu, Z. Jiao, and J. Y. Lee, "One-dimensional SnO_2 nanostructures: facile morphology tuning and lithium storage properties," *Nanotechnology*, vol. 20, no. 34, article 345704, 2009.

[161] N. Ramgir, N. Datta, M. Kaur et al., "Metal oxide nanowires for chemiresistive gas sensors: issues, challenges and prospects," *Colloids and Surfaces A: Physicochemical and Engineering Aspects*, vol. 439, pp. 101–116, 2013.

[162] S. Choopun, N. Hongsith, and E. Wongrat, "Chapter 1. Metal-oxide nanowires for gas sensors," in *Nanowires*, pp. 3–24, IntechOpen Limited, London, 2012.

[163] A. Galadima and O. Muraza, "A review on glycerol valorization to acrolein over solid acid catalysts," *Journal of the Taiwan Institute of Chemical Engineers*, vol. 67, pp. 29–44, 2016.

[164] A. Chieregato, J. M. López Nieto, and F. Cavani, "Mixed-oxide catalysts with vanadium as the key element for gas-phase reactions," *Coordination Chemistry Reviews*, vol. 301-302, pp. 3–23, 2015.

[165] A. Azzouz, S. K. Kailasa, S. S. Lee et al., "Review of nanomaterials as sorbents in solid-phase extraction for environmental samples," *TrAC Trends in Analytical Chemistry*, vol. 108, pp. 347–369, 2018.

[166] R. Liu, L. Chi, X. Wang, Y. Sui, Y. Wang, and H. Arandiyan, "Review of metal (hydr)oxide and other adsorptive materials for phosphate removal from water," *Journal of Environmental Chemical Engineering*, vol. 6, no. 4, pp. 5269–5286, 2018.

[167] N. Yamazoe, "Toward innovations of gas sensor technology," *Sensors and Actuators B*, vol. 108, no. 1-2, pp. 2–14, 2005.

[168] L. B. Tahar, M. H. Oueslati, and M. J. A. Abualreish, "Synthesis of magnetite derivatives nanoparticles and their application for the removal of chromium (VI) from aqueous solutions," *Journal of Colloid and Interface Science*, vol. 512, pp. 115–126, 2018.

[169] R. D. Ambashta and M. Sillanpää, "Water purification using magnetic assistance: a review," *Journal of Hazardous Materials*, vol. 180, no. 1–3, pp. 38–49, 2010.

[170] A. R. Mahdavian and M. A.-S. Mirrahimi, "Efficient separation of heavy metal cations by anchoring polyacrylic acid on superparamagnetic magnetite nanoparticles through surface modification," *Chemical Engineering Journal*, vol. 159, no. 1–3, pp. 264–271, 2010.

[171] P. Xu, G. M. Zeng, D. L. Huang et al., "Use of iron oxide nanomaterials in wastewater treatment: a review," *Science of the Total Environment*, vol. 424, pp. 1–10, 2012.

[172] X. Hu, G. Li, and J. C. Yu, "Design, fabrication, and modification of nanostructured semiconductor materials for environmental and energy applications," *Langmuir*, vol. 26, no. 5, pp. 3031–3039, 2010.

[173] F.-L. Fan, Z. Qin, J. Bai et al., "Rapid removal of uranium from aqueous solutions using magnetic Fe_3O_4@SiO_2 composite particles," *Journal of Environmental Radioactivity*, vol. 106, pp. 40–46, 2012.

[174] D. Jing and D. Song, "Optical properties of nanofluids considering particle size distribution: experimental and theoretical investigations," *Renewable and Sustainable Energy Reviews*, vol. 78, pp. 452–465, 2017.

[175] Y. Xianyu, Q. Wang, and Y. Chen, "Magnetic particles-enabled biosensors for point-of-care testing," *TrAC Trends in Analytical Chemistry*, vol. 106, pp. 213–224, 2018.

[176] D. Lisjak and A. Mertelj, "Anisotropic magnetic nanoparticles: a review of their properties, syntheses and potential

applications," *Progress in Materials Science*, vol. 95, pp. 286–328, 2018.

[177] J. M. Munyalo and X. Zhang, "Particle size effect on thermophysical properties of nanofluid and nanofluid based phase change materials: a review," *Journal of Molecular Liquids*, vol. 265, pp. 77–87, 2018.

[178] P. A. Maurice and M. F. Hochella, "Chapter 5. Nanoscale particles and processes: a new dimension in soil science," *Advances in Agronomy*, vol. 100, pp. 123–153, 2008.

[179] M. Dragoman and D. Dragoman, "Plasmonics: applications to nanoscale terahertz and optical devices," *Progress in Quantum Electronics*, vol. 32, no. 1, pp. 1–41, 2008.

[180] S. Hashimoto, D. Werner, and T. Uwada, "Studies on the interaction of pulsed lasers with plasmonic gold nanoparticles toward light manipulation, heat management, and nanofabrication," *Journal of Photochemistry and Photobiology C: Photochemistry Reviews*, vol. 13, no. 1, pp. 28–54, 2012.

[181] Z. Li, H. Jiang, C. Xu, and L. Gu, "A review: using nanoparticles to enhance absorption and bioavailability of phenolic phytochemicals," *Food Hydrocolloids*, vol. 43, pp. 153–164, 2015.

[182] D. Kandi, S. Martha, and K. M. Parida, "Quantum dots as enhancer in photocatalytic hydrogen evolution: a review," *International Journal of Hydrogen Energy*, vol. 42, no. 15, pp. 9467–9481, 2017.

[183] L. Moro, M. Turemis, B. Marini, R. Ippodrino, and M. T. Giardi, "Better together: strategies based on magnetic particles and quantum dots for improved biosensing," *Biotechnology Advances*, vol. 35, no. 1, pp. 51–63, 2017.

[184] A. Dan, H. C. Barshilia, K. Chattopadhyay, and B. Basu, "Solar energy absorption mediated by surface plasma polaritons in spectrally selective dielectric-metal-dielectric coatings: a critical review," *Renewable and Sustainable Energy Reviews*, vol. 79, pp. 1050–1077, 2017.

[185] R. Tucceri, "A review about the surface resistance technique in electrochemistry," *Surface Science Reports*, vol. 56, no. 3–4, pp. 85–157, 2004.

[186] F. Pan, C. Song, X. J. Liu, Y. C. Yang, and F. Zeng, "Ferromagnetism and possible application in spintronics of transition-metal-doped ZnO films," *Materials Science and Engineering: R: Reports*, vol. 62, no. 1, pp. 1–35, 2008.

[187] S. J. Lee, S. Souma, G. Ihm, and K. J. Chang, "Magnetic quantum dots and magnetic edge states," *Physics Reports*, vol. 394, no. 1, pp. 1–40, 2004.

[188] J. Pan, H. Shen, and S. Mathur, "One-dimensional SnO_2 nanostructures: synthesis and applications," *Journal of Nanotechnology*, vol. 2012, Article ID 917320, 12 pages, 2012.

[189] T. Zhai, X. Fang, M. Liao et al., "A comprehensive review of one-dimensional metal-oxide nanostructure photodetectors," *Sensors*, vol. 9, no. 8, pp. 6504–6529, 2009.

[190] M. M. Arafat, B. Dinan, S. A. Akbar, and A. S. M. A. Haseeb, "Gas sensors based on one dimensional nanostructured metal-oxides: a review," *Sensors*, vol. 12, no. 6, pp. 7207–7258, 2012.

[191] T. A. Dontsova, S. V. Nagirnyak, V. V. Zhorov, and Y. V. Yasiievych, "SnO_2 nanostructures: effect of processing parameters on their structural and functional properties," *Nanoscale Research Letters*, vol. 12, no. 1, pp. 332–337, 2017.

[192] C. Guillén and J. Herrero, "TCO/metal/TCO structures for energy and flexible electronics," *Thin Solid Films*, vol. 520, no. 1, pp. 1–17, 2011.

[193] K. Ellmer, R. Mientus, and S. Seeger, "Metallic oxides (ITO, ZnO, SnO_2, TiO_2)," in *Transparent Conductive Materials: Materials, Synthesis, Characterization, Applications*, pp. 31–80, Wiley-VCH Verlag GmbH & Co. KGaA, 2018.

[194] G. Yang, Z. Yan, and T. Xiao, "Preparation and characterization of SnO_2/ZnO/TiO_2 composite semiconductor with enhanced photocatalytic activity," *Applied Surface Science*, vol. 258, no. 22, pp. 8704–8712, 2012.

[195] K. Rajeshwar, M. E. Osugi, W. Chanmanee et al., "Heterogeneous photocatalytic treatment of organic dyes in air and aqueous media," *Journal of Photochemistry and Photobiology C: Photochemistry Reviews*, vol. 9, no. 4, pp. 171–192, 2008.

[196] A. McEvoy, L. Castañer, and T. Markvart, Eds., *Solar Cells: Materials, Manufacture and Operation*, 2nd edition2nd edition, , 2013.

[197] M. E. Osugi, M. V. B. Zanoni, C. R. Chenthamarakshan et al., "Toxicity assessment and degradation of disperse azo dyes by photoelectrocatalytic oxidation on Ti/TiO_2 nanotubular array electrodes," *Journal of Advanced Oxidation Technologies*, vol. 11, no. 3, pp. 425–434, 2008.

[198] T. Sekino, "Synthesis and applications of titanium oxide nanotubes," *Inorganic and Metallic Nanotubular Materials*, vol. 117, pp. 17–32, 2010.

[199] S. Munnix and M. Schmeits, "Surface electronic structure of SnO_2(110)," *Solid State Communications*, vol. 43, no. 11, pp. 867–871, 1982.

[200] T. A. Miller, S. D. Bakrania, C. Perez, and M. S. Wooldridge, "Nanosturctured tin dioxide materials for gas sensor applications," *Functional Nanomaterials*, vol. 30, pp. 1–24, 2006.

[201] D. Barreca, D. Bekermann, E. Comini et al., "1D ZnO nanoassemblies by plasma-CVD as chemical sensors for flammable and toxic gases," *Sensors and Actuators B: Chemical*, vol. 149, no. 1, pp. 1–7, 2010.

[202] A. Iannaci, B. Mecheri, A. D'Epifanio, and S. Licoccia, "Sulfated zirconium oxide as electrode and electrolyte additive for direct methanol fuel cell applications," *International Journal of Hydrogen Energy*, vol. 39, no. 21, pp. 11241–11249, 2014.

[203] Y. Hirata, S. Daio, A. Kai et al., "Performance of yttria-stabilized zirconia fuel cell using H_2-CO_2 gas system and CO-O_2 gas system," *Ceramics International*, vol. 42, no. 16, pp. 18373–18379, 2016.

[204] D. A. Agarkov, M. A. Borik, V. T. Bublik et al., "Structure and transport properties of melt grown Sc_2O_3 and CeO_2 doped ZrO_2 crystals," *Solid State Ionics*, vol. 322, pp. 24–29, 2018.

[205] H. Kwak and S. Chaudhuri, "Role of vacancy and metal doping on combustive oxidation of Zr/ZrO_2 core-shell particles," *Surface Science*, vol. 604, no. 23–24, pp. 2116–2128, 2010.

[206] A. S. Teja and P.-Y. Koh, "Synthesis, properties, and applications of magnetic iron oxide nanoparticles," *Progress in Crystal Growth and Characterization of Materials*, vol. 55, no. 1–2, pp. 22–45, 2009.

[207] S. P. Gubin, Y. A. Koksharov, G. B. Khomutov, and G. Y. Yurkov, "Magnetic nanoparticles: production methods, structure and properties," *Successes Chemistry*, vol. 74, no. 6, pp. 539–574, 2005.

[208] G. E. Zilberman, *Electricity and Magnetism*, Science, Moscow, 1970.

[209] A. Moezzi, A. M. McDonagh, and M. B. Cortie, "Zinc oxide particles: synthesis, properties and applications," *Chemical Engineering Journal*, vol. 185-186, pp. 1–22, 2012.

[210] S. Das and V. Jayaraman, "SnO_2: a comprehensive review on structures and gas sensors," *Progress in Materials Science*, vol. 66, pp. 112–255, 2014.

[211] S. Park, S. Lim, and H. Choi, "Chemical vapor deposition of iron and iron oxide thin films from Fe(II) dihydride complexes," *Chemistry of Materials*, vol. 18, no. 22, pp. 5150–5152, 2006.

[212] M. J. Lawrence, A. Kolodziej, and P. Rodriguez, "Controllable synthesis of nanostructured metal oxide and oxyhydroxide materials via electrochemical methods," *Current Opinion in Electrochemistry*, vol. 10, pp. 7–15, 2018.

[213] I. N. Ivanenko, T. A. Dontsova, I. M. Astrelin, and V. V. Trots, "Low-temperature synthesis, structure-sorption characterisics and photocatalytic activity of TiO_2 nanostructures," *Journal of Water Chemistry and Technology*, vol. 38, no. 1, pp. 14–20, 2016.

[214] G. Chatel, "Sonochemistry in nanocatalysis: the use of ultrasound from the catalyst synthesis to the catalytic reaction," *Current Opinion in Green and Sustainable Chemistry*, vol. 15, pp. 1–6, 2019.

[215] C. Y. Teh, T. Y. Wu, and J. C. Juan, "An application of ultrasound technology in synthesis of titania-based photocatalyst for degrading pollutant," *Chemical Engineering Journal*, vol. 317, pp. 586–612, 2017.

[216] S. Vallejos, F. di Maggio, T. Shujah, and C. Blackman, "Chemical vapour deposition of gas sensitive metal oxides," *Chemosensors*, vol. 4, no. 1, pp. 4–18, 2016.

[217] D. Zappa, V. Galstyan, N. Kaur, H. M. M. Munasinghe Arachchige, O. Sisman, and E. Comini, "Metal oxide-based heterostructures for gas sensors: a review," *Analytica Chimica Acta*, vol. 1039, pp. 1–23, 2018.

[218] Y. Luo, C. Zhang, B. Zheng, X. Geng, and M. Debliquy, "Hydrogen sensors based on noble metal doped metal-oxide semiconductor: a review," *International Journal of Hydrogen Energy*, vol. 42, no. 31, pp. 20386–20397, 2017.

[219] F. C. Vásquez, F. Paraguay-Delgado, J. E. Morales-Mendoza et al., "Shape and size controlled growth of SnO_2 nanoparticles by efficient approach," *Superlattices and Microstructures*, vol. 90, pp. 274–287, 2016.

[220] W. Wei, Z. Wang, Z. Liu et al., "Metal oxide hollow nanostructures: fabrication and Li storage performance," *Journal of Power Sources*, vol. 238, pp. 376–387, 2013.

[221] L. Qiao and M. T. Swihart, "Solution-phase synthesis of transition metal oxide nanocrystals: morphologies, formulae, and mechanisms," *Advances in Colloid and Interface Science*, vol. 244, pp. 199–266, 2017.

[222] G. L. J. P. da Silva, M. L. C. P. da Silva, and T. Caetano, "Preparation and characterization of hydrous zirconium oxide formed by homogeneous precipitation," *Materials Research*, vol. 5, no. 2, pp. 149–153, 2002.

[223] Q. Yang, Z. Lu, J. Liu et al., "Metal oxide and hydroxide nanoarrays: hydrothermal synthesis and applications as supercapacitors and nanocatalysts," *Progress in Natural Science: Materials International*, vol. 23, no. 4, pp. 351–366, 2013.

[224] H. Ou and S. Lo, "Review of titania nanotubes synthesized via the hydrothermal treatment: fabrication, modification, and application," *Separation and Purification Technology*, vol. 58, no. 1, pp. 179–191, 2007.

[225] D. C. Manfroi, A. dos Anjos, A. A. Cavalheiro, L. A. Perazolli, J. A. Varela, and M. A. Zaghete, "Titanate nanotubes produced from microwave-assisted hydrothermal synthesis: photocatalytic and structural properties," *Ceramics International*, vol. 40, no. 9, pp. 14483–14491, 2014.

[226] E. Arpaç, F. Sayılkan, M. Asiltürk, P. Tatar, N. Kiraz, and H. Sayılkan, "Photocatalytic performance of Sn-doped and undoped TiO_2 nanostructured thin films under UV and vis-lights," *Journal of Hazardous Materials*, vol. 140, no. 1–2, pp. 69–74, 2007.

[227] M. Á. L. Zavala, S. A. L. Morales, and M. Ávila-Santos, "Synthesis of stable TiO_2 nanotubes: effect of hydrothermal treatment, acid washing and annealing temperature," *Heliyon*, vol. 3, no. 11, article e00456, 2017.

[228] A. Solmaz, S. Balci, and T. Dogu, "Synthesis and characterization of V, Mo and Nb incorporated micro–mesoporous MCM-41 materials," *Materials Chemistry and Physics*, vol. 125, no. 1–2, pp. 148–155, 2011.

[229] B. K. Mutuma, G. N. Shao, W. D. Kim, and H. T. Kim, "Sol-gel synthesis of mesoporous anatase-brookite and anatase-brookite-rutile TiO_2 nanoparticles and their photocatalytic properties," *Journal of Colloid and Interface Science*, vol. 442, pp. 1–7, 2015.

[230] Z. Li, Z. J. Yao, A. A. Haidry et al., "Resistive-type hydrogen gas sensor based on TiO_2: a review," *International Journal of Hydrogen Energy*, vol. 43, no. 45, pp. 21114–21132, 2018.

[231] O. Carp, C. L. Huisman, and A. Reller, "Photoinduced reactivity of titanium dioxide," *Progress in Solid State Chemistry*, vol. 32, no. 1–2, pp. 33–177, 2004.

[232] A. Kutuzova and T. Dontsova, "Synthesis, characterization and properties of titanium dioxide obtained by hydrolytic method," in *2017 IEEE 7th International Conference Nanomaterials: Application & Properties (NAP)*, pp. 01NNPT02-1–01NNPT02-5, Odessa, Ukraine, 2017.

[233] T. Dontsova, I. Ivanenko, and I. Astrelin, "Synthesis and characterization of titanium (IV) oxide from various precursors," *Nanoplasmonics, Nano-Optics, Nanocomposites, and Surface Studies*, vol. 167, pp. 275–293, 2015.

[234] J. G. Lu, P. Chang, and Z. Fan, "Quasi-one-dimensional metal oxide materials—synthesis, properties and applications," *Materials Science and Engineering: R: Reports*, vol. 52, no. 1–3, pp. 49–91, 2006.

[235] B. B. Wang, K. Zhu, J. Feng et al., "Low-pressure thermal chemical vapour deposition of molybdenum oxide nanorods," *Journal of Alloys and Compounds*, vol. 661, pp. 66–71, 2016.

[236] H. Coskun, A. Aljabour, L. Uiberlacker et al., "Chemical vapor deposition-based synthesis of conductive polydopamine thin-films," *Thin Solid Films*, vol. 645, pp. 320–325, 2018.

[237] S. V. Nagirnyak, V. A. Lutz, T. A. Dontsova, and I. M. Astrelin, "Synthesis and characterization of tin (IV) oxide obtained by chemical vapor deposition method," *Nanoscale Research Letters*, vol. 11, no. 1, pp. 343–347, 2016.

[238] E. Comini, "Metal oxide nano-crystals for gas sensing," *Analytica Chimica Acta*, vol. 568, no. 1–2, pp. 28–40, 2006.

[239] M. K. Baek, S. J. Park, and D. J. Choi, "Synthesis of zirconia (ZrO_2) nanowires via chemical vapor deposition," *Journal of Crystal Growth*, vol. 459, pp. 198–202, 2017.

[240] K. Assim, J. Jeschke, A. Jakob et al., "Manganese half-sandwich complexes as metal-organic chemical vapor deposition precursors for manganese-based thin films," *Thin Solid Films*, vol. 619, pp. 265–272, 2016.

[241] C. J. Brinker and D. R. Dunphy, "Morphological control of surfactant-templated metal oxide films," *Current Opinion in Colloid & Interface Science*, vol. 11, no. 2–3, pp. 126–132, 2006.

[242] L. Zhang, W. Yu, C. Han et al., "Large scaled synthesis of heterostructured electrospun TiO_2/SnO_2 nanofibers with an enhanced photocatalytic activity," *Journal of the Electrochemical Society*, vol. 164, no. 9, pp. H651–H656, 2017.

[243] J. Gong, H. Qiao, S. Sigdel et al., "Characteristics of SnO_2 nanofiber/TiO_2 nanoparticle composite for dye-sensitized solar cells," *AIP Advances*, vol. 5, no. 6, article 067134, 2015.

[244] G. Elango and S. M. Roopan, "Efficacy of SnO_2 nanoparticles toward photocatalytic degradation of methylene blue dye," *Journal of Photochemistry and Photobiology B: Biology*, vol. 155, pp. 34–38, 2016.

[245] M. V. Arularasu, J. Devakumar, and T. V. Rajendran, "An innovative approach for green synthesis of iron oxide nanoparticles: characterization and its photocatalytic activity," *Polyhedron*, vol. 156, pp. 279–290, 2018.

[246] A. Marzec, Z. Pędzich, and W. Maziarz, "Preparation of nanocrystalline composite TiO_2-SnO_2 powders using sol-gel method combined with hydrothermal treatment," *Processing and Application of Ceramics*, vol. 10, no. 4, pp. 249–256, 2016.

[247] K. H. Lee, H. J. Jung, J. H. Lee et al., "Facile solid-state synthesis of oxidation-resistant metal nanoparticles at ambient conditions," *Solid State Sciences*, vol. 79, pp. 38–47, 2018.

[248] Y. Fedenko, T. Dontsova, and I. Astrelin, "Physico-chemical and sorptive properties of nanocomposites based on zirconium oxide," *Chemistry & Chemical Technology*, vol. 8, no. 1, pp. 51–55, 2014.

[249] O. V. Makarchuk, T. A. Dontsova, and A. E. Perekos, "Chapter 54. Magnetic nanocomposite sorbents on mineral base," *Nanophysics, Nanomaterials, Interface Studies, and Applications*, vol. 195, pp. 705–719, 2017.

[250] X. Qu, P. J. J. Alvarez, and Q. Li, "Applications of nanotechnology in water and wastewater treatment," *Water Research*, vol. 47, no. 12, pp. 3931–3946, 2013.

[251] D. Sethi and R. Sakthivel, "ZnO/TiO_2 composites for photocatalytic inactivation of *Escherichia coli*," *Journal of Photochemistry and Photobiology B*, vol. 168, pp. 117–123, 2017.

[252] L. Chen, C. H. Zhou, S. Fiore et al., "Functional magnetic nanoparticle/clay mineral nanocomposites: preparation, magnetism and versatile applications," *Applied Clay Science*, vol. 127-128, pp. 143–163, 2016.

[253] O. Makarchuk, T. Dontsova, and G. Krymets, "Magnetic mineral nanocomposite sorbents for removal of surfactants," in *2017 IEEE 7th International Conference Nanomaterials: Application & Properties (NAP)*, pp. 02MFPM02-1–02MFPM02-6, Odessa, Ukraine, 2017.

[254] O. V. Makarchuk, T. A. Dontsova, and I. M. Astrelin, "Magnetic nanocomposites as efficient sorption materials for removing dyes from aqueous solutions," *Nanoscale Research Letters*, vol. 11, no. 1, pp. 161–167, 2016.

[255] J. Xu, X. Wang, F. Pan et al., "Synthesis of the mesoporous carbon-nano-zero-valent iron composite and activation of sulfite for removal of organic pollutants," *Chemical Engineering Journal*, vol. 353, pp. 542–549, 2018.

[256] T. Wang, L. Liang, R. Wang, Y. Jiang, K. Lin, and J. Sun, "Magnetic mesoporous carbon for efficient removal of organic pollutants," *Adsorption*, vol. 18, no. 5–6, pp. 439–444, 2012.

[257] L. Feng, M. Cao, X. Ma, Y. Zhu, and C. Hu, "Superparamagnetic high-surface-area Fe_3O_4 nanoparticles as adsorbents for arsenic removal," *Journal of Hazardous Materials*, vol. 217-218, pp. 439–446, 2012.

[258] M. Kokate, K. Garadkar, and A. Gole, "One pot synthesis of magnetite-silica nanocomposites: applications as tags, entrapment matrix and in water purification," *Journal of Materials Chemistry A*, vol. 1, no. 6, pp. 2022–2029, 2013.

[259] S. Malik, "Nanotubes from Atlantis: magnetite in pumice as a catalyst for the growth of carbon nanotubes," *Polyhedron*, vol. 152, pp. 90–93, 2018.

[260] M. F. Horst, V. Lassalle, and M. L. Ferreira, "Nanosized magnetite in low cost materials for remediation of water polluted with toxic metals, azo- and antraquinonic dyes," *Frontiers of Environmental Science & Engineering*, vol. 9, no. 5, pp. 746–769, 2015.

[261] T. A. Dontsova, E. I. Yanushevskaya, S. V. Nahirniak et al., "Directional control of the structural adsorption properties of clays by magnetite modification," *Journal of Nanomaterials*, vol. 2018, Article ID 6573016, 9 pages, 2018.

[262] E. A. Deliyanni, E. N. Peleka, and K. A. Matis, "Modeling the sorption of metal ions from aqueous solution by iron-based adsorbents," *Journal of Hazardous Materials*, vol. 172, no. 2-3, pp. 550–558, 2009.

[263] M. N. Chong, B. Jin, C. W. K. Chow, and C. Saint, "Recent developments in photocatalytic water treatment technology: a review," *Water Research*, vol. 44, no. 10, pp. 2997–3027, 2010.

[264] M. Muruganandham, R. P. S. Suri, S. Jafari et al., "Recent developments in homogeneous advanced oxidation processes for water and wastewater treatment," *International Journal of Photoenergy*, vol. 2014, Article ID 821674, 21 pages, 2014.

[265] D. B. Miklos, C. Remy, M. Jekel, K. G. Linden, J. E. Drewes, and U. Hübner, "Evaluation of advanced oxidation processes for water and wastewater treatment—a critical review," *Water Research*, vol. 139, pp. 118–131, 2018.

[266] H. Zazou, H. Afanga, S. Akhouairi et al., "Treatment of textile industry wastewater by electrocoagulation coupled with electrochemical advanced oxidation process," *Journal of Water Process Engineering*, vol. 28, pp. 214–221, 2019.

[267] C. Descorme, "Catalytic wastewater treatment: oxidation and reduction processes. Recent studies on chlorophenols?," *Catalysis Today*, vol. 297, pp. 324–334, 2017.

[268] D. Kanakaraju, B. D. Glass, and M. Oelgemöller, "Advanced oxidation process-mediated removal of pharmaceuticals from water: a review," *Journal of Environmental Management*, vol. 219, pp. 189–207, 2018.

[269] S. Jiménez, M. Andreozzi, M. M. Micó, M. G. Álvarez, and S. Contreras, "Produced water treatment by advanced oxidation processes," *Science of the Total Environment*, vol. 666, pp. 12–21, 2019.

[270] J. Khatri, P. V. Nidheesh, T. S. Anantha Singh, and M. Suresh Kumar, "Advanced oxidation processes based on zero-valent aluminium for treating textile wastewater," *Chemical Engineering Journal*, vol. 348, pp. 67–73, 2018.

[271] E. Güneş, E. Demir, Y. Güneş, and A. Hanedar, "Characterization and treatment alternatives of industrial container and drum cleaning wastewater: comparison of Fenton-like

process and combined coagulation/oxidation processes," *Separation and Purification Technology*, vol. 209, pp. 426–433, 2019.

[272] L. G. M. Silva, F. C. Moreira, A. A. U. Souza, S. M. A. G. U. Souza, R. A. R. Boaventura, and V. J. P. Vilar, "Chemical and electrochemical advanced oxidation processes as a polishing step for textile wastewater treatment: a study regarding the discharge into the environment and the reuse in the textile industry," *Journal of Cleaner Production*, vol. 198, pp. 430–442, 2018.

[273] A. Sharma, J. Ahmad, and S. J. S. Flora, "Application of advanced oxidation processes and toxicity assessment of transformation products," *Environmental Research*, vol. 167, pp. 223–233, 2018.

[274] C. W. Lai, J. C. Juan, W. B. Ko, and S. Bee Abd Hamid, "An overview: recent development of titanium oxide nanotubes as photocatalyst for dye degradation," *International Journal of Photoenergy*, vol. 2014, Article ID 524135, 14 pages, 2014.

[275] M. A. Kanjwal, N. A. M. Barakat, F. A. Sheikh, M. S. Khil, and H. Y. Kim, "Functionalization of electrospun titanium oxide nanofibers with silver nanoparticles: strongly effective photocatalyst," *International Journal of Applied Ceramic Technology*, vol. 7, pp. E54–E63, 2010.

[276] T. Pradeep and Anshup, "Noble metal nanoparticles for water purification: a critical review," *Thin Solid Films*, vol. 517, no. 24, pp. 6441–6478, 2009.

[277] F. Huang, A. Yan, and H. Zhao, "Influences of doping on photocatalytic properties of TiO_2 photocatalyst," in *Semiconductor Photocatalysis, Materials, Mechanisms and Applications*, pp. 31–80, IntechOpen, 2016.

[278] H. Park, Y. Park, W. Kim, and W. Choi, "Surface modification of TiO_2 photocatalyst for environmental applications," *Journal of Photochemistry and Photobiology C: Photochemistry Reviews*, vol. 15, pp. 1–20, 2013.

[279] M. Anpo, S. Kishiguchi, Y. Ichihashi et al., "The design and development of second-generation titanium oxide photocatalysts able to operate under visible light irradiation by applying a metal ion-implantation method," *Research on Chemical Intermediates*, vol. 27, no. 4-5, pp. 459–467, 2001.

[280] S. Ghosh and A. P. Das, "Modified titanium oxide (TiO_2) nanocomposites and its array of applications: a review," *Toxicological & Environmental Chemistry*, vol. 97, no. 5, pp. 491–514, 2015.

[281] M. Huang, J. Yu, B. Li et al., "Intergrowth and coexistence effects of TiO_2-SnO_2 nanocomposite with excellent photocatalytic activity," *Journal of Alloys and Compounds*, vol. 629, pp. 55–61, 2015.

[282] K. Majrik, E. Tálas, Z. Pászti et al., "Enhanced activity of sol-gel prepared SnO_x-TiO_2 in photocatalytic methanol reforming," *Applied Catalysis A: General*, vol. 466, pp. 169–178, 2013.

[283] I. J. Ani, U. G. Akpan, M. A. Olutoye, and B. H. Hameed, "Photocatalytic degradation of pollutants in petroleum refinery wastewater by TiO_2- and ZnO-based photocatalysts: recent development," *Journal of Cleaner Production*, vol. 205, pp. 930–954, 2018.

[284] M. Pirhashemi, A. Habibi-Yangjeh, and S. Rahim Pouran, "Review on the criteria anticipated for the fabrication of highly efficient ZnO-based visible-light-driven photocatalysts," *Journal of Industrial and Engineering Chemistry*, vol. 62, pp. 1–25, 2018.

[285] X. Chen, Z. Wu, D. Liu, and Z. Gao, "Preparation of ZnO photocatalyst for the efficient and rapid photocatalytic degradation of azo dyes," *Nanoscale Research Letters*, vol. 12, no. 1, pp. 143–148, 2017.

[286] N. Kumaresan, K. Ramamurthi, R. R. Babu, K. Sethuraman, and S. M. Babu, "Hydrothermally grown ZnO nanoparticles for effective photocatalytic activity," *Applied Surface Science*, vol. 418, pp. 138–146, 2017.

[287] K. Nakata and A. Fujishima, "TiO_2 photocatalysis: design and applications," *Journal of Photochemistry and Photobiology C: Photochemistry Reviews*, vol. 13, no. 3, pp. 169–189, 2012.

[288] S.-Y. Lee and S.-J. Park, "TiO_2 photocatalyst for water treatment applications," *Journal of Industrial and Engineering Chemistry*, vol. 19, no. 6, pp. 1761–1769, 2013.

[289] R. Lamba, A. Umar, S. K. Mehta, and S. Kumar Kansal, "Well-crystalline porous ZnO-SnO_2 nanosheets: an effective visible-light driven photocatalyst and highly sensitive smart sensor material," *Talanta*, vol. 131, pp. 490–498, 2015.

[290] S. Chaudhary, A. Umar, K. Bhasin, and S. Baskoutas, "Chemical sensing applications of ZnO nanomaterials," *Materials*, vol. 11, no. 2, p. 287, 2018.

[291] R. Kumar, O. Al-Dossary, G. Kumar, and A. Umar, "Zinc oxide nanostructures for NO_2 gas–sensor applications: a review," *Nano-Micro Letters*, vol. 7, no. 2, pp. 97–120, 2015.

[292] S. V. Nagirnyak and T. A. Dontsova, "Gas sensor device creation," in *Proceedings of the 2017 IEEE 7th International Conference on Nanomaterials: Applications and Properties*, pp. 01NNPT13-1–01NNPT13-4, Odessa, Ukraine, 2017.

[293] G. Velmathi, S. Mohan, and R. Henry, "Analysis and review of tin oxide-based chemoresistive gas sensor," *IETE Technical Review*, vol. 33, no. 3, pp. 323–331, 2015.

[294] F. A. Akgul, C. Gumus, A. O. Er et al., "Structural and electronic properties of SnO_2," *Journal of Alloys and Compounds*, vol. 579, pp. 50–56, 2013.

[295] D.-W. Cho, B.-H. Jeon, Y. Jeong et al., "Synthesis of hydrous zirconium oxide-impregnated chitosan beads and their application for removal of fluoride and lead," *Applied Surface Science*, vol. 372, pp. 13–19, 2016.

[296] C. B. Amphlett, L. A. McDonald, and M. J. Redman, "Synthetic inorganic ion-exchange materials—II: hydrous zirconium oxide and other oxides," *Journal of Inorganic and Nuclear Chemistry*, vol. 6, no. 3, pp. 236–245, 1958.

[297] N. I. Chubar, V. A. Kanibolotskyy, V. V. Strelko et al., "Adsorption of phosphate ions on novel inorganic ion exchangers," *Colloids and Surfaces A: Physicochemical and Engineering Aspects*, vol. 255, no. 1-3, pp. 55–63, 2005.

[298] S. M. Yakout and H. S. Hassan, "Adsorption characteristics of sol gel-derived zirconia for cesium ions from aqueous solutions," *Molecules*, vol. 19, no. 7, pp. 9160–9172, 2014.

[299] S. G. Botta, J. A. Navío, M:. C. Hidalgo, G. M. Restrepo, and M. I. Litter, "Photocatalytic properties of ZrO_2 and Fe/ZrO_2 semiconductors prepared by a sol-gel technique," *Journal of Photochemistry and Photobiology A: Chemistry*, vol. 129, no. 1–2, pp. 89–99, 1999.

[300] S. N. Basahel, T. T. Ali, M. Mokhtar, and K. Narasimharao, "Influence of crystal structure of nanosized ZrO_2 on photocatalytic degradation of methyl orange," *Nanoscale Research Letters*, vol. 10, no. 1, 2015.

[301] B. Pan, H. Qiu, B. Pan et al., "Highly efficient removal of heavy metals by polymer-supported nanosized hydrated

Fe(III) oxides: behavior and XPS study," *Water Research*, vol. 44, no. 3, pp. 815–824, 2010.

[302] T. A. Doncova, I. M. Astrelin, and J. N. Fedenko, "Regularities of cation sorption from water by an activated carbon-based nanocomposite," *Water and Ecology*, vol. 3, pp. 29–38, 2015.

[303] L. A. Zemskova, "Modified carbon fibers: sorbents, electrode materials, catalysts," *Bulletin of the Far Eastern Branch of the Russian Academy of Sciences*, vol. 144, no. 2, pp. 39–52, 2009.

[304] M. Shahadat, T. T. Teng, M. Rafatullah, and M. Arshad, "Titanium-based nanocomposite materials: a review of recent advances and perspectives," *Colloids and Surfaces B: Biointerfaces*, vol. 126, pp. 121–137, 2015.

[305] D. Papoulis, "Halloysite based nanocomposites and photocatalysis: a review," *Applied Clay Science*, vol. 168, pp. 164–174, 2019.

[306] T. R. Sahoo, *Polymer Nanocomposites for Environmental Applications*, in The Book: Properties and Applications of Polymer Nanocomposites, Springer, Germany, 2017.

[307] J. Zuo, X. Li, W. Jiang, X. Yang, and X. Wang, "Preparation of ZnO photocatalysts and study on photocatalytic degradation of antibiotic wastewater," in *Proceedings of the 4th International Conference on Mechatronics, Materials, Chemistry and Computer Engineering 2015*, pp. 2866–2869, Xi'an, China, 2015.

[308] F. S. Omar, H. Nay Ming, S. M. Hafiz, and L. H. Ngee, "Microwave synthesis of zinc oxide/reduced graphene oxide hybrid for adsorption-photocatalysis application," *International Journal of Photoenergy*, vol. 2014, Article ID 176835, 8 pages, 2014.

[309] S. Adhikari and D. Sarkar, "Preparation of mixed semiconductors for methyl orange degradation," *Journal of Nanomaterials*, vol. 2015, Article ID 269019, 8 pages, 2015.

[310] E. Llobet, "Gas sensors using carbon nanomaterials: a review," *Sensors and Actuators B: Chemical*, vol. 179, pp. 32–45, 2013.

[311] N. D. Hoa, N. van Quy, and D. Kim, "Nanowire structured SnO_x-SWNT composites: high performance sensor for NO_x detection," *Sensors and Actuators B: Chemical*, vol. 142, no. 1, pp. 253–259, 2009.

[312] S. Dhall and N. Jaggi, "Room temperature hydrogen gas sensing properties of Pt sputtered F-MWCNTs/SnO_2 network," *Sensors and Actuators B: Chemical*, vol. 210, pp. 742–747, 2015.

[313] G. Korotcenkov and B. K. Cho, "Metal oxide composites in conductometric gas sensors: achievements and challenges," *Sensors and Actuators B: Chemical*, vol. 244, pp. 182–210, 2017.

[314] H. Liang, F. Chen, R. Li, L. Wang, and Z. Deng, "Electrochemical study of activated carbon-semiconducting oxide composites as electrode materials of double-layer capacitors," *Electrochimica Acta*, vol. 49, no. 21, pp. 3463–3467, 2004.

[315] H. R. Rajabi, H. Arjmand, S. J. Hoseini, and H. Nasrabadi, "Surface modified magnetic nanoparticles as efficient and green sorbents: synthesis, characterization, and application for the removal of anionic dye," *Journal of Magnetism and Magnetic Materials*, vol. 394, pp. 7–13, 2015.

[316] S. C. N. Tang and I. M. C. Lo, "Magnetic nanoparticles: essential factors for sustainable environmental applications," *Water Research*, vol. 47, no. 8, pp. 2613–2632, 2013.

[317] N. A. Mikhailenko, O. V. Makarchuk, T. A. Dontsova, S. V. Horobets, and I. M. Astrilin, "Purification of aqeous media by magnetically operated saponite sorbents," *Eastern European Journal of Enterprise Technologies*, vol. 4, pp. 13–20, 2015.

[318] S. K. Giri, N. N. Das, and G. C. Pradhan, "Synthesis and characterization of magnetite nanoparticles using waste iron ore tailings for adsorptive removal of dyes from aqueous solution," *Colloids and Surfaces A: Physicochemical and Engineering Aspects*, vol. 389, no. 1-3, pp. 43–49, 2011.

[319] M. Hua, S. Zhang, B. Pan, W. Zhang, L. Lv, and Q. Zhang, "Heavy metal removal from water/wastewater by nanosized metal oxides: a review," *Journal of Hazardous Materials*, vol. 211-212, pp. 317–331, 2012.

[320] I. Larraza, M. López-Gónzalez, T. Corrales, and G. Marcelo, "Hybrid materials: magnetite-polyethylenimine-montmorillonite, as magnetic adsorbents for Cr(VI) water treatment," *Journal of Colloid and Interface Science*, vol. 385, no. 1, pp. 24–33, 2012.

[321] Z. Orolínová, A. Mockovčiaková, V. Zeleňák, and M. Myndyk, "Influence of heat treatment on phase transformation of clay-iron oxide composite," *Journal of Alloys and Compounds*, vol. 511, no. 1, pp. 63–69, 2012.

Hindawi
Journal of Nanomaterials
Volume 2019, Article ID 4239764, 9 pages
https://doi.org/10.1155/2019/4239764

Research Article

MnO_x-CeO_x Nanoparticles Supported on Graphene Aerogel for Selective Catalytic Reduction of Nitric Oxides

Zhuo Yao,[1] **Yuxiang Guo**,[1] **Yujing Yang**,[2] **Hong Huang**,[3] **and Dianli Qu**[1]

[1]*High Temperature Materials and Magnesite Resources Engineering, University of Science and Technology Liaoning, Anshan, Liaoning 114001, China*
[2]*General Petrochemical Plant of Petrochina Liaohe Oilfield, Panjin, Liaoning 124000, China*
[3]*Department of Mechanical and Materials Engineering, Wright State University, Dayton, OH 45435, USA*

Correspondence should be addressed to Hong Huang; hong.huang@wright.edu and Dianli Qu; qudianli@126.com

Received 3 August 2018; Accepted 13 September 2018; Published 8 January 2019

Guest Editor: Soubantika Palchoudhury

Removal of nitric oxides (NO_x) from stationary and transportation sources has been desired for environmental benefits. Selective catalytic reduction (SCR) of NO_x by NH_3 is attractive for its cost effectiveness and high efficiency but still technically challenging in consideration of operable temperatures. In this research, MnO_x-CeO_x hybrid nanoparticles supported on graphene aerogel (MnO_x-CeO_x/GA) are fabricated as the monolithic catalysts for potential applications to low-temperature SCR. The impacts of the particle size along with the amount and valency of catalytic elements in the nanocomposite on the catalytic activities are studied with the help of scanning electron microscopy (SEM), transmission electron microscopy (TEM), and X-ray photoelectron spectroscopy (XPS). The catalyst crystallites are a few tens of nanometers and uniformly disperse on the surface of three-dimensional (3D) directionally aligned hierarchical porous graphene aerogel (GA) networks. The novel nanocomposite catalysts exhibit over 90% NO_x conversion rate in a broad temperature range (200–300°C). Addition of CeO_x into the MnO_x-GA catalysts significantly reduces the operational temperature at the same conversion rate. In addition to Mn^{4+} ions in the catalysts, the adsorbed oxygen species which can be increased by the presence of low-valence cerium contribute to high catalytic activities in the MnO_x-CeO_x/GA catalysts.

1. Introduction

Nitric oxides (NO_x) have raised global awareness for their serious impacts on the environment such as acid rain, photochemical smog, ozone depletion, and greenhouse effects. With the increasingly stringent legislation and regulation on NO_x emission, both industrial and academic laboratories have dedicated extensive efforts to developing novel catalysts towards effective reduction of NO_x. Among various technologies, selective catalytic reduction (SCR) of NO_x with NH_3 as reductant is favorable for its low cost, high efficiency, and good stability [1, 2]. However, the present commercialized SCR catalysts applied in power plants and diesel vehicles, represented by V_2O_5-WO_3/TiO_2, still encounter some inevitable challenges. In particular, the high operating temperatures (300~400°C) in diesel engine emission result in a technical dilemma [3–6]. If the SCR system is installed before the dust collector and desulfurization tower, the catalyst is readily poisoned and deactivated. If the SCR system is located after desulfurization and particle removal process, the temperature of the flue gas can hardly meet the catalyst requirement. Therefore, developing high-performance SCR catalysts operable at temperatures lower than 300°C, preferable in the range of 100–250°C, is highly demanded.

Mn-based catalysts are attractive candidates because they exhibit good low-temperature SCR activities [1, 2, 7–11]. Ce is commonly added in theses catalysts for the benefits of improved catalytic efficiency. According to Qi et al. [7], MnO_x-CeO_x catalyst with the mole ratio Mn/(Mn + Ce) of 0.4 increased NO conversion starting at 150°C. Various supporting materials for the catalysts are reported, such as Al_2O_3, TiO_2, and active carbon fibers. Appropriate support not only provides large surface area to anchor the catalysts but also supplies the space to facilitate catalyst homogeneous

distribution. Cao et al. [12, 13] found out that in the Mn-Ce/γ-Al_2O_3 series the high surface area of γ-Al_2O_3 was an important factor to increase the active catalytic sites. Lee et al. [9] reported that MnO_x-CeO_2 catalyst supported on TiO_2 exhibited high NO conversion of 30~90% from 120 to 180°C at a space velocity of 60,000 h^{-1}. Although the MnO_x/TiO_2 catalysts exhibited much higher catalytic activity at temperature below 200°C, they have various deficiencies including low acidity, low surface area, and poor temperature endurance [10]. Better performances using carbon-based supports such as activated carbons, carbon nanotubes, and graphene have been demonstrated in SCR under excess oxygen and temperatures around 200°C [11].

We recently fabricated MnO_x-CeO_x nanoparticles supported on three-dimensional graphene aerogel (GA), i.e., MnO_x-CeO_x/GA, of different compositions and explored their SCR performances at low temperatures. Graphene aerogel inherits all the advantages of 2D graphene such as superior electrical conductivity, high chemical stability, and good mechanical properties [14]. In addition, graphene aerogel possesses the characteristics of 3D aerogel which has ultra-low density and porous network on micro-, meso-, and macroscales. The hierarchical pore structure in GA provides not only high surface area for anchoring nanoparticles but also good accessibility for gases to the active surface. These structure and property merits render GA an ideal catalyst support. In the study, the novel nanocomposite catalysts MnO_x-CeO_x/GA were subjected to systematic morphological, structural, compositional, and chemical analyses in order to gain insights of the key factors correlated with their catalytic activities.

2. Experimental

2.1. Synthesis of GA-MnCe Nanocomposite Catalysts. Firstly, graphene oxide (GO) was synthesized using the modified Hummers method [15, 16]. Typically, in the experiment, 1 gram graphite (300 mesh with 99.9% purity) and 0.5 gram sodium nitrite were mixed in the 70 mL concentrated sulfuric acid. Then, 3 grams of potassium permanganate was gradually added to the mixture and stirred in a water bath at 35°C. After 2 hours, 15 mL hydrogen peroxide was slowly added to the mixture until the color of the mixture turned into bright yellow. The resultant mixture was then rinsed thoroughly with deionized water and diluted hydrochloric acid (10 wt%) until the pH value reached around 7. The resulted graphene oxide powders were filtered out and completely dried in a vacuum furnace.

An appropriate amount of the as-prepared GO powders was added into an aqueous solution of manganese acetate with or without cerium nitrate at the predetermined composition. Gradually, ammonium hydroxide was added until the pH value of the solution reached 10. After the precipitation reaction finished, the concentration of GO in the solution was adjusted to 2 mg/mL and ultrasonicated for 2 hrs. Later, ethylenediamine was added as the reducing agent. The mixture was then sealed in a cylindrical vessel and heated at 95°C for 6 hrs. Subsequently, the obtained hydrogel was on dialysis for 24 hours, followed by the freeze-drying process. To remove all the volatile components, the aerogel complex was heated to 500°C at the ramping rate of 10°C/min in a tube furnace under the flowing Argon gas. The as-prepared MnO_x-CeO_x/GA catalysts were referred to as GA-Mn(X) or GA-Mn(X)Ce(Y), where X represents the nominal weight percentage in the composite and Y represents the molar ratio of Mn/Ce. The specimens and their corresponding nominal compositions are listed in Table 1.

Table 1: Nomination and compositions of the as-prepared GA-Mn and GA-MnCe catalysts.

Sample	Mn (wt%)	Mn/Ce (molar ratio)
GA-Mn5	5	NA
GA-Mn10	10	NA
GA-Mn15	15	NA
GA-Mn20	20	NA
GA-Mn10Ce81	10	8 : 1
GA-Mn10Ce41	10	4 : 1
GA-Mn10Ce21	10	2 : 1
GA-Mn10Ce11	10	1 : 1

2.2. Material Characterizations and Analyses. The morphologies of the as-prepared MnO_x-CeO_x/GA nanocomposite catalysts were analyzed with the help of field emission scanning electron microscopy (FESEM, ZEISS-ΣIGMA HD) and transmission electron microscopy TEM (JEOL 2100).

The weight percentages of manganese and cerium in the catalysts were determined by using inductively coupled plasma (ICP) atomic emission spectroscopy (Thermo IRIS Intrepid II). For this analysis, the catalysts were dissolved in an acid solution.

The phases of the components in the catalysts were determined using X-ray diffraction (XRD) (PANalytical X'pert Powder Diffractometer, Cu K$\alpha\lambda$ = 0.154178 nm). The operating current and voltage were 40 mA and 40 kV, respectively. The diffraction profiles were collected in the 2θ range of 10–80° at the step length of 0.013 s and the residence time of 5 s.

The elements' bonding state and valency were analyzed using X-ray photoelectron spectroscopy (XPS) collected on ESCALAB250Xi (Thermo-Fisher). The XPS peaks were fitted to Voigt functions using the XPSpeak 4.1 software having 80% Gaussian and 20% Lorentzian character, after performing a Shirley background subtraction.

2.3. SCR Activity Tests. The SCR activity tests were performed on a fixed-bed reactor in the temperature range of 60 to 320°C. The reactor contains 2 mL catalyst with a gas space velocity of 30,000 h^{-1}. The schematic reactor diagram is shown in Figure 1. A simulate gas consists of 500 ppm NO, 500 ppm NH_3, 5 vol. % O_2, and balanced with N_2. Flue gas analyzer (ZR-3200, Qingdao) was used to analyze the concentrations of NO, NO_2, and O_2 at the gas outlet. The activity data were collected and recorded when the NH_3-SCR reaction reached the steady state at each temperature point. NO conversion was calculated as follows:

$$\text{NO coversion } (\%) = 100 \times \frac{c_{\text{NO}}^{\text{in}} - c_{\text{NO}}^{\text{out}}}{c_{\text{NO}}^{\text{in}}}, \quad (1)$$

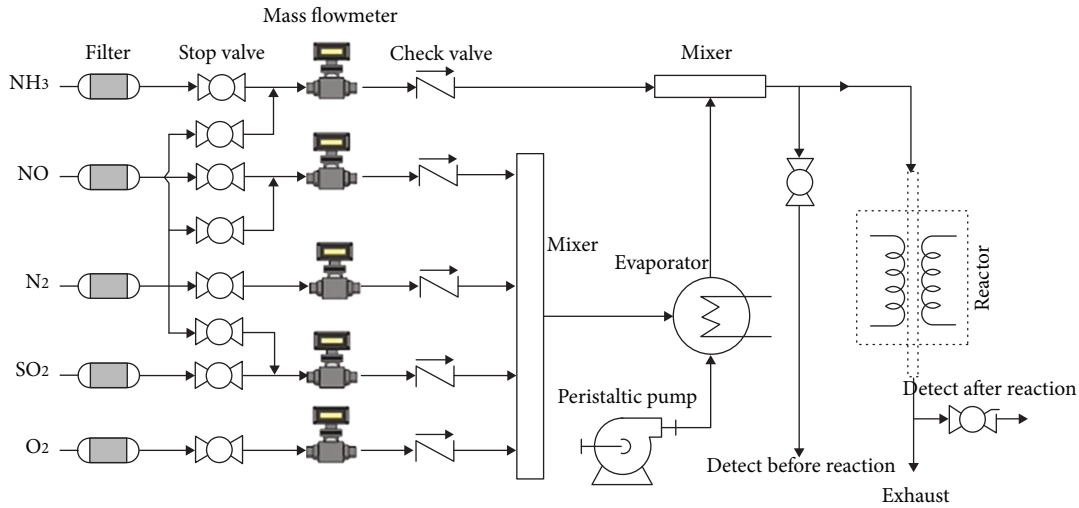

Figure 1: Schematic diagram of the flue gas analyzer used to assess NO conversion efficiency with the presence of the GA-MnCe catalysts.

Table 2: Comparison of the nominal and actual Mn and Ce loadings in the GA-MnCe catalysts.

Sample	Nominal composition		Actual composition determined by ICP	
	Mn (wt%)	Ce (wt%)	Mn (wt%)	Ce (wt%)
GA-Mn10Ce81	10	3.2	8.80	2.97
GA-Mn10Ce41	10	6.4	10.13	5.52
GA-Mn10Ce21	10	12.8	9.27	12.18
GA-Mn10Ce11	10	25.5	8.98	23.32

where c_{NO}^{in} and c_{NO}^{out} represent the inlet and outlet concentration of NO, respectively.

3. Results and Discussion

The ICP results of the as-prepared GA-MnCe catalysts are listed in Table 2. Apparently, the actual weight percentages of both Mn and Ce loadings in the composite catalyst products are in general consistent with the nominal compositional values, with error less than 1 wt%.

The morphology and microstructure of the as-prepared nanocomposite catalysts GA-Mn and GA-MnCe series are elucidated by FESEM and TEM. Figures 2(a)–2(h) exhibit representative images illustrating the morphological characteristics of the GA-Mn and GA-MnCe catalysts. Clearly seen in Figures 2(a) and 2(b), the graphene aerosol has a three-dimensional network structure made up of directionally aligned macropores with the pore diameter in the range of 20–30 μm. On the pore wall, there also exist pores of submicrometers. High-resolution TEM reveals that the pore walls are self-assembled by the intertwisted graphene sheets around 5 nm thick (see Figure 2(g)). The large pores and thin porous walls of the GA network structure ensure the high gas flow and large amount of anchor sites for nanoparticle catalysts.

As seen in Figures 2(c) and 2(d), the MnO_x catalyst nanoparticles disperse uniformly on the surface of graphene sheets. Upon increasing the catalyst loading, more particles are visualized (compared Figure 2(c) for GA-Mn5 with Figure 2(d) for GA-Mn10). When increasing MnO_x loading to 15–20 wt%, some agglomerates in the micrometer size are also observed (see Figure 2(e) for GA-Mn15). Such agglomerates are anticipated to reduce the effective active sites and hence catalytic activity.

High-resolution SEM images reveal that the sizes of catalyst particles, whether MnO_x or CeO_x, are a few tens of nanometers. Figure 2(f) is a representative image. Under TEM, it is also seen that some catalysts are having crystallite size less than 10 nanometers (see Figure 2(g)), which may be hardly visible under SEM.

The XRD profiles of the as-prepared GA-Mn and GA-MnCe hybrid materials are shown in Figure 3. In both GA-Mn and GA-MnCe series, there are broad peaks located at 26° and 44°, which originate from graphene aerosol supports. These two peaks correspond to the diffractions from (002) plane and (100) plane in the hexagonal graphitic structure, respectively. In addition, there are peaks observed at 18.3°, 32.7°, 35.2°, 40.7°, and 59.1° in the GA-Mn catalysts (see Figure 3(a)), confirming the coexistence of crystalline Mn_3O_4 and MnO. As the Mn loading increased, these peaks are more prominent. Upon adding Ce and gradually increasing the Ce loading, it is seen that the peaks from MnO_x become weaker and broader. For the samples with high content of Ce, like GA-Mn10Ce41, GA-Mn10Ce21, and GA-Mn10Ce11, the distinguishable peaks located at 28.7°, 47.6°, 56.8°, and 78° are all from CeO_2. These observations indicate the potential formation of amorphous or nanocrystalline solid-solution of MnO_x and CeO_x. The occurrence of Mn^{4+} replacing Ce^{4+} lattice position in the fluorite structure is most likely due to their size and structural similarity [17].

Figure 4 presents the NO conversion efficiency as a function of operating temperature in the presence of GA-Mn or GA-MnCe catalysts with different manganese loading or different Mn/Ce molar ratio. The SCR catalytic activities of the

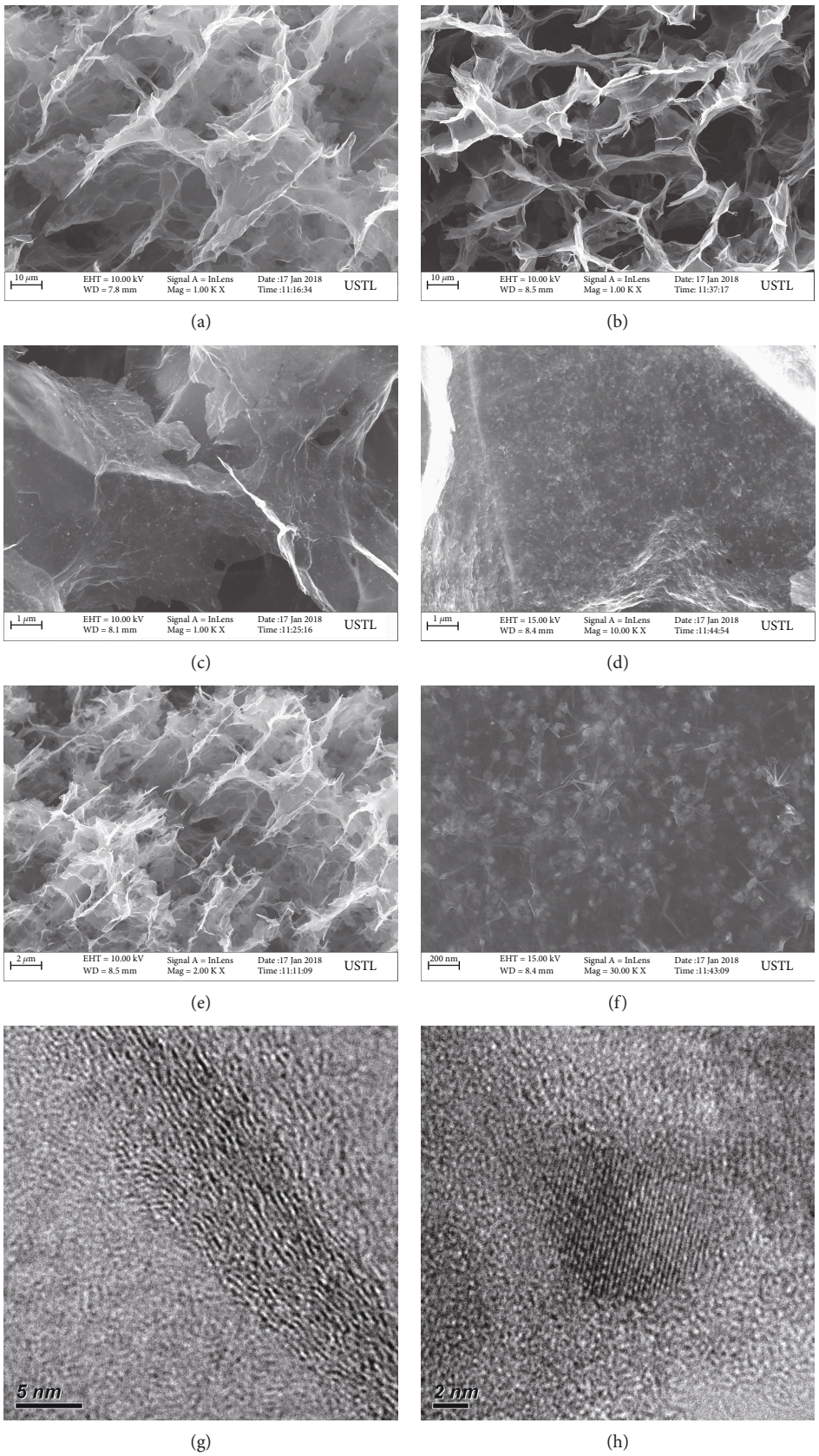

Figure 2: Representative SEM and TEM images of GA-Mn and GA-MnCe catalysts. (a) Low-mag SEM of GA-Mn10; (b) low-mag SEM of GA-Mn10Ce41; (c) medium-mag SEM of GA-Mn5; (d) medium-mag SEM of GA-Mn10; (e) medium-mag SEM of GA-Mn20; (f) high-mag SEM GA-Mn10Ce41; (g) TEM image of GA; and (h) TEM image of a catalyst particle.

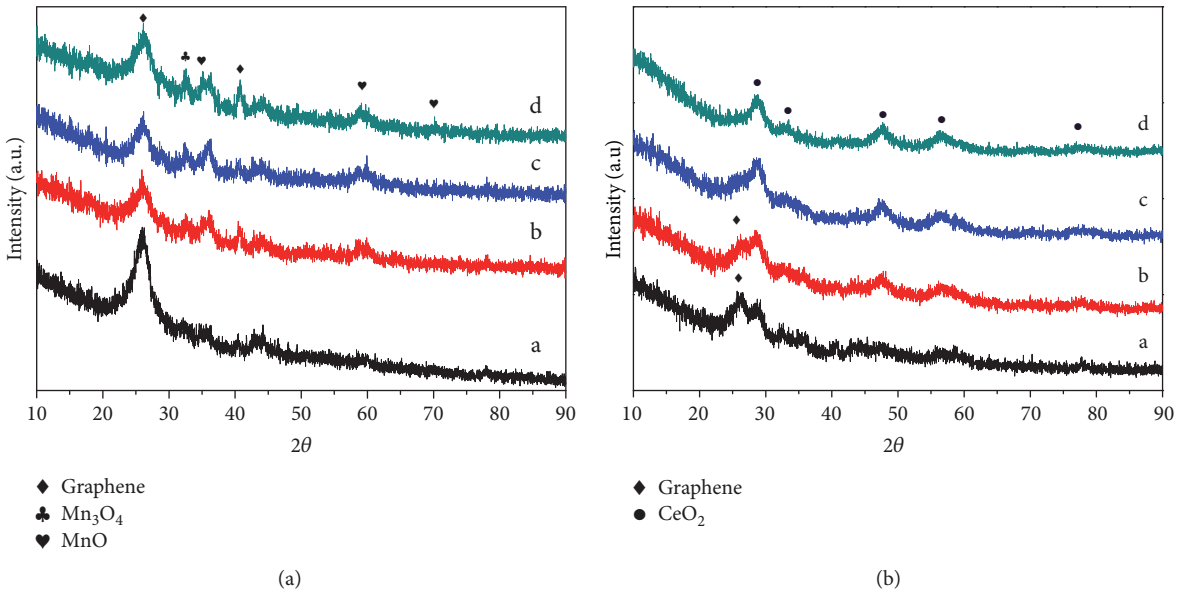

Figure 3: XRD profiles of GA-Mn and GA-MnCe catalysts. (a) (A) GA-Mn5, (B) GA-Mn10, (C) GA-Mn15, (D) GA-Mn20, and GA-Mn10Ce; (b) (A) GA-Mn10Ce81, (B) GA-Mn10Ce41, (C) GA-Mn10Ce21, (D) GA-Mn10Ce11.

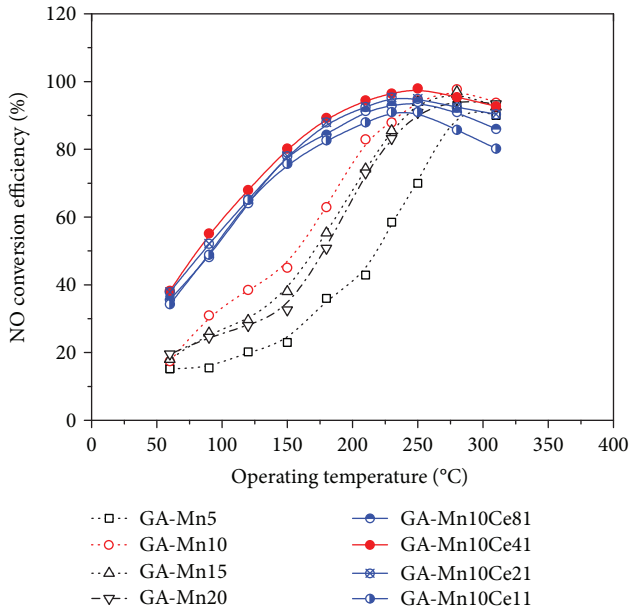

Figure 4: NO conversion efficiency as a function of operating temperature during SCR reaction with the presence of the GA-Mn or GA-MnCe catalysts. Reaction conditions: 1000 ppm NO, 1000 ppm NH_3, 5 vol. % O_2, and N_2 to balance, GHSV = 30,000 h^{-1}.

catalysts are strongly dependent on the operating temperatures. For the GA-Mn catalyst series, the NO conversion efficiency increases exponentially at low-temperature regions. The conversion efficiency reaches maximum at 280°C. Further increasing the temperature to 310°C, the NO conversion starts to decrease due to the NH_3 oxidation, which is a competitive reaction with SCR reaction [18, 19]. Among the four Mn loading, GA-Mn5 has the lowest NO conversion attributed to the insufficient Mn loading. The catalytic activity increases with Mn loading and appears to saturate when Mn loading is over 10 wt%. The slightly lower performances of GA-Mn15 and GA-Mn20 may be related to the agglomeration of the excessive amount of MnO_x nanoparticles, manifested in SEM images. The enlarged agglomerates will lead to the reduced active sites and hence the reduced conversion efficiency.

As seen also in Figure 4, the GA-MnCe catalysts exhibit superior low-temperature activity compared to the GA-Mn catalysts. The GA-Mn10Ce catalysts show 80% NO conversion at 150°C, which is over 50°C lower than GA-Mn10. The novel nanocomposite catalysts exhibit over 90% NO conversion rate in a broad temperature range (200–300°C). The molar ratio of Mn/Ce has slight impacts on the SCR activities for the GA-MnCe catalysts. GA-MnCe41 is the best throughout the entire temperature range and reached the highest NO conversion of 98% at 250°C.

Further, the stability/durability of the GA-MnCe catalysts was assessed. Figure 5 shows NO conversion efficiency as a function of time obtained from the GA-MnCe series at 250°C. At the initial stage, the NO conversion efficiency reduced gradually with time on stream for all the four GA-MnCe catalysts, possibly resulting from the catalyst sintering. However, the conversion efficiency tends to reach a steady value after a few hours. The GA-Mn10Ce41 remains the highest SCR catalytic activity with efficiency of 89% after 14 h continuous conversion.

To gain insights of the key factors affecting the SCR catalytic activities, the elemental composition and valency of nanocomposite catalysts anchored on GA surface were semi-quantified with the help of XPS analyses. The survey spectra confirm the existence of four elements, i.e., C, O, Mn, and Ce, in the GA-MnCe nanocomposite catalysts. Figures 6(a)–6(g) present the typical deconvoluted spectra of C1s, O1s, Mn2p, and Ce3d spectra. For comparison, the spectra of GA-Mn

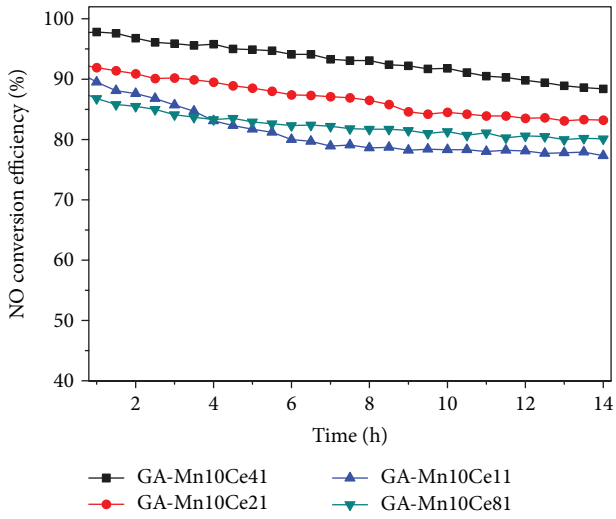

FIGURE 5: NO conversion efficiency of the GA-MnCe catalysts as a function of time on stream. Reaction conditions: 1000 ppm NO, 1000 ppm NH_3, 5 vol. % O_2, and N_2 to balance, GHSV = 30,000 h^{-1}.

(Figures 6(a), 6(c), and 6(e)) and GA-MnCe (Figures 6(b), 6(d), 6(f), and 6(g)) are presented side-by-side. The values of the computed composition are summarized in Table 3.

As seen in Figures 6(a) and 6(b), the C1s spectra can be deconvoluted into five peaks both in GA-Mn and in GA-MnCe series. Peak centered at 284.3 eV is well known corresponding to sp^2 C-C bonded carbons. The peak at 284.7 eV can be assigned to sp^3 component in the amorphous carbon residue. The peaks between 285 eV and 289 eV resulted from carbons bonded with oxygen, including single bond C-O (epoxy, carboxyl) and double bond C=O (carbonyl and quinzone) functional groups on the graphene surfaces. The weak broad peak around 290 eV is related to π-π^* shakeup [20, 21]. Based on the relative intensities, it is calculated that the amount of carbon bonded with oxygen is in average around 20% in all the specimens.

The O 1s spectra were fitted well with three peaks (see Figures 6(c) and 6(d)). The peak around 529.5 eV represents the lattice oxygen bonding with Mn or Ce (denoted as O_{latt}). It is noticeable that the binding energy of O_{latt} shifts to a low value with the addition of Ce. The amount of O_{latt} in GA-MnCe is lower than that in GA-Mn10. The peak at 532.7 eV is correlated with oxygen anchored on the graphene surface associated with C-O bonding, which is denoted as O_C. Oxygen species bonded to carbon or metal usually have insignificant impacts on the SCR reactions [22, 23]. The peak centered at 531.5 eV is assigned to the chemisorbed oxygen like O- and O_2^- on the catalytic metallic oxides and hence denoted as O_{ads} [24, 25]. The chemisorbed oxygen O_{ads} is known as the strong oxidizing agent which is involved in the activation of NH_3 and oxidation of NO in the SCR reaction. It is noteworthy that this peak is higher in GA-MnCe than in GA-Mn (compare Figures 6(c) and 6(d)). Quantitatively, the amount of chemisorbed oxygen O_{ads} in GA-Mn is consistently lower, i.e., over 5%, than that in GA-MnCe (see Table 3). The observed higher O_{ads} in the GA-MnCe catalysts corroborated well with the better NO conversion efficiency at lower temperatures.

In the Mn 2p spectra, a spin-orbit doublet of Mn 2p 1/2 and Mn 2p 3/2 with a binding energy gap of 11.5 eV is observed. The deconvoluted Mn 2p 3/2 spectra for all samples display in four peaks (see Figures 6(e) and 6(f)). The first three peaks with binding energies of 640.5 eV, 641.8 eV, and 643.2 eV originate from the different valency of manganese, i.e., Mn (II), Mn (III), and Mn (IV), respectively [11, 26, 27]. The fourth peak at 644.5 eV is a shakeup from the charge transfer between the outer electron shell and an unoccupied orbit with higher energy during the photoelectron process. The Mn 2p binding energies in GA-MnCe, compared those in GA-Mn, slightly shift to lower values, confirming the existence of interactions between manganese and cerium and formation of a solid solution. This observation is consistent with Qi and Yang's report [28] and corroborates with our XRD results. As seen in Table 3, GA-Mn5 has the lowest amount of Mn^{4+}, i.e., 12%, while all others contain Mn^{4+} in the amount of 17–19%. Since GA-Mn5 has the lowest catalytic activity throughout the operating temperature, Mn^{4+} is believed to be another key factor affecting the SCR catalytic activity. Mn^{4+} readily promotes SCR reaction because its strong oxidizing state enhances the oxidation of NH_3 [13].

Ce 3d XPS spectra are presented in Figure 6(g). In the binding energies range 880–890 eV, the first three characteristic peaks are attributed to Ce^{3+} and Ce^{4+} [29]. The assignment of the last peak is inconclusive, which varies from Ce^{3+} to Ce^{2+}. In all the GA-MnCe catalysts, peaks from Ce^{4+} are prevailing but there exists a decent amount of Ce^{3+} species. As seen in Table 3, upon the addition of Ce into the catalyst, the percentage of O_{latt} is reduced from average 43% to 29%. In contrast, O_{ads} and O_c increase to 40% and 30%, respectively. It is reported that the existence of Ce^{3+} causes the oxygen deficiencies and unsaturated chemical bonds, which cannot only promote the transformation of O_{latt} to O_{ads} but also help to adsorb more gaseous oxygen [30, 31]. As a consequence, the transfer process of the active oxygen is accelerated and the SCR activity is enhanced, which is observed in this study.

4. Conclusions

In this study, a series of novel 3D monolithic MnO_x-CeO_x nanocatalysts supported on graphene aerogel, i.e., MnO_x-CeO_x/GA, was successfully fabricated through an in situ hydrothermal and freeze-drying method. The GA support has directionally aligned micropore networks and thin porous walls, ensuring the high gas flow and large amount of anchor sites for nanoparticle catalysts. The catalyst nanoparticles are a few tens of nanometers and uniformly disperse on the surface of GA. The catalytic activity increases with Mn loading and appears to saturate when Mn loading is over 10 wt%. The slightly reduced performances of GA-Mn series at higher Mn loadings are attributed to the agglomeration of the excessive amount of MnO_x nanoparticles. Upon addition of cerium, the agglomeration is alleviated and the SCR operable temperature is lowered by 50°C at the same NO

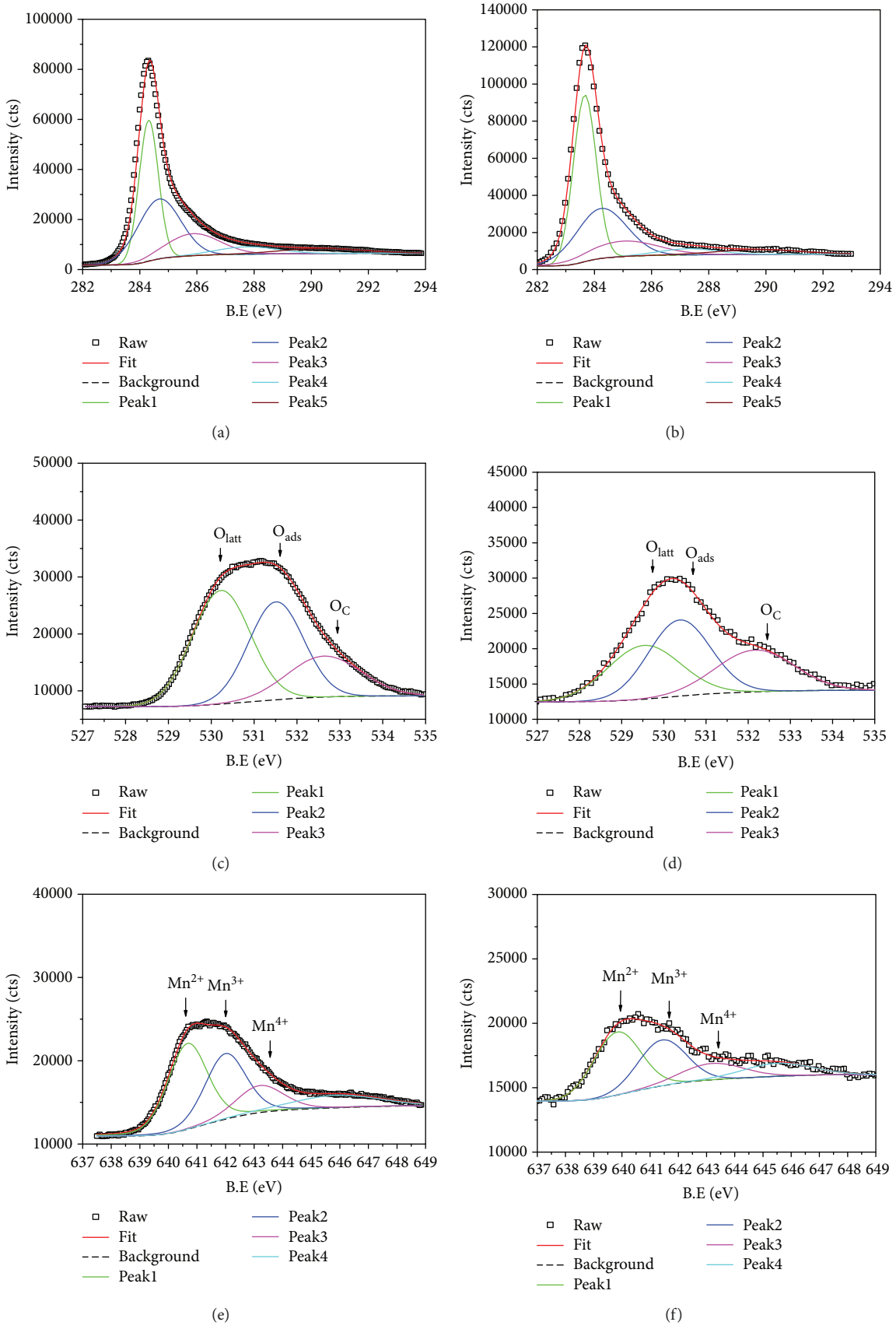

Figure 6: Continued.

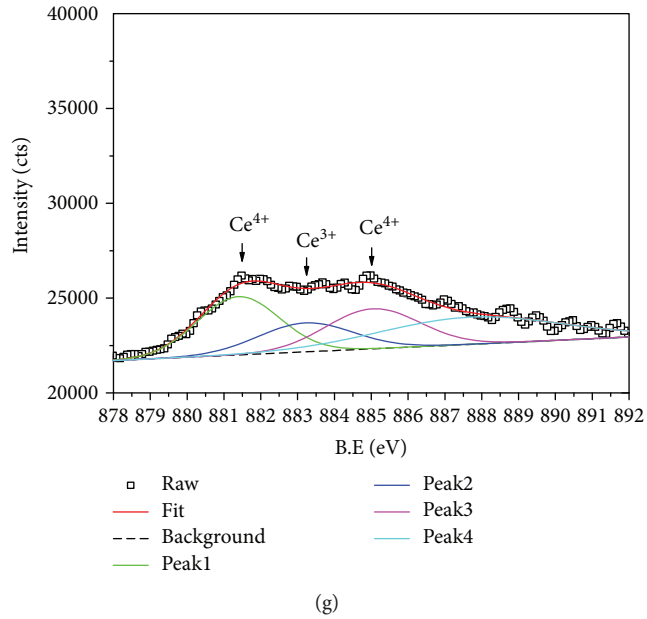

(g)

Figure 6: Representative XPS spectra, deconvoluted and fitting results of GA-Mn (a, c, e) and GA-MnCe (b, d, f, g). (a, b) C 1 s; (c, d) O 1 s; (e, f) Mn 2p; and (g) Ce 3d.

Table 3: Relative composition of different state of carbon, manganese, and oxygen in GA-Mn and GA-MnCe catalysts based on XPS analyses.

Sample	Mn (%)			O (%)		
	Mn^{2+}	Mn^{3+}	Mn^{4+}	O_{latt}	O_{ads}	O_C
GA-Mn5	53	35	12	36	36	27
GA-Mn10	46	36	17	44	36	20
GA-Mn15	48	35	17	45	34	20
GA-Mn20	48	34	18	43	34	23
GA-MnCe41	48	35	17	30	40	30
GA-MnCe21	46	34	19	28	41	31

conversion rate. The novel nanocomposite GA-MnCe catalysts exhibit over 90% NO_x conversion rate in a broad temperature range (200–300°C). GA-MN10Ce41 has over 98% conversion efficiency at 250°C with relatively good stability. Based on the XPS analyses, Mn^{4+} and O_{ads} are believed to be the two key factors contributing the SCR catalytic activity in the as-prepared GA-Mn and GA-MnCe series. Increasing Mn loading and adding Ce can slightly increase the amount of Mn^{4+}. The presence of Ce^{3+} in the GA-MnCe catalysts appears to promote the transformation of O_{latt} to O_{ads} leading to the enhancement of the SCR activity.

Data Availability

Raw data were generated at corresponding facilities described in the paper. Upon the acceptance/publishing of the paper, the derived data supporting the findings of this study are available from the corresponding author [YZ] upon request. YZ's contact info is yaozhuo1986@163.com; +8613029368800.

Conflicts of Interest

The authors declare that there is no conflict of interest regarding the publication of this paper.

Acknowledgments

The financial support of National Science-Technology Support Plan Projects of China (no. 2014BAB02B03) is gratefully acknowledged.

References

[1] T. Boningari and P. G. Smirniotis, "Impact of nitrogen oxides on the environment and human health: Mn-based materials for the NO_x abatement," *Current Opinion in Chemical Engineering*, vol. 13, pp. 133–141, 2016.

[2] M. Fu, C. Li, P. Lu et al., "A review on selective catalytic reduction of NO_x by supported catalysts at 100–300°C–Catalysts, mechanism, kinetics," *Catalysis Science & Technology*, vol. 4, no. 1, pp. 14–25, 2014.

[3] I. Nova, L. Lietti, E. Tronconi, and P. Forzatti, "Dynamics of SCR reaction over a TiO_2-supported vanadia–tungsta commercial catalyst," *Catalysis Today*, vol. 60, no. 1-2, pp. 73–82, 2000.

[4] M. Casanova, E. Rocchini, A. Trovarelli, K. Schermanz, and I. Begsteiger, "High-temperature stability of V_2O_5/TiO_2-WO_3-SiO_2 SCR catalysts modified with rare-earths," *Journal of Alloys and Compounds*, vol. 408–412, pp. 1108–1112, 2006.

[5] X. Shang, G. Hu, C. He et al., "Regeneration of full-scale commercial honeycomb monolith catalyst (V_2O_5–WO_3/TiO_2) used in coal-fired power plant," *Journal of Industrial and Engineering Chemistry*, vol. 18, no. 1, pp. 513–519, 2012.

[6] C. Qi, W. Bao, L. Wang, H. Li, and W. Wu, "Study of the V_2O_5-WO_3/TiO_2 catalyst synthesized from waste catalyst on

selective catalytic reduction of NO_x by NH_3," *Catalysts*, vol. 7, no. 12, 2017.

[7] G. Qi, R. T. Yang, and R. Chang, "MnO_x-CeO_2 mixed oxides prepared by co-precipitation for selective catalytic reduction of NO with NH_3 at low temperatures," *Applied Catalysis B: Environmental*, vol. 51, no. 2, pp. 93–106, 2004.

[8] F. Cao, J. Xiang, S. Su, P. Wang, S. Hu, and L. Sun, "Ag modified Mn–Ce/γ-Al_2O_3 catalyst for selective catalytic reduction of NO with NH_3 at low-temperature," *Fuel Processing Technology*, vol. 135, pp. 66–72, 2015.

[9] S. M. Lee, K. H. Park, and S. C. Hong, "MnO_x/CeO_2–TiO_2 mixed oxide catalysts for the selective catalytic reduction of NO with NH_3 at low temperature," *Chemical Engineering Journal*, vol. 195-196, pp. 323–331, 2012.

[10] J. Li, J. Chen, R. Ke, C. Luo, and J. Hao, "Effects of precursors on the surface Mn species and the activities for NO reduction over MnO_x/TiO_2 catalysts," *Catalysis Communications*, vol. 8, no. 12, pp. 1896–1900, 2007.

[11] Z. Tong, X. Lu, and C. Song, "The CeO_X and MnO_X nanocrystals supported on TiO_2–graphene oxide catalysts and their selective catalytic reduction properties at low temperature," *Crystals*, vol. 7, no. 6, p. 159, 2017.

[12] F. Cao, S. Su, J. Xiang et al., "The activity and mechanism study of Fe–Mn–Ce/γ-Al_2O_3 catalyst for low temperature selective catalytic reduction of NO with NH_3," *Fuel*, vol. 139, pp. 232–239, 2015.

[13] F. Cao, J. Xiang, S. Su et al., "The activity and characterization of MnO_x–CeO_2–ZrO2/γ-Al_2O_3 catalysts for low temperature selective catalytic reduction of NO with NH_3," *Chemical Engineering Journal*, vol. 243, pp. 347–354, 2014.

[14] K. S. Novoselov, A. K. Geim, S. V. Morozov et al., "Two-dimensional gas of massless Dirac fermions in graphene," *Nature*, vol. 438, no. 7065, pp. 197–200, 2005.

[15] W. S. Hummers and R. E. Offeman, "Preparation of graphitic oxide," *Journal of the American Chemical Society*, vol. 80, no. 6, pp. 1339–1339, 1958.

[16] S. Cheekati, Y. Xing, Y. Zhuang, and H. Huang, "Graphene platelets and their manganese composites for lithium ion batteries," *ECS Transactions*, vol. 33, pp. 23–32, 2011.

[17] F. Eigenmann, M. Maciejewski, and A. Baiker, "Selective reduction of NO by NH_3 over manganese–cerium mixed oxides: relation between adsorption, redox and catalytic behavior," *Applied Catalysis B: Environmental*, vol. 62, no. 3-4, pp. 311–318, 2006.

[18] A. Boyano, M. J. Lázaro, C. Cristiani, F. J. Maldonado-Hodar, P. Forzatti, and R. Moliner, "A comparative study of V_2O_5/AC and V_2O_5/Al_2O_3 catalysts for the selective catalytic reduction of NO by NH_3," *Chemical Engineering Journal*, vol. 149, no. 1-3, pp. 173–182, 2009.

[19] G. Zhou, B. Zhong, W. Wang et al., "*In situ* DRIFTS study of NO reduction by NH_3 over Fe–Ce–Mn/ZSM-5 catalysts," *Catalysis Today*, vol. 175, no. 1, pp. 157–163, 2011.

[20] S. Drewniak, R. Muzyka, A. Stolarczyk, T. Pustelny, M. Kotyczka-Morańska, and M. Setkiewicz, "Studies of reduced graphene oxide and graphite oxide in the aspect of their possible application in gas sensors," *Sensors*, vol. 16, no. 1, p. 103, 2016.

[21] D. Ferrah, O. Renault, C. Petit-Etienne et al., "XPS investigations of graphene surface cleaning using H2- and Cl2-based inductively coupled plasma," *Surface and Interface Analysis*, vol. 48, no. 7, pp. 451–455, 2016.

[22] L. Wang, B. Huang, Y. Su et al., "Manganese oxides supported on multi-walled carbon nanotubes for selective catalytic reduction of NO with NH_3: catalytic activity and characterization," *Chemical Engineering Journal*, vol. 192, pp. 232–241, 2012.

[23] S. Ponce, M. A. Peña, and J. L. G. Fierro, "Surface properties and catalytic performance in methane combustion of Sr-substituted lanthanum manganites," *Applied Catalysis B: Environmental*, vol. 24, no. 3-4, pp. 193–205, 2000.

[24] D. Zhang, L. Zhang, L. Shi et al., "In situ supported MnO_x–CeO_x on carbon nanotubes for the low-temperature selective catalytic reduction of NO with NH_3," *Nanoscale*, vol. 5, no. 3, pp. 1127–1136, 2013.

[25] H. Hu, S. Cai, H. Li, L. Huang, L. Shi, and D. Zhang, "Mechanistic aspects of deNO_x processing over TiO_2 supported Co–Mn oxide catalysts: structure–activity relationships and in situ DRIFTs analysis," *ACS Catalysis*, vol. 5, no. 10, pp. 6069–6077, 2015.

[26] Q. Tang, L. Jiang, J. Liu, S. Wang, and G. Sun, "Effect of surface manganese valence of manganese oxides on the activity of the oxygen reduction reaction in alkaline media," *ACS Catalysis*, vol. 4, no. 2, pp. 457–463, 2014.

[27] X. Zeng, X. Huo, T. Zhu, X. Hong, and Y. Sun, "Catalytic oxidation of NO over MnO_x–CeO_2 and MnO_x–TiO_2 catalysts," *Molecules*, vol. 21, no. 11, p. 1491, 2016.

[28] G. Qi and R. T. Yang, "Characterization and FTIR studies of MnO_x–CeO_2 catalyst for low-temperature selective catalytic reduction of NO with NH_3," *The Journal of Physical Chemistry B*, vol. 108, no. 40, pp. 15738–15747, 2004.

[29] M. Romeo, K. Bak, J. el Fallah, F. le Normand, and L. Hilaire, "XPS study of the reduction of cerium dioxide," *Surface and Interface Analysis*, vol. 20, no. 6, pp. 508–512, 1993.

[30] G. Carja, Y. Kameshima, K. Okada, and C. D. Madhusoodana, "Mn–Ce/ZSM5 as a new superior catalyst for NO reduction with NH_3," *Applied Catalysis B: Environmental*, vol. 73, no. 1-2, pp. 60–64, 2007.

[31] B. Guan, H. Lin, L. Zhu, and Z. Huang, "Selective catalytic reduction of NO_x with NH_3 over Mn, Ce substitution $Ti_{0.9}V_{0.1}O_{2-\delta}$ nanocomposites catalysts prepared by self-propagating high-temperature synthesis method," *The Journal of Physical Chemistry C*, vol. 115, no. 26, pp. 12850–12863, 2011.